Taming rotationally supported disks using state of the art numerical methods

Oliver Benedikt Zier

SIGILL: UNIVERSITAT: LUDOVIC: MAXIM:

München 2023

Taming rotationally supported disks using state of the art numerical methods

Oliver Benedikt Zier

Dissertation
an der Fakultät für Physik
der Ludwig–Maximilians–Universität
München

vorgelegt von
Oliver Benedikt Zier
aus Marktredwitz, Deutschland

München, den 15.02.2023

Erstgutachter: Prof. Dr. Volker Springel
Zweitgutachter: PD Dr. Klaus Dolag
Tag der mündlichen Prüfung: 31.03.2023

Contents

List of Figures

List of Tables

Zusammenfassung

Während des gravitativen Kollapses eines Objekts bleibt der Drehimpuls erhalten. Im Fall eines endlichen Drehimpulses im System kann sich eine rotierende Scheibe bilden, die durch die Rotation stabilisiert wird. Aufgrund der Einfachheit dieses Mechanismus sind Scheiben allgegenwärtig in der Astrophysik, beispielsweise als protoplanetare Scheiben, Akkretionsscheiben um Schwarze Löcher oder Spiralgalaxien. Insbesondere kalte Gasscheiben sind allerdings schwierig numerisch zu simulieren, da die Rotationsgeschwindigkeit deutlich über der Schallgeschwindigkeit liegt und bereits geringe Ungenauigkeiten in der verwendeten numerischen Methode zu einem unphysikalischem Wachstum von Fluidinstabilitäten führen können. Dies ist besonders dann problematisch, wenn man echte, physikalische Instabilitäten in diesen Systemen analysieren möchte.

Eine Methode, die im Prinzip besonders geeignet für die Analyse von Scheibensystemen sein sollte, ist die Berechnung der magnetohydrodynamischen Gleichungen auf einem mitbewegten Gitter, wie sie in dem kosmologischen Code AREPO realisiert ist. Hierdurch kann die Überschallströmung des Gases aufgrund der Rotationsgeschwindigkeit in die Bewegung des Gitters aufgenommen und dadurch eliminiert werden. Die Bewegung und permanente Verzerrung der Gitterzellen aufgrund differentieller Rotation führt jedoch in der ursprünglichen Version von AREPO zu numerischem Rauschen, was die Nützlichkeit des Codes für kalte Scheiben deutlich reduziert hat. Das Ziel dieser Arbeit war es zunächst, die Ursache des Rauschens zu ermitteln und zu beheben. Anschließend sollte evaluiert werden, wie gut die verbesserte Methode kalte Scheiben beschreiben kann, insbesondere in Situationen, in denen Turbulenz durch Magnetfelder oder durch die Wechselwirkung von Strahlungskühlung und Gravitation erzeugt wird.

Im Rahmen dieser Arbeit habe ich zuerst die sogenannte "Shearing-Box" Näherung in AREPO entwickelt, die es ermöglicht, einen kleinen Teil einer rotierenden Scheibe mit sehr hoher Auflösung zu simulieren. Im Gegensatz zu Implementierungen in anderen Codes bietet meine Lösung eine adaptive Gitterauflösung sowie vollständige Translationinvarianz. Daneben konnte ich durch eine präzisere numerische Integration der Flussfunktion über die Grenzflächen aneinanderstoßender Zellen das Rauschen auf Zellebene beheben und damit die Genauigkeit des Codes für Scherströmungen stark erhöhen.

Auf Basis dieser Verbesserungen habe ich anschließend die magnetische Rotationsinstabilität (MRI) in der Shearing-Box und die dabei auftretenden magnetischen Dynamo-Effekte analysiert. Sowohl im linearen als auch im nichtlinearen Bereich habe ich gute Übereinstimmung mit früheren Ergebnissen in der Literatur gefunden, die mit statischen

Gittercodes erzielt wurden. In einer weiteren Studie habe ich eine Codeerweiterung entwickelt, welche die Gravitationskräfte zwischen Massenelementen innerhalb der Simulationsregion unter Einbeziehung der speziellen Randbedingungen der Shearing-Box und ohne Auflösungsbeschränkungen berechnen kann. Mit Hilfe des sogenannten β-Kühlens konnte ich zeigen, dass bei schwachem Strahlungskühlen unter Eigengravitation und Scherung ein gravitoturbulenter Zustand entsteht, während sich bei effizienterem Kühlen Fragmente aus kollabierenden Gaswolken herausbilden können. Schließlich habe ich die sogenannte Rossby-Wellen-Instabilität in globalen, zweidimensionalen Scheibensimulationen analysiert. Hierbei konnte ich sowohl im linearen als auch im nichtlinearen Bereich gute Übereinstimmung mit der Literatur erzielen.

Die Entwicklung der Shearing-Box-Näherung und die Beseitigung des Rauschens auf Gitterebene in dem Verfahren mit einem bewegten Gitter ermöglicht vielfältige Forschungsanwendungen in der Zukunft. Einerseits kann die Wechselwirkung verschiedener Instabilitäten in Scheiben mit Hilfe der Shearing-Box präzise analysiert werden, andererseits sind nun auch globale Simulationen von ganzen Scheiben mit der Methode des bewegten Gitters möglich. Dieses Verfahren ermöglicht wesentlich größere Zeitschritte und geringere Advektionsfehler als herkömmliche Methoden mit stationären Gittern. Auch können Teile einer galaktischen Scheibe mit meiner Shearing-Box Methode in einem “Zoom” Modus simuliert werden, wobei insbesondere die geometrisch flexible, adaptive Auflösung der Methode von Vorteil ist.

Abstract

During the gravitational collapse of an object, the angular momentum is conserved. In the case of a finite angular momentum in the system, a rotating disk can form, stabilized by the rotation. Due to the simplicity of this mechanism, disks are ubiquitous in astrophysics, with prominent examples being protoplanetary disks, accretion disks around black holes, or spiral galaxies. However, cold gas disks in particular are difficult to be simulated numerically because the rotational velocity is much larger than the speed of sound and even small inaccuracies in the used numerical method can lead to the unphysical growth of fluid instabilities. This is particularly problematic when one tries to analyze real, physical instabilities in these systems.

A method that in principle should be particularly suitable for the analysis of disk systems is the solution of the magnetohydrodynamic equations on a moving mesh, as realized in the cosmological code AREPO. This allows the supersonic flow of the gas due to the rotational velocity to be included in the mesh motion and thereby to be eliminated. However, the motion and constant distortion of the grid cells due to differential rotation introduce numerical noise in the original version of AREPO, which has significantly reduced the usefulness of the code for cold disks. The goal of this work was first to identify and remove the origin of this “grid noise”, and second to evaluate how well the improved method can describe cold disks, especially in situations where turbulence is generated by magnetic fields or by the interaction of radiative cooling and gravity.

As part of this thesis, I first implemented the so-called “shearing-box” approximation in AREPO, which allows a small portion of a rotating disk to be simulated at very high resolution. Unlike implementations in other codes, my solution provides an adaptive spatial resolution as well as full translation invariance. Additionally, by integrating the flux function more precisely over the interfaces of neighbouring cells, I was able to remove the grid noise, greatly increasing the accuracy of the code for shear flows.

Based on these improvements, I analyzed the magnetorotational instability (MRI) in the shearing box and the magnetic dynamo effects that one can observe. In both the linear and nonlinear regimes, I found good agreement with previous results in the literature obtained with static grid codes. In a further line of work, I have developed a code extension that can compute gravitational forces between mass elements within the simulation box, including the special boundary conditions of the shearing box and without resolution constraints. Using the so-called β-cooling, I was able to show that weak radiative cooling in combination with self-gravity and shear can produce a gravito-turbulent state, while more efficient cooling can produce fragments in the form of collapsing gas clouds. Finally, I analyzed the so-called Rossby wave instability in global, two-dimensional disk simulations. Here I was able to obtain good agreement with the literature in both the linear and nonlinear regimes.

The development of the shearing-box approximation and the elimination of the grid noise in the moving mesh method allows a variety of research applications in the future. On the one hand, the interaction of different fluid instabilities in disks can be precisely analyzed using the shearing box, and on the other hand, global simulations of entire disks are now possible using the moving mesh method. This approach allows much larger time steps and smaller advection errors than conventional methods with stationary grids. Also, parts of a galactic disk can be simulated with my shearing box method in a “zoom” mode, where the geometrically flexible, adaptive resolution of the method is a particular advantage.

Chapter 1

Introduction

On large scales, the evolution of the universe is dominated by the attractive force of gravity, which is described by Einstein's theory of general relativity. This force can amplify relative overdensities in dense regions, which explains how small perturbations observed in the cosmic microwave background radiation can form giant structures like the cosmic web. During gravitational collapse, when matter falls into an overdensity due to its gravitational attraction, several conservation laws must be upheld. These include the total momentum and energy, as well as angular momentum. During a collapse, material releases gravitational energy, which must be converted either into macroscopic kinetic energy or microscopic energy (thermal energy). If the material only interacts through gravity (such as dark matter), it is unable to rid itself of small-scale, random motion, resulting in the formation of an extended object, like a dark matter halo. In contrast, baryonic matter can lose thermal energy by emitting radiation, which allows it to cool over time. However, also in this case, a remaining constraint coming from the conservation laws is the conservation of angular momentum. The material can then settle into a differentially rotating disk, with the rotational axis approximately aligned with the total angular momentum vector.

This process of disk formation due to angular momentum conservation can occur on many different scales, including the formation of galactic disks, disks around massive black holes, disks around protostars, and disks around protoplanets. It is thus of central importance for structure formation in the universe.

1.1 Overview of different rotationally supported disk systems

Rotationally supported disks are characterized by an approximate equilibrium between the centrifugal, gravitational, pressure and magnetic forces. In most systems, the former two are the dominant ones, and the latter two can be treated as perturbations. When a system is axisymmetric, we can define the rotation curve $v_{\mathrm{rot}}(r)$, which gives the equilibrium rotation velocity as a function of radius r. Closely related is the rotational frequency $\Omega(r) = v_{\mathrm{rot}}(r)/r$, which is connected to the orbital time via $T(r) = 2\pi/\Omega(r)$. In many

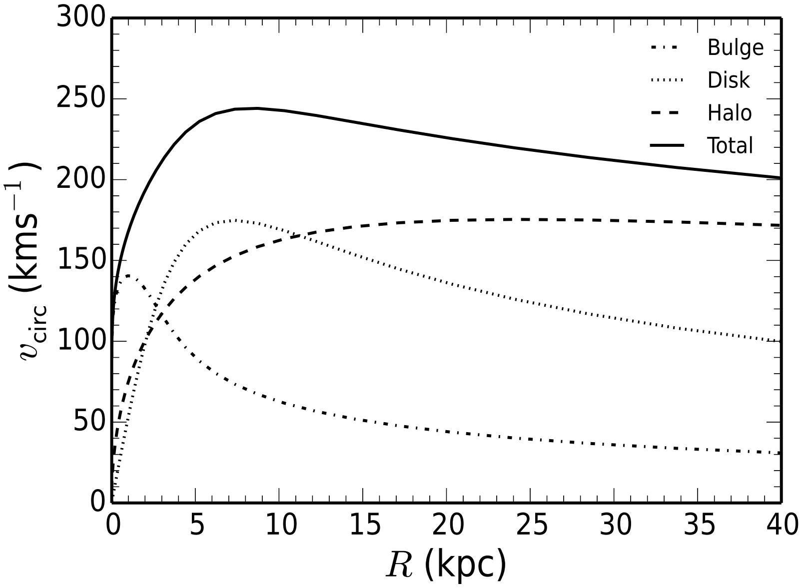

Figure 1.1: Contribution of the different components of the Milky Way to its rotation curve. The dark matter halo dominates for $R > 12$kpc. Figure from Kafle et al. (2014).

cases, the gravitational field is dominated by a central object with mass M, such as a protostar or a massive black hole. In this case one finds a so-called Keplerian orbit with:

$$v_{\rm rot}(r) = \sqrt{GM/r}, \tag{1.1}$$

$$\Omega(r) = \sqrt{GM/r^3}. \tag{1.2}$$

We introduced here the gravitational constant $G = 6.674 \times 10^{-11}\mathrm{m}^3 \cdot \mathrm{kg}^{-1} \cdot \mathrm{s}^{-2}$ (Haynes, 2014). The rotational frequency and velocity both decrease with radius, while the specific angular momentum for a circular orbit,

$$l = \sqrt{GMr}, \tag{1.3}$$

increases. This means that matter must lose angular momentum to come closer to the central object and eventually be accreted. We will return to this condition, which is an important constraint in accretion disks, later on.

Disks also exist in systems with multiple compact objects, such as binary systems (so-called circumbinary disks) or systems without a central compact object but an extended source of the gravitational field, like galactic disks. In the latter case, the dominant component of the gravitational force changes with distance from the centre of mass. In Fig. 1.1 we give as an example the rotation curve for our Milky Way galaxy, and in the following, we will discuss a number of different disk systems.

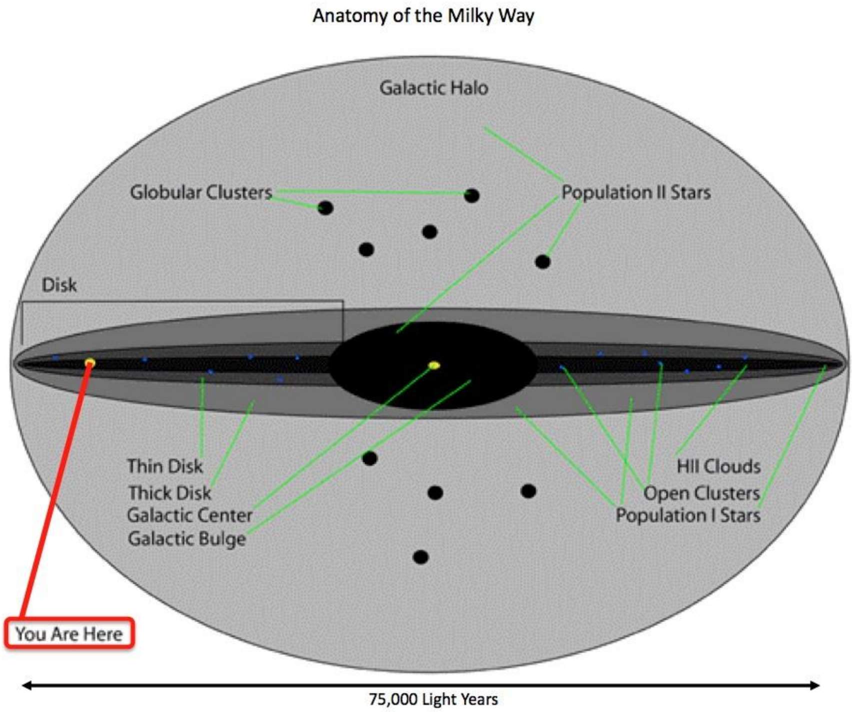

Figure 1.2: Illustration of the structure of the Milky Way. Figure from O'Connell (2018).

1.1.1 Galactic disks

Galactic disks can be found in spiral as well as in lenticular galaxies. In the following, we will concentrate on the former case, since spirals still contain a significant amount of gas that is of special interest in this thesis. In contrast to elliptical galaxies, their stellar mass is dominated by a flat, rotating disk of stars embedded in the interstellar gas. A superimposed spiral pattern gives this type of galaxy its name and our own Milky Way galaxy is a prominent example for this class. We refer to Mo et al. (2010) for an overview of galaxy formation and a discussion of the influence of the cosmological environment. We also take the data about the Milky Way used below from Mo et al. (2010).

The majority of the Milky Way's baryonic mass can be found in the disk that contains stars as well as gas. The stellar component can be divided into a thin disk with mass $\approx 5 \times 10^{10}\,\mathrm{M}_\odot$ and vertical scale height of 0.3 kpc, and a thick disk of mass $\approx 1 \times 10^{10}\,\mathrm{M}_\odot$ and vertical scale height of 3 kpc. The thin disk rotates faster than the thick disk and most of the star formation happens in the disk. Around $\approx 5 \times 10^{9}\,\mathrm{M}_\odot$ of cold gas can be found between the stars in the interstellar medium (ISM). In the centre of the galaxy, one can find a supermassive black hole with a mass of $2 \times 10^{6}\,\mathrm{M}_\odot$, which is surrounded by a stellar bulge with $\approx 10^{10}\,\mathrm{M}_\odot$. The bulge mostly contains old stars (Population II) and only has a very small star formation rate. The disk and the bulge are surrounded by a stellar halo which has similar properties to the bulge but only 3% of its mass and a radius of at least 40 kpc. The halo contains mostly old stars, including globular clusters, and is metal-poor.

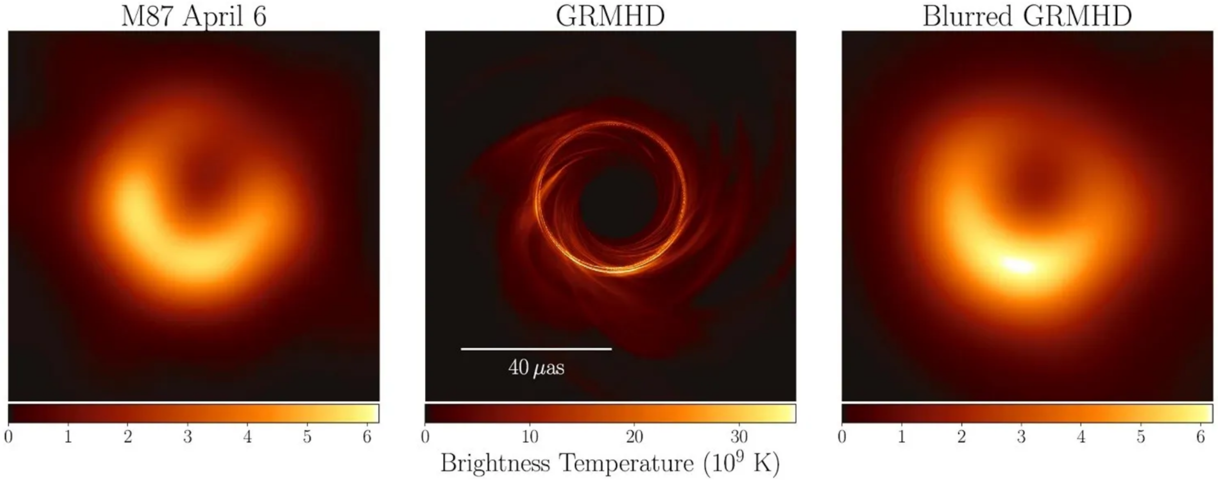

Figure 1.3: A comparison of the observation (left) of the photon ring around M87 with the results of a general relativistic MHD simulation (middle) and a blurred image obtained from the simulation (right). Figure from Event Horizon Telescope Collaboration et al. (2019a).

The total mass of the galaxy is dominated by the dark matter halo, which is not directly observable. From the rotation curve one infers a mass of around $10^{12} M_{\odot}$ and a radius of more than 100kpc for the dark matter halo. In Fig. 1.2 we give a schematic illustration of the structure of the Milky Way.

Although only a small part of the mass can be found in the interstellar medium, its evolution is of special interest since from it new stars can form. Massive stars have only a short lifetime, and therefore their evolution is tightly coupled to the evolution of the ISM. Self-gravity as well as shocks can form over-densities in the gas that can induce the formation of molecular gas. In these molecular clouds, denser regions can further increase their density and finally collapse under their own gravitational attraction. This leads to the formation of protostars that can accrete more mass from the surrounding cloud and which are surrounded by a protostellar disk. The newborn stars inject energy into the ambient medium through winds as well as radiation, which can disperse the molecular cloud. Massive stars explode as supernovae at a later time, which injects energy and newly formed metals into the ISM. Overall, star formation is thought to be a self-regulated process where higher star formation leads to more feedback, causing a reduction of the star formation rate.

Following the formation of single stars and their feedback requires a resolution which is typically not feasible in simulations of full disks. One solution is to only simulate a small part of the ISM (Walch et al., 2015; Kim & Ostriker, 2017) but even this is computationally very expensive, and of course requires accurate numerical methods.

1.1.2 AGN accretion disks

Recently, it became for the first time possible to visually prove the existence of a black hole at the centre of the M87 galaxy (Event Horizon Telescope Collaboration et al., 2019b). The compact object in the heart of this galaxy belongs to the family of supermassive black holes (SMBH), whose masses can vary from $10^5\,\mathrm{M}_\odot$ to several billion solar masses. SMBHs can grow by accreting mass from the surrounding interstellar medium or by merging with other black holes. Due to angular momentum conservation, the infalling gas will form an accretion disk. Turbulent motion in the disk leads to an effective viscosity which transports angular momentum outwards, allowing matter to sink towards the black hole. During the accretion, the gravitational energy is converted into kinetic and thermal energy, which can be further converted into radiation. The maximum luminosity possible by accretion can be estimated by the Eddington luminosity:

$$L_{\mathrm{edd}} = \frac{4\pi G M c}{\kappa}, \tag{1.4}$$

where M is the mass of the black hole and κ is the opacity. For ionized hydrogen one finds:

$$L_{\mathrm{edd}} \approx 3.2 \times 10^4 \left(\frac{M}{M_\odot}\right) L_\odot, \tag{1.5}$$

where $L_\odot$ stands for the solar luminosity (Rybicki & Lightman, 1986). Above this luminosity, the radiation pressure becomes too large and outflows are generated. Strong magnetic fields in the disk can fuel powerful jets (Liska et al., 2020) that can influence the physics of galaxies on large scales. Especially close to the black hole general relativistic effects have to be modelled (see Fig. 1.3), whereas further away the black hole can still be approximated by a point mass with Newtonian gravity. A good understanding of accretion disks is essential to unravel the growth of SMBHs and their backreaction on the galaxy through jets and outflows.

1.1.3 Protostellar and protoplanetary disks

Stars can form when an over-dense core in a molecular cloud collapses under its own self-gravity. Most of the mass ends up in the central object while some of the material forms a rotating envelope. The envelope flattens over time, leading to the formation of a protoplanetary disk. However, this disk only forms if angular momentum transfer is not too efficient, which can be the case when one considers strong magnetic fields that can be described by the ideal magnetohydrodynamics (MHD) approximation. This phenomenon is called the magnetic braking catastrophe and can be circumvented by taking into account nonideal MHD effects, which are necessary because protoplanetary disks are typically cold close to the mid-plane and have a low ionization fraction (Wurster et al., 2016).

The disk can grow further by inflows from the envelope whereas mass loss can occur through accretion onto the central object and outflows. To achieve accretion of rotationally supported material, angular momentum must be transferred outwards in the disk, which

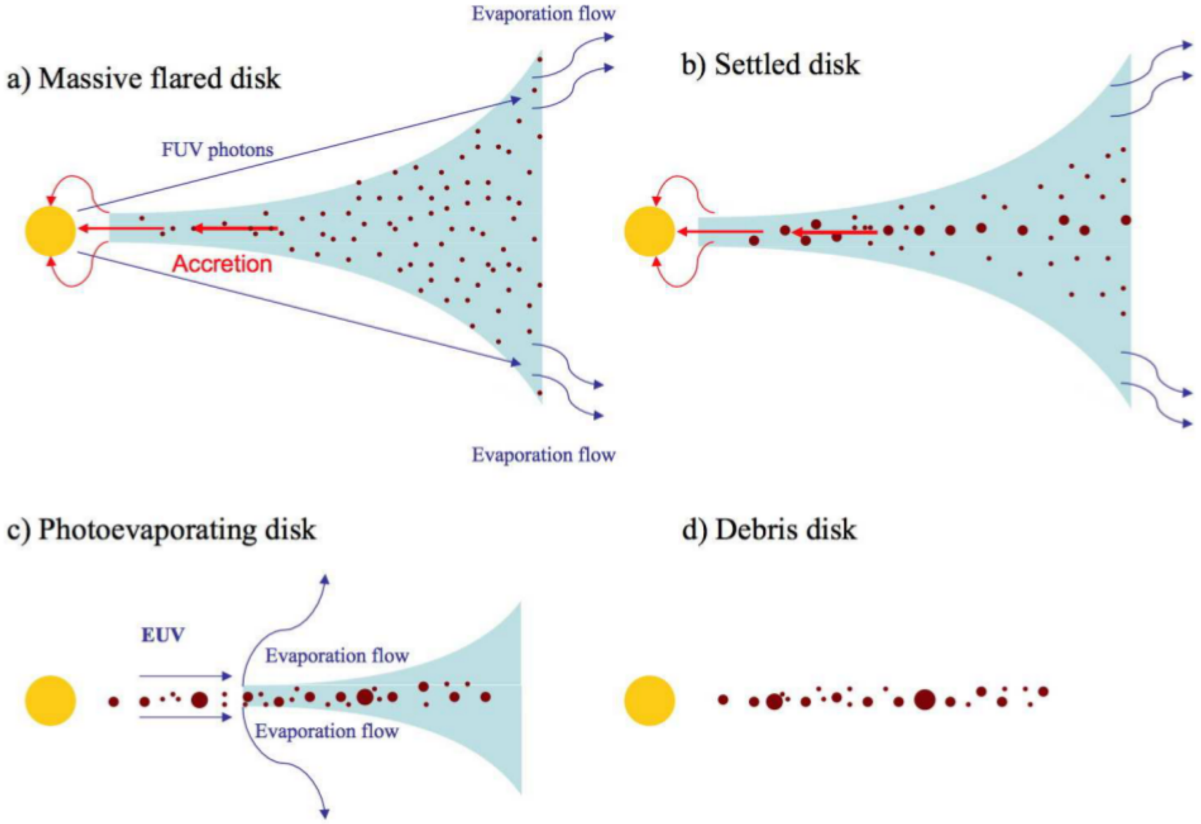

Figure 1.4: Different stages in the evolution of a protoplanetary disk. Some of the gas (blue) gets accreted onto the central object while at the same time, FUV photons evaporate gas. Small dust particles start to grow and settle in the mid-plane. After the evaporation of the gas a debris disk forms. Figure from Williams & Cieza (2011).

requires some form of viscosity, such as turbulence (see section 1.2.3 for a more in-detailed discussion). Especially at the beginning of their evolution, disks can be quite massive (up to 10% of the total mass of the central object, Armitage, 2011), which can also trigger gravitational instability. The disk is typically cold in the mid-plane. Further away from the star, the MRI can be quenched, so that it is only active on the surface of the disk and close to the star. This leads to the definition of the "dead zone", where resistivity prevents the MRI from growing and which contains only a small amount of turbulence. The gas disk eventually disperses over time due to accretion onto the central object and photoevaporation by radiation from the central object, with a typical lifetime of 5 to 10 million years (Ribas et al., 2015).

Protoplanetary disks are considered to be the main birthplace of planets. The relatively low lifetime of the gas disk itself requires a rather fast formation and growth of those planets. In general, there are two main mechanisms for forming protoplanets: through direct collapse or through core accretion. Direct collapse occurs when a part of the disk becomes unstable to gravitational instability and collapses into a bound object. This requires a massive enough disk and efficient thermal relaxation to prevent the collapse from being stopped by thermal pressure. It is therefore especially likely to happen after the formation of the disk and at the outskirts of the disk, where some massive planets were found and can therefore be explained by the direct collapse scenario. One example is HR 8799 with 4 planets with masses 5 to 10 times the mass of Jupiter at radii between 15 AU and 70 AU (Marois et al., 2008). Since the protoplanet would have a similar composition as the disk its mass would be dominated by the gas. This makes it hard to explain the solid core expected even in gas giants (Kreidberg et al., 2014) as well as their typically higher metallicity in comparison to the ISM (Bolton et al., 2017). Additionally, only massive protoplanets form and gravitational instability cannot explain the formation of Earth-like planets. One solution could be the inwards migration of planets that can change their composition and also their size.

Another mechanism to form protoplanets is through core accretion (CA). Protoplanetary disks contain around 1% of their mass as dust particles, which can collide and stick to each other, leading to the formation of larger and larger particles. After reaching a diameter of around 1 km they are massive enough to become self-gravitating such that they can focus more and more mass into collisions. An envelope consisting of gas can also form around them, which can explain the formation of gas giants. However, one problem with this theory is that collisions between dust particles can also lead to destruction rather than growth, which becomes more likely for larger particles and is especially severe for meter-sized objects. Additionally, those larger dust particles can decouple from the gas motion and orbit with a Keplerian velocity around the central object. Since gas orbits typically with a slightly lower velocity, this leads to a frictional force and a deacceleration of the dust, causing it to migrate inwards and fall into the central object. This leads to the so-called radial drift barrier, which can be overcome if a local pressure minimum exists within the disk (Dullemond, 2013).

For example, these can be rings or also vortices, in which dust particles can be efficiently trapped until their concentration becomes large enough to trigger a gravitational collapse.

The CA mechanism is typically used to explain the formation of Earth-like planets and gas giants in the inner part of the disk. In reality, both processes might play a role. For a more detailed discussion and review of the problem of planet formation, we refer to Armitage (2011) and in Fig. 1.4 we illustrate the typical evolution of a protoplanetary disk.

1.2 Mathematical description of a rotationally supported disk

In this section, we introduce the equations to describe the evolution of a gas disk interacting with a magnetic field. We will use the fluid approximation, which means that the gas has to be collisional so that the velocity distribution of gas particles follows a Maxwellian distribution. To achieve a high enough number of collisions, the mean free path as well as the time between collisions have to be significantly smaller than the length and time scales of interest. Those are given for a disk by the radius or scale height as well as the orbital frequency Ω^{-1}.

In accretion disks, these conditions are typically fulfilled, especially close to the midplane (Lesur, 2020). The fluid approximation allows us to define a density ρ, velocity $\boldsymbol{v}$, as well as pressure P at any point $\boldsymbol{x}$ in space. In general, it is possible to have several fluid species with individual densities and velocities that are coupled to each other via interaction terms. But in this thesis, we will concentrate on the single-fluid case, which means that fluid quantities are described in terms of, for example, the total density ρ and the velocity at the centre of mass of resolution elements. The evolution of these quantities is given by the Euler equations if one neglects viscous effects.

We also do not follow the evolution of the radiation field but in some cases allow for a simplified cooling description. In addition to the normal properties of a gaseous fluid, there exists a magnetic field $\boldsymbol{B}$, whose interaction with the fluid can be described by the Maxwell equations. We will use the so-called ideal magnetohydrodynamics (MHD) approximation, which assumes that the resistivity due to collisions can be neglected. In this case, the magnetic field lines are frozen into the fluid, which means they have to move along with the fluid.

1.2.1 The ideal MHD equations

The ideal MHD equations in the Heaviside–Lorentz unit system considered in this thesis can be written as

$$\frac{\partial \boldsymbol{U}}{\partial t} + \nabla \cdot \boldsymbol{F}(\boldsymbol{U}) = \boldsymbol{S}_{\mathrm{grav,self}} + \boldsymbol{S}_{\mathrm{grav,ext}} + \dot{Q}. \tag{1.6}$$

Here, we introduced the state vector $\boldsymbol{U}$, the flux vector $\boldsymbol{F}$, the source term $\boldsymbol{S}_{\mathrm{grav,self}}$ due to the gravitational force of the fluid itself, the source term $\boldsymbol{S}_{\mathrm{grav,ext}}$ describing the gravitational force from an external object such as, e.g., a central object, and finally the source term $\dot{Q}$ describes cooling and heating processes. In more explicit form, these terms are given by:

$$\boldsymbol{U} = \begin{pmatrix} \rho \\ \rho\boldsymbol{v} \\ \rho e \\ \boldsymbol{B} \end{pmatrix}, \quad F(\boldsymbol{U}) = \begin{pmatrix} \rho\boldsymbol{v} \\ \rho\boldsymbol{v}\boldsymbol{v}^T + P - \boldsymbol{B}\boldsymbol{B}^T \\ \rho e\boldsymbol{v} + P\boldsymbol{v} - \boldsymbol{B}(\boldsymbol{v}\cdot\boldsymbol{B}) \\ \boldsymbol{B}\boldsymbol{v}^T - \boldsymbol{v}\boldsymbol{B}^T \end{pmatrix},$$

$$\boldsymbol{S}_{\text{grav,self}} = \begin{pmatrix} 0 \\ -\nabla\phi_{\text{self}} \\ -(\nabla\phi_{\text{self}})\cdot\boldsymbol{v} \\ 0 \end{pmatrix}, \quad \boldsymbol{S}_{\text{grav,ext}} = \begin{pmatrix} 0 \\ -\nabla\phi_{\text{ext}} \\ -(\nabla\phi_{\text{ext}})\cdot\boldsymbol{v} \\ 0 \end{pmatrix}, \dot{Q} = \begin{pmatrix} 0 \\ 0 \\ H - L \\ 0 \end{pmatrix}, \tag{1.7}$$

where we introduced the density ρ, velocity $\boldsymbol{v}$, specific energy $e = u + \frac{1}{2}\boldsymbol{v}^2 + \frac{1}{2\rho}\boldsymbol{B}^2$, magnetic field strength $\boldsymbol{B}$, pressure $P = p_{\text{gas}} + \frac{1}{2}\boldsymbol{B}^2$, gravitational potential ϕ_{self} due to the fluid itself, an external gravitational potential ϕ_{ext}, a heating term H as well as a cooling term L. The specific energy consists of a kinetic component $\frac{1}{2}\rho v^2$ as well as a thermal component u, and a magnetic contribution $\frac{1}{2\rho}\boldsymbol{B}^2$. Similarly, the pressure P is given as the sum of a thermal component p_{gas} and a magnetic component $\frac{1}{2}\boldsymbol{B}^2$.

To close the equations we require an equation of state (EOS) that connects the thermal pressure with the density and the thermal energy. In this thesis, we use the adiabatic equation of state

$$p_{\text{gas}} = (\gamma - 1)\rho u \tag{1.8}$$

of an ideal gas, where we introduced the adiabatic index γ (the ratio of specific heats). For a mono-atomic gas, it is typically $\gamma = 5/3$. The adiabatic sound speed

$$c_s = \sqrt{\gamma P/\rho}, \tag{1.9}$$

gives the phase velocity of ordinary adiabatic sound waves. Another option we sometimes use is an isothermal equation of state

$$p_{\text{gas}} = c_s^2 \rho, \tag{1.10}$$

where the isothermal sound speed c_s is constant. In this case, we effectively assume that the heating and cooling effects are efficient enough to keep the temperature of the gas constant. This means that in equation (1.6) the energy component needs not to be evolved explicitly and can be omitted.

The gravitational potential due to the disk itself can be calculated by solving the Poisson equation:

$$\phi = 4\pi G\rho. \tag{1.11}$$

The external potential of a point-mass with mass M (i.e. $\rho = \delta(\boldsymbol{x})M$), the most common case we analyze in this thesis, is given by:

$$\phi_{\text{ext}}(r) = -\frac{GM}{r}. \tag{1.12}$$

One can integrate equation (1.6) over a volume V to better understand the naming conventions we used. The vector $\boldsymbol{Q} = \int_V \boldsymbol{U}$ contains the conserved quantities mass, momentum, energy as well as magnetic flux. The vector $\boldsymbol{F}$ describes how those quantities move in space and time but does not change the global conservation of $\boldsymbol{Q}$. The source terms on the other hand can change the total $\boldsymbol{Q}$ in the system (note that $\boldsymbol{Q}$ is only conserved in an isolated system). The gravitational force can add momentum as well as kinetic energy to the system but does not influence directly the mass distribution or the magnetic field. The heating and cooling terms can change the thermal energy of the gas and therefore the total energy. We note that one can also change the definition of the total energy to contain the gravitational potential energy. Since all gravitational forces we take into account originate from a potential, in this case, the new total energy is conserved and the gravitational source terms can be incorporated in the flux term.

1.2.2 Equilibrium state

To analyse the evolution of disks it is useful to use cylindrical coordinates. In the following, we will use the polar angle φ and two-dimensional radius $r = \sqrt{x^2 + y^2}$ as well as the vertical coordinate z. We choose the rotation axis to be parallel to the z-direction and $x = y = z = 0$ as the centre of rotation. An isolated disk is in equilibrium if all the time derivatives in equation (1.6) vanish and we will concentrate on axisymmetric discs (no dependency on φ) around a central object of mass M. We will also first neglect magnetic fields and self-gravity, and so find the momentum equation:

$$\frac{\partial \boldsymbol{v}}{\partial t} + (\boldsymbol{v} \cdot \nabla)\, \boldsymbol{v} = -\frac{1}{\rho} \nabla P - \nabla \phi_{\text{ext}}. \tag{1.13}$$

The vertical component of this equation is, under the equilibrium assumption $v_z = 0$ and $\partial v_z / \partial z = 0$,

$$\frac{1}{\rho} \frac{\partial P}{\partial z} = -\nabla \phi_{\text{ext}} = -\frac{GM}{r^2 + z^2} \frac{z}{\sqrt{r^2 + z^2}}. \tag{1.14}$$

This equation can be simplified by assuming a vertically isothermal disc with sound speed $c_s = c_s(r)$:

$$\frac{c_s^2}{\rho} \frac{\partial \rho}{\partial z} = -\frac{GM}{r^2 + z^2} \frac{z}{\sqrt{r^2 + z^2}} \tag{1.15}$$

with the solution

$$\rho(z) = C \exp\left[\frac{GM}{c_s^2 \left(r^2 + z^2\right)^{1/2}} \right]. \tag{1.16}$$

The integration constant C is determined by the mid-plane density ρ_0. If we consider regions close to the mid-plane ($z = 0$), we can use the approximation $z \ll r$ and $\Omega = \sqrt{GM/r^3}$ to rewrite equation (1.16):

$$\rho(z) = \rho_0 \exp\left[-z^2 / \left(2H^2\right) \right]. \tag{1.17}$$

We introduced here the scale height $H = c_s/\Omega$, which is a measure of how fast the density declines with z. The mid-plane density can be expressed as a function of the surface density $\Sigma(r) = \int_z \rho(z)$:

$$\rho_0(r) = \frac{1}{\sqrt{2\pi}} \frac{\Sigma(r)}{H(r)}. \tag{1.18}$$

If we allow for self-gravity, the disk becomes more compact.

The radial component of equation (1.13) with $v_r = 0 = \partial v_r/\partial t$ is given by

$$\frac{v_\phi^2}{r} = \frac{GM}{r^2} + \frac{1}{\rho}\frac{\partial P}{\partial r} \tag{1.19}$$

close to the mid-plane ($z \ll r$). Typically, the pressure decreases as a function of the radius close to the mid-plane, which means that the last term is negative and gas typically orbits with slightly smaller velocity than a point mass (see equation 1.1). This becomes especially important if one takes into account dust particles since they are not affected by the pressure term and therefore orbit with the Keplerian velocity.

The radial distribution of the surface density $\Sigma(r)$ as well as the sound speed profile $c_s(r)$ cannot be determined by the momentum equation alone but instead depends on the thermodynamic evolution of the disk. In the equilibrium case, there is additionally an equilibrium between cooling and heating effects.

1.2.3 Temporal evolution with the α viscosity model

Especially accretion disks are not in prefect equilibrium, instead matter is moving inwards to be accreted onto the central object. Since for an approximate Keplerian orbit the angular momentum per unit mass

$$l = \sqrt{GMr} \tag{1.20}$$

is increasing with increasing distance to the central object, matter has to lose angular momentum to be able to move to smaller orbits.

The angular momentum transport requires some kind of torque, and one natural option for this would be some type of viscous friction between neighbouring rings of the disk. The viscosity would deaccelerate the inner ring and accelerate the outer ring, which is equivalent to a net transport of angular momentum. In the case of a geometrically thin, axisymmetric disk this leads to the disk evolution equation (Pringle, 1981):

$$\frac{\partial \Sigma}{\partial t} = \frac{3}{r}\frac{\partial}{\partial r}\left[r^{1/2}\frac{\partial}{\partial r}\left(\nu \Sigma r^{1/2}\right)\right], \tag{1.21}$$

which describes the time dependence of the surface density Σ in the presence of a kinematic viscosity ν. The diffusive nature of this equation becomes clear if one starts with the mass m being concentrated in a small part of the disk, $\Sigma(r, t = 0) = \delta(r - r_0)\frac{m}{2\pi r_0}$. Its solution is given by:

$$\Sigma(x, \tau) = \frac{m}{\pi r_0^2 \tau x^{1/4}} \exp\left[-\frac{1 + x^2}{\tau}\right] I_{1/4}\left(\frac{2x}{\tau}\right), \tag{1.22}$$

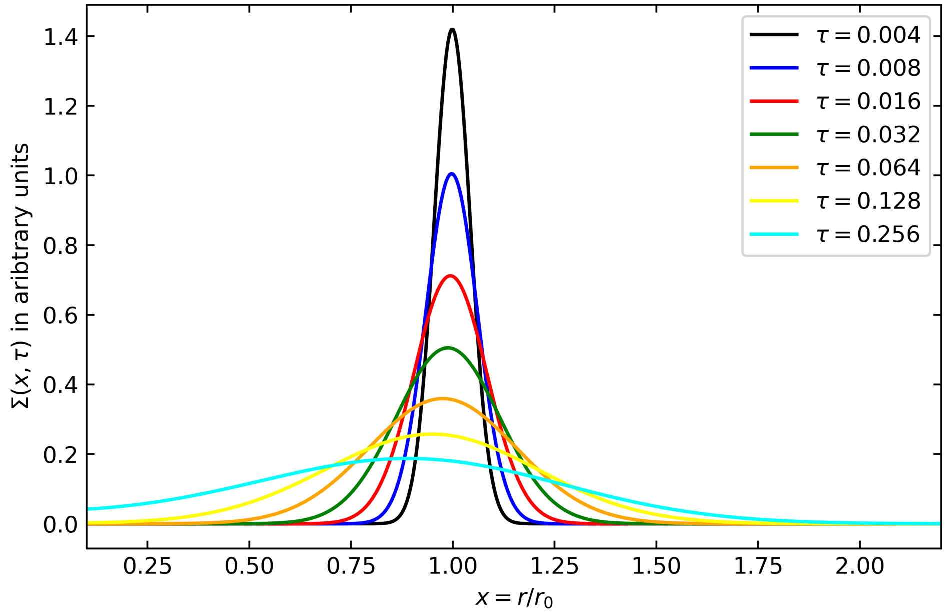

Figure 1.5: The surface density $\Sigma(x, \tau)$ as a function of the nondimensional radial coordinate x and temporal coordinate $\tau = 12\nu r_0^{-2} t$. At $\tau = 0$, all mass is concentrated in $x = 1$ and $\Sigma(x, \tau)$ is given as the solution of equation (1.21).

where we introduced the modified Bessel-function of the first kind $I_{1/4}$, the dimensionless radius $x = r/r_0$, and the new time variable $\tau = 12\nu r_0^{-2} t$. We show in Fig. 1.5 the time evolution of Σ and see how mass moves inwards while angular momentum gets transported outwards.

An interesting quantity to consider is the viscous time scale $\tau_{\text{vis}} = R^2/\nu$. Armitage (2011) finds $\tau_{\text{vis}} \approx 10^{13}$ yr for a protoplanetary disk if ν is given by the molecular viscosity. This time scale is much larger than the lifetime of such a disk and it is clear that other processes have to be responsible for the angular momentum transfer. Shakura & Sunyaev (1973) circumvent this problem by parameterizing the viscosity:

$$\nu = \alpha c_s H \tag{1.23}$$

as a product of the sound speed c_s and the scale height H. α is a free parameter and can be adjusted to match observations. This parametrization is motivated by the assumption that the effective viscosity is caused by subsonic turbulence, but the question of the source of this turbulence remains open. We will discuss in section 1.3 further fluid instabilities that can be responsible for this turbulence.

In general, α is related to the radial stress

$$\overline{W_{r\phi}} = \alpha \overline{P}, \tag{1.24}$$

where we use time and space averaged values. The stress itself can be written as a sum of

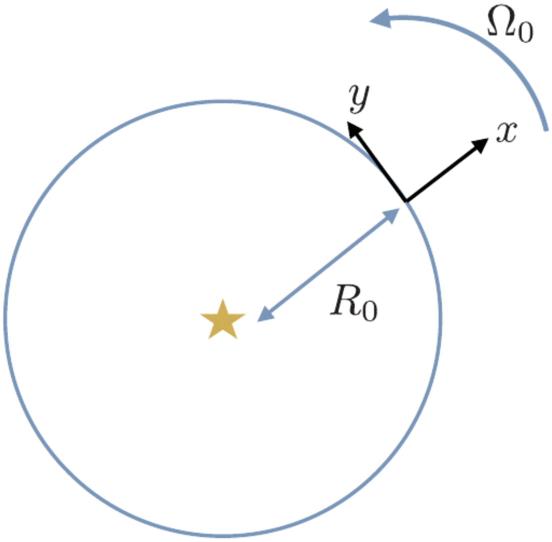

Figure 1.6: The local Cartesian coordinate system used in the Hill's approximation rotating on a circular orbit. Figure from Lesur (2020).

hydrodynamic, magnetic and gravitational terms:

$$\overline{W_{r\phi}} = \overline{\rho v_r \left(v_\varphi - v_{\mathrm{rot}}\right)} - \overline{B_\varphi B_r} + \overline{\frac{1}{4\pi G}\frac{\partial \phi}{\partial r}\frac{\partial \phi}{\partial \varphi}}. \tag{1.25}$$

1.2.4 Hill's approximation

Because for most disks the scale height H is much smaller than the radius r, one can try to separate the local dynamics on the scale of order the scale height from the global evolution in the radial direction. This leads to the idea of Hill's approximation (Hill, 1878; Goldreich & Lynden-Bell, 1965), which was later employed in numerical realizations of the so-called shearing-box approximation (Hawley et al., 1995). We first fix a radius r_0 at which we are interested in the local dynamics and calculate the local angular velocity $\Omega_0 = \Omega(r_0)$. Now we define a Cartesian coordinate system (x, y, z) that rotates with Ω_0, so that x corresponds to the radial direction, y to the azimuthal direction and z to the vertical direction. In Fig. 1.6 we show an example for this coordinate system.

After performing a coordinate transformation into the rotating, accelerated frame, one finds additional terms, namely the Coriolis force as well as the centrifugal force, which both can be written as new source terms on the right-hand side of equation (1.6):

$$\boldsymbol{S}_{\mathrm{cor}} = \begin{pmatrix} 0 \\ -2\rho\Omega_0 \hat{e}_z \times \boldsymbol{v} \\ 0 \\ 0, \end{pmatrix}, \quad \boldsymbol{S}_{\mathrm{centr}} = \begin{pmatrix} 0 \\ \rho\Omega_0 R^2 \hat{e}_r \\ \rho\Omega_0 R^2 \hat{e}_r \cdot \boldsymbol{v} \\ 0 \end{pmatrix}. \tag{1.26}$$

The centrifugal force depends on the cylindrical radius $r = \sqrt{(r_0 + x)^2 + y^2}$ and can be derived from a potential $\phi_c = -\Omega_0^2 r^2/2$. The effective potential around a point source with mass M is given by:

$$\phi_{\text{eff}} = \phi_c + \phi_{\text{ext}} = -\frac{\Omega_0^2}{2}\left[(r_0+x)^2 + y^2\right] - \frac{GM}{\sqrt{(r_0+x)^2 + y^2 + z^2}} \tag{1.27}$$

and can be expanded as:

$$\phi_{\text{eff,Hill}} = \Omega_0^2\left[-\frac{3r_0^2}{2} - \frac{3}{2}x^2 + \frac{1}{2}z^2 + O\left(\frac{H^3}{r_0}\right)\right]. \tag{1.28}$$

In Hill's approximation, with the assumption $H \ll r_0$, only the first non-trivial terms are kept. The resulting potential does not depend on y and is also independent of r_0 except in the constant term. There are also no cross-terms such as xz, and this simplicity makes Hill's approximation especially suited for analytical and numerical studies. Higher order expansions of ϕ_{eff} contain curvature terms $\propto 1/r_0$ as well as cross terms which makes the handling of the equations much more tedious.

In Fig. 1.7 we show a comparison between the full and the approximated potential. The Hill potential has a symmetry $x \to -x$, which means that no centre of attraction can be defined, and importantly, no accretion rates can be measured in the shearing box. The full potential has an asymptotical value of $-3\Omega_0^2 r_0^2/2$ for $z \to \infty$ at $x = r_0\left(\sqrt{3}-1\right)$ which is absent in the Hill potential. This means that in the reduced potential no outflows can reach $z \to \infty$, which implies a dependence on the vertical box size for outflows. We note that, for example, Brandenburg et al. (1996) used a higher-order expansion of equation (1.27), which breaks the symmetry $x \to -x$ and allows a measurement of accretion, albeit with the cost of higher computational complexity.

Hill's approximation can be generalized to central potentials with equilibrium rotational profiles $\Omega \propto r^{-q}$, where $q = 3/2$ for the Keplerian case. The final equations in Hill's approximation are given by:

$$\frac{\partial \boldsymbol{U}}{\partial t} + \nabla \cdot \boldsymbol{F}(\boldsymbol{U}) = \boldsymbol{S}_{\text{grav,e}} + \boldsymbol{S}_{\text{cor}} + \boldsymbol{S}_{\text{grav,self}} + \dot{Q}, \tag{1.29}$$

with the state vector $\boldsymbol{U}$, flux function $\boldsymbol{F}$, a source term accounting for self-gravity $\boldsymbol{S}_{\text{grav,self}}$, and a heating/cooling term $\dot{Q}$, as already defined in equation (1.7). The Coriolis force $\boldsymbol{S}_{\text{cor}}$ is defined in equation (1.26), and the source term of the effective external gravitational that follows from Hill's potential is given by:

$$\boldsymbol{S}_{\text{grav,e}} = \begin{pmatrix} 0 \\ \rho\Omega_0^2\left(2qx\hat{e}_x - z\hat{e}_z\right) \\ \rho\Omega_0^2 \boldsymbol{v}\cdot\left(2qx\hat{e}_x - z\hat{e}_z\right) \\ 0 \end{pmatrix}. \tag{1.30}$$

In the case that the external potential does not originate from a central potential and $\Omega(r)$ is not a pure power law, one can still define the shear parameter

$$q = -\left.\frac{d\ln\Omega}{d\ln r}\right|_{r=r_0}, \tag{1.31}$$

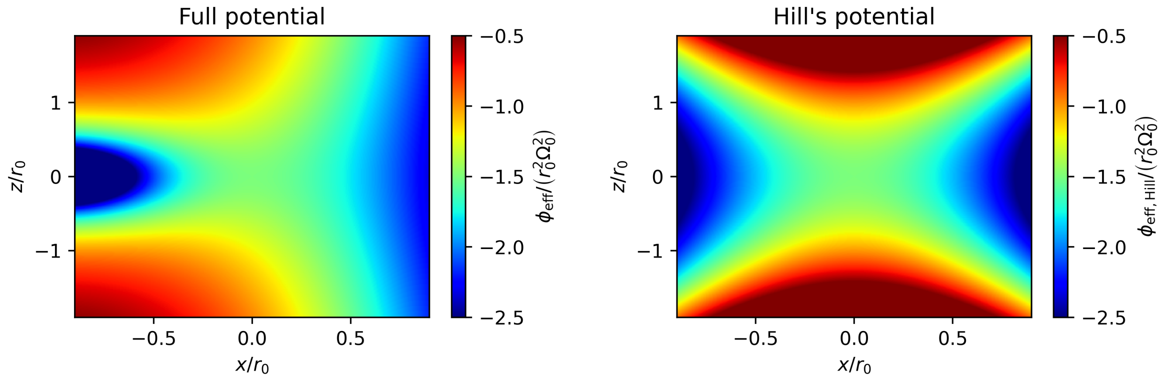

Figure 1.7: The effective potential in a rotating system as a function of the radial (x) and vertical (z) coordinate. The left side shows the full potential while the right side shows Hill's approximation.

which now depends on the radius one is interested in. In this case, the vertical potential has to be modified to represent the actual physical system.

A closer inspection of equation (1.29) shows that the Coriolis and tidal forces cancel each other for a purely azimuthal velocity field:

$$v_{y0} = -q\Omega_0 x. \tag{1.32}$$

This linear shear flow corresponds to a radial dependence of the rotational velocity in a global disk, and the linearity is a consequence of the property of Hill's approximation to only keep the lowest order terms in the expansion. Hill's approximation can be further simplified by neglecting the gravitational term in the z-direction in equation (1.29). This so-called unstratified or small shearing box assumes a box size $L \ll H$ close to the midplane and further simplifies the numerical treatment. In contrast to that, the system with the gravitational term in the z-direction is called a large or stratified shearing box. We refer to Regev & Umurhan (2008) for a detailed discussion of the assumptions and restrictions for both shearing box types. Although the shearing box does not allow the measurement of accretion rates, one can still measure

$$W_{xy} = \overline{\rho v_x (v_y - v_{y0})} - \overline{B_x B_y} + \overline{\frac{1}{4\pi G}\frac{\partial \phi}{\partial x}\frac{\partial \phi}{\partial y}}, \tag{1.33}$$

which is equivalent to the radial stress term in (1.25).

1.3 Instabilities as a source of effective viscosity

As previously discussed in section 1.2.3, accretion requires some kind of viscosity to transport angular momentum. One potential source of effective viscosity is turbulence within the disk, which can be generated by different instabilities associated with the rotational motion. In this section, we analyze the stability of accretion disks using analytical methods. While a global stability analysis is possible in certain cases with the Wentzel-Kramers-Brillouin (WKB) approximation, it is often more complex. Instead, we will focus on the shearing box model we derived in section 1.2.4 to analyze the local stability of the disk's motion.

1.3.1 Hydrodynamical stability

We start with the purely hydrodynamical case and concentrate on the evolution of a point particle in Hill's potential. Its evolution is given by:

$$\frac{\mathrm{d}}{\mathrm{d}t}\boldsymbol{v} = \begin{pmatrix} 2q\Omega_0^2 x + 2\Omega_0 v_y \\ -2\Omega_0 v_x \\ -\Omega_0^2 z \end{pmatrix}, \tag{1.34}$$

where the vertical equation describes an oscillation around the mid-plane with frequency Ω_0. The equation for the y-component of the velocity can be integrated and one obtains

$$L = v_y + 2\Omega_0 x, \tag{1.35}$$

which is equivalent to the angular momentum in the shearing box approximation (Lesur, 2020). If we start with a particle at $x = 0$ and a purely radial motion, we find $L = 0$ and the evolution of the radial velocity simplifies to

$$\frac{\mathrm{d}^2 x}{\mathrm{d}t^2} = -2\Omega_0^2 \left(2 - q\right) x, \tag{1.36}$$

which describes for $q < 2$ a harmonic oscillator with the so-called epicycle frequency

$$\kappa^2 = 2\Omega_0^2 \left(2 - q\right). \tag{1.37}$$

For the special case $q = 3/2$ we find $\kappa = \Omega_0$, which leads to the well-known result that orbits for the two body problem are closed. For $q > 2$ the system is unstable to the so-called centrifugal instability, which is equivalent to results already found by Rayleigh (1917), namely that for

$$\frac{\mathrm{d}\left(\Omega R^2\right)}{\mathrm{d}R} < 0 \tag{1.38}$$

an axially symmetric, incompressible and inviscid fluid is unstable. The criterion might be fulfilled for jets launched from accretion disks and can be generalized to relativistic hydrodynamics (Gourgouliatos & Komissarov, 2018). We refer to Klahr et al. (2018) for a derivation of the Rayleigh criterion using the Euler equations (1.6) for an unstratified disk. The linear stability of the flow for $q = 3/2$ does not mean that no non-linear or subcritical instabilities exist. The question of the existence of subcritical instabilities led to a plethora of numerical and experimental studies that however did not find one for Reynolds number of several 10^5. We refer to Fromang & Lesur (2019) for a more detailed overview of the stability of purely hydrodynamic Keplerian shear flows. In stratified and also nonisothermal disks new instabilities can emerge, which we discuss further in section 1.3.5.

1.3.2 Magnetorotational instability

The stability properties of a Keplerian flow drastically change if we add an external magnetic field. We will start with an incompressible fluid in an unstratified shearing box with a constant vertical magnetic field, $\boldsymbol{B}_0 = B_0\hat{e}_z$. We now add small axisymmetric perturbations with wavevector $\boldsymbol{k} = (0, 0, k_z)$ to the ground state, using the ansatz $\boldsymbol{v} = (0, v_{y0}, 0) + \boldsymbol{w} \exp[\sigma t + ik_z z]$ and $\boldsymbol{B} = B_0 + \boldsymbol{b} \exp[\sigma t + ik_z z]$. We can plug these terms into equation (1.29) to find:

$$k_z w_z = 0, \tag{1.39}$$

$$k_z b_z = 0, \tag{1.40}$$

$$\sigma \boldsymbol{w} = i\frac{k_z B_0}{\rho}\boldsymbol{b} + 2\Omega_0 u_y \hat{e}_x - (2-q)\Omega_0 u_x \hat{e}_y, \tag{1.41}$$

$$\sigma \boldsymbol{b} = i(k_z B_0)\boldsymbol{w} - q\Omega_0 b_x \hat{e}_y. \tag{1.42}$$

The first equation follows from the incompressibility and simplifies to $w_z = 0$. The remaining four equations can be written as a matrix equation:

$$\begin{pmatrix} \sigma & -2\Omega_0 & -i\frac{k_z B_0}{\rho} & 0 \\ (2-q)\Omega_0 & \sigma & 0 & -i\frac{k_z B_0}{\rho} \\ -ik_z B_0 & 0 & \sigma & 0 \\ 0 & -ik_z B_0 & q\Omega_0 & \sigma \end{pmatrix} \begin{pmatrix} w_x \\ w_y \\ b_x \\ b_z \end{pmatrix} = 0, \tag{1.43}$$

which only has a nontrivial solution if the matrix on the left hand side is not invertible, which means its determinant is 0. This leads to the dispersion relation

$$\sigma^4 + \sigma^2\left(2k_z^2 v_A^2 + 2(2-q)\Omega_0^2\right) + k_z^2 v_A^2\left(k_z^2 v_A^2 - 2q\Omega_0^2\right) = 0, \tag{1.44}$$

where we introduced the Alfvén velocity $v_A = B_0/\sqrt{\rho}$. For $q < 2$, the quadratic term is always positive and therefore the constant term has to be negative so that a solution with a real σ exists. This condition is fulfilled for perturbations with $k_z < \Omega_0/v_a\sqrt{2q}$, and therefore the disc becomes unstable on large enough scales independent of the magnitude of the external magnetic field.

In Fig. 1.8 we show σ as a function of $v_A k_z$. We see that $\sigma(k_z v_A)$ takes a maximum at $k_z v_A = \sqrt{2q}\Omega_0/2$ with $\sigma_{\max} = 0.75\,\Omega^{-1}$, which means that if the disk is unstable the perturbations grow on the order of the orbital time. Considering the long lifetime of, e.g., protostellar disks (several 100 orbits at $r = 100$AU around a solar-type star, Laughlin & Bodenheimer, 1994) we do not expect to observe any disc in the linear phase but instead have to take into account the nonlinear regime of this so-called magnetorotational instability (MRI). The eigenvectors of the matrix problem (1.43) are called channel modes and become unstable to parasitic instabilities which stop the exponential growth. This break down leads to the creation of turbulence and a nonlinear, saturated state can form. The saturation of the MRI for different setups will be further analyzed and discussed in Chapter 3.

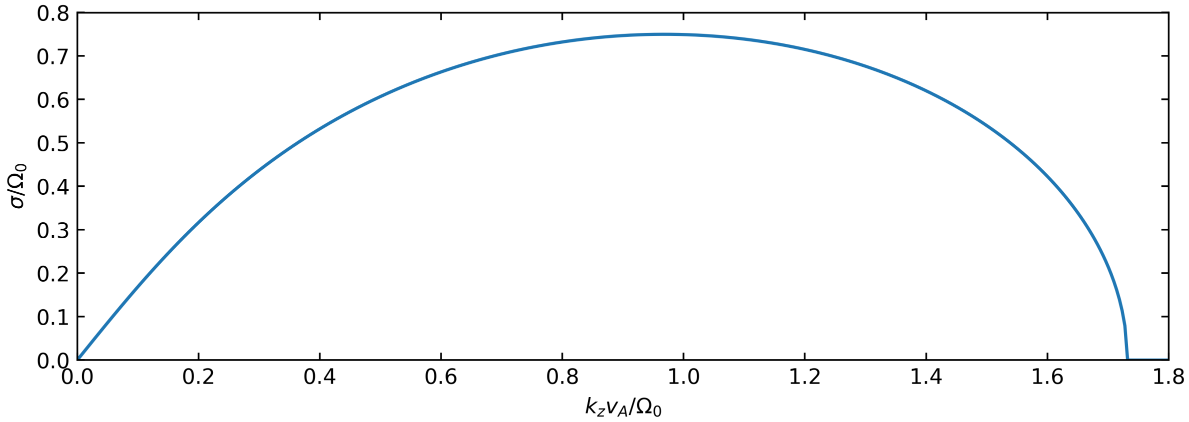

Figure 1.8: The linear growth rate σ of channel modes of the MRI as a function of the vertical wavenumber k_z and the vertical Alfvén velocity v_A.

It is easy to understand the physical origin of the linear regime of the MRI for this simple setup. If one imagines a vertical field line in a homogeneous disk and slightly displaces two fluid packages that are connected by the line to a smaller and larger radius, the field line gets stretched by the shear due to the flux freezing condition. This leads to a magnetic tension which will decelerate the inner fluid parcel and accelerate the outer fluid parcel, which is equivalent to an outwards transport for angular momentum. This increases the distance between the fluid elements and increases the shearing rate of the field line, which in turn leads to exponential growth (see also Fig. 1.9).

We performed our analysis for an unstratified box and allowed k_z to be a continuous parameter. The approximation of an unstratified disk breaks down if the wavelength of the perturbation becomes larger than one scale height, and therefore the minimum k_z we allow is $k_{z,\mathrm{min}} = 2\pi/H$. If the magnetic field is therefore larger than $v_A = \sqrt{2q}\Omega_0 H/(2\pi)$, the disk becomes stable to this instability.

In the previous calculation, we assumed $k_x = 0$ but one can show that this kind of perturbation corresponds to the fastest growing modes (Lesur, 2020). We also assumed that $k_y = 0$, since otherwise the perturbations might temporarily grow but for $t \to \infty$ would finally die out (Lesur, 2020). We note that non-axisymmetric modes nevertheless play an important role in the nonlinear regime since they allow for transient (nonmodal) growth (Squire & Bhattacharjee, 2014). If we would allow for a net radial magnetic field, the average azimuthal magnetic field would start to continuously grow in time. But we could also perform this study with an additional net azimuthal field which does not influence the linear growth of the channel modes. We note that the MRI can also be studied in a global system in which additional magnetic instabilities exist, that depend on the explicit curvature terms (Ebrahimi & Pharr, 2022).

So far we only analyzed the case that the disk can be described by the ideal MHD approximation. Especially in cold accretion disks such as protoplanetary disks the ionization rate is small and nonideal effects have to be taken into account. The most prominent ones

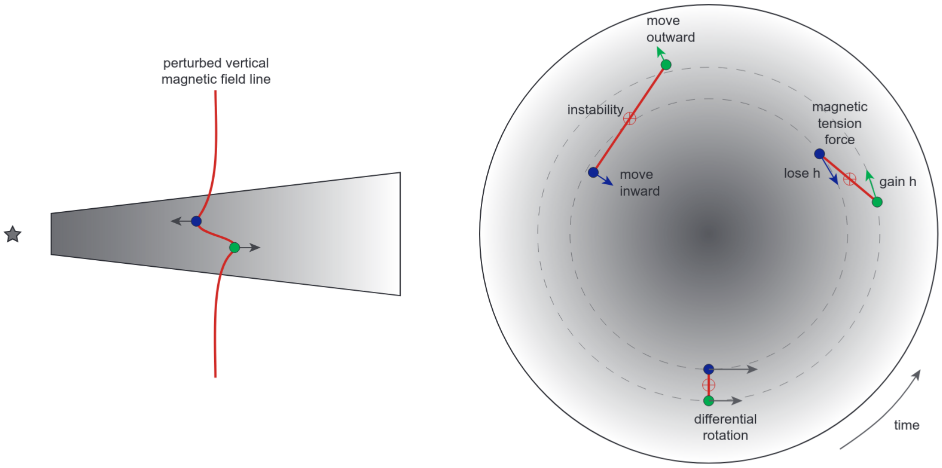

Figure 1.9: Sketch of the magnetorotational instability with an external vertical magnetic field. The field line gets stretched by the shear which leads to a magnetic force deaccelerating the inner fluid parcel and accelerating the outer fluid parcel. This leads to an angular momentum transfer outwards. Figure from Armitage (2022).

relevant in this case are the Ohmic and ambipolar diffusion as well as the Hall effect.

Their strength depends on the magnetic field strength as well as on density, and they are therefore relevant in different areas of the disk (see Fig. 1.10). We refer to Lesur (2020) for the full dispersion relation of the linear MRI with nonideal MHD and also for an in-depth discussion. In general, Ohmic diffusion leads to a damping of all perturbations and is especially efficient for small-scale perturbations. It can even fully suppress the MRI for weak enough fields. Ambipolar diffusion also acts as a resistivity and reduces the growth rates of perturbations, but in this case, oblique modes with $k_x \neq 0$ can have the largest growth rates. There exists a branch with $k_x \neq 0$ which always has a positive growth rate even for $k_x, k_z \to \infty$.

The Hall effect is only dispersive, and its effect depends on the orientation of the rotational axis relative to the vertical magnetic field. If they are parallel one finds the so-called Hall shearing instability (HSI), which always allows for a maximum growth rate $0.75\,\Omega^{-1}$ but moves the growth rates to smaller k. In the anti-aligned case, one finds the ion-cyclotron instability, which moves the instability to larger k. This difference between the instabilities becomes especially important if Ohmic diffusion additionally exists. It can efficiently suppress the growth of the ion-cyclotron instability whereas the HSI is less affected by it.

The strengths of the different nonideal MHD effects depend on the microscopic composition of the disk and are sensitive to the radiation field and temperature distribution. Their exact importance in the evolution of disks is therefore uncertain and one often relies instead on simplified models where constant nonideal MHD coefficients are assumed.

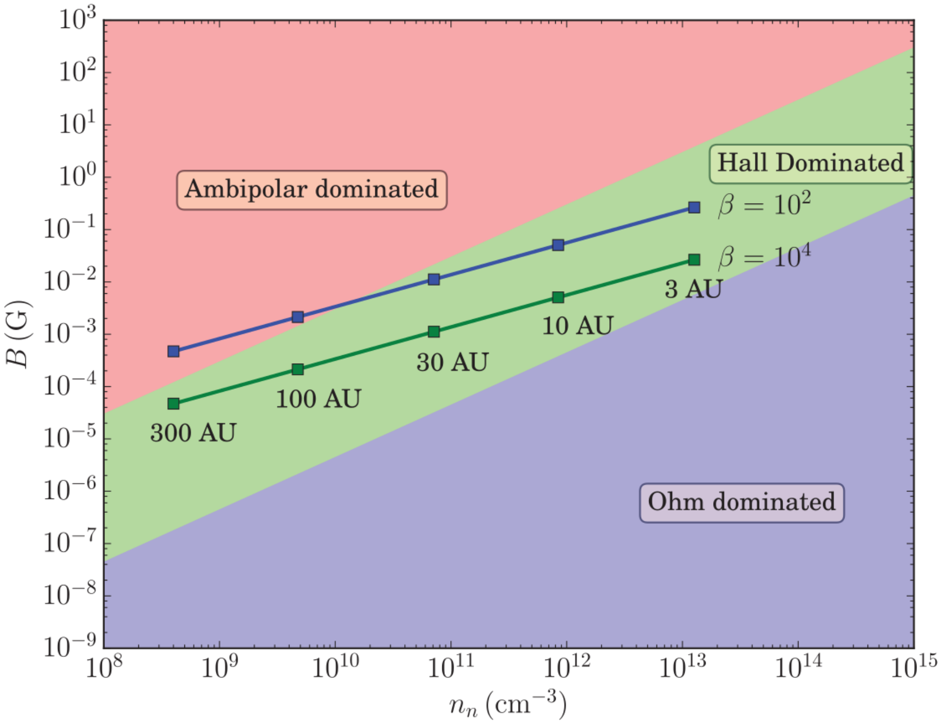

Figure 1.10: Importance of different nonideal MHD effects as a function of magnetic field strength and density of neutrals computed for an electron-ion plasma with $T < 100$K. The blue and green lines correspond to typical values found close to the mid-plane of protoplanetary disks for different plasma β. Figure from Lesur (2020)

1.3.3 Gravitational instability

Self-gravity is another mechanism which can lead to instability and the creation of turbulence. In this section, we do not take into account the magnetic field although recent studies showed that the gravitational instability and the MRI can interact with each other (Riols & Latter, 2018; Löhnert & Peeters, 2022). This can lead to a stronger magnetic field amplification which can also be observed in global simulations (Deng et al., 2020).

We start with the Euler equations (1.6) without any external gravitational potential and an isothermal equation of state. As the initial state, we use a constant density ρ_0 with background velocity $\boldsymbol{v}_0$ and constant sound speed c_{s0}. We add small perturbations ρ_1 and $\boldsymbol{v}_1$ to the initial state and linearize the equations:

$$\frac{\partial \rho_1}{\partial t} + \rho_0 \nabla \cdot \boldsymbol{v}_1 + \boldsymbol{v}_0 \cdot \nabla \rho_1 = 0, \tag{1.45a}$$

$$\frac{\partial \boldsymbol{v}_1}{\partial t} + \boldsymbol{v}_0 \cdot \nabla \boldsymbol{v}_1 = -\nabla \phi_1 - \frac{1}{\rho_0} \nabla p = -\nabla \phi_1 - \frac{1}{\rho_0} c_s^2 \nabla \rho_1. \tag{1.45b}$$

We assume a uniform, infinite background and therefore set $\phi_0 = 0$. The equations can be further simplified by transforming into the rest frame of the background, which leads to $\boldsymbol{v}_0 = 0$. We then take a temporal derivative of (1.45a) and a spatial derivative of (1.45b), and use Poisson's equation $\nabla^2 \phi_1 = 4\pi G \rho_1$:

$$\frac{\partial^2 \rho_1}{\partial t^2} + \rho_0 \frac{\partial}{\partial t} \nabla \cdot \boldsymbol{v}_1 = 0, \tag{1.46a}$$

$$\nabla \cdot \frac{\partial \boldsymbol{v}_1}{\partial t} = -\nabla^2 \phi_1 - \frac{1}{\rho_0} c_s^2 \nabla^2 \rho_1 = -4\pi G \rho_1 - \frac{1}{\rho_0} c_s^2 \nabla^2 \rho_1. \tag{1.46b}$$

By plugging (1.46b) into (1.46a) we find:

$$\frac{\partial^2 \rho_1}{\partial t^2} = 4\pi G \rho_1 \rho_0 + c_s^2 \nabla^2 \rho_1. \tag{1.47}$$

We expand ρ_1 in Fourier modes $\rho_1 = \sum_k A(k) \exp\left[i\left(\boldsymbol{k} \cdot \boldsymbol{x} + \omega t\right)\right]$ and get:

$$\omega^2 = c_s^2 k^2 - 4\pi G \rho_0. \tag{1.48}$$

For $k^2 < k_J^2 = \frac{4\pi G \rho_0}{c_s^2}$ the perturbations grow exponentially and the background state is unstable. This leads to the definition of the Jeans length

$$\lambda_J = \frac{2\pi}{k_j} = c_s \left(\frac{\pi}{G\rho_0}\right)^{1/2}, \tag{1.49}$$

and of the Jeans mass

$$M_J = \frac{4\pi}{3} \rho_0 \left(\frac{\lambda_J}{2}\right)^3 = \frac{\pi^{5/2}}{6} \left(\frac{c_s^2}{G}\right)^{3/2} \rho_0^{-1/2}. \tag{1.50}$$

It is important to note that all structures larger than the Jeans length become unstable and so violate the assumption of a static background (the so-called "Jeans swindle").

In a rotating disc, one additionally has to take into account the shear of the rotational motion. It becomes especially important for large perturbations, which are otherwise the most unstable ones. Furthermore, the disk only has a finite size in the z-direction. To simplify the calculations we will use the shearing box approximation and additionally the thin disc approximation. This assumes that all of the mass of the disc is concentrated in the mid-plane, and instead of solving for the density we solve for the surface density $\Sigma = \int_{-\inf}^{\inf} \rho \, \mathrm{d}z$. We will use an isothermal equation of state and additionally only take into account axisymmetric perturbations (i.e. $\partial/\partial y = 0$, for non-axisymmetric perturbations see section 4.7.1). The linearized equations are given by:

$$\frac{\partial \Sigma_1}{\partial t} = -\Sigma_0 \nabla \cdot (\boldsymbol{v}_1), \tag{1.51}$$

$$\frac{\partial v_{x1}}{\partial t} = 2\Omega_0 v_{y1} - \frac{c_s^2}{\Sigma_0}\frac{\partial \Sigma_1}{\partial x} - \frac{\partial \phi_1}{\partial x}, \tag{1.52}$$

$$\frac{\partial v_{y1}}{\partial t} = q\Omega_0 v_{x1} - 2\Omega_0 v_{x1}, \tag{1.53}$$

$$\nabla^2 \phi_1 = 4\pi G \Sigma_1 \delta(z), \tag{1.54}$$

and all equations except the last one are two-dimensional. Quantities with subscript 0 correspond to the background state while quantities with subscript 1 correspond to perturbations. We use the Ansatz

$$\begin{pmatrix} \Sigma_1 \\ v_{x1} \\ v_{y1} \\ \phi_1 \end{pmatrix} = e^{i(k_x x - \omega t)} \begin{pmatrix} \Sigma_{1,c} \\ v_{x1,c} \\ v_{y1,c} \\ \phi_{1,c} e^{-k_x |z|} \end{pmatrix}, \tag{1.55}$$

which leads to $\phi_{1,c} = 2\pi G \Sigma_{1,c}/k_x$. The full equations take the form of a matrix problem

$$\begin{pmatrix} \omega & -\Sigma_0 k_x & 0 \\ -c_s^2 k_x/\Sigma_0 + 2\pi G & \omega & -2i\Omega_0 \\ 0 & (2-q)\Omega_0 i & \omega \end{pmatrix} \begin{pmatrix} \Sigma_{1,c} \\ v_{x1,c} \\ v_{y1,c} \end{pmatrix} = 0, \tag{1.56}$$

which only has a non-trivial solution if the determinant of the matrix on the left hand side vanishes. The dispersion relation following from this condition is given by:

$$\omega^2 = c_s^2 k_x^2 - 2\pi G k_x \Sigma_0 + 2(2-q)\Omega_0^2. \tag{1.57}$$

As one might expect it is quite similar to the dispersion relation (1.48) of the Jeans instability. On small scales, the term $k_x^2 c_s^2$ stabilizes the disk, while the destabilizing term $2\pi G k_x \Sigma_0$ now additionally depends on k_x and therefore becomes weaker for larger wavelengths. This is a consequence of the finite size of the disk in the z-direction. With these two terms, the disk would still become unstable for small enough k_x but there is additionally the constant

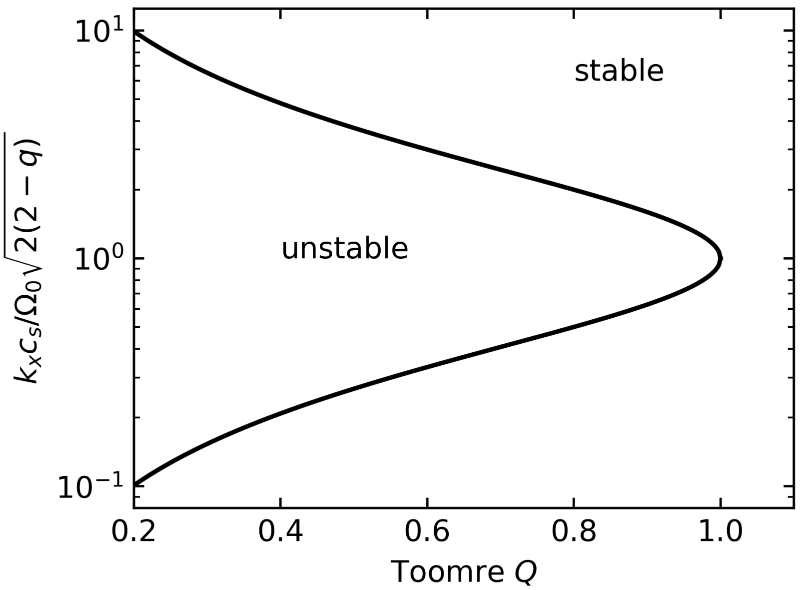

Figure 1.11: The stability of a self-gravitating, isothermal disk as a function of the Toomre parameter Q and the wavelength of the perturbation. The boundaries of the stable and unstable regime are given in equation (1.58).

term $2(2-q)\Omega_0^2$, which further stabilizes the disk for $q < 2$. Especially for small k_x this term dominates and therefore large perturbations get stabilized by the rotation. We can define the Toomre parameter $Q = \Omega_0\sqrt{2\,(2-q)}c_s/(\pi G\Sigma_0)$ and find the condition $Q < 1$, such that there exists a k_x for which the disk becomes unstable. The range of allowed k_x becomes larger if we decrease the Toomre Q:

$$\frac{\Omega_0\sqrt{2\,(2-q)}}{c_s}\left(\frac{1}{Q}-\sqrt{\frac{1}{Q^2}-1}\right) \leq k_x \leq \frac{\Omega_0\sqrt{2\,(2-q)}}{c_s}\left(\frac{1}{Q}+\sqrt{\frac{1}{Q^2}-1}\right), \qquad (1.58)$$

which we also visualize in Fig. 1.11. We note that the same criteria can also be derived by performing a global stability analysis using the WKB approximation (Binney & Tremaine, 2008).

The analysis can also be generalized to a fully three-dimensional disk, for which one finds instability only for smaller Toomre numbers between 0.6 and 0.7 (Nipoti, 2023). The stratification in this case leads to a smoothing of the gravitational force which can stabilise the system. If the disk itself is not isothermal, the compression due to the gravitational collapse generates heat which can stabilize the system. In this case, a turbulent state can form and we refer to Chapter 4 for an in-depth numerical study of this problem.

1.3.4 Rossby wave instability

The vorticity

$$\omega = \nabla \times \boldsymbol{v}, \tag{1.59}$$

is an important quantity to describe the structure of hydrodynamic flows. By applying the rotation operator to the momentum equation and ignoring magnetic fields, it follows:

$$\frac{\partial}{\partial t}\left(\frac{\omega}{\rho}\right) + (\boldsymbol{v}\cdot\nabla)\left(\frac{\omega}{\rho}\right) = \left(\frac{\omega}{\rho}\cdot\nabla\right)\boldsymbol{v} + \frac{1}{\rho^3}\nabla\rho\times\nabla P \tag{1.60}$$

When the equation of state is barotropic, meaning that the pressure is a function of density only, the last term disappears, as density gradients are parallel to pressure gradients in this case. In this special scenario, the quantity ω/ρ is conserved and simply advected by the flow. This means that vortices once formed can survive for a long time. Jupiter's Great Red Spot is a prominent example for this phenomenon.

One possible way to create vortices is the Rossby wave instability (RWI, Lovelace et al., 1999; Armitage, 2011). It is a linear instability that can be triggered by the presence of sharp boundaries in a disk. More specifically, one can define a generalized potential vorticity

$$\mathcal{L} = \frac{\Omega\Sigma}{\kappa^2} S^{2/\gamma}, \tag{1.61}$$

where we introduced the entropy $S = P/\Sigma^\gamma$ and used the epicycle frequency κ and the adiabatic coefficient γ. A necessary condition to trigger the RWI is the existence of an extremum of $\mathcal{L}$. It is hard to define a sufficient condition and we refer to Ono et al. (2016) for a more detailed discussion of the problem. Massive planets can carve gaps into protoplanetary disks which lead to an extremum in $\mathcal{L}$, but also the boundary between the dead zone and an active MRI region can trigger the RWI.

If the RWI is triggered, it results in the formation of several anticyclonic vortices that often merge into a single large vortex. The vortex can trigger density waves, which can transport angular momentum. For a more in-depth study of the RWI with numerical simulations, we refer to Chapter 5.

1.3.5 Further instabilities

Besides the instabilities we discussed in the previous sections and which we will analyse in this thesis in more depth numerically, there exist a plethora of different additional instabilities that rely, e.g., on the stratification, thermal structure or interaction of different disk components. We refer to Klahr et al. (2018) for a mathematical description of several of them and only shortly summarize the physical origin of a subset of them.

A prominent example is the vertical shear instability (VSI, Arlt & Urpin, 2004; Nelson et al., 2013), which requires that the angular frequency $\Omega(r,z)$ has a vertical gradient. In this case, a fluid parcel can move along the iso-surface of angular momentum and gain kinetic energy, which leads to its acceleration and linear instability. This effect is also

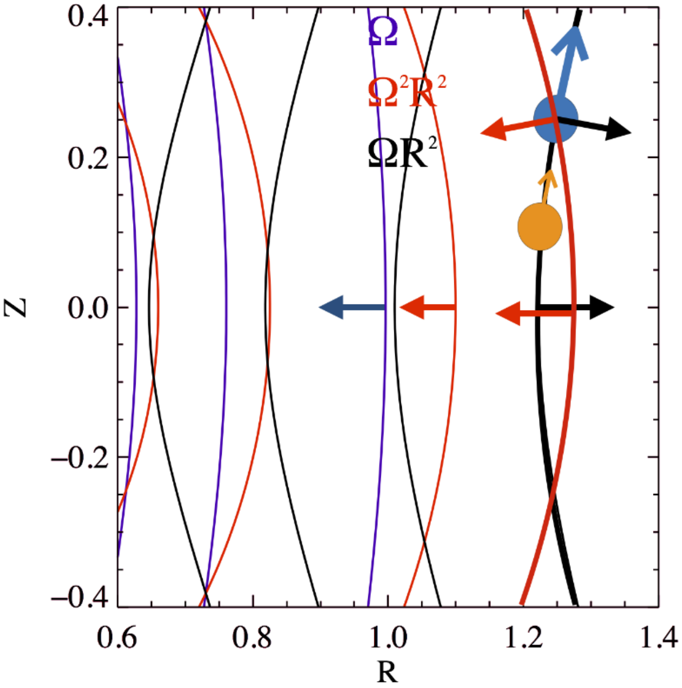

Figure 1.12: Illustration of the mechanism behind the vertical shear instability (VSI). If there are radial temperature gradients, $\Omega(r, z)$ depends on the vertical coordinate z and contours of constant Ω bent inwards. Since in disks around a central object $\Omega \propto R^{-1.5}$ holds, the specific kinetic energy of the rotation $\Omega^2 R^2 \propto R^{-1}$ decreases with radius. In contrast the specific angular momentum $\Omega R^2 \propto R^{0.5}$ increases with radius. In one moves a fluid parcel upwards it will follow the line of constant angular momentum upwards (black line). It has at the same time a higher kinetic energy than its surrounding which means it accelerates and will move further on the black line. This leads to an instability. We obtained the figure from Klahr et al. (2018).

sketched in Fig. 1.12. If the system is not locally isothermal, the stratification can lead to buoyant forces, which hinder the growth of the instability. A fast thermal relaxation to the background temperature is therefore required to reduce this effect.

Another instability that depends on the thermal structure of the disk is the convective overstability (Klahr & Hubbard, 2014). Let us assume that the entropy decreases as a function of radius and that there exists a finite time scale for thermal relaxation. If we now perturb the position of a fluid parcel in the radial direction, it will undergo an epicyclic oscillation. While the parcel moves outwards, its temperature is larger than the surrounding area, and thus it feels a buoyancy force pointing outwards. If thermal relaxation is efficient enough, it reaches the equilibrium temperature at its point of return, but its temperature is now lower than its environment while moving inwards. This leads to a buoyancy force pointing inwards, so that the amplitude of the oscillation increases. If the thermal relaxation is too efficient, the temperature difference between the fluid parcel and its environment is too small during its motion, and the instability cannot grow.

The finite amplitude of the convective overstability can trigger the subcritical baroclinic instability (Klahr & Bodenheimer, 2003; Petersen et al., 2007a,b; Lyra, 2014), which generates and amplifies vortices. The introduction of dust grains in addition to the gas allows for further instabilities such as the streaming instability (Youdin & Johansen, 2007; Johansen & Youdin, 2007), which we will however not discuss in this thesis.

1.4 Numerical methods

As we have shown in the last section, analytical methods are useful to understand the existence and growth of instabilities. But after some time their linear, exponential growth ends when nonlinear terms become important. To analyze this nonlinear regime, numerical methods are typically required to solve the equation (1.6). There exist many different methods, but they can typically be divided into Lagrangian and Eulerian methods. In the first one, one is interested how a specific part of the fluid evolves and one typically discretizes mass, which means one follows the evolution of particles. Smoothed-particle hydrodynamics (SPH, Gingold & Monaghan, 1977; Lucy, 1977; Springel, 2010b; Price, 2012) or the meshless finite mass (MFM, Hopkins, 2015) method are frequently used examples for Lagrangian methods. In the Eulerian case, one is interested in how the fluid properties at a specific position in space change and one discretizes typically the volume. Both types of methods have their advantages and disadvantages. We will use in this thesis a hybrid method that is approximately Lagrangian but uses mostly algorithms one can typically find in Eulerian methods.

1.4.1 Finite volume method on a static grid

In this section, we describe the finite volume method on a static, uniform Cartesian grid with grid size Δx. Our starting point is the state vector $\boldsymbol{U}$ (see equation 1.7), which we integrate for each cell i over its volume V_i. We end up with the vector $\boldsymbol{Q}_i = \int_{V_i} \boldsymbol{U}$ of conserved quantities in this cell, which corresponds to the total mass, momentum, energy and magnetic flux. We assume now that the state vector $\boldsymbol{U}_i$ within the cell is constant, which means $\boldsymbol{U}_i = \boldsymbol{Q}_i/V_i$ holds. The temporal change of $\boldsymbol{Q}_i$ can be calculated by integrating equation (1.6) over the volume V_i. We find:

$$\frac{\partial \boldsymbol{Q}_i}{\partial t} = -\int_{V_i} \nabla \cdot \boldsymbol{F}(\boldsymbol{U}) + \int_{V_i} \boldsymbol{S} = -\int_{\partial V_i} \boldsymbol{F}(\boldsymbol{U}) \cdot \boldsymbol{n} + \int_{V_i} \boldsymbol{S}, \tag{1.62}$$

where we used in the second step Gauss's theorem, introduced the normal vector $\boldsymbol{n}$ and the sum of all source terms $\boldsymbol{S}$. The flux function defines how the conserved quantities are exchanged between neighbouring cells while the source terms can change the global amount of conserved quantities. The flux and source terms can be calculated and applied separately in discrete time integration schemes (so-called operator splitting), and we will come back to this later when we discuss the time integration. To calculate the effect of the flux function on $\boldsymbol{Q}_i$, we first have to find its value at any point of the boundary of each cell and afterwards perform the integration. The integral over the surface of each cell can be written as a sum of integrals over the interfaces A_{ij} between the cell and its neighbours j:

$$\boldsymbol{I}_i(t) = \int_{\partial V_i} \boldsymbol{F}(\boldsymbol{U}) \cdot \boldsymbol{n} = \sum_j \int_{\partial A_{ij}} \boldsymbol{F}(\boldsymbol{U}) \cdot \boldsymbol{n}_{ij} = \sum_j \boldsymbol{I}_{ij}. \tag{1.63}$$

To get the state at the interface which we require to calculate the flux, we have to solve a so-called Riemann problem. The input to the Riemann problem are the left and right states of the two adjacent cells, and it then returns the state at the interface. We refer to Toro (2013) for a detailed introduction and discussion of Riemann solvers.

Since the state vectors within the cells are constant, the flux function is also constant on an interface. The integral $\boldsymbol{I}_{ij}$ is therefore just equal to $\boldsymbol{F}(\boldsymbol{U}_{ij})A_{ij}$. The volume integrals over the source terms can be calculated by evaluating the source terms within a cell and multiplying it with V_i. We now discussed how to calculate the right side of the equation (1.62) and how we can integrate the equation over a time interval Δt. We then find:

$$\boldsymbol{Q}_i(t_0 + \Delta t) = \boldsymbol{Q}_i(t_0) - \int_{t_0}^{t_0+\Delta t} \boldsymbol{I}_i(t)\,\mathrm{d}t + \int_{t_0}^{t_0+\Delta t} \boldsymbol{S}\,V_i\,\mathrm{d}t \tag{1.64}$$

and thus have to approximate the time integral of the form $\int_{t_0}^{t_0+\Delta t} \boldsymbol{I}_i(t)\mathrm{d}t$. The simplest approach would be the use of the first-order forward Euler method:

$$\int_{t_0}^{t_0+\Delta t} I_i(t)\mathrm{d}t \approx I_i\,(t_0)\,\Delta t. \tag{1.65}$$

This method is however only first-order in time, which means the error in this integral is proportional to Δt^2. If one decreases the time step by a factor of 2, the error per time step decreases by a factor of 4 but at the same time, the number of time steps doubles. This means that the global error to perform the time integration over a fixed amount of time is proportional to Δt. A better choice would be to approximated the time integral by:

$$\int_{t_0}^{t_0+\Delta t} \boldsymbol{I}_i(t)\mathrm{d}t \approx \left[\boldsymbol{I}_i\left(t_0\right) + \boldsymbol{I}_i\left(t_0+\Delta t\right)\right]\frac{\Delta t}{2}, \tag{1.66}$$

which is second-order accurate (error per time step is proportional to Δt^3). However, this approximation is inconvenient since $\boldsymbol{Q}(t+\Delta t)$ depends on $\boldsymbol{I}_i\left(t_0+\Delta t\right)$ and vice versa, which means we end up with an implicit equation. As we will show later, this can be overcome if one does not use the actual state $\boldsymbol{U}_i(t_0+\Delta t)$ for the flux calculation but instead uses a linear extrapolation from $\boldsymbol{U}(t_0)$ to the time $t_0+\Delta t$. Other possibilities include the use of a higher-order time integration method taken from the family of Runge-Kutta schemes.

Too large time steps can destabilize the integration, and one therefore introduces a maximum allowed time step

$$\Delta t_i = C_{\text{courant}}\frac{\Delta x}{c_{s,i} + \sqrt{v_{x,i}^2 + v_{y,i}^2 + v_{z,i}^2}}, \tag{1.67}$$

where the Courant number C_{courant} is a constant smaller than 1. A better spatial resolution therefore also requires a better temporal resolution.

To accurately model the time integration of source terms and fluxes, we use the Strang splitting. This is second-order accurate in time. We first calculate the source terms and apply them for half a time step. The new values for $\boldsymbol{U}_i$ are then used to perform the flux integration with a full-time step according to approximation (1.66), and afterwards we apply the source term again for another half time step.

One can show that for the assumption of a uniform state within a cell, the errors for smooth problems are proportional to Δx. The method is therefore only first-order accurate, but one can construct higher-order schemes by assuming that $\boldsymbol{U}$ can be described by a higher-order polynomial within each cell. In the simplest case, one assumes it is a linear function, which leads to a second-order accurate scheme. Note that the linear gradients in space can also be used to calculate time derivatives of $\boldsymbol{U}$, which can in turn be employed to extrapolate $\boldsymbol{U}\left(t_0+\Delta t\right)$ (see equation (2.10)). In contrast to discontinuous Galerkin schemes (Cockburn et al., 2012) one does not follow the evolution of the linear gradient within a cell in a finite volume method but instead calculates in each time step a new gradient estimate based on the values of the neighbours. To calculate the integral (1.63) one can then extrapolate $\boldsymbol{U}$ to the interface and use the two extrapolated values from both cells as inputs for the Riemann problem. To avoid the introduction of new extrema, which can lead to oscillations one has to use a so-called flux limiter (see also section 2.4.3). Since $\boldsymbol{U}$ is not constant anymore over the interface, also the flux is not a constant function on the interface which complicates the evaluation of the integral $\boldsymbol{I}_{ij}$. An approximation typically performed in Cartesian grid codes is to assume the flux to be constant over the face and just evaluate it at the middle of the interface. In Chapter 2 we will show that this can be problematic for unstructured meshes.

The scheme we discussed so far only allows for a constant spatial resolution. This can be problematic in astrophysics since one might want to resolve only a small part of the simulation box with a high resolution. In this case one can use adaptive mesh refinement (AMR, Berger & Colella, 1989) which allows splitting cells into 8 equally sized, smaller cells. This scheme can be applied recursively, and one can introduce more or less arbitrary criteria to trigger the splitting of cells.

Although AMR also allows one to zoom in on regions of interest, it can become hard to split cells early enough if the region of interest is moving rapidly through space. The method we described in this section is also not Galilei invariant at the discretized level, which means that if one adds a constant velocity boost to the whole system the numerical evolution might change even though the physics is invariant. Additionally, if one considers cold flows one can observe stochastic heating or cooling. The reason is that thermal energy is only defined as the difference between the total energy and the sum of the kinetic and magnetic energy. If the kinetic energy dominates the total energy, this creates a situation where small relative errors in the kinetic energy can lead to large relative errors in the thermal energy. Furthermore, as we have seen in equation (1.67), the maximum allowed time step depends on the local fluid velocity relative to the mesh. The moving mesh method we will discuss in the next section allows for a less restrictive time step criterion and can also help to overcome the other problems of a static finite volume code.

1.4.2 Moving mesh method

The moving mesh method was introduced by Springel (2010a) in astrophysics and implemented in the AREPO code, which we exclusively use in this thesis. It is based on the Voronoi tesselation, which discretizes space into non-overlapping Voronoi cells. The starting point is a set of mesh-generating points. For each mesh-generating point, one introduces a Voronoi cell that consists of all points in space that are closer to this mesh-generating point than to any other mesh-generating point. In Fig. 1.13 we show an example of a Voronoi mesh in two dimensions. As in the case of a static grid, we define again the vector of conserved quantities $\boldsymbol{Q}_i$ per cell i. The evolution of $\boldsymbol{Q}_i$ is given by equation (1.62), and in general all equations from the previous section are still valid for the Voronoi mesh including the introduction of a linear gradient within a cell. As we will discuss in section 2.4.2 the approximation to only evaluate the flux at the middle of an interface and multiplying the result with the area of the interface can however lead to local numerical noise. This can be circumvented by using a higher-order approximation of the surface integral.

The important feature of the moving-mesh method is that it allows the mesh-generating points (and therefore indirectly the Voronoi cells) to move in space. Their velocities can be chosen arbitrarily but one typically sets them equal to the fluid velocity of each cell. Sometimes it is advantageous to add additional small velocity components to improve the geometrical regularity of mesh cells. The motion of the interfaces with velocity $\boldsymbol{w}$ requires the introduction of a new advection term $\int_{\partial V_i} \boldsymbol{U}\boldsymbol{w}^T \cdot \boldsymbol{n}$ on the right side in equation (1.62). One can absorb this term into solving the Riemann problem on each interface in the rest frame of an interface, which also makes the method Galilei invariant.

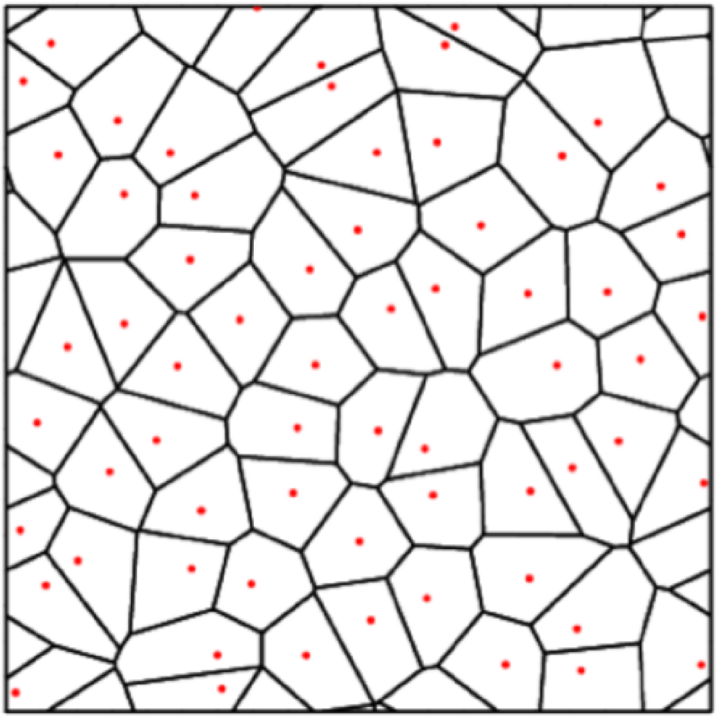

Figure 1.13: An example for a Voronoi mesh in two dimensions. The red points are the mesh-generating points and periodic boundary conditions were used. The figure was obtained from Springel (2010a).

In general, the moving mesh method is quasi-Lagrangian, which means that the mesh moves approximately with the fluid but small mass fluxes between cells are still allowed. This reduces advection errors and naturally leads to a higher resolution in dense regions. If one requires an even higher local resolution one can also merge and split cells. Another advantage is that in the time step criterion (2.29) one only has to take into account the sound speed and can neglect the velocity of the fluid relative to the mesh. This becomes especially important in cold disks, where the total velocity from the rotation is much larger than the sound speed.

1.5 Challenges in modelling rotating disks and overview of this thesis

Although the dynamics of rotating disks is on the largest scales determined by the rotation, small-scale effects such as turbulence or stellar feedback are crucial to model their long-term evolution. This is very challenging and expensive for numerical simulations, as both scales must be followed with high accuracy and resolution. Analytical models can typically only be used to estimate average values or the linear growth of instabilities, and therefore cannot be used to represent the full physics present in such disks. One solution to separate the two scales is the shearing box approximation we discussed in section 1.2.4, which allows simulations of local patches of a disk with high resolution. In the past, mostly two different numerical methods were used: The Lagrangian SPH method for global simulations, and the Eulerian finite volume method for shearing box simulations. SPH requires artificial viscosity and thermal conduction to resolve fluid instabilities and offers in general lower accuracy than the finite volume method but does not suffer from artificial heating if the energy is dominated by the kinetic energy. This is crucial for global simulations, as otherwise the rotational motion could artificially heat the disk, influencing fragmentation and other physical processes. Especially codes using static grids suffer from this problem, as the rotational motion leads to a continuous advection of material over the grid. Finite volume methods generally offer higher accuracy than SPH when large bulk velocities are absent, making them attractive for shearing box simulations, since the bulk of the background shear can be removed by using the orbital advection scheme (Masset, 2000).

For a comparison of local and global simulations, it would however be useful to be able to use the same numerical algorithms. Recently, the Lagrangian MFM method has been used successfully in both global and shearing box simulations (Deng et al., 2017, 2019, 2020, 2021). This method combines the particle nature of SPH with a more accurate force calculation using a Riemann solver, making it a hybrid between SPH and static, finite volume schemes. However, Deng et al. (2019) also showed that it still suffers from large numerical resistivity preventing it from sustaining MRI turbulence in shearing box simulations without an average magnetic field.

Another method that tries to combine the advantages of a Lagrangian method with those of a finite volume algorithm is the moving mesh method we discussed in the last section. Since the mesh moves with the flow, most of the rotational motion can be absorbed into the mesh motion which reduces artificial heating and advection errors. Additionally, this approach allows for full second-order convergence in space and time, as it uses the same algorithms as static, finite-volume methods. However, this method has been rarely applied to accretion disks thus far, as it has previously suffered from small noise on the grid scale, reducing its accuracy. In studies of circumbinary disks, this problem has been circumvented by using a locally isothermal disk with viscosity, which washes out the noise and prevents artificial heating (Miranda et al., 2017; Muñoz et al., 2019, 2020). Another option to prevent this problem is to restrict the mesh motion to the analytical rotational motion, increasing the symmetry in the mesh. This method was implemented in the DISCO code (Duffell, 2016) but it offers less flexibility, especially if the flow patterns significantly deviate from the imposed mesh motion.

The goal of this thesis is to assess how well the moving mesh method as implemented in the AREPO code can describe important processes that might be of importance for the evolution of accretion disks. The focus will be on studying the linear and nonlinear evolution of the magnetorotational, gravitational, and Rossby wave instabilities, as well as developing new algorithms to improve the accuracy of the code for these physics applications.

The thesis is structured as follows: In Chapter 2 we describe the first implementation of the shearing box approximation on a moving mesh code. We extensively test the implementation and realize several improvements in the code that remove the noise that was previously observed on the grid scale. In Chapter 3 we apply the method from the previous chapter to the problem of the growth and saturation of the MRI, and we compare our results with those found in the literature, finding generally good agreement. We extend the shearing box in Chapter 4 by implementing a self-gravity solver based on the TreePM method and by applying it to the gravitational instability in cold disks. Depending on the cooling efficiency we find a gravito-turbulent state or the formation of bound fragments. In Chapter 5 we perform global, two-dimensional simulations of a rotating disk with an axisymmetric overdensity. The system is unstable to the Rossby wave instability and we compare its linear growth rate with analytic expectations. In the nonlinear regime of evolution, we find the merging of several vortices into a single one. Finally, at the end of the thesis, we summarise in Chapter 6 our results and discuss possible extensions of the work and future research directions.

Chapter 2

Simulating cold shear flows on a moving mesh

This work has been published in the Monthly Notices of the Royal Astronomical Society, Volume 515, Issue 1, Pages 525-542.

Rotationally supported, cold, gaseous disks are ubiquitous in astrophysics and appear in a diverse set of systems, such as protoplanetary disks, accretion disks around black holes, or large spiral galaxies. Capturing the gas dynamics accurately in these systems is challenging in numerical simulations due to the low sound speed compared to the bulk velocity of the gas, the resolution limitations of full disk models, and the fact that numerical noise can easily source spurious growth of fluid instabilities if not suppressed sufficiently well, negatively interfering with real physical instabilities present in such disks (like the magnetorotational instability). Here, we implement the so-called shearing-box approximation in the moving-mesh code AREPO in order to facilitate achieving high resolution in local regions of differentially rotating disks and to address these problems. While our new approach offers manifest translational invariance across the shearing-box boundaries and offers continuous local adaptivity, we demonstrate that the unstructured mesh of AREPO introduces unwanted levels of "grid-noise" in the default version of the code. We show that this can be rectified by high-order integrations of the flux over mesh boundaries. With our new techniques we obtain highly accurate results for shearing-box calculations of the magnetorotational instability that are superior to other Lagrangian techniques. These improvements are also of value for other applications of the code that feature strong shear flows.

2.1 Introduction

Computer simulations are one of the main methods to understand the nonlinear evolution of gaseous flows in accretion disks and other differentially rotating systems. However, following key local instabilities such as the magnetorotational instability (MRI) (Velikhov, 1959; Chandrasekhar, 1960; Fricke, 1969; Balbus & Hawley, 1991) requires high resolution, which makes global simulations overly expensive. But the MRI is by no means the only instability of interest. For example, in protoplanetary disks, the Rossby wave instability appears (Lovelace et al., 1999), and radially stratified disks give rise to a variety of further instabilities that may drive turbulence in the disk (e.g. Klahr & Hubbard, 2014). In the context of the interstellar medium, differential shear is also considered an important source of turbulence, but one that is challenging to capture accurately in global disk models as a result of the limited resolution available in such calculations.

A general difficulty in the numerical treatment of rotationally supported gas flows lies in the "coldness" of the gas relative to the rotational bulk motion. The gas velocities in the rest frame of the disk are dominated by the coherent rotational motion and can be far higher than the involved sound speeds, making the flow formally highly supersonic. This causes small timesteps and large advection errors in standard finite-volume hydrodynamical grid codes. On the other hand, standard Lagrangian methods such as smoothed particle hydrodynamics (SPH) are prone to seed spurious instabilities in the disks due to their inherent, comparatively large numerical noise.

An interesting alternative lies in the use of a local approximation (Hill, 1878; Goldreich & Lynden-Bell, 1965) as realized in the shearing box approach, that was first applied in Hawley et al. (1995) to the MRI. The equations describing the evolution of the system are here expressed in a local, Cartesian reference frame that is co-rotating with the local angular velocity $\Omega_0 = \Omega(r_0)$ at a radius r_0 in the disk. This is typically combined with imposing periodic boundaries in the azimuthal direction (i.e. one covers only a region $\Delta y = r_0 \Delta\phi$), and a special 'shear-periodic' boundary condition in the radial direction (i.e. one only covers a radial region Δr). The transformation to a non-inertial frame of reference leads to two new source terms compared to the standard ideal magnetohydrodynamical (MHD) equations: The Coriolis force and the centrifugal force. The latter can also be written as an effective gravity force, defined as the difference of the external gravitational force and the centrifugal force. This effective force cancels for an equilibrium solution with a linear shear flow in the azimuthal direction, corresponding to a plain differential rotation in the disk. Fluid instabilities around this "cold ground state" can then be studied with high accuracy with Eulerian methods.

The shearing box approximation is only valid as long as the size of the used box, $L_r = \Delta r$, is much smaller than r_0. As a result, it does not readily allow for measurements of global disk properties such as the net mass accretion rates, or radial density and temperature profiles (Regev & Umurhan, 2008). Despite these limitations, it has become a very important standard method to analyze the nonlinear saturation of the MRI (Hawley et al., 1995). In particular, due to its much lower computational cost compared to global disk models, it allows the exploration of large parameter spaces, and thus ultimately yields important predictions for full simulations as well. For example, Riols & Latter (2018, 2019) found that gravoturbulence can act as a dynamo and amplify MHD fields even in the presence of strong resistivity, a result later confirmed by Deng et al. (2020) using global simulations.

So far simulations with the shearing box approximation have mostly employed Eulerian codes that require a special mapping of the fluid states at the radial boundary conditions. Examples for such implementations are the finite volume codes ATHENA (Stone et al., 2008; Stone & Gardiner, 2010), PLUTO (Mignone et al., 2007) and RAMSES (Fromang et al., 2006), or the finite difference codes PENCIL (Brandenburg et al., 2020) and ZEUS (Stone & Norman, 1992a,b; Hawley et al., 1995).

Although Lagrangian methods have often been used for global disk simulations due to their lower advection errors, they have only rarely been used for shearing box simulations, despite the fact that they in principle allow for a translationally invariant implementation of the radial boundary conditions. One reason is that particle-based methods have problems sustaining MRI turbulence without a net magnetic field, as shown by Deng et al. (2019) with the GIZMO code (Hopkins, 2015). However, Wissing et al. (2022) demonstrated recently that some SPH implementations are able to sustain the turbulence after all, which is a prerequisite for more complicated shearing box studies.

In this work, we present the first implementation of the shearing box approximation in a moving-mesh code, specifically the AREPO code (Springel, 2010a; Weinberger et al., 2020), which can be viewed as a hybrid method between a static grid code and a Lagrangian particle method. A full implementation of the shearing box approximation consists of the source terms and a treatment of the special radial boundary conditions. In contrast to Eulerian codes, the moving-mesh approach allows a fully translationally invariant implementation of the radial boundary conditions at the discretized level of the equations, so that the radial boundaries are manifestly indistinguishable from interior regions of the flow. Another advantage is that the moving-mesh approach retains its ability to continuously and seamlessly adjust the local resolution, making it particularly suitable for calculations of fragmentation and local gravitational collapse. Interestingly, our results for the ground-state of the shearing-box show that the default version of AREPO produces comparatively large 'grid-noise' errors when the mesh becomes geometrically completely unstructured due to strong local shear. We found that these errors can be eliminated, however, with a novel high-order flux integration that we develop as part of this chapter.

This chapter is structured as follows: In Section 2.2 we summarize the most important ingredients of the moving mesh method as currently implemented in AREPO. In Section 2.3 we present our implementation of the source terms and boundary conditions for the shearing box. We show in Section 2.4 that the vanilla version of AREPO leads to significant noise in the ground state, discuss several improvements that reduce this noise and show that they can also improve the results in other problems such as the simulation of a full cold Keplerian disk. In Section 2.5 we run several test problems for the shearing box and show that our implementation converges with close to second-order, as expected. Finally, we show in Section 2.6 that AREPO is able to sustain MRI turbulence for several hundred orbits without a background magnetic field and compare our results to those from Shi et al. (2016) obtained with the ATHENA code. In Section 2.7 we summarize our results and present our conclusions.

2.2 Ideal magnetohydrodynamics in AREPO

The moving-mesh code AREPO (Springel, 2010a; Weinberger et al., 2020) solves the ideal magnetohydrodynamical (MHD) equations on an unstructured Voronoi mesh using the finite volume method (Pakmor et al., 2011; Pakmor & Springel, 2013). The computational mesh is constructed using mesh-generating points that can move with an arbitrary velocity, but which is typically close to the fluid velocity. Due to this movement, the Voronoi mesh changes its structure and topology in time and the method becomes manifestly Galilei-invariant when the mesh motion is tied to the fluid motion itself.

The ideal MHD equations in differential form can be expressed as:

$$\frac{\partial \boldsymbol{U}}{\partial t} + \nabla \cdot \boldsymbol{F}(\boldsymbol{U}) = 0, \tag{2.1}$$

which exposes the hyperbolic conservation law for the mass, momentum, energy and integrated magnetic field. $\boldsymbol{U}$ defines here the conserved quantities and $\boldsymbol{F}$ is the flux function. The flux function is defined in a local rest frame by:

$$\boldsymbol{U} = \begin{pmatrix} \rho \\ \rho\boldsymbol{v} \\ \rho e \\ \boldsymbol{B} \end{pmatrix}, \qquad F(\boldsymbol{U}) = \begin{pmatrix} \rho\boldsymbol{v} \\ \rho\boldsymbol{v}\boldsymbol{v}^T + P - \boldsymbol{B}\boldsymbol{B}^T \\ \rho e\boldsymbol{v} + P\boldsymbol{v} - \boldsymbol{B}(\boldsymbol{v}\cdot\boldsymbol{B}) \\ \boldsymbol{B}\boldsymbol{v}^T - \boldsymbol{v}\boldsymbol{B}^T, \end{pmatrix}, \tag{2.2}$$

where ρ, $\boldsymbol{v}$, e, $\boldsymbol{B}$, P are the density, velocity, total energy per mass, magnetic field strength and pressure, respectively. The total energy density $e = u + \frac{1}{2}\boldsymbol{v}^2 + \frac{1}{2\rho}\boldsymbol{B}^2$ consists of the thermal energy per mass u, the kinetic energy density $\frac{1}{2}\boldsymbol{v}^2$ and the magnetic field energy density $\frac{1}{2\rho}\boldsymbol{B}^2$. The pressure $P = p_{\rm gas} + \frac{1}{2}\boldsymbol{B}^2$ has a thermal and a magnetic component. The system of equations is closed by the equation of state (EOS), which expresses $p_{\rm gas}$ as a function of the other thermodynamical quantities. We shall adopt the usual ideal gas EOS, $p_{\rm gas} = (\gamma - 1)\rho u$, with an adiabatic index γ.

The ideal MHD equations fulfill the condition $\nabla \cdot \boldsymbol{B} = 0$ for all times if the initial field is divergence-free. This property of the continuum equations is unfortunately lost in discretized versions of the equations, unless elaborate constrained transport formulations are used that can retain the divergence-free conditions also at the discrete level. In this chapter, we will instead use the Dedner scheme (Dedner et al., 2002) for divergence control as implemented in Pakmor et al. (2011). It diffuses away local deviations of the divergence constraint and damps them. We note that in many studies with AREPO the Powell scheme (Powell et al., 1999) as implemented in Pakmor & Springel (2013) is used instead, but all results except those in Section 2.6 are insensitive to the details of the divergence cleaning. We therefore defer a comparison between the two methods in the context of the shearing box to a future chapter. We set the parameter c_h required in the Dedner approach to the maximum signal speed in the system, and choose $c_p = \sqrt{2c_h r}$ in proportion to the cell radius r (see Pakmor et al. (2011) for details).

The ideal MHD equations are discretized on the cells of the dynamic Voronoi mesh. Volume averages of the conserved quantities for a cell i can be calculated by integrating

$\boldsymbol{U}$ over the corresponding volume V_i:

$$\boldsymbol{Q}_i = \int_{V_i} \boldsymbol{U}. \tag{2.3}$$

By integrating equation (2.1) over V_i and applying Gauss's law we find for the change of $\boldsymbol{Q}_i$:

$$\frac{\mathrm{d}\boldsymbol{Q}_i}{\mathrm{d}t} = \int_{\partial V_i} \boldsymbol{F}(\boldsymbol{U}) \cdot \hat{n}. \tag{2.4}$$

$\hat{n}$ is the outward normal on the surface ∂V_i of cell i. The temporal evolution of $\boldsymbol{Q}_i$ over one time step of size Δt can therefore be written as:

$$\boldsymbol{Q}_i^{n+1} = \boldsymbol{Q}_i^n + \int_{t_0}^{t_0+\Delta t} \mathrm{d}t \int_{\partial V_i} \boldsymbol{F}(\boldsymbol{U}) \cdot \hat{\boldsymbol{n}}. \tag{2.5}$$

The time integral is discretized in AREPO using a second-order accurate hybrid between a Runge–Kutta method and the MUSCL-Hancock scheme (see Pakmor et al., 2016b). By defining $\boldsymbol{I}(t) = \int_{\partial V_i} \boldsymbol{F}(\boldsymbol{U}) \cdot \hat{\boldsymbol{n}}$, equation (2.5) can be approximated by:

$$\boldsymbol{Q}_i^{n+1} = \boldsymbol{Q}_i^n + \frac{\Delta t}{2} \left[\boldsymbol{I}(t_0) + \boldsymbol{I}(t_0 + \Delta t)\right]. \tag{2.6}$$

The integral $\boldsymbol{I}(t)$ can be expressed as a sum of integrals $\boldsymbol{I}_{ij}$ over all outer faces of the cell. Such a face integral is then approximated as

$$\boldsymbol{I}_{ij}(t) = \int_{A_{ij}} \boldsymbol{F}(\boldsymbol{U}) \cdot \hat{\boldsymbol{n}}_{ij} dA_{ij} \approx A_{ij} \boldsymbol{F}[\boldsymbol{U}(\boldsymbol{f})] \cdot \hat{\boldsymbol{n}}_{ij}, \tag{2.7}$$

where $\boldsymbol{U}(\boldsymbol{f})$ is the state at the geometric centre $\boldsymbol{f}$ of the face, and A_{ij} is the interface between cell i and j.

The state at the interface is taken as the solution of a Riemann problem with the (linearly extrapolated) state of the cells i and j at this point as input. These extrapolations are calculated based on a slope-limited piece-wise linear spatial reconstruction step in each cell. For the calculation of $\boldsymbol{I}(t + \Delta t)$, an additional first-order time extrapolation of the fluid states by Δt is applied. This reconstruction is done using primitive variables for expressing the fluid state:

$$\boldsymbol{W} = \begin{pmatrix} \rho \\ \boldsymbol{v} \\ p_{\mathrm{gas}} \\ \boldsymbol{B} \end{pmatrix}, \tag{2.8}$$

which can be easily obtained from the conserved quantities.

The gradients of the primitive variables are estimated using a least-square fit around every cell (see Pakmor et al., 2016b, for details) and the reconstruction takes the following form for the left and right state:

$$\boldsymbol{W}'_{L,R}(t_0 + \Delta t) = \boldsymbol{W}_{L,R}(t_0) + \left.\frac{\partial \boldsymbol{W}}{\partial \boldsymbol{r}}\right|_{L,R} (\boldsymbol{f} - \boldsymbol{s}_{L,R}) + \left.\frac{\partial \boldsymbol{W}}{\partial t}\right|_{L,R} \Delta t, \tag{2.9}$$

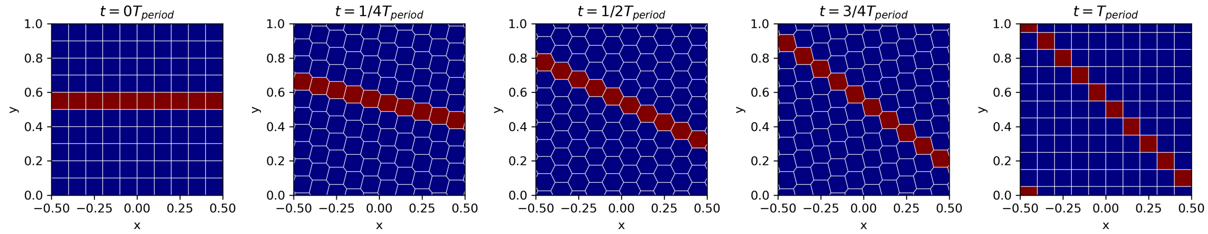

Figure 2.1: The shearing of an initially Cartesian grid by the background flow (2.15). We define $T_{\mathrm{period}} = \Omega_0 L_y/(qL_x)$ as the time it takes to evolve the grid into a new Cartesian grid. During this time the geometry of the grid continuously changes while retaining a residual symmetry of the cells (see, e.g., the red colored cells).

where $\boldsymbol{s}$ is the center of mass of each cell. $\frac{\partial \boldsymbol{W}}{\partial t}$ is only required in the second flux calculation and can be obtained from the linearized ideal MHD equations:

$$\frac{\partial}{\partial t}\begin{pmatrix}\rho \\ \boldsymbol{v} \\ p_{gas} \\ \boldsymbol{B}\end{pmatrix} = \begin{pmatrix} -\boldsymbol{v}\nabla\rho - \rho\nabla v \\ -\frac{\nabla P}{\rho} - \boldsymbol{v}\boldsymbol{v}^T + \boldsymbol{B}\cdot(\nabla\boldsymbol{B}) \\ -\gamma p_{gas}\nabla\cdot\boldsymbol{v} - \boldsymbol{v}\cdot\nabla P \\ \boldsymbol{B}\cdot(\nabla\boldsymbol{v}) - (\nabla\cdot\boldsymbol{v})\boldsymbol{B} - \boldsymbol{v}\cdot(\nabla\boldsymbol{B})\end{pmatrix}. \tag{2.10}$$

As detailed in Pakmor et al. (2011) we first try, in consecutive order, the HLLD Riemann solver (Miyoshi & Kusano, 2005), the HLL solver (Harten et al., 1983), and in case both fail, the Rusanov solver (Rusanov, 1961).

If the mesh itself is moving with velocity $\boldsymbol{v}_m$ one has to add the term $\boldsymbol{U}\boldsymbol{v}_m^T$ to the flux function. The velocity of a point on the interface can then be calculated as in Springel (2010a, their eqn. 33), to which we refer for more details. It only requires the local geometry of the two neighbouring cells of the interface as well as their velocities. The motion of the mesh generating points is typically kept as close as possible to the velocity of the fluid, but AREPO also adds small additional velocity corrections to improve the local regularity of the Voronoi mesh. We will refer to the latter as mesh regularisation in the following. As measure for the local mesh quality we use the maximum angle under which any cell face is seen by a mesh generating point, as described in full in Vogelsberger et al. (2012); Weinberger et al. (2020). Unless specified otherwise, we use the parameters $\beta = 2$ and $f_{\mathrm{shaping}} = 0.5$ as defaults for this method.

2.3 Implementation of the shearing box approximation

The local shearing box approximation (Goldreich & Lynden-Bell, 1965) solves the ideal MHD equations in a frame that is rotating with a frequency $\Omega_0 = \Omega(r_0)$ at radius r_0. Upon transformation into the non-inertial rotating system, the equations can be written

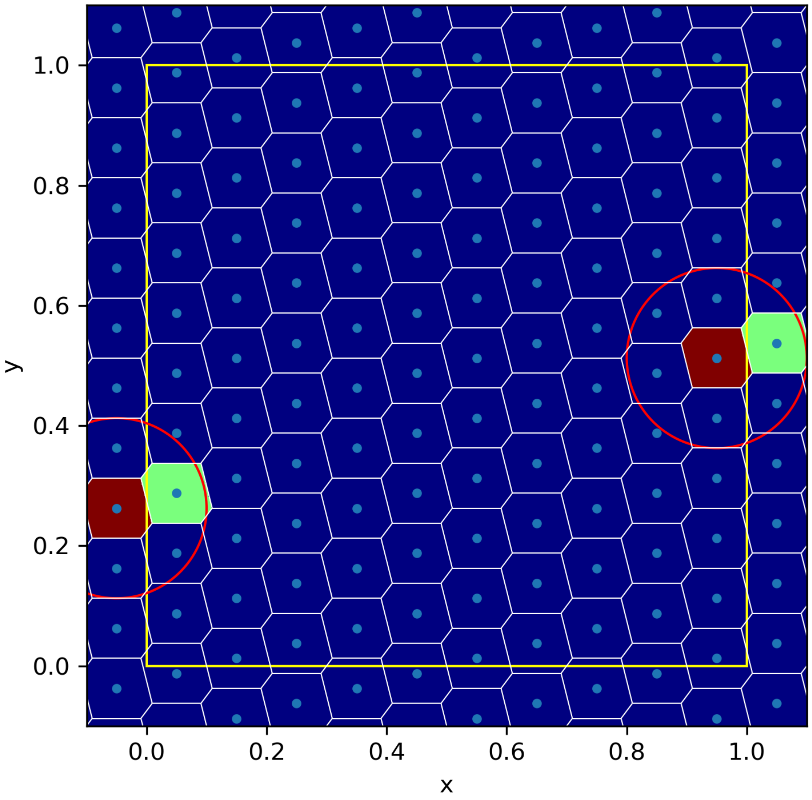

Figure 2.2: Illustration of the mesh construction for the shearing box boundary conditions in the x-direction: The inside of the yellow square represents the two-dimensional simulation domain. All cells whose mesh generating points (blue circles) lie in the box are primary cells, the other ones are so-called ghost cells arising as duplicates due to the boundary conditions. During the construction of the mesh, we need to repeatedly find all mesh-generating points that lie within a sphere of some radius r around a mesh-generating point. These are in-circle tests for the circumspheres of triangles, carried out to make sure that the corresponding triangle is a valid Delaunay triangle of the tessellation (see as example the red circle around a cell colored in red). If this sphere intersects an x-boundary, we have to calculate an additional search position by shifting the x-coordinate by $\pm L_x$ and the y-coordinate by $\mp wt$, see eqn. (2.3.2). For this new position, another in-circle test has to be carried out, which may in turn return both primary points or other shifted ghost points. Note that in our example, the interface between the red and the green cell exists twice in the final tessellation: Once on the left hand side with the red cell as ghost cell, and once on the right side with the green one as ghost cell. It is however sufficient to calculate the corresponding fluxes, together with the boost of eqn. (2.22), only once.

in Cartesian coordinates x, y, and z, with corresponding units vectors $\hat{e}_x$, $\hat{e}_y$ and $\hat{e}_z$, as:

$$\frac{\partial \boldsymbol{U}}{\partial t} + \nabla \cdot \boldsymbol{F}(\boldsymbol{U}) = \boldsymbol{S}_{\text{grav}} + \boldsymbol{S}_{\text{cor}}. \tag{2.11}$$

The left hand side is formally equivalent to equation (2.1), and the flux is still given by (2.2), but the coordinate transformation leads to two additional source terms for the momentum and energy equations. $\boldsymbol{S}_{\text{grav}}$ contains one of the terms, the centrifugal force, as well as the external gravitational force expanded to first order in the x- and z-directions, while $\boldsymbol{S}_{\text{cor}}$ represents the Coriolis force. Explicitly, they are given by:

$$\boldsymbol{S}_{\text{grav}} = \begin{pmatrix} 0 \\ \rho\Omega_0^2 \left(2qx\hat{e}_x - z\hat{e}_z\right) \\ \rho\Omega_0^2 \boldsymbol{v} \cdot \left(2qx\hat{e}_x - z\hat{e}_z\right) \\ 0 \end{pmatrix} \tag{2.12}$$

and

$$\boldsymbol{S}_{\text{cor}} = \begin{pmatrix} 0 \\ -2\rho\Omega_0\hat{e}_z \times \boldsymbol{v} \\ 0 \\ 0 \end{pmatrix}. \tag{2.13}$$

The term $\boldsymbol{S}_{\text{grav}}$ depends on the shearing parameter

$$q = -\frac{1}{2}\frac{d\ln\Omega^2}{d\ln r}, \tag{2.14}$$

which takes on the value $q = 3/2$ for a Keplerian rotation curve.

In the azimuthal y-direction one typically uses standard periodic boundary conditions. In the z-direction, one can use periodic boundary conditions in the case of an unstratified box (no gravitational term in the z-direction) or inflow-outflow boundary conditions for a stratified box (gravitational field towards the $z = 0$ plane). The boundary conditions in the radial direction are more complicated and will be discussed separately below.

We note that equation (2.11) admits a ‘ground state’ solution with

$$\boldsymbol{v}_0(x) = (0, -q\Omega_0 x, 0), \quad \rho = \text{const.}, \quad P = \text{const.}, \tag{2.15}$$

in the unstratified case. For a global disk simulation, this is equivalent to the intrinsic radial dependence of the rotational velocity being given by $r\Omega(r)$ everywhere. This background flow alone leads to a continuous shearing between neighbouring cells in the x-direction (see Fig. 2.1).

2.3.1 Implementation of the source terms

To implement the source terms we use a second-order accurate Strang splitting scheme, which means we first evolve the system for half a time step using the source terms, then for a full time step using the methods from Section 2.2, and then apply another half step for the source terms. We apply both source terms together and actually rewrite the momentum equation to:

$$\boldsymbol{S}_{\mathrm{tot,mom}} = \begin{pmatrix} 2(v_y - v_{0,y})\rho\Omega_0 \\ -2v_x\rho\Omega_0 \\ -\rho\Omega^2 z \end{pmatrix}, \tag{2.16}$$

because this term vanishes for the ground state solution. To conserve the total energy accurately we first subtract the kinetic energy from the total energy, apply the momentum source term and then add the new kinetic energy to the total energy. To avoid an unphysical growth of the amplitude of epicycle oscillations (see section 2.5.2), we add a prediction step for the second half step of the source terms. In practice, this means we first apply the source term (2.16) for a half time step, calculate the new velocity and use this velocity for the actual update of the momentum. This method is similar to the implementation the of Crank-Nicholson time difference method in Stone & Gardiner (2010), which actually can conserve the amplitude to machine precision.

2.3.2 Boundary conditions

While we can use the standard implementation of periodic or inflow/outflow boundary conditions in the y- and z-directions, we have to take care of the background shear flow (2.15) in the x-direction. This leads to the so-called shearing box boundary conditions:

$$f(x,y,z,t) = f(x \pm L_x, y \mp wt, z, t); f = (\rho, \rho v_x, \rho v_z, \boldsymbol{B}), \tag{2.17}$$

$$\rho v_y(x,y,z,t) = \rho v_y(x \pm L_x, y \mp wt, z, t) \mp \rho w, \tag{2.18}$$

$$e(x,y,z,t) = e(x \pm L_x, y \mp wt, z, t) \mp \rho v_y v_w + \frac{\rho w^2}{2}, \tag{2.19}$$

where L_x is the box size in the (radial) x-direction, and $w \equiv q\Omega_0 L_x$.

To implement standard periodic boundary conditions, AREPO uses ghost cells. During the mesh construction, all cells closer than a specific radius r to a cell have to be found. If this sphere of influence intersects a box boundary, the search will be continued on the opposite boundary of the box. The cells found there will be built into the local Voronoi mesh as a ghost cell at the original position of the cell shifted by one box length, and the properties of the original cell are copied to the ghost cell. Updates of the conserved quantities of such ghost cells are applied to the original cell (for details of the mesh construction see Springel, 2010a). The creation of ghost cells may cause some cell interfaces to be duplicated in the constructed tessellation (in particular also if parallelization subdivides the fiducial global mesh into several logical pieces stored on different processors), but the fluxes are calculated always only once, such that the conserved quantities of both involved cells get updated only once in a manifestly conservative fashion.

The radial shearing box boundary conditions can be treated very similarly with some extra modifications. First, if the search sphere overlaps with the box boundary, the centre of the search region does not only have to be shifted by $\pm L_x$ in the x-direction, but also by $\mp wt$ in the y-direction. When copying the properties of the original cell to the ghost cells, we have to add a velocity boost $\mp w$ to the y-component of the velocity, as well as to the velocity of the corresponding mesh generating point. The Riemann solver then returns the state $\boldsymbol{U}(\rho, \boldsymbol{v}, p, \boldsymbol{B})$, which can then be used to calculate the flux $\boldsymbol{F}(\boldsymbol{U})$ that is applicable to a real (unboosted) cell at the interface. If we are dealing with a ghost cell instead, the conserved quantities of the corresponding original cell need to be updated with a modified flux:

$$\Delta\boldsymbol{F} = \boldsymbol{F}'(\boldsymbol{U}'(\rho, \boldsymbol{v} \pm w\hat{e}_y, p, \boldsymbol{B})) \mp \boldsymbol{U}'(\rho, \boldsymbol{v} \pm w\hat{e}_y, \boldsymbol{B})(w\hat{e}_y)^T - \boldsymbol{F}(\boldsymbol{U}). \tag{2.20}$$

$\boldsymbol{U}'$ is here the state we obtain by adding the velocity shift $\pm w\hat{e}_y$ to $\boldsymbol{U}$. Using equation (2.2) for the flux, this can explicitly be expressed as:

$$\Delta\boldsymbol{F} = \begin{pmatrix} 0 \\ (0, \pm wQ_1, 0) \\ \pm Q_{2,y}w + 1/2Q_1w^2 \\ (0, \mp w(\boldsymbol{B}\cdot\hat{n}), 0) \end{pmatrix} \tag{2.21}$$

with

$$\boldsymbol{F}(\boldsymbol{U}) = \begin{pmatrix} Q_1 \\ (Q_{2,x}, Q_{2,y}, Q_{2,z}) \\ Q_3 \\ (Q_{4,x}, Q_{4,y}, Q_{4,z}) \end{pmatrix}, \tag{2.22}$$

where $\hat{n}$ is the normal of the interface.

Note that this boost shows that in the shearing box approximation the momentum and energy are not conserved. Whereas the mean radial and vertical magnetic field,

$$\langle B_{x,z}\rangle = \frac{\int_{\mathrm{Box}} B_{x,z}\mathrm{d}V}{\int_{\mathrm{Box}}\mathrm{d}V} = \mathrm{const.} \tag{2.23}$$

are conserved, the azimuthal field grows linear with the net radial magnetic field flux through the radial boundary (Gressel & Ziegler, 2007):

$$\frac{\partial\langle B_y\rangle}{\partial t} = -\frac{w}{V}\int_{\partial x} B_x\,\mathrm{d}y\,\mathrm{d}z. \tag{2.24}$$

For $\nabla\cdot\mathbf{B} = 0$, the last condition also implies that $\langle B_y\rangle$ is constant if there is no net radial field.

On a moving mesh, cells can also leave the simulation box and reappear on the opposite side. If this happens in the x-direction, we also have to modify the y-position and velocity component of the cell, as well as its energy. Fig. 2.2 further illustrates the implementation of the boundary conditions during the mesh construction. We note that this implementation of the boundary conditions does not introduce any special treatment of the boundaries at the level of the flux calculation, and therefore the whole simulation box stays isotropic and translationally invariant.

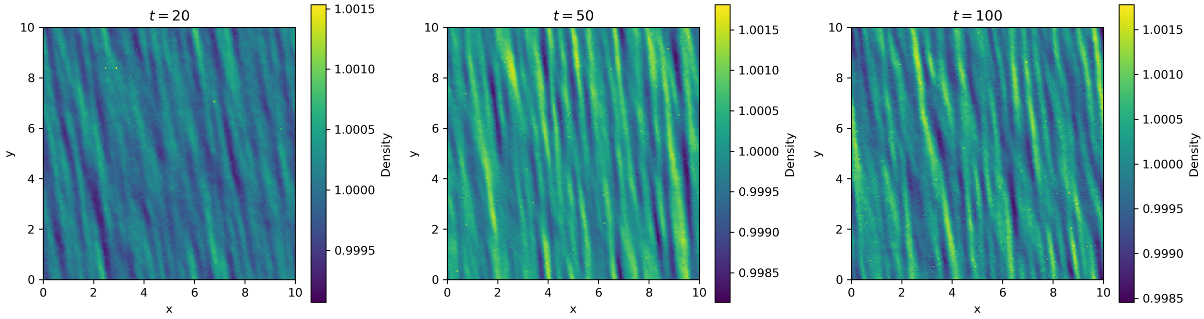

Figure 2.3: The density field at different times in a two-dimensional calculation that simulates the ground state of the shearing box with an initially constant density, $\rho = 1$, using the old default version of the AREPO code, as described in Section 2.2. The simulation seeds small ‘grid-noise’ at the level of 10^{-3} which is stretched by the shearing motion into vertically oriented bands. This effect has a purely numerical origin and cannot be eliminated by resorting to finer time-stepping.

2.4 Reducing numerical noise in AREPO

In this section, we first test the accuracy of the shearing box implementation in AREPO when the default integration method of the code is used. As this exposes an unwanted level of ‘grid-noise’ that can influence the growth of instabilities and act as a numerical viscosity, we then introduce several improvements to the code that substantially increase the achieved accuracy.

2.4.1 Simulations of the ground state of the shearing box

A conceptionally simple but nevertheless highly illuminating test case of the basic code performance lies in simulating the ground state (2.15) of the shearing box with an isothermal equation of state. This state should be stable (because the shearing motion is stabilized by the centrifugal force), and indeed, static grid codes are able to maintain this state to machine precision on a Cartesian grid. However, the free mesh motion of AREPO allows for the occurrence of diverse cell geometries, potentially introducing much larger deviations from the ground state.

For testing this, we set up a two-dimensional box of size $L_x = L_y = 10$, density $\rho = 1$, and an isothermal equation of state with sound speed $c_s = 1$ and $\Omega_0 = 1$. The initial mesh is created by two nested Cartesian grids with 200^2 mesh-generating points, effectively creating a hexagonal mesh. We add to these positions of the mesh-generating points some random noise with a maximum of 5% of the lattice constant of the grid, and set the velocity of the cells to the value of the ground state (2.15) at the centers of mass of the resulting mesh cells. In Fig. 2.3, we show the time evolution of the computed density field. We see that the code is not able to stably keep the imposed ground state to machine precision, rather a time-dependent stripe pattern forms, apparently due to local noise peaks that are subsequently sheared away by the fluid motion.

Since there are no spatial scales in the problem that need to be resolved in the ground state, the only sources of error are of numerical origin. If they are related to the temporal discretization of the updates of the fluid state, the error in the density field should decrease with the size of the time step. However, if we rerun the simulation with different Courant coefficients (see also eqn. 2.29) and compare the L_1 errors of the resulting density fields, we find that the error does not decrease with smaller time steps sizes, i.e. it does not arise from truncation errors of the temporal discretization and will still be present even for arbitrarily small timesteps.

This raises the suspicion that the errors are directly related to the unstructured cell geometries used in our calculation. To test for this possibility, we run our code with a static grid, although this requires a special trick to deal with the shearing box boundary conditions because the approach used for this purpose in Eulerian codes is not implemented in our moving-mesh approach. However, we can still compute test simulations of the shearing box with a static mesh by defining buffer zones on both sides of the simulation domain close to the boundaries in the x-direction. In every time step, we then simply override the fluid quantities in these regions and reset them to the analytically expected values. In this way, we can effectively restrict the live calculation of the code to the regions in between, allowing us to examine the sources of errors there without having to actually solve the boundary conditions problem for stationary meshes in a clean way.

Using this approach, we find that both a stationary Cartesian mesh, as well as a stationary hexagonal mesh (formed from two nested grids of mesh-generating points), are able to keep the ground state to machine precision after all. Furthermore, this ground state is also maintained with this precision if we let the mesh move but *prescribe* the motion such that a symmetry of the cells is always maintained (for example, in practice we start from a Cartesian mesh and set the velocities of the mesh generating points to the initial fluid velocity, and then keep them constant). In contrast, if we use asymmetric cell geometries and a prescribed motion, this accuracy immediately breaks down. This leads to the conclusion that the symmetry of the Cartesian/hexagonal grid is a key factor in allowing the code to avoid the creation of local deviations from the ground state. In the next subsection, we will see that this behaviour is ultimately not surprising, because the symmetric cell geometries benefit from a fortuitous cancellation of flux area integration errors on opposite sides of mesh cells. Additional effort beyond the standard integration scheme is needed to achieve the same final accuracy also for general mesh geometries.

2.4.2 Higher order flux integration

A clear potential source for inaccuracies is the approximation (2.7) for the area integral of the flux over a cell interface. This approximation is only exact if the flux varies linearly across the interface. However, this condition is, for example, not fulfilled if there is a finite velocity gradient, since in this case, the momentum flux becomes a quadratic function in space, see eqn. (2.2). If a linear gradient in density and velocity exists, the maximum polynomial order of the flux function occurs for the energy flux and is fourth order in space. This ultimately means that an accurate calculation of the surface integral I_{ij} that is free of truncation errors requires a method that can integrate polynomials of order up to 4 exactly (or order 3 in case of an isothermal EOS, or if density gradients can be neglected).

The approximation (2.7) can be viewed as the simplest low-order case of the general class of Gauss-Legendre integration rules, that can be used in any dimension. In two-dimensional simulations, the integral I_{ij} is a line integral and can be transformed into the form:

$$I = \int_{-1}^{1} f(x)\,\mathrm{d}x \approx \sum_{i=1}^{n} f(x_i)\,w_i, \tag{2.25}$$

where $f(x)$ represents the flux function in normalized coordinates with $x \in [-1, 1]$ marking the position on the interface. The integral can be approximated by a weighted sum of values of f obtained at different evaluation points x_i, the so-called Gauss points. For an appropriate choice of x_i and w_i, the approximation can be made exact for polynomials up to a certain order m, but achieving higher-order m also requires more function evaluations, i.e. a higher n. In Appendix 2.8.1 we give the exact values for x_i and w_i as implemented in our code, but for all test cases in this chapter, two points, $n = 2$, exact up to third order polynomials, are sufficient. For every x_i we require an additional reconstruction of the states at the interface as well as a call to the Riemann solver. Since those costs are typically significantly smaller than the mesh construction in two dimensions, we adopt this method as the (new) default one in the AREPO code.

In three-dimensional simulations, the interfaces of cells are polygons. Although methods exist that try to find the minimum amount of evaluation points for a specified target accuracy (e.g. Mousavi et al., 2010), there exist no general equations for polygons with more than four edges that employ the minimum number of evaluation points needed for a targeted exact polynomial accuracy. We, therefore, split the interface into triangles over which we can integrate the flux accurately using standard Gauss-Legendre integration. The triangles themselves can be easily obtained during the construction of the Voronoi mesh from the Delaunay triangulation. For a third-order accurate method, we have to use 4 points per triangle, which means we require on average more than 15 flux evaluations per surface integral to realize this accuracy for arbitrary cell geometries. While this sounds like a significant cost increase, using simulations of the background shear flow (2.15) we found an overhead of only around 110% for a naive implementation of this method. However, we were able to reduce this overhead to around 30% by performing the time extrapolation only once per face and not for every evaluation point separately, and by an explicit vectorization of the flux calculation with AVX-2 instructions available on modern CPUs. In Appendix 2.8.2 we discuss further details of the application of the Gauss-Legendre integration in three dimensional Voronoi meshes.

2.4.3 Less strict slope limiter

In regions with a smooth flow, the linear reconstruction of equation (2.9) leads to a second-order accurate method in space. But in regions with physical discontinuities, the standard reconstruction scheme can induce under- or overshoots, and thus oscillatory behaviour, unless a non-linear slope limiter is applied to reduce the local gradients such that no new extrema are introduced into the solution. As this reduces the order of the method to first-order accuracy close to discontinuities, it is important to choose a limiting scheme that only reduces the gradient where really required, and by the least amount needed to accurately capture shocks and contact discontinuities, and to prevent numerical instabilities.

Thus far, AREPO by default uses the scheme from Springel (2010a): The original estimate of the gradient of a quantity ϕ is replaced by

$$\left\langle \vec{\nabla}\phi \right\rangle_i' = \alpha_i \left\langle \vec{\nabla}\phi \right\rangle_i , \tag{2.26}$$

where $0 \leq \alpha_i \leq 1$ is the value of the limiter of the given cell. It is computed as

$$\alpha_i = \min_j(1, \psi_{ij}), \tag{2.27}$$

where ψ_{ij} is here defined for every interface of the cell i as

$$\psi_{ij} = \begin{cases} (\phi_i^{\max} - \phi_i)/\Delta\phi_{ij} & \text{for} \quad \Delta\phi_{ij} > 0 \\ (\phi_i^{\min} - \phi_i)/\Delta\phi_{ij} & \text{for} \quad \Delta\phi_{ij} < 0 \\ 1 & \text{for} \quad \Delta\phi_{ij} = 0 \end{cases} \tag{2.28}$$

and $\Delta\phi_{ij} = \langle \nabla\phi \rangle_i \cdot (\boldsymbol{f}_{ij} - \boldsymbol{s}_i)$ is the estimated change between the centroid $\boldsymbol{f}_{ij}$ of the face and the centre of cell i, while $\phi_i^{\max} = \max(\phi_j)$ and $\phi_i^{\min} = \min(\phi_j)$ are the maximum and minimum values occurring for ϕ among all neighbouring cells of cell i, including i itself.

However, this scheme can lead to a too restrictive limiting of the gradient of the background shear flow (2.15) for an unstructured mesh. This can happen for special cell geometries where the face connecting two cells is displaced quite far from the line connecting the corresponding mesh generating points. As a result, one can end up with $\alpha_i < 1$ even if there is no discontinuity in the flow. But this in turn increases the local truncation error of the solution, introducing unwanted ‘grid-noise’ into the solution. To prevent this, we replace $\boldsymbol{f}_{ij}$ in the above formulation of the slope limiter by the mid-point $\frac{1}{2}(\boldsymbol{s}_i + \boldsymbol{s}_j)$ of the center of mass of the cells i and j. We found that this formulation prevents post-shock oscillations close to discontinuities in all our test simulations just as well as the original formulation, while it safely avoids being triggered in situations with a uniform linear gradient in combination with a highly irregular Voronoi mesh.

2.4.4 Improved temporal and spatial extrapolation

Equation (2.9) does not specify in which frame we perform the spatial reconstruction and temporal extrapolation. The simplest choice would be the lab frame, in this case, $\boldsymbol{s} = \boldsymbol{s}_{\text{old}}$ is the centre of mass at the time we calculate the gradient and not the current centre of mass. A more natural choice would be the moving frame of the gas. In this case we use $\boldsymbol{s} = \boldsymbol{s}_{\text{old}} + \boldsymbol{v}\Delta t$ as the origin of the spatial reconstruction and set $\boldsymbol{v} = 0$ in equation (2.10). We realized through our sensitive tests that the current version of AREPO implemented

simulation name	initial grid	improvements enabled?	order time integration
CO2	cart.	no	2
PO2	polar	no	2
CI2	cart.	yes	2
PI2	polar	yes	2
CI3	cart.	yes	3
PI3	polar	yes	3

Table 2.1: Overview of the different code configurations used for the isentropic Yee vortex test. The simulations differ in the topology of the initial grid layout (with is either Cartesian or polar), whether or not the improvements (but without higher-order time integration) presented in this chapter are enabled, and finally whether a second or third order time-integration is used.

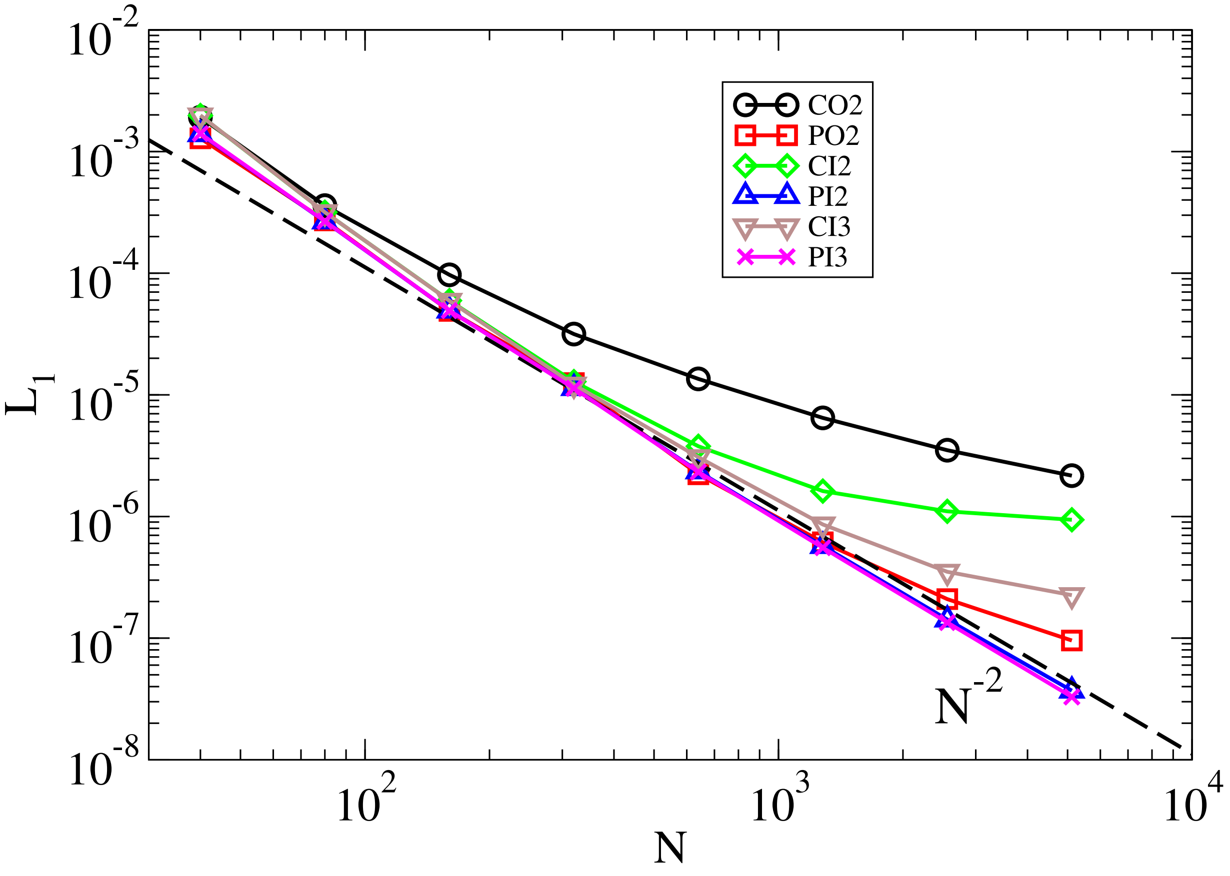

Figure 2.4: L_1 norm of the error of the density field for the Yee vortex at simulation time $t = 10$ when evolved with different hydrodynamical schemes, as defined in Table 2.1. Our improved version of AREPO robustly obtains second-order convergence independent of the initial grid geometry, whereas the old default version achieves this only for polar grids over a limited range of resolutions.

the reconstruction and extrapolation in the moving frame in a slightly inconsistent way. It transformed into the moving frame of the interface and performed the reconstruction from the current centre of mass.

Since the velocity of the cell is close to the velocity of the gas and the velocity of the frame is close to the velocity of the adjacent cells, this generally only leads to small errors. These are however especially strong (and superfluous) in cases where strong mesh regularisation motions are applied, and then can be observed in simulations of the ground state of the shearing box as spurious noise. This noise is now eliminated in our improved version of the code.

2.4.5 Higher-order Runge-Kutta time integration

The approximation (2.5) for the time integration is in general second order accurate, which means that its error $E_{t,s}$ for a single time step scales a $E_{t,s} \propto \Delta t^3$ with timestep size, and the accumulated error for the integration over a fixed time interval scales as $E_{t,i} \propto \Delta t^2$. In many simulations, the total error is typically dominated by the error E_x of the spatial discretization, which should be proportional to the square of the local cell size Δx in smooth flows.

This is because the size of the time step and the local spatial resolution are connected by the stability criterion:

$$\Delta t = C_{\mathrm{CFL}} \frac{\Delta x}{v_{\mathrm{signal}}}, \tag{2.29}$$

where v_{signal} is the local signal speed and C_{CFL} the Courant factor as a free parameter. This implies that an increase in the spatial resolution reduces also the error of the time integration by a comparable factor, and the whole scheme converges with second order, typically also keeping the time integration error subdominant.

Since there are no spatial scales to resolve in the ground state of the shearing box (see Section 2.5.1), the error in this case is however dominated by the error in the time integration, and can be observed as noise in the unstructured grid case. To verify this and reduce this noise if desired, we also implemented a formally third order accurate Runge Kutta method for the integration of the ideal MHD equations:

$$\boldsymbol{Q}_i^{n+1} = \boldsymbol{Q}_i^n + \frac{\Delta t}{6}\left[\boldsymbol{I}(t_0) + 4\boldsymbol{I}\left(t_0 + \frac{\Delta t}{2}\right) + \boldsymbol{I}(t_0 + \Delta t)\right]. \tag{2.30}$$

This adds an extra mid-timestep evaluation of the integral $\boldsymbol{I}$, for which we use again the linear time extrapolation (2.10). We note that other parts of the code, for example the source terms, are still only integrated with the second-order accurate method (2.5), which means that if those terms are dominating the error, the error will still only decrease with second order in time.

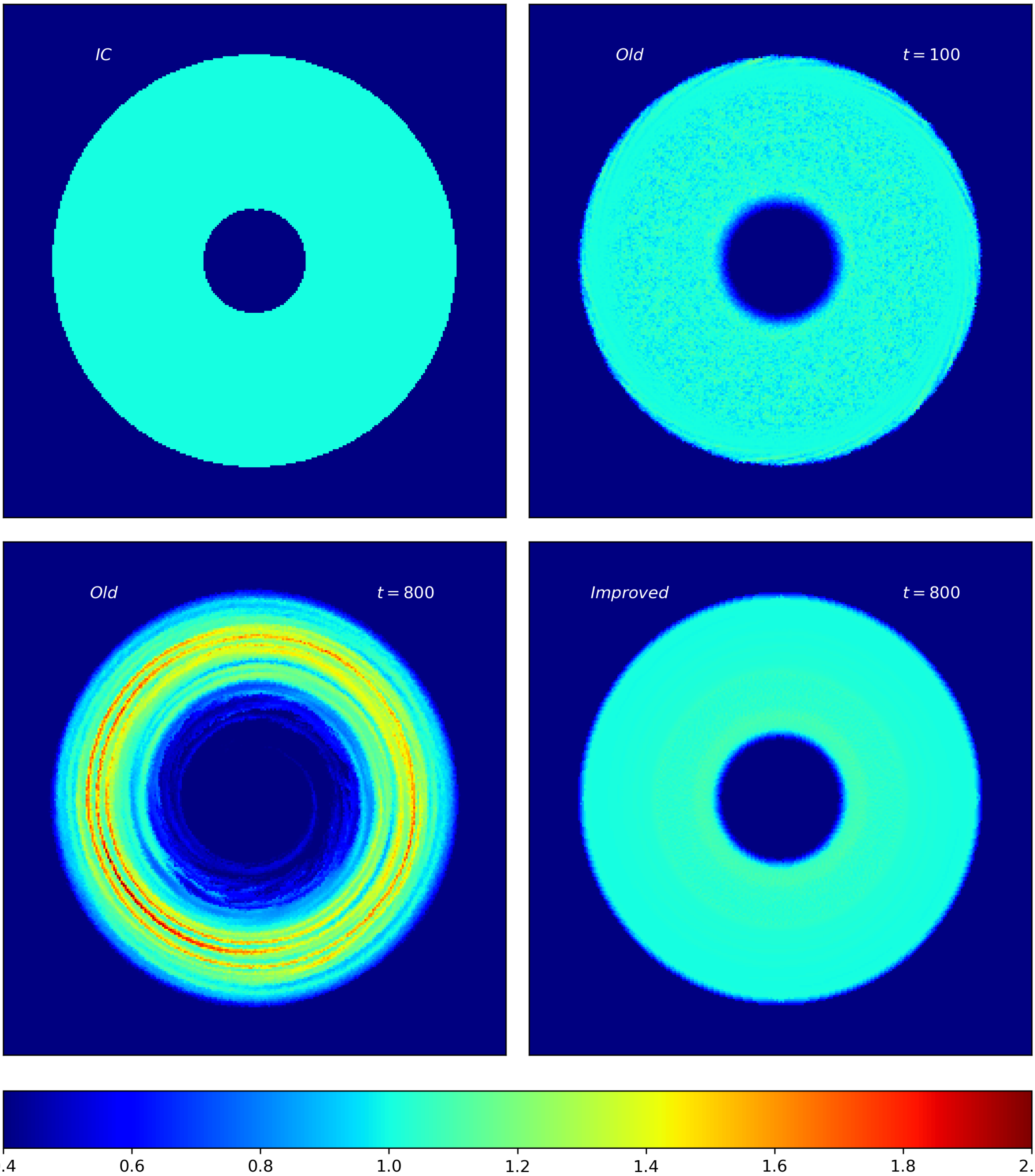

Figure 2.5: The density distribution of a cold Keplerian disk evolved with different simulation methods and at different times, as labelled. The method marked ‘old’ corresponds to the default version of AREPO without the modifications proposed here, while the run marked ’improved’ contains all modifications except for the third order time integration. We here use a polar grid for the initial conditions.

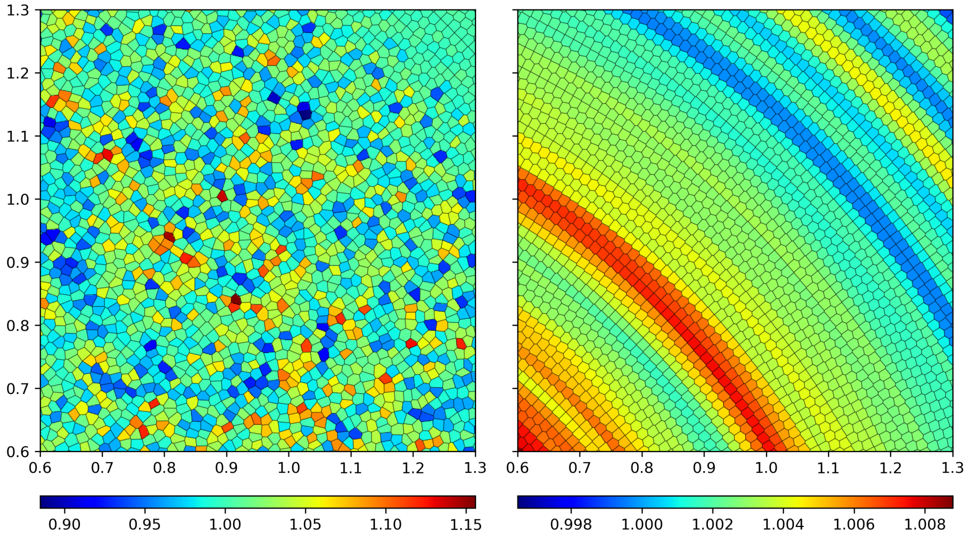

Figure 2.6: A zoom into the density field for a Keplerian disk simulation at time $t = 100$. The left hand side shows the disk evolved without the code improvements proposed here while the right hand side includes the modifications. Both simulations were initialized with a polar grid of mesh-generating points. The right simulation has much smaller, spherical, residual density perturbations (note the different stretches of the color tables).

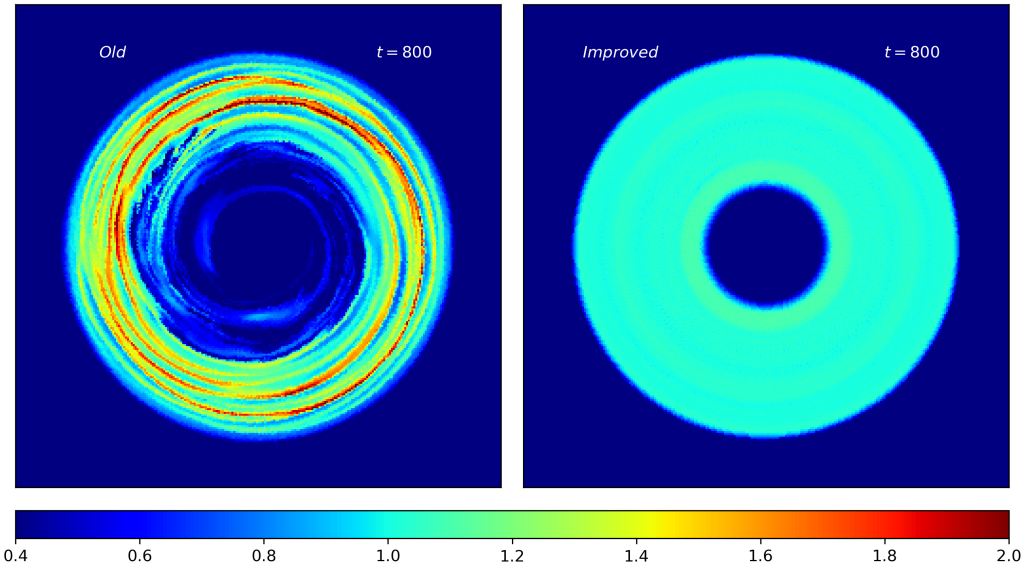

Figure 2.7: The same as the lower row of panels in Fig. 2.5 but for a simulation with an initially Cartesian grid and not a polar grid. Even in this case, our improved simulation code exhibits a drastically reduced noise level in this setup, and thus a much better long-term stability of the cold, rotationally supported disk.

2.4.6 Testing the accuracy improvements

Although all of the modifications of AREPO presented in this section were developed specifically to reduce the noise of the background flow in a shearing box, they are also useful for other applications of the code. In this subsection, we will briefly examine some representative examples to highlight this welcome effect.

Yee vortex

The isentropic Yee vortex test consists of a rotating, quasi-stationary flow with a differentially shearing velocity profile. Since the flow is smooth and free of discontinuities, it can be used to verify second-order convergence for a non-trivial two-dimensional flow. The test was used in Pakmor et al. (2016b) to show that the very first version of AREPO (Springel, 2010a) did not manage to guarantee full second-order convergence for this problem due to a comparatively noisy gradient estimation scheme and inaccuracies in time integration. Pakmor et al. (2016b) introduced improvements to both points that have since been used by default in the code. As shown in Pakmor et al. (2016b), using this updated code the Yee vortex then converges with second order, but this still requires a specially prepared polar grid whereas a start from a cubical grid that is ignorant of the spherical symmetry of the mesh motion still spoils the high convergence rate.

We here return to examining this issue and rerun the Yee vortex with and without the improvements presented in the previous subsections. For definiteness, we use both an initially polar grid as well as a Cartesian grid. Also, we run the test simulations with the standard second order accurate time integration (2.5) as well as with the improved third order accurate one (2.30). The details of the initial conditions can be found in Appendix 2.9.1, and in Table 2.1 we give a schematic overview of the different test runs.

To measure the convergence rate we define the L_1 error as

$$L_1 = \frac{1}{V} \sum_{i=1}^{N_{\rm cell}} |f_i|, \tag{2.31}$$

where $|f_i|$ is the deviation of the density of a cell i from the theoretical value at the coordinate of its center of mass. In Fig. 2.4, we show the error norm as a function of spatial resolution for our different simulation schemes.

We confirm that the previous version of the AREPO code was indeed only able to achieve second order convergence for this problem if an optimized polar grid (PO2) is used for the initial conditions, while a Cartesian grid (CO2) shows substantially higher errors. Interestingly, for very high resolution (5120^2 cells) we also find for the polar grid (PO2) a slight decrease in the order of the method. This effect vanishes if we use our improved formulation for the polar grid (PI2 and PI3) because this eliminates spurious activations of the slope limiter.

If we start with a Cartesian grid instead, our new formulation (CI2) achieves second-order convergence for low to moderate resolutions, but this becomes worse again for very high resolution. This degradation at very high resolution can be avoided by using our new improved time integration accuracy (CI3), suggesting that for low to moderate resolution the total error is dominated by errors of the spatial discretization, while for very high resolution the total error becomes dominated by the temporal discretization. The reason for this is presumably related to the local mesh regularization that we apply, and a faster change of the local topology of the grid when the resolution is higher.

Keplerian disc

A challenging problem for many hydrodynamical methods is the evolution of a pressureless gas disk orbiting around a central object on a Keplerian orbit (Cullen & Dehnen, 2010; Hopkins, 2015; Pakmor et al., 2016b). In particular, Hopkins (2015) reported that many state-of-the-art SPH and mesh codes show severe problems in this test. However, using their new MFM method they were able to evolve the disk for more than 250 inner orbits ($t = 600$). Although the disk showed noise in the density evolution of the order unity, the disk seemed to stay stable.

Pakmor et al. (2016b) used the same test to show that AREPO with his improved gradient estimates was also able to stably evolve the disk until $t = 600$. But at this time the disk started to break up at its inner boundary, and during the whole evolution, some noise in the density profile of the disk could be observed.

We rerun this test with the improved methods presented in the previous subsections (except for the higher-order time integration), with the exact same initial conditions as Pakmor et al. (2016b) (for details see Appendix 2.9.2) and at a resolution of 320x320 cells. As we show in Fig. 2.5, we reproduce their result that the original version of AREPO is able to evolve the disk for several hundred code units, and that at around $t = 600$ the inner boundary of the disk starts to break up, which only becomes worse with time. However, the improved integration method we proposed earlier allows us to evolve the disk for a much longer time. In fact, even at $t = 800$ the disk remains stable and only shows a small increase in density at the inner edge of the disk due to a weak influence of the inner boundary condition. In addition, the new scheme at the same time significantly reduces the noise in the density field throughout the disk.

In Fig. 2.6 we show a zoom into the density field, including the geometry of the Voronoi mesh at $t = 100$. While in the simulation with the old scheme the initial polar grid is destroyed and the local noise has a relative size of 10%, the initial grid stays stable in the simulation with the improved scheme. The maximum deviation from the theoretical density field is only around 1% (observe that the color scale is stretched accordingly) and those deviations do not take the form of local 'grid noise', but rather are ring-like structures that are coherent for the whole disk.

To further analyze the sensitivity of this simulation problem to the initial grid layout, we rerun simulations with an initial Cartesian grid of size 320×320 cells, once with the old code and once with our improved method. In Fig. 2.7 we show the density distribution at $t = 800$. In the simulation without the improvements proposed in this chapter, the disk starts to break up earlier compared to the simulation started with an initial polar grid. In contrast to this, the simulation with the improvements looks very similar to the simulation with an initially polar grid, and thus is insensitive to the initial grid geometry, as desired.

2.5 Test problems for the shearing box

In this section, we analyze the performance of our implementation of the shearing box approximation in several test cases. We consider many of the problems used in Stone & Gardiner (2010) to analyze the accuracy of the shearing box implementation in the ATHENA code, and we employ in several cases similar initial conditions as they did. As in Section 2.4.6 we define the L_1 error of a quantity f as

$$L_1 = \frac{1}{V} \sum_{i=1}^{N_{\rm cell}} |f_i|, \tag{2.32}$$

where $|f_i|$ is the difference of the value of a cell i from the theoretical value of f at its center of mass.

Although the use of a perfect Cartesian grid sometimes leads to better results due to the additional symmetry in the mesh configuration, we deliberately avoid this by adding a random displacement of 2% of the mean particle spacing to the positions of the mesh-generating points in the initial conditions. The background shear flow, together with mesh regularisation motions introduced by the code, then rapidly create a fully unstructured mesh, which is more representative for the mesh configurations encountered in realistic production runs with AREPO. To initialize our test simulations, we set the fluid properties of a cell to the value assumed by the continuous fields at the coordinate of the centre of mass of the cell. If not stated otherwise, we impose a global time step for all cells. As default shear parameters we use $q = 3/2$ and $\Omega_0 = 1$, and for all isothermal simulations we use an isothermal sound speed of $c_s = 1$.

2.5.1 Ground state of the shearing box

In Section 2.4.1 we showed that the default version of AREPO fails to accurately simulate the ground state of the shearing box, prompting us to develop several accuracy improvements of the code. We now revisit this problem in this section, but with these improvements enabled. As a first initial step, we use an *unstructured static* mesh with buffer zones close to the x-direction boundaries so that we can ignore the shear-periodic boundary conditions. In this case, the ground state is now stable up to machine precision, implying that the fluxes are calculated exactly by the higher-order Gauss-Legendre integration we introduced.

Next, we allow the mesh to move arbitrarily, so that the geometries of the surfaces of the cells change continuously in time. This change does not have to be a polynomial function in time, which means that the second-order accurate time integration scheme of equation (2.5) is associated with small errors. These can be observed as small noise in the velocity and density fields that lies substantially above machine precision. The noise can be decreased by either using a smaller time step, or by using a higher-order time integration scheme, for example the third-order Runge Kutta method we described in Section 2.4.5.

To analyze the effect of the time step size and integration scheme, we use a two-dimensional box of size $L_x = L_y = 10$, and set up a Cartesian grid with 200^2 cells and random displacements of 1% in the coordinates of the mesh-generating points. The initial conditions are given by the ground state of the shearing box, and we run the simulation until time $t = 1000$. This leads to a dynamic unstructured mesh with a quasi-stationary equilibrium between the mesh regularisation motions introduced by the code and the tendency of the local shear to degrade the local mesh regularity. We then use this “relaxed” unstructured mesh geometry and reinitialize the fluid variables with the analytical values of the ground state at its centre of mass to start out once more with a perfectly quiet state. Afterwards, we let the system evolve for time $t = 1$ and examine how accurately the quiet shear flow of the ground state is maintained.

We repeat this last simulation for different time step sizes, imposed here by changing the Courant number. We then measure the average L_1 error of the fluid quantities, as well as the maximum L_1 error that is realized for any of the cells. In the first row of Fig. 2.8, we show the L_1 errors of different hydrodynamic quantities as a function of the Courant number for the second and third-order Runge Kutta schemes. We also fit the expression

$$L_1 = A_0 \, C_{\mathrm{CFL}}^{A_1} \tag{2.33}$$

to the measurements. A_1 gives us the order of convergence of the corresponding fluid quantity. As expected for a second-order method, all errors decrease with second order for smaller time step sizes. This also shows that the error in this problem is indeed fully dominated by errors in the time integration, not the spatial integration, because the latter is eliminated by our higher order flux integration. The use of the third-order RK method reduces the amplitude of the total error (A_0) by about one order of magnitude, but the convergence rates (A_1) stay still close to 2 and do not approach the value of 3 we may have expected. To further analyze this discrepancy, we have repeated the test in three dimensions with $L_x = L_y = L_z = 10$ and 50^3 cells.

In the second row of Fig. 2.8 we show the corresponding L_1 errors as a function of the Courant number now in the three-dimensional case. We again find, as expected, $A_1 \approx 2$ for the second-order RK method, but now we recover a significantly better convergence rate than 2 for the third-order RK time integration. In the latter case, the maximum error decreases slower than the average errors, which means that for small time step sizes relatively large local errors dominate the average error budget. The fact that the third-order RK method does not decrease the error with full third order is a hint that the code likely still contains some inaccuracies that more prominently show up in two dimensions, and less so in three dimensions. One culprit might lie in the estimate of the spatial velocity of an interface, which only takes into account the movement of the two adjacent cells and not the movement of other neighbouring cells, even though they introduce changes in the size of the facets.

Finally, we note again that we can completely suppress the errors in the time integration by starting with a perfectly structured mesh like a Cartesian or hexagonal grid, and only allow for a restricted mesh movement with $\vec{v}_{\mathrm{mesh}} = (0, -q\Omega_0 x, 0)$ that is independent of

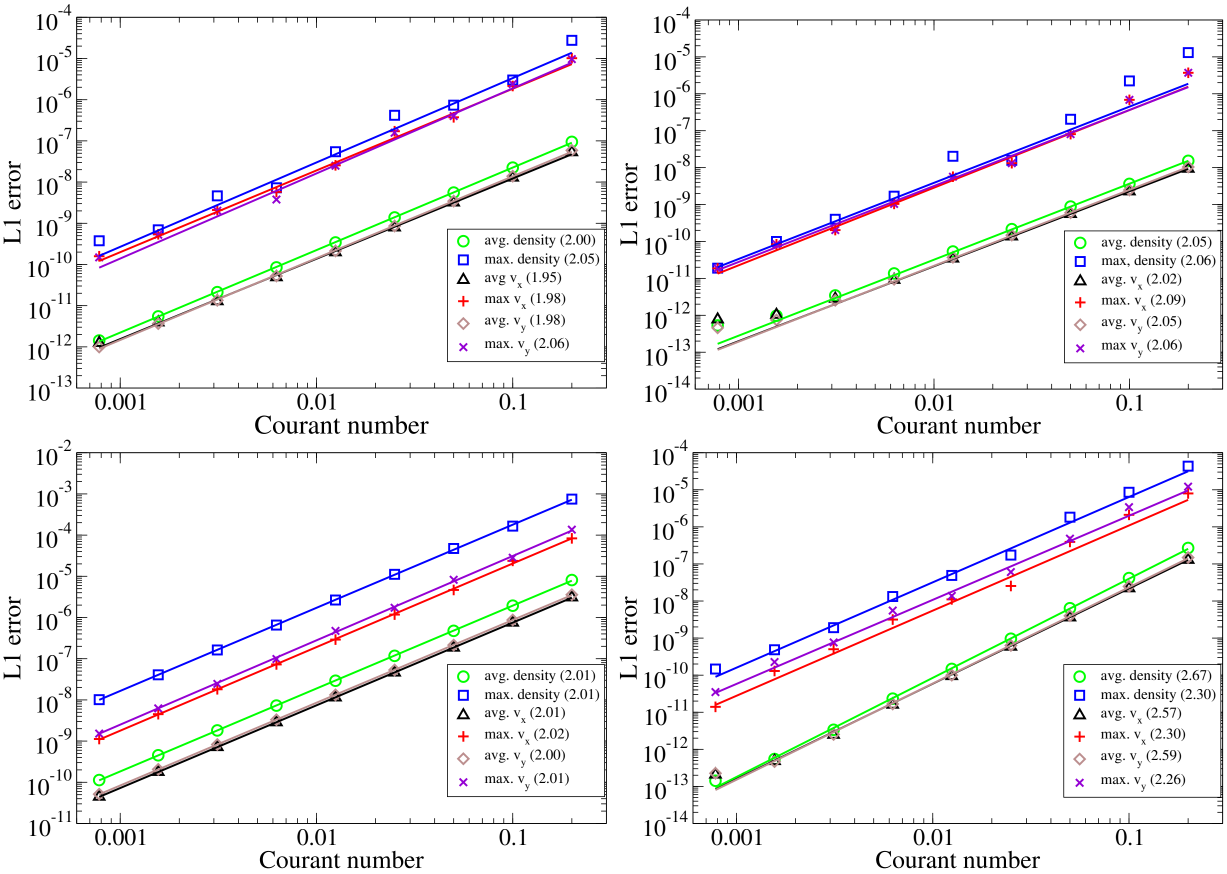

Figure 2.8: The L_1 error norm of different hydrodynamic quantities (as labelled) as a function of the time step size (here parameterized through the Courant number) at time $t = 1$ for simulations of the ground state of the shearing box (for details, see Section 2.5.1). The upper row shows results in two dimensions, the lower one in three dimensions. The panels on the left use the second order accurate time integration of equation (2.5), the ones on the right the third order accurate method of equation (2.30). In brackets we give the fitted values of the slope A_1, see equation (2.33).

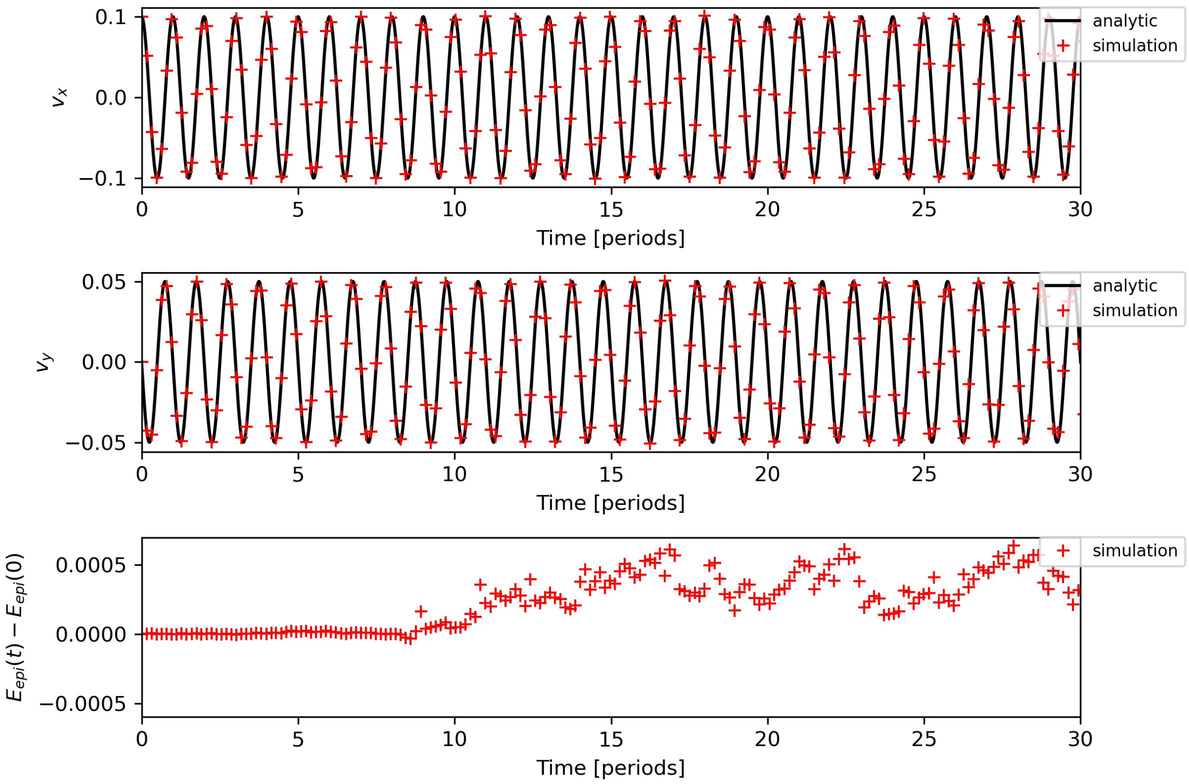

Figure 2.9: Epicycle oscillations in the velocities v_x and v_y (first and second row panels) compared between analytic solution (solid lines) and numerical measurements (crosses) for a simulation with a resolution of 10^2 mesh-generating points. The temporal evolution of the epicycle energy (equation 2.36) in the simulation is shown in the bottom panel.

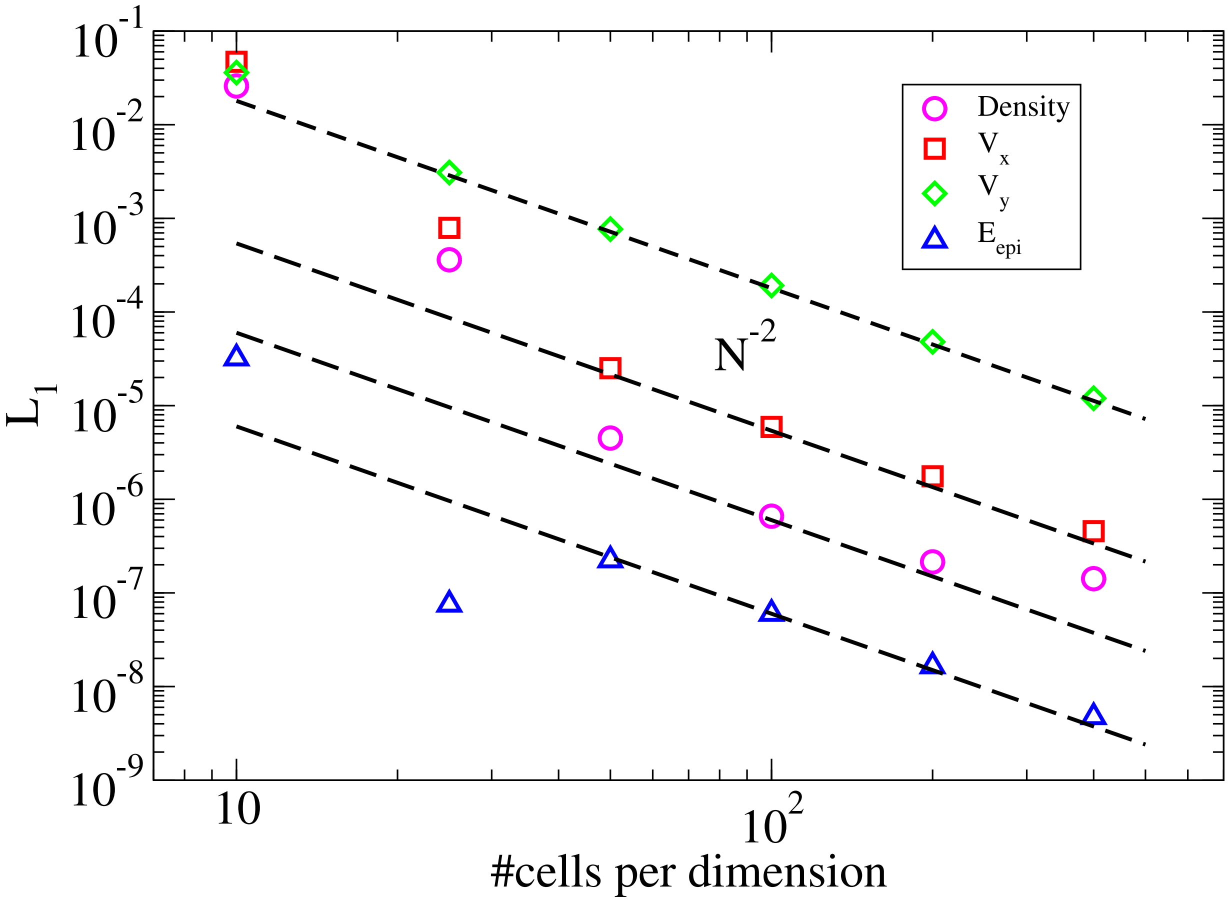

Figure 2.10: L_1 norm of the error of the density field, the velocity fields v_x and v_y, as well as of the epicycle energy (eqn. 2.36) for a test simulation of epicycle oscillations. The measurements were performed at time $t = 666$, which corresponds to around 103 completed epicycle oscillations.

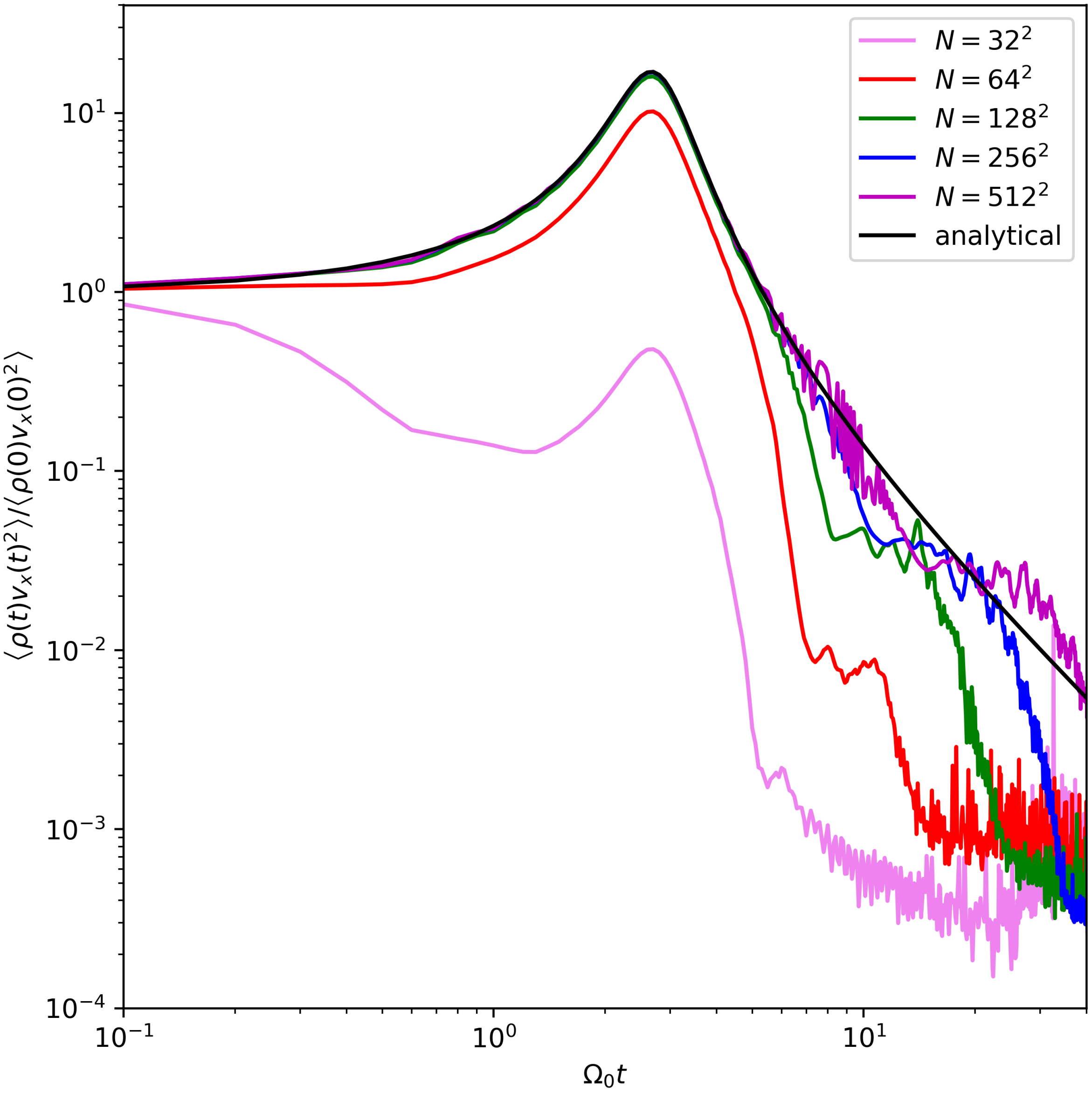

Figure 2.11: The evolution of the total kinetic energy associated with the movement in the x-direction for an incompressible hydrodynamic shearing wave. The black line corresponds to the analytical solution of eqn. (2.38) while the colored lines give measurements for simulations with different numerical resolutions, as labelled.

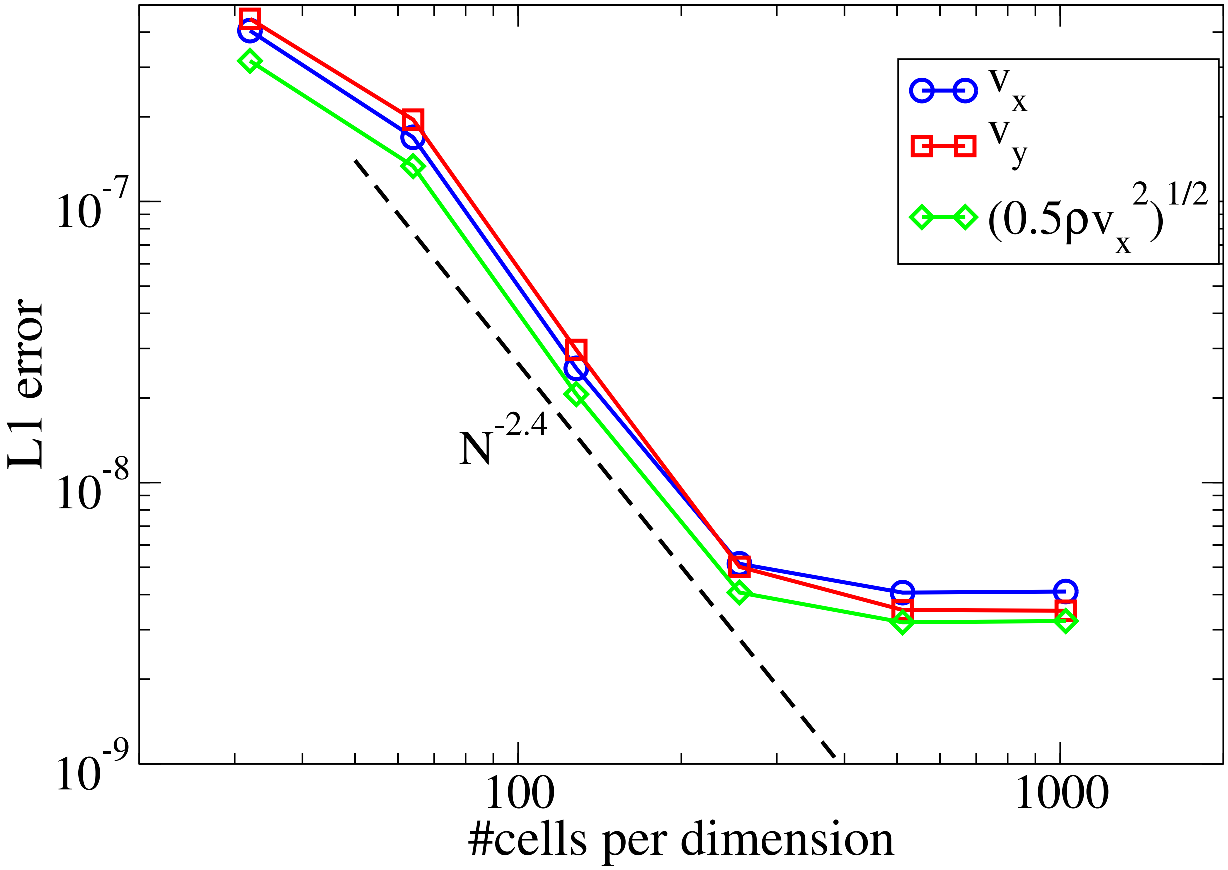

Figure 2.12: The L_1 error of the velocity and the kinetic energy density of the motion in the x-direction as a function of resolution for the simulation of an incompressible hydrodynamic shearing wave. The L_1 error was averaged over the time interval $0 \leq \Omega_0\, t < 6$.

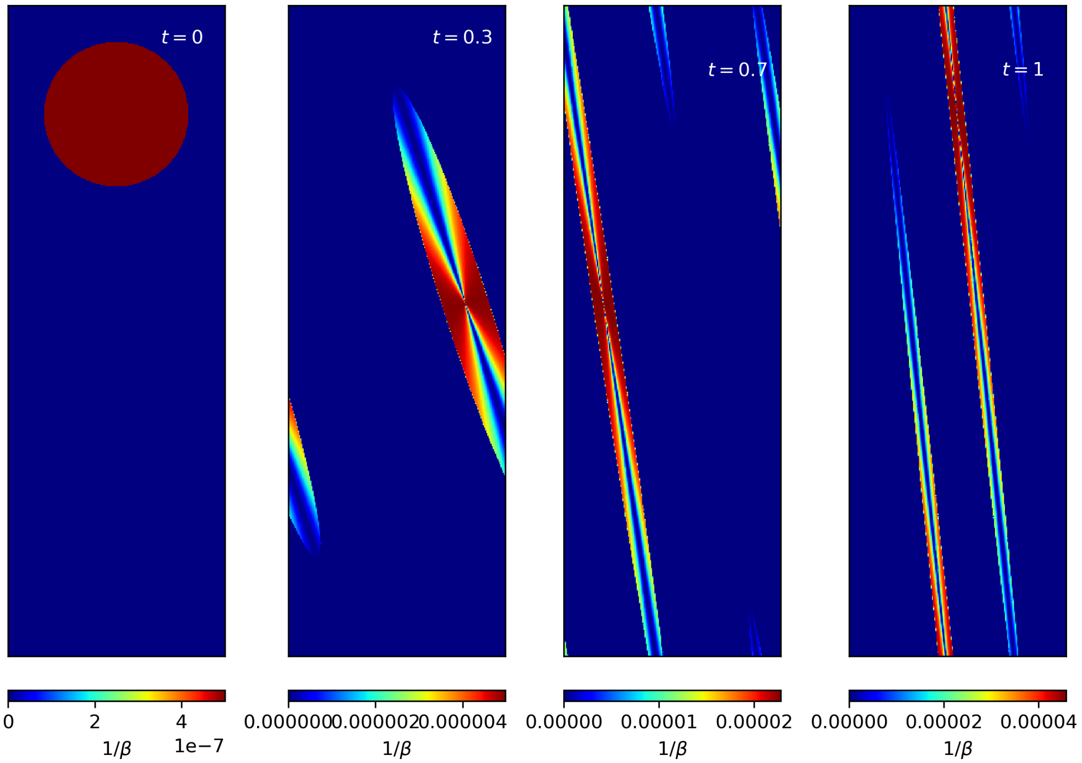

Figure 2.13: Strength of the magnetic field at different times in a simulation of the advection of a magnetic field loop in a shearing box.

time. At all subsequent times, the mesh cells then still contain symmetries that cancel truncation errors in the time integration, which typically leads to similar or even better results than for the unstructured mesh cases. Note that this approach still removes the background bulk velocity from the calculation of the size of the time steps, it does have lower and spatially uniform advection errors compared to a Eulerian treatment, and the handling of the boundaries is manifestly translationally invariant. These properties are attractive, and thus such a scheme can be viewed as an interesting hybrid between a freely moving mesh and a static grid code. However, we will not discuss this scheme further in this chapter, but it might nevertheless be of interest in cases where a very small level of numerical noise is required.

2.5.2 Epicycle oscillations

Small perturbations to the velocity of the ground state of the shearing box do not get damped but instead lead to oscillations. In the case of $q = 1.5$, they correspond to elliptical orbits in global disk simulations. If one assumes a perturbation $v_x = v_{x0}$ at $t = 0$, the evolution of the velocities is given analytically by:

$$v_x(t) = v_{x0} \cos(\Omega t), \tag{2.34}$$

$$v_y(t) = -v_{x0}\sqrt{\frac{2-q}{2}}\sin(\Omega t). \tag{2.35}$$

An important conserved quantity for these motions is the so-called epicycle energy

$$E_{epi} = \frac{\left(v_x^2 + \frac{2}{2-q}v_y^2\right)}{2} = \text{const.} \tag{2.36}$$

Obtaining this conservation numerically requires special care in the implementation of the source terms of the shearing box.

To test for this, we add a perturbation $v_{x0} = -0.1c_s$ to the ground state of a two-dimensional shearing box with $\Omega = 1.5$ and $c_s = 10^{-3}$. We use a box size $L_x = L_y = 10$ and start with a randomly perturbed Cartesian grid. In Fig. 2.9 we show that even for the low resolution of 10^2 cells the errors in the epicycle energy do not grow with time. However, if we do not add the predictor step for the second application of the source terms, as described in Section 2.3.1, the epicycle energy grows exponentially. In Fig. 2.10, we show that the errors in the velocity as well as in the epicycle energy decrease with second order in the spatial resolution, confirming that epicycle oscillations are accurately treated by our shearing box implementation.

2.5.3 Evolution of a hydrodynamic shearing wave

To test the implementation of our boundary conditions for non-axisymmetric conditions we simulate the evolution of a hydrodynamic shearing wave (Johnson & Gammie, 2005; Balbus & Hawley, 2006; Shen et al., 2006). The setup follows Stone & Gardiner (2010). We use a two-dimensional box of size $L_x = L_y = 1$, an isothermal equation of state with sound speed $c_s = 1.29 \times 10^{-3}$, $\Omega_0 = 10^{-3}$ and initial wave vector $2\pi\boldsymbol{k}_0/L_x = (-8, 2)$. We choose initial amplitudes $v_{x,0} = 10^{-4}c_s$ and $v_{y,0} = -k_{x,0}/k_{y,0}v_{x,0}$, and a constant background density $\rho = 1$.

The shearing box leads to a time-dependence of the wave (Shen et al., 2006):

$$k_x(t) = k_{x0} + q\Omega_0 k_{y0} t, \tag{2.37a}$$

$$v_x(t) = v_{x,0}\sqrt{\frac{k_{x,0}^2 + k_{y,0}^2}{k_x^2 + k_{y,0}^2}}\cos(k_x(t)x + k_{y,0}y), \tag{2.37b}$$

$$v_y(t) = -v_{x,0}\sqrt{\frac{k_{x,0}^2 + k_{y,0}^2}{k_x^2 + k_{y,0}^2}}\frac{k_x(t)}{k_y}\cos(k_x(t)x + k_{y,0}y). \tag{2.37c}$$

The kinetic energy gets amplified and reaches a maximum at $t = 8/(3\Omega_0)$. In Fig. 2.11, we compare the evolution of the total kinetic energy in the x-direction for different resolutions with the analytical value

$$E_{\mathrm{kin},x} = \int_0^1 \mathrm{d}x \int_0^1 \mathrm{d}y \frac{1}{2}\rho v_x^2 = \frac{\rho v_{x,0}^2}{4}\frac{k_{x,0}^2 + k_{y,0}^2}{k_x^2 + k_{y,0}^2}. \tag{2.38}$$

For high resolution ($N = 128^2$ and higher), we accurately recover the amplification of the kinetic energy. At later time, the kinetic energy decreases in our simulations due to numerical viscosity, but this effect becomes smaller if we increase the resolution, as expected. If there are only 4 cells per initial wavelength, the numerical viscosity starts to noticeably damp the wave already at the beginning.

In Fig. 2.12 we show the average L_1 error for different fluid quantities as a function of resolution in the time interval $0 < t < 6/\Omega_0$. As discussed earlier, for low resolution the numerical viscosity is high and we find large deviations from the analytical solution and a slow convergence rate. We then find a regime with seemingly faster than second-order convergence for high resolution, while eventually the errors start to become constant. The latter issue could be explained by the fact that the analytical solution was derived under the assumption of incompressibility, which is not actually compatible with the small density variations observed in our simulations.

2.5.4 Advection of a weak magnetic field loop

As a first test for the implementation of magnetic fields in the shearing box, we evolve a dynamically unimportant magnetic field loop in a homogeneous medium in the presence of background shear. We use a box with size $L_x = 3$ and $L_y = 8$, a background density $\rho = 1$, an isothermal equation of state with sound speed $c_s = 1$, and the parameters $\Omega = 1$ and $q = 3/2$ for describing the shearing of the box. The field loop has a radius $r = 1$ with magnetic strength $\beta = \frac{2c_s^2\rho_0}{B_0^2} = 2 \times 10^6$, so the magnetic pressure is very small compared to the thermal pressure. Besides the background shear flow, we add a velocity $v_x = c_s$ to seed an epicycle oscillation of the field loop. This allows us to also check the implementation of the boundary conditions. We use a uniform resolution of 1800×600 cells and add random displacements of 1% of the mean particle spacing to the mesh generating points. In Fig. 2.13, we show the resulting β at different times. One can see no traces of the boundary conditions, and the shape of the field loop is well preserved throughout the evolution.

2.5.5 Evolution of a compressible magnetic shearing wave

Another sensitive MHD test for our shearing box implementation is the evolution of a compressible magnetic shearing wave in three dimensions (Johnson, 2007; Stone & Gardiner, 2010). We use a box of size $L_x = L_y = L_z = 0.5$, an initially Cartesian grid with a constant number of cells per dimension, and an isothermal equation of state with sound speed $c_s = 1$. As initial conditions we specify

$$\rho(\boldsymbol{x}) = 1 + 5.4808210^{-6}\cos(\boldsymbol{k}_0 \cdot \boldsymbol{x}), \tag{2.39a}$$

$$\boldsymbol{v}(\boldsymbol{x}) = \begin{pmatrix} -4.5856 \\ 2.29279 \\ 2.29279 \end{pmatrix} 10^{-6}\cos(\boldsymbol{k}_0 \cdot \boldsymbol{x}) - \begin{pmatrix} 0 \\ q\Omega_0 x \\ 0 \end{pmatrix}, \tag{2.39b}$$

Origin sim.	100 $\langle\alpha_{\rm tot}\rangle$	100 $\langle\alpha_M\rangle$	100$\langle\alpha_R\rangle$	$\langle B^2/2\rangle/P_0$	$\langle\rho v^2/2\rangle/P_0$
Shi et al. (2016)	5.16	4.17	0.99	0.1301	0.0417
This work ($c_{h0} = 0.1$)	3.21	2.56	0.65	0.066	0.027
This work ($c_{h0} = 0.2$)	3.59	2.89	0.71	0.069	0.032
This work ($c_{h0} = 0.5$)	4.16	3.34	0.82	0.093	0.035
This work ($c_{h0} = 1$)	2.20	1.74	0.46	0.043	0.020
This work ($c_{h0} = 2$)	1.04	0.81	0.23	0.021	0.010
This work ($c_{h0} = 5$)	0.42	0.33	0.09	0.011	0.005

Table 2.2: A comparison of different time-averaged fluid quantities in simulations of the MRI using a tall box without net field. We give our results for a number of different settings of the Dedner cleaning speed (c_{h0}) and compare them to the results from Shi et al. (2016) (their simulation x1y4z4r32). All simulations use 32 cells per scale height and are based on identical initial conditions. The fluid quantities are averaged over 150 orbits, starting after the first 50 orbits.

$$\boldsymbol{B}(\boldsymbol{x})/\sqrt{4\pi} = \begin{pmatrix} 5.48082 \\ 10.962 \\ 0 \end{pmatrix} 10^{-7}\cos(\boldsymbol{k}_0\cdot\boldsymbol{x}) + \begin{pmatrix} 0.1 \\ 0.2 \\ 0 \end{pmatrix}, \tag{2.39c}$$

with a wavevector $\boldsymbol{k}_0 = (-2, 1, 1) \times 2\pi/L$.

Due to shearing motion, the wavevector $\boldsymbol{k}(t) = \boldsymbol{k}_0 + (q\Omega_0 t, 0, 0) \times 2\pi/L$ as well as the y-component of the average magnetic field $\hat{B}_y(t)/\sqrt{4\pi} = 0.2 - 0.1q\Omega_0 t$ evolve as a function of time. To obtain the evolution of the amplitudes of the wave we integrate the system of differential equations given in Johnson (2007, their eqns. 13–16). In Fig. 2.14 we compare the real part of the amplitude of the y-component of the magnetic field in our simulations, defined as

$$\delta B_y = 2\int_V (B_y - \hat{B}_y)\cos[\boldsymbol{k}(t)\boldsymbol{x}]\mathrm{d}\boldsymbol{x}, \tag{2.40}$$

with the analytic values, as a function of the employed numerical resolution.

The wave gets damped by numerical viscosity and resistivity. Both dissipative effects decrease with increasing resolution, allowing us to follow the evolution of the wave for longer times if the resolution is higher. To more quantitatively analyze the convergence properties of our code, we show in Fig. 2.15 the L_1 error of different quantities averaged over the time period $0 < \Omega_0 t < 2$, as a function of resolution. For sufficiently high resolution, we find a close to second-order convergence in all quantities.

2.6 Nonlinear magnetorotational instability without net field

Finally, as a first example for an application of our new shearing box implementation to an interesting nonlinear problem we consider a simulation of the magnetorotational instability (MRI), here without a mean magnetitic field and in an unstratified box. In a standard

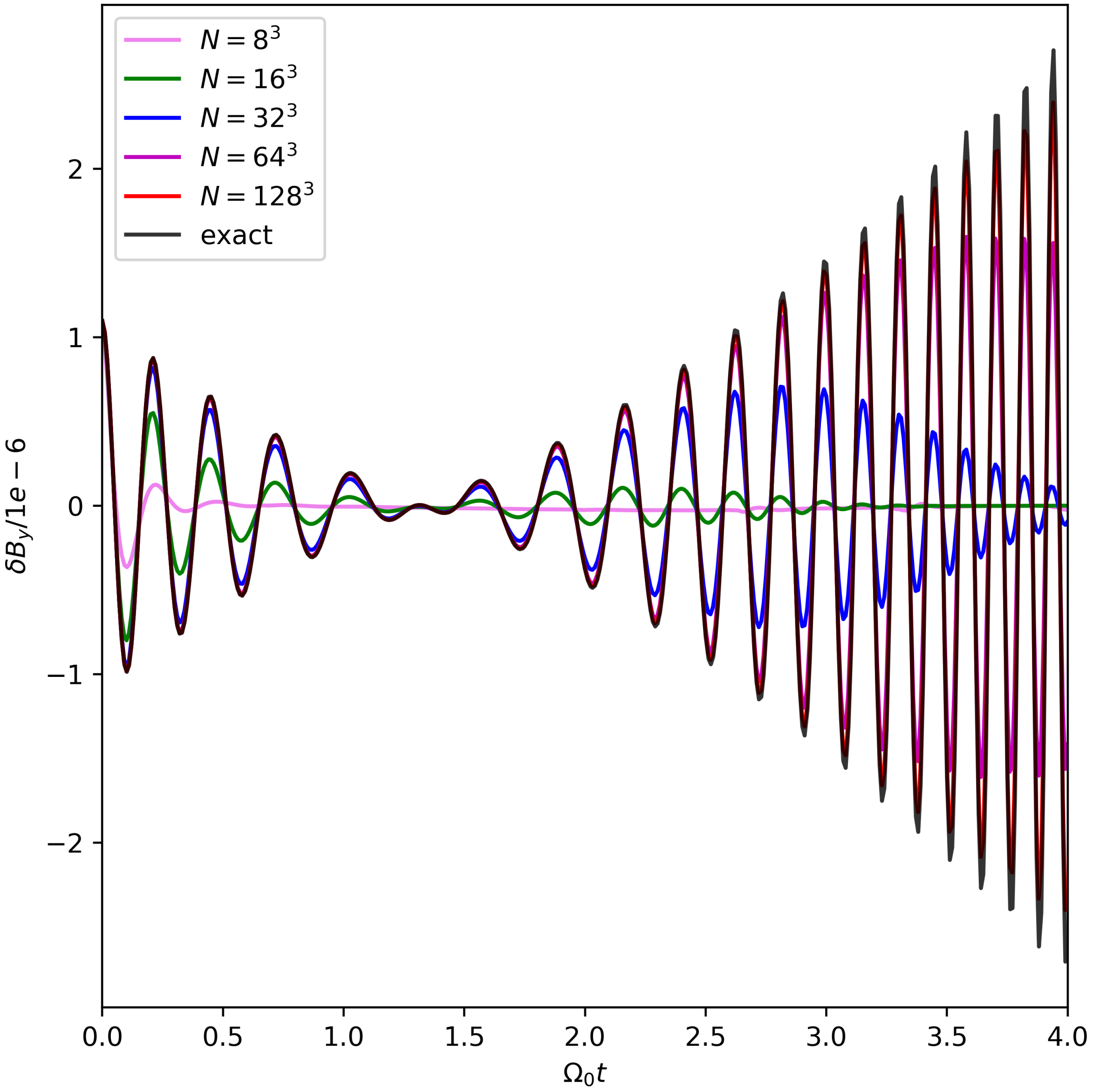

Figure 2.14: Evolution of the amplitude of the magnetic field δB_y as a function of time in a compressible MHD shearing wave test, for different numerical resolutions, as labelled.

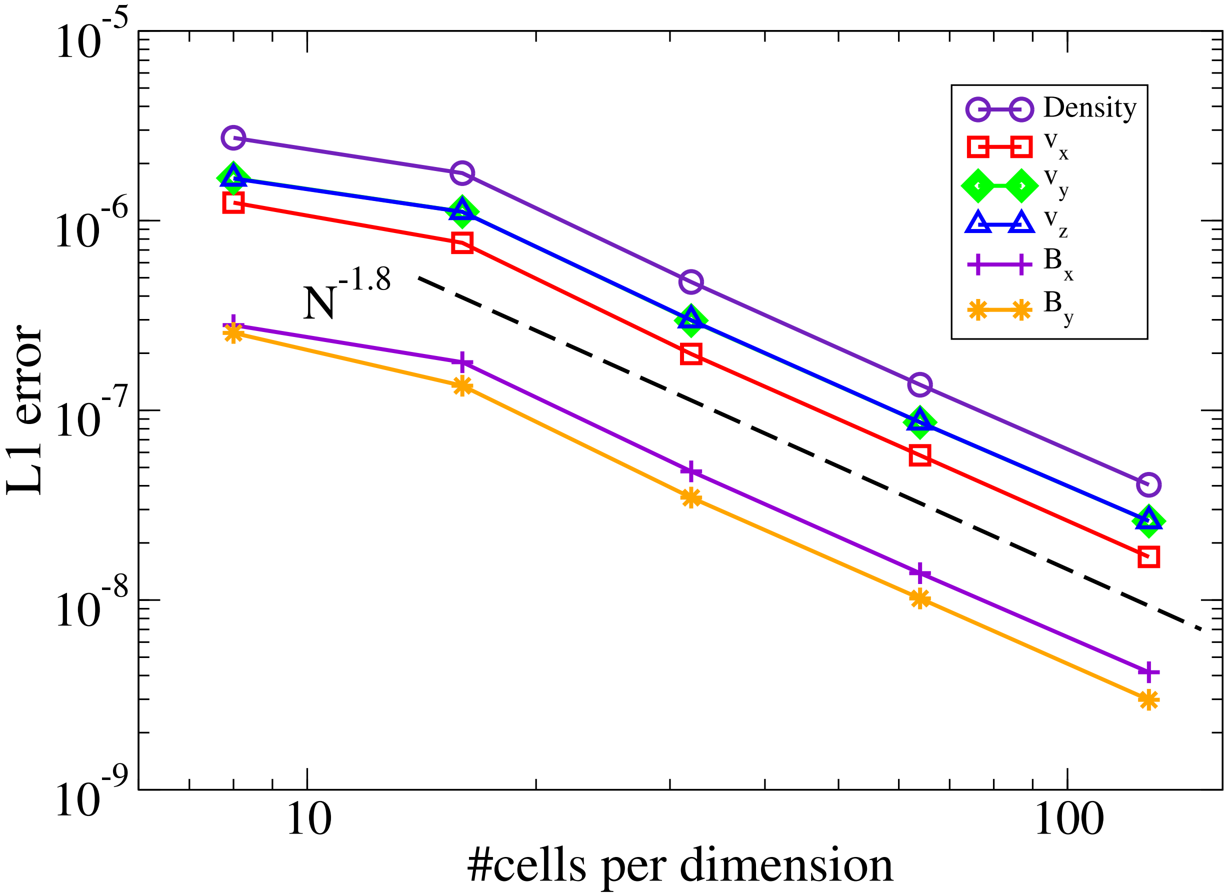

Figure 2.15: The L_1 error norm for different fluid quantities averaged over the time period $0 < \Omega_0 t < 2$ in a compressible MHD shearing wave test. The black dashed line shows the slope of -2 that we would ideally expect from our code, while the actual measurements as a function of resolution are shown by colored lines, as labelled.

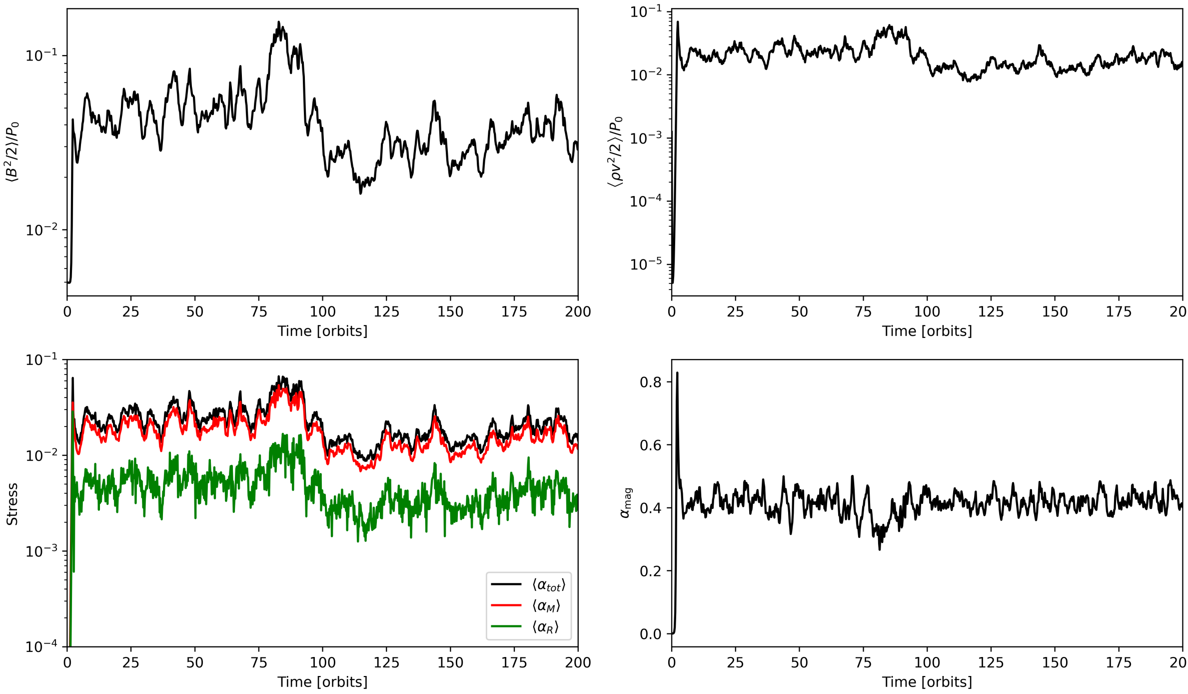

Figure 2.16: The temporal evolution of the average magnetic energy density (top left), kinetic energy density (top right), Maxwell and Reynolds stresses (bottom left), and of the normalized magnetic stress (bottom right) for a simulation of the magnetorotational instability (MRI) without mean field and using standard Dedner divergence cleaning (i.e. $c_{h0} = 1$). The simulation method shows a sustained quasi-stationary MRI even at moderate numerical resolution.

box size ($L_x = L_z = 1\,H$) previous studies found a non-converged behaviour of the MRI (Fromang & Papaloizou, 2007; Fromang et al., 2007). We therefore adopt a tall box setup ($L_y = L_z = 4H = 4L_x$) as in Shi et al. (2016) who achieved with this configuration convergence with the ATHENA code (Stone et al., 2008; Stone & Gardiner, 2010). This test was also used in Deng et al. (2019) to show that with a resolution of 48 particles per scale height $H = c_s/\Omega_0$, the GIZMO code (Hopkins, 2015) was not able to sustain the MRI for more than 20 orbits.

We use a comparatively low resolution of 32 cells per scale height, an isothermal equation of state with $c_s = 1$, and the shearing box parameters $q = 3/2$ and $\Omega_0 = 1$. For the initial conditions, we use the ground state of the shearing box (2.15) with constant density $\rho = 1$, a purely vertical magnetic field

$$\boldsymbol{B} = B_0 \sin\left(2\pi x/L_x\right) \hat{e}_z, \tag{2.41}$$

and we add uniformly distributed random noise of maximum amplitude $0.05\,c_s$ to the initial velocities of all cells in order to seed the MRI. The initial field strength B_0 is defined by the parameter $\beta = 2c_s^2\rho_0/B_0^2 = 400$, and we use the Dedner approach for divergence cleaning. We vary the strength of the cleaning by multiplying the standard variable c_h in the Dedner scheme with a constant prefactor c_{h0}. Smaller values mean weaker cleaning, and an effectively lower numerical resistivity.

To analyse the simulations we define the volume weighted average of a quantity X as

$$\langle X \rangle = \frac{\int X \mathrm{d}V}{\int \mathrm{d}V}, \tag{2.42}$$

as well as the Maxwell stress

$$\alpha_M = -\frac{B_x B_y}{P_0}, \tag{2.43}$$

and the Reynolds stress

$$\alpha_R = \frac{\rho v_x (v_y - \overline{v_y})}{P_0}, \tag{2.44}$$

where $\overline{v_y}$ denotes the background mean flow and $P_0 = 1$ is the initial pressure. The saturation of the MRI can be measured in terms of the relative Maxwell stress:

$$\alpha_{\mathrm{mag}} = -\frac{\langle B_x B_y \rangle}{\langle B^2 \rangle}, \tag{2.45}$$

which goes to 0 if the MRI dies out.

In Fig. 2.16 we show the evolution of different fluid quantities relevant for the MRI. After an initial growth of the magnetic energy, we find as expected a saturated state. In Table 2.2 we compare several time-averaged quantities with the equivalent simulations from Shi et al. (2016). The measured stresses and energies are all slightly smaller than in ATHENA, which hints that the Dedner cleaning is more diffusive than the constrained transport scheme used in Shi et al. (2016). For $c_{h0} = 0.5$ we find the strongest stresses in the saturated phase. For higher c_{h0}, the stresses decrease due to a larger numerical resistivity.

Overall, the results are very positive as they are superior compared to previous studies of the MRI with Lagrangian techniques, and are nearly as good as those obtained with a Eulerian constrained transport method. Given that our method uses a fully dynamic and unstructured mesh, which does not benefit from fortuitous cancellations of truncation errors, this encourages the use of the new method for more complicated physics applications. In a future study we for example plan to further analyse this system by modifying the resolution, the cleaning speed c_h, and the initial magnetic field, and it will be especially interesting to study the case of a stratified shearing box as well. We will also further compare our results with the studies in Deng et al. (2019) and Wissing et al. (2022) that both used Lagrangian techniques.

2.7 Summary and conclusions

In this work, we have focused on the technical realization of the shearing-box approximation in the moving-mesh code AREPO. The shearing-box is ideal to achieve very high local resolution in rotationally supported disk flows, much higher than can be readily obtained in global disk simulations. This allows, for example, a study of the non-linear behaviour of crucial fluid instabilities in such disks, such as the magnetorotational instability.

While the mesh construction algorithm of AREPO can be straightforwardly generalized to cope with the special shear-periodic boundary conditions appearing in the radial direction, we found that the default version of the AREPO code produces an uncomfortably high level of 'grid-noise' in the ground-state flow of the shearing box. In previous applications of AREPO, it had often been noted that the code's accuracy was reduced in situations with strong shear, because here mesh faces turn rapidly, and the distortion and time variation of the geometry of mesh cells are particularly strong. In this sense, the shearing-box is the worst situation one can possibly imagine, because shear appears *everywhere*, and *all the time*. In this chapter, we were thus compelled to identify the origin of these inaccuracies in a clearer way and in more detail than had been understood before. But this then led also the way to overcome these sources of noise and develop a significant improvement of the accuracy of the integration scheme of AREPO. This advance is of particular importance for cold, strongly shearing flows, but it ultimately is also beneficial for all other applications of the code.

In particular, we found that for general unstructured Voronoi meshes it can be necessary to integrate the fluxes over mesh faces with more than one Gauss point in order to reduce truncation errors to a level that is achieved by symmetric cells in part through cancellation effects on opposite sides of cells. We have also found that a minor change in the slope limiting scheme of AREPO is helpful to avoid that the slope limiting can be needlessly triggered in situations with highly distorted cell geometries. Finally, we rectified a minor inconsistency in the time integration scheme when mesh regularization motions are applied by the code. We note that to identify these improvements, examining the ground state of the shearing box in detail, a seemingly trivial state, proved essential.

With the newly proposed improvements in place, we have shown that AREPO is able to very accurately simulate the shearing-box. Also, our improvements are beneficial for other types of simulations where strong shear is present, such as the Yee vortex. An advantage compared to Eulerian schemes is that the local truncation error of our approach is fully uniform within the shearing box, and does not increase towards the radial box boundaries as in Eulerian methods. In fact, the calculation is fully translationally invariant. When replicating multiple copies of the primary simulation domain using the (shear) periodic boundary conditions, and sticking them together at the boundaries to cover a larger domain, one could not tell any more where the original box boundary had been.

As a first important application, we have considered the magnetorotational instability without a background field. AREPO is able to sustain the MRI even at comparatively low resolution, unlike the Lagrangian MFM approach. Our results show evidence for a somewhat higher numerical resistivity compared to the constrained transport method used by the ATHENA code. Perhaps different methods for magnetic divergence control can improve on this in the future, but already now AREPO should be a versatile and flexible tool for studying disks with the shearing-box approximation, in particular due to its ability to seamlessly increase the local resolution in situations with fragmentation and local (gravitational) collapse. We will consider such physics problems in forthcoming applications of the code.

2.8 Appendix: Gauss-Legendre integration

The class of Gauss-Legendre quadrature rules numerically integrates functions $f(\boldsymbol{x})$ as a weighted sum of the function evaluations $f(\boldsymbol{x}_i)$ at different $\boldsymbol{x}_i$.

2.8.1 One dimensional integrals

In one dimension, any integral over a finite interval can be transformed into the form (2.25). In Table 2.3 we give the corresponding evaluation points x_i and weights w_i up to order $P = 5$.

2.8.2 Two dimensional integrals

In two dimensions, we are integrating over polygons. There exists no general equation for polygons with more than four edges that could conveniently give us the minimum number of evaluation points needed to integrate a polynomial of order $N > 1$ exactly. For the unit square $[-1, 1] \times [-1, 1]$ one can construct such rules as tensor product of one-dimensional Gauss-Legendre integrations. But the coordinate transformation from a general quadrilateral to the unit square is in general nonlinear, which means that by transforming the original polynomial to the natural variables of the unit square, one also increases the order of the polynomial. This would in turn require a higher-order rule for the

P	x_i	w_i
1	0	2
3	$-1/\sqrt{3}$	1
	$1/\sqrt{3}$	1
5	$-\sqrt{3/5}$	5/9
	0	8/9
	$\sqrt{3/5}$	5/9

Table 2.3: The maximum order P of the polynomials that can be integrated exactly with the corresponding evaluation points x_i and weighting factors w_i.

P	N	L_1	L_2	L_3	w_i
1	1	1/3	1/3	1/3	1
2	3	2/3	1/6	1/6	1/3
3	1	1/3	1/3	1/3	−9/16
	3	3/5	1/5	1/5	25/48
4	3	0.108103018168070	0.445948490915965	0.445948490915965	0.223381589678011
	3	0.816847572980459	0.091576213509771	0.091576213509771	0.109951743655322

Table 2.4: The maximum order P of the polynomials over the unit triangle that can be integrated exactly with the corresponding evaluation points and weighting factors w_i. The two coordinates of the evaluation points can be constructed by N cyclic uses of L_1, L_2 and L_3. The table values are adopted from Akin (2005).

unit square, increasing the computational cost. We therefore choose a different approach and split the original polygon into triangles. Integrals of polynomials over any triangle can be transformed into integrals of polynomials of the same order over the unit triangle defined by the local coordinates $0 \leq r \leq 1$, $0 \leq s \leq 1 - r$.

The integration rule then takes the form:

$$I = \int_0^1 \int_0^{1-r} f(r,s)\,\mathrm{d}s\,\mathrm{d}r \approx \sum_{i=1}^{M} f(r_i, s_i) w_i. \tag{2.46}$$

As in the one-dimensional case, the integral gets approximated by a weighted sum of function evaluations f at different points (r_i, s_i). In Table 2.4 we give the coordinates and weights of those points that can be used to integrate polynomials of order $\leq P$ exactly. For a polynomial of order 3 (e.g. the velocity flux function or the energy flux function for constant density) we require 4 evaluations.

2.9 Appendix: Details of test problem setups

2.9.1 Yee vortex

For the setup of the Yee vortex, we follow Yee et al. (2000) and Pakmor et al. (2016b). The mesh covers the interval $[-5, 5] \times [-5, 5]$, and we set the density ρ, velocity $\boldsymbol{v}$ and specific energy u of each cell to the value of the continuous fields at the centres of mass of the cells. The continuous initial conditions are given at point $\boldsymbol{r} = (x, y)$ by:

$$T(\boldsymbol{r}) = T_{\mathrm{inf}} - \frac{(\gamma - 1)}{8\gamma\pi^2} e^{1-r^2}, \tag{2.47a}$$

$$\rho(\boldsymbol{r}) = T^{\frac{1}{1-\gamma}}, \tag{2.47b}$$

$$v_x(\boldsymbol{r}) = -y \frac{\beta}{2\pi} e^{\frac{1-r^2}{2}}, \tag{2.47c}$$

$$v_y(\boldsymbol{r}) = x \frac{\beta}{2\pi} e^{\frac{1-r^2}{2}}, \tag{2.47d}$$

$$u(\boldsymbol{r}) = \frac{T}{\gamma - 1}. \tag{2.47e}$$

We use the parameters $T_{\mathrm{inf}} = 1$, $\gamma = 1.4$ and $\beta = 5$.

For the setup of the Cartesian grid we use cells with side length $10/N$, where N is the linear resolution. To set-up a polar grid we use the method of Pakmor et al. (2016b): We place the mesh-generating points in rings with size $d_{\mathrm{ring}} = 10/N$. We equidistantly add $2\pi r_{\mathrm{ring}}/d_{\mathrm{ring}}$ new mesh-generating points in every ring at radius $r_{\mathrm{ring}} = i\, d_{\mathrm{ring}}$. We only add points which lie in the simulation domain.

2.9.2 Keplerian disk

The setup is the same as in Pakmor et al. (2016b). We use a periodic box spanning the domain $[-2.5, 2.5] \times [-2.5, 2.5]$. The disk itself is cold, which means the pressure forces are negligible compared to the gravitational force. As for the Yee-vortex, we again create a polar grid as initial condition and set the density ρ, the velocity $\boldsymbol{v}$ and the specific internal energy u to the analytic values at the centres of mass of each cell. As background medium for $r = |\boldsymbol{r}| = |\,(x, y)\,| < 0.5$ and $r > 2$ we use

$$\rho = 10^{-5}, \tag{2.48a}$$

$$\boldsymbol{v} = 0, \tag{2.48b}$$

$$u = \frac{5\gamma}{2\rho} \times 10^{-5}. \tag{2.48c}$$

For the disk itself $(0.5 < r < 2)$ we use

$$\rho = 1, \tag{2.49a}$$

$$\boldsymbol{v}(x, y) = \frac{1}{r^{3/2}} \begin{pmatrix} -y \\ x \end{pmatrix}, \tag{2.49b}$$

$$u = \frac{5\gamma}{2\rho} \times 10^{-5}. \tag{2.49c}$$

Here $\gamma = 5/3$ is the adiabatic index. As gravitational acceleration we use

$$\boldsymbol{g} = -\frac{\boldsymbol{r}}{r\left(r^2 + \epsilon^2\right)}, \tag{2.50}$$

with $\epsilon = 0.25$ for $r < 0.25$, and $\epsilon = 0$ everywhere else.

Chapter 3

Simulating the magnetorotational instability on a moving mesh with the shearing box approximation

This work has been published in the Monthly Notices of the Royal Astronomical Society, Volume 517, Issue 2, Pages 2639-2658.

The magnetorotational instability (MRI) is an important process in sufficiently ionized accretion disks, as it can create turbulence that acts as an effective viscosity, mediating angular momentum transport. Due to its local nature, it is often analyzed in the shearing box approximation with Eulerian methods, which otherwise would suffer from large advection errors in global disk simulations. In this work, we report on an extensive study that applies the quasi-Lagrangian, moving-mesh code AREPO, combined with the Dedner cleaning scheme to control deviations from $\nabla \cdot \boldsymbol{B} = 0$, to the problem of magnetized flows in shearing boxes. We find that we can resolve the analytical linear growth rate of the MRI with mean background magnetic field well. In the zero net flux case, there is a threshold value for the strength of the divergence cleaning above which the turbulence eventually dies out, and in contrast to previous Eulerian simulations, the strength of the MRI does not decrease with increasing resolution. In boxes with larger vertical aspect ratio we find a mean-field dynamo, as well as an active shear current effect that can sustain MRI turbulence for at least 200 orbits. In stratified simulations, we obtain an active $\alpha\omega$ dynamo and the characteristic butterfly diagram. Our results compare well with previous results obtained with static grid codes such as ATHENA. We thus conclude that AREPO represents an attractive approach for global disk simulations due to its quasi-Lagrangian nature, and for shearing box simulations with large density variations due to its continuously adaptive resolution.

3.1 Introduction

The molecular viscosity of diffuse gas is by several orders of magnitude too small to explain the required amount of angular momentum transported in accretion disks. A possible solution is an effective viscosity that can be created by turbulence in the disk, and which in turn can be generated by different fluid instabilities (Shakura & Sunyaev, 1973; Lynden-Bell & Pringle, 1974). Besides the gravitational instability due to self-gravity (Gammie, 2001), there exist a plethora of other possible hydrodynamic and thermodynamic instabilities such as the Rossby wave instability (Lovelace et al., 1999) or the convective overstability (Klahr & Hubbard, 2014) that could be involved.

One of the most promising candidates for the main culprit is the magnetorotational instability (MRI) (Velikhov, 1959; Chandrasekhar, 1960; Fricke, 1969; Balbus & Hawley, 1991) in ionized regions, which is a linear instability that is active in Keplerian-like shear flows and only requires a very small seed magnetic field to get started in the limit of ideal magnetohydrodynamics (MHD). The MRI's linear properties are nowadays well understood (Balbus & Hawley, 1991, 1992; Curry et al., 1994; Goodman & Xu, 1994; Kersalé et al., 2004) but its nonlinear behaviour is considerably more complicated and requires an analysis with computer simulations. Previous studies can be broadly categorized into global simulations that simulate the whole disk and into local simulations that compute only a small patch of the disk using the shearing sheet approximation (Hill, 1878; Goldreich & Lynden-Bell, 1965). While the former allow capturing of global effects such as accretion, and the formation of winds and jets, they are also very expensive and only allow the analysis of a small part of the parameter space (Penna et al., 2010; Hawley et al., 2011, 2013; Parkin & Bicknell, 2013b; Duffell, 2016; Deng et al., 2020). Local simulations, in contrast, allow much higher resolution and are also cheaper, which means a much larger parameter space can be analyzed.

Shearing box simulations can again be split into two groups: Stratified simulations that take the vertical gravitational force of the central object into account, and unstratified simulations neglecting this force component so that the focus lies on approximating the conditions in the mid-plane of the disk. An important property to characterize shearing box simulations is the mean magnetic flux, $\langle \boldsymbol{B} \rangle = \int_V \boldsymbol{B}\, \mathrm{d}V$, whose radial and vertical component is conserved both for unstratified and stratified simulations except if there are outflows in the vertical direction. The azimuthal component on the other hand is only conserved if there is no mean radial field. These properties motivate the definition of simulations with net-flux (NF, $\langle \boldsymbol{B} \rangle \neq 0$, Hawley et al., 1995; Sano et al., 2004; Guan et al., 2009; Simon et al., 2009; Gong et al., 2020), and zero-net flux simulations (ZNF, $\langle \boldsymbol{B} \rangle = 0$, Hawley et al., 1996; Fromang & Papaloizou, 2007; Simon & Hawley, 2009; Bodo et al., 2011). We note that this characterisation is however a simplification since in global simulations the mean net field in patches of the disk can change.

In the vertical NF case of unstratified simulations, one can first observe an exponential growth of so-called channel modes, which are a solution to the nonlinear ideal MHD equations. They grow until parasitic (secondary) instabilities destabilize them (Goodman & Xu, 1994) and turbulence sets in. This turbulence alone decays but the background net field can revive the MRI which leads to self-sustaining cycles. For the ZNF case, this background field is missing, and therefore perturbations in the velocity and magnetic field have to mutually sustain each other. Since the unstratified case is statistically symmetric it is harder to generate local mean fields, but Shi et al. (2016) nevertheless found an active dynamo in this situation, especially in tall boxes (large vertical aspect ratio). Three possible solutions are the stochastic α-effect (Vishniac & Brandenburg, 1997; Silant'ev, 2000; Heinemann et al., 2011), the magnetic shear current effect (Rogachevskii & Kleeorin, 2003, 2004; Squire & Bhattacharjee, 2015c) or the interplay of linear transient (nonmodal) growth of the MRI and the nonlinear transverse cascade that redistributes energy between different Fourier modes (Squire & Bhattacharjee, 2014; Gogichaishvili et al., 2017, 2018; Mamatsashvili et al., 2020; Held & Mamatsashvili, 2022).

In the stratified case, the system becomes anisotropic and consists typically of a turbulent, MRI unstable mid-plane surrounded by a magnetically dominated corona (Shi et al., 2010; Guan & Gammie, 2011). A mean-field dynamo is active in the mid-plane, where the sign of the mean field changes periodically, which leads to the typical 'butterfly' diagram (Brandenburg et al., 1995; Stone et al., 1996; Hirose et al., 2006; Gressel, 2010; Davis et al., 2010; Simon et al., 2011). Different effects such as the $\alpha\omega$ dynamo (Vishniac & Cho, 2001; Subramanian & Brandenburg, 2004) and turbulent pumping (Gressel, 2010) have been invoked to explain this behaviour but also the effects already discussed for the unstratified case can have an influence on this evolution.

Fromang & Papaloizou (2007) found that for the unstratified ZNF case in small boxes the strength of the MRI decreases if the resolution is increased, and that for infinite resolution the MRI could even completely die out. However, convergence can be regained by explicitly accounting for viscosity and magnetic diffusivity (Fromang et al., 2007), and there seems to exist a critical magnetic Prandtl number below which the ZNF MRI dies out. Interestingly, Shi et al. (2016) found convergence in larger boxes which they attributed to a large-scale mean field created by the shear current effect.

In most studies of the MRI in shearing boxes, Eulerian methods were used that can benefit from the constrained transport method (Evans & Hawley, 1988) to preserve the condition $\nabla \cdot \boldsymbol{B} = 0$ up to machine precision. But they suffer from advection errors especially in global simulations with large bulk velocities, and they also cannot easily increase their resolution in the shearing box using adaptive mesh refinement (AMR). Lagrangian methods on the other hand require some type of cleaning method to keep $\nabla \cdot \boldsymbol{B}$ errors small (but see Mocz et al., 2014, for a recent implementation of constrained transport for the moving mesh method), but they can achieve Galilei invariance and easily allow a constant mass resolution. Deng et al. (2019) applied the particle-based MFM (Hopkins, 2015) and SPH methods to the MRI and were able to show that MFM is able to accurately describe the linear growth of the MRI in unstratified boxes, and also sustains MRI turbulence for the unstratified NF case. In unstratified ZNF simulations, the turbulence died out however for SPH as well as MFM, and while MFM was able to reproduce the butterfly diagram for a stratified simulation with a time-varying net azimuthal field in the mid plane for around 50 to 70 orbits, the turbulence eventually still died out. Furthermore, in stratified simulations with SPH unphysically strong azimuthal fields grew. These findings underline the particular sensitivity of this problem to numerical errors of various kinds, making it challenging to obtain accurate and robust results.

Wissing et al. (2022) performed a similar study with a modified version of standard SPH, the so-called geometrically-averaged density SPH (GDSPH) that can improve the accuracy of SPH in systems with large density gradients, as for example in the stratified simulations (Wadsley et al., 2017; Wissing & Shen, 2020). Interestingly, they were able to sustain turbulence in the unstratified ZNF case, but did not find a large-scale mean-field dynamo in tall boxes. The authors attributed this to a missing shear current effect, unlike found in Shi et al. (2016). In stratified simulations, they however obtained an active $\alpha\omega$ dynamo and also reproduced the butterfly diagram for 200 orbits. These latter results compare quite well with previous Eulerian methods, and similar to them, they also show a dependence on the numerical Prandtl number. However, since GDSPH could not reproduce the shear current effect, and because the geometric density averaging has been demonstrated to be problematic in cooling flows (Springel & Hernquist, 2002), it is unclear how universally applicable this variant of SPH is.

The moving mesh method (Springel, 2010a; Weinberger et al., 2020) is a Lagrangian approach that tries to combine the advantages of a Galilei invariant Lagrangian method with the high accuracy of the finite volume method typically employed in Eulerian codes. This makes it especially interesting for global disk simulations but also for local simulations with large density gradients that can benefit from the code's high flexibility to continuously adapt cell sizes, and to increase and decrease the local resolution by splitting and merging individual computational cells. Pakmor & Springel (2013) has shown in a global simulation that the code can accurately capture the linear growth of the MRI, but only recently in Zier & Springel (2022a) we implemented the shearing box approximation in this code, and, importantly, we considerably reduced its residual numerical noise by means of higher-order flux integrations. The latter are particularly important in situations where cell shapes are constantly distorted at a high rate, such as in strongly shearing flow.

The goal of this chapter is to analyse the performance of this improved method for simulating the MRI in different setups, and to compare the results with those obtained with Eulerian methods as well as Lagrangian methods described in Deng et al. (2019) and Wissing et al. (2022). We also put a special emphasis on the tensorial turbulent transport coefficients that allow us to understand the evolution of mean fields and therefore active dynamo processes in more detail. The detailed verification of the code accuracy we aim for here is clearly also a prerequisite for trusting predictions obtained with the code in planned future global disk simulations.

This chapter is structured as follows: In Section 3.2 we introduce the moving mesh method and especially the shearing box approximation as implemented in the AREPO code. We also analyze the linear growth of the MRI and introduce different quantities we will use subsequently to characterize the nonlinear, saturated state of the MRI as a function of the divergence cleaning strength as well as numerical resolution. In Section 3.3, we discuss unstratified shearing box simulations. We analyze both the cases with a vertical NF as well as the case with ZNF in a standard and tall box, and show that in the latter situation a large-scale mean-field dynamo as in Shi et al. (2016) becomes active that is created by the shear current effect. In Section 3.4, we run four different stratified simulations and demonstrate a sustained and active MRI with turbulence in the mid-plane for 200 orbits, while above the mid-plane we find a magnetically dominated corona. Finally, in Section 3.5 we discuss and summarize our results.

3.2 Numerical methods

3.2.1 The shearing box approximation

The shearing box approximation is widely used in the study of the magnetorotational instability. It allows a higher spatial resolution in comparison to global disk simulations, and additionally delivers clearly defined boundary conditions which simplify the comparison of different studies. To implement the shearing box, we simulate a small patch of a disk centred at radius r_0. The rotational frequency of the disk at this point is given by Ω_0 and we use a Cartesian coordinate system with $\hat{e}_x$ pointing in the radial direction, $\hat{e}_y$ in the azimuthal direction and $\hat{e}_z$ being perpendicular to the other two unit vectors. By transforming into the rotating system and linearizing the gravitational and centrifugal forces, the governing ideal MHD equations read as follows:

$$\frac{\partial \boldsymbol{U}}{\partial t} + \nabla \cdot \boldsymbol{F}(\boldsymbol{U}) = \boldsymbol{S}_{\text{grav}} + \boldsymbol{S}_{\text{cor}}. \tag{3.1}$$

Here, we introduced the state vector $\boldsymbol{U}$, the flux vector $\boldsymbol{F}$, the source terms $\boldsymbol{S}_{\text{grav}}$ due to the gravitational and centrifugal forces, and a source term $\boldsymbol{S}_{\text{cor}}$ describing the Coriolis force. They are given by:

$$\boldsymbol{U} = \begin{pmatrix} \rho \\ \rho \boldsymbol{v} \\ \rho e \\ \boldsymbol{B} \end{pmatrix}, \qquad F(\boldsymbol{U}) = \begin{pmatrix} \rho \boldsymbol{v} \\ \rho \boldsymbol{v}\boldsymbol{v}^T + P - \boldsymbol{B}\boldsymbol{B}^T \\ \rho e \boldsymbol{v} + P\boldsymbol{v} - \boldsymbol{B}(\boldsymbol{v}\cdot\boldsymbol{B}) \\ \boldsymbol{B}\boldsymbol{v}^T - \boldsymbol{v}\boldsymbol{B}^T \end{pmatrix}, \tag{3.2}$$

$$\boldsymbol{S}_{\text{grav}} = \begin{pmatrix} 0 \\ \rho\Omega_0^2\left(2qx\hat{e}_x - z\hat{e}_z\right) \\ \rho\Omega_0^2\boldsymbol{v}\cdot\left(2qx\hat{e}_x - z\hat{e}_z\right) \\ 0 \end{pmatrix}, \qquad \boldsymbol{S}_{\text{cor}} = \begin{pmatrix} 0 \\ -2\rho\Omega_0\hat{e}_z \times \boldsymbol{v} \\ 0 \\ 0 \end{pmatrix}, \tag{3.3}$$

where ρ, $\boldsymbol{v}$, e, $\boldsymbol{B}$, P are the density, velocity, total energy per unit mass, magnetic field strength, and pressure, respectively. The specific energy $e = u + \frac{1}{2}\boldsymbol{v}^2 + \frac{1}{2\rho}\boldsymbol{B}^2$ consists of the thermal energy per mass u, the kinetic energy density $\frac{1}{2}\boldsymbol{v}^2$, and the magnetic field energy density $\frac{1}{2\rho}\boldsymbol{B}^2$. The pressure $P = p_{\text{gas}} + \frac{1}{2}\boldsymbol{B}^2$ includes a thermal and a magnetic component. The system of equations is closed by the equation of state (EOS), which expresses p_{gas} as a function of the other thermodynamical quantities.

In this chapter we use an isothermal EOS,

$$p_{\text{gas}} = \rho c_s^2, \tag{3.4}$$

with constant isothermal sound speed $c_s = 1$. $\boldsymbol{S}_{\rm grav}$ depends on the shearing parameter

$$q = -\frac{d\ln\Omega}{d\ln r}, \tag{3.5}$$

which simplifies to $q = 3/2$ for the Keplerian case that we exclusively discuss in this chapter. In general, we will use $\Omega_0 = 1$ and measure lengths in units of the scale height $H = c_s/\Omega_0$. $\boldsymbol{S}_{\rm grav}$ contains an optional term that represents a gravitational force in the z-direction. We will perform in this chapter simulations with (stratified case) and without this term (unstratified case).

The above system allows for a ground-state solution with velocity field

$$\boldsymbol{v}_0 = (0, -q\Omega_0 x, 0), \tag{3.6}$$

at constant pressure and constant density field in an unstratified box, or with density field

$$\rho(z) = \rho_0 \exp\left(-\frac{z^2}{2H^2}\right) \tag{3.7}$$

in the case of a stratified box. To close the system of equations we also have to define boundary conditions (BCs). In the y-direction, we use standard periodic BCs, and in the z-direction periodic BCs. In the x-direction we use the so-called shearing box BCs that are similar to standard periodic BCs but take into account the background shear flow (3.6):

$$f(x,y,z,t) = f(x \pm L_x, y \mp wt, z, t), \quad f \in \{\rho, \rho v_x, \rho v_z, \boldsymbol{B}\}, \tag{3.8a}$$

$$\rho v_y(x,y,z,t) = \rho v_y(x \pm L_x, y \mp wt, z, t) \mp \rho w, \tag{3.8b}$$

$$e(x,y,z,t) = e(x \pm L_x, y \mp wt, z, t) \mp \rho v_y v_w + \frac{\rho w^2}{2}, \tag{3.8c}$$

where L_x is the box size in the x-direction and $w = q\Omega_0 L_x$. The boundary conditions therefore do not conserve the azimuthal momentum, nor the total energy or the azimuthal component of the volume-weighted averaged magnetic field (Gressel & Ziegler, 2007):

$$\frac{\partial \langle B_y \rangle}{\partial t} = -\frac{w}{V}\int_{\partial x} B_x \,\mathrm{d}y\,\mathrm{d}z. \tag{3.9}$$

Here ∂x denotes the boundary in the x-direction, and V is the total volume of the box. Only in the case that the magnetic field has no mean radial component and $\nabla \cdot \boldsymbol{B} = 0$ holds, the azimuthal field is conserved.

To solve equation (3.1) we use the moving mesh code AREPO (Springel, 2010a; Pakmor et al., 2016b; Weinberger et al., 2020) that employs a moving, unstructured Voronoi mesh in combination with the finite volume method. We refer to Zier & Springel (2022a) for technical details of the implementation of the shearing box in this code. For all simulations, we use the higher-order integration method for the flux as well as a second-order accurate Runge-Kutta time integration scheme recently introduced in the code (Zier & Springel, 2022a).

3.2.2 The divergence constraint of the magnetic field

A close inspection of equation (3.1) shows that if the initial conditions fulfill $\nabla \cdot \boldsymbol{B} = 0$ this condition will remain true for all times. Numerical schemes that only find approximate solutions to the underlying analytical equations do not automatically fulfill this condition, and can sometimes be prone to developing numerical instability or large errors once a sizable divergence of the magnetic field appears. To reduce the influence of this error one can try to either remove it somehow, or to diffuse it away from its original site. AREPO supports both the Powell scheme (Powell et al., 1999; Pakmor & Springel, 2013) that diffuses the error, and the Dedner cleaning (Dedner et al., 2002; Pakmor et al., 2011) approach that advects the error away and damps it. In contrast, the constrained transport method (Evans & Hawley, 1988; Mocz et al., 2014) avoids deviations from $\nabla \cdot \boldsymbol{B} = 0$ to machine precision. Although this latter approach ensures negligible errors in the divergence constraint, it also tends to be somewhat more diffusive, and the construction of a constrained transport updating scheme algorithm is very difficult for meshes with changing topology.

The Powell scheme adds additional source terms to the underlying MHD equations that try to stabilize the system for the case of $\nabla \cdot \boldsymbol{B} \neq 0$:

$$S_{\text{powell}} = \begin{pmatrix} 0 \\ -\left(\nabla \cdot \boldsymbol{B}\right) \boldsymbol{B} \\ -\left(\nabla \cdot \boldsymbol{B}\right) \left(\boldsymbol{v} \cdot \boldsymbol{B}\right) \\ -\left(\nabla \cdot \boldsymbol{B}\right) \boldsymbol{v} \end{pmatrix} . \tag{3.10}$$

The additional term in the induction equation depends on the absolute velocity $\boldsymbol{v}$, which unfortunately breaks the Galilei invariance of the moving-mesh method. This becomes problematic at the radial boundary of a shearing box set-up, since here the velocity of cells jumps discontinuously if they move through the boundary. Additionally, the source terms can modify and even generate a mean magnetic field in the vertical and radial directions due to this issue. This is especially problematic since according to equation (3.9) a mean radial field will continuously amplify the azimuthal component of the magnetic field.

The Dedner scheme adds an additional scalar field ψ to the equations to be solved. The modified induction equation and the evolution of ψ are given by:

$$\frac{\partial}{\partial t} \begin{pmatrix} \boldsymbol{B} \\ \psi \end{pmatrix} + \nabla \begin{pmatrix} \boldsymbol{B}\boldsymbol{v}^T - \boldsymbol{v}\boldsymbol{B}^T + \psi \boldsymbol{I} \\ c_h^2 \boldsymbol{B} \end{pmatrix} = \begin{pmatrix} 0 \\ -c_h^2/c_p^2 \psi \end{pmatrix} . \tag{3.11}$$

Here c_h is the velocity with which deviations from $\nabla \cdot \boldsymbol{B} = 0$ are diffused away, and c_p defines the time scale over which ψ decays. A larger value of c_h typically leads to smaller errors in $\nabla \cdot \boldsymbol{B}$ but also to higher numerical resistivity. Both effects can in principle influence the MRI. By default we set c_h to the largest signal speed in our simulation, but we allow it to be multiplied with a prescribed constant factor c_{h0} to analyze the effect of the cleaning speed on our results.

The signal speed is set equal to the velocity

$$c_f = \sqrt{c_s^2 + \frac{B^2}{\rho}} \tag{3.12}$$

of the fastest magneto-acoustic wave in the system. We use $c_p = \sqrt{2c_h r}$, where r is the effective radius of a cell. Since the Dedner scheme does not add any new source terms to the induction equation, the radial and vertical mean fields are conserved to machine precision. Although in the case of a magnetic field without a radial component the average azimuthal field should be conserved, this is not the case for $\nabla \cdot \boldsymbol{B} \neq 0$. A larger c_h can in this case also help to reduce the magnitude of this spurious field component.

3.2.3 Linear growth of channel flows

The linear eigenmodes of the magnetorotational instability with a net vertical flux are called channel flows. They are solutions of the nonlinear ideal MHD equations, and their amplitude grows exponentially until parasitic instabilities destabilize them and a turbulent flow forms (Goodman & Xu, 1994). We set up a box of size $L_x = L_y = L_z = 1$, initial background field $B = (0, 0, B_0)$, an isothermal equation of state with sound speed $c_s = 1$, and with a background shear flow (3.6). We choose $\beta = 2p_{\mathrm{gas}}/B_0^2 = 84$ since in this case the wavelength $\lambda_{\mathrm{fast}} = 1$ of the fastest growing mode is equal to our box size, with a growth rate given by $0.75\,\Omega^{-1}$ (Latter et al., 2009). As perturbation seed for the initial conditions we use:

$$\delta B = 0.001 \times B_0 \cos(2\pi z)\, \frac{\hat{e}_x - \hat{e}_y}{\sqrt{2}}, \tag{3.13a}$$

$$\delta v = 0.001 \times \frac{3}{8\pi} \sin(2\pi z)\, \frac{\hat{e}_x + \hat{e}_y}{\sqrt{2}}. \tag{3.13b}$$

As in Deng et al. (2019), we run our simulation for $t = 8\,\Omega_0^{-1}$ and calculate the average growth rate s_{sim} in the simulation by using the amplitude of δB at $t = 0$ and at $t = 8\,\Omega_0^{-1}$. We start with a Cartesian grid and rerun the simulation several times with different numbers of cells. As an error measure we define $e = (0.75 - s_{\mathrm{sim}}\Omega_0)/0.75$.

In Fig. 3.1 we show the error in the growth rate s as a function of the employed resolution. Reassuringly, the results converge with close to third order to the analytical value. Also, the absolute values compare well with the results from the ATHENA code shown in Deng et al. (2019). While the two particle-based methods SPH and MFM show larger absolute errors if we define the local resolution as the mean particle distance, MFM still manages to show the same third-order convergence as the grid-based methods.

To formally reduce the absolute error, Deng et al. (2019) defined the local spatial resolution in terms of the face-area weighted inter-neighbour separation, which leads to similar results as ATHENA and AREPO. We note, however, that this still implies a larger computational cost for the same spatial resolution, which becomes even worse than in standard MFM since the relatively large Wendland C4 kernel with 200 neighbours had to be used.

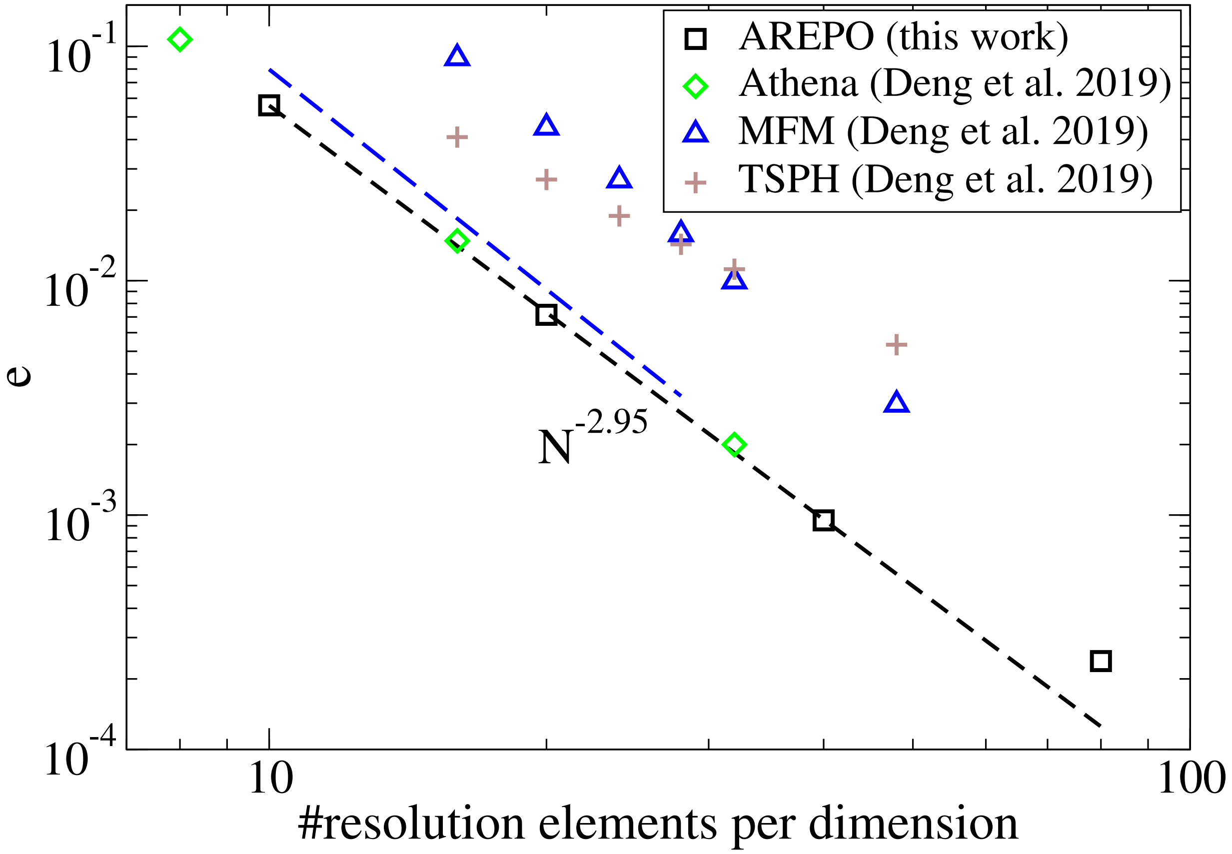

Figure 3.1: The error e of the growth rate of the magnetic field of a channel flow as a function of the resolution. The error converges with close to third order and the results compare well with results presented in Deng et al. (2019) with the ATHENA code. We also show results with the MFM and TSPH implementations in GIZMO if we assume that each particle represents one resolution element. The blue-dashed line represents the results for MFM if we define the local resolution not as the mean particle distance but as the face-area weighted inter-neighbor separation (see Deng et al., 2019, for details).

Type	Initial field	Box size	Base resolution	Res. multiplier	c_{h0}	Section
Unstratified	$B_0\hat{e}_z$, $\beta = 400$	$1 \times 6.28 \times 1$	$16 \times 100 \times 16$	1, 2, 3, 4	0.1, 0.5, 1, 2, 5	3.3.1
Unstratified	$B_0\hat{e}_z$, $\beta = 330$	$1 \times 4 \times 1$	$16 \times 64 \times 16$	1,2,3,4	0.1, 0.5, 1, 2, 5	3.6
Unstratified	$B_0 \sin{(2\pi x)}\, \hat{e}_z$, $\beta = 400$	$1 \times \pi \times 1$	$16 \times 50 \times 16$	1, 2, 3, 4	0.1, 0.5, 1, 2, 5	3.3.2
Unstratified	$B_0 \sin{(2\pi x)}\, \hat{e}_z$, $\beta = 400$	$1 \times 4 \times 4$	$16 \times 64 \times 64$	1, 2, 3	0.1, 0.5, 1, 2, 5	3.3.3
Stratified	$B_0\hat{e}_y$, $\beta = 25$	$\sqrt{2} \times 4\sqrt{2} \times 24$	$\approx 1.5 \times 10^6$ cells	1	0.5, 1	3.4
Stratified	$B_0\hat{e}_y$, $\beta = 25$	$\sqrt{2} \times 4\sqrt{2} \times 24$	$\approx 3 \times 10^6$ cells	1	0.5, 1	3.4

Table 3.1: Overview of all simulations discussed in this chapter. The initial field strength is determined by the plasma beta $\beta = 2p_{\text{gas}}/B_0^2$. For some simulations we analyze the influence of resolution by multiplying the number of cells of the base resolution with a constant factor in all dimensions. We also analyze the effect of the cleaning speed c_{h0} of the Dedner scheme on our results. In the stratified simulations we allow cells to merge and be split, and we enforce an approximately constant mass per cell.

3.2.4 Analysis and overview of simulations

To analyze our simulations we define the volume-weighted average of a quantity X as

$$\langle X\rangle = \frac{\int X\mathrm{d}V}{\int \mathrm{d}V}, \tag{3.14}$$

as well as the temporal average of X,

$$\langle X\rangle_t = \frac{\int X\mathrm{d}t}{\int \mathrm{d}t}. \tag{3.15}$$

For the first quantity, we integrate over the whole simulation box if not stated otherwise, while for the second one we typically only integrate over the time interval during which the MRI is saturated in the nonlinear regime. For clarity, we will always mention the start of this averaging time interval.

To measure the angular momentum transport and the saturation level of the MRI it is useful to calculate the Maxwell stress

$$\alpha_M = -\frac{B_x B_y}{P}, \tag{3.16}$$

as well as the Reynolds stress

$$\alpha_R = \frac{\rho v_x \delta v_y}{P}, \tag{3.17}$$

where P is the pressure and $\delta v_y = v_y - v_{y,0}$ is equal to the velocity relative to the background shear flow. A related quantity is the normalized magnetic stress:

$$\alpha_{\mathrm{mag}} = -\frac{\langle B_x B_y\rangle}{\langle B^2\rangle}. \tag{3.18}$$

As in Shi et al. (2016) and Wissing et al. (2022), we decompose the magnetic field into a mean field $\overline{\boldsymbol{B}}$ and a turbulent field $\boldsymbol{b}$, where the first component is defined as the horizontal average

$$\overline{X} = \frac{\int X\,\mathrm{d}x\mathrm{d}y}{\int \mathrm{d}x\mathrm{d}y}. \tag{3.19}$$

While the volume integrals can be directly calculated using a Voronoi mesh, the horizontal average is more complicated. We address this by first binning our simulation data to a uniform Cartesian grid with typically twice the number of cells per dimension as in the initial conditions, followed by carrying out the integral using this mesh.

As we have discussed in Section 3.2.2, our implementation of the MHD equations does not preserve the condition $\nabla \cdot \boldsymbol{B} = 0$. To measure the potential impact of numerically induced magnetic monopole errors we define the relative divergence error

$$\epsilon_{\nabla\cdot B,i} = \frac{(\nabla \cdot \boldsymbol{B}_i)\, r_i}{|\boldsymbol{B}_i|}, \tag{3.20}$$

where $r_i = [3V_i/(4\pi)]^{1/3}$ is the effective radius of the Voronoi cell i. In the case of $\langle B_x \rangle = 0$ the mean azimuthal component $\langle B_y \rangle$ of the magnetic field can only change for $\nabla \cdot \boldsymbol{B} \neq 0$. The evolution of $\langle B_y \rangle$ can therefore be used to measure the impact of divergence errors on our simulation results.

Linear stability analysis leads to the definition of the quality factor (Noble et al., 2010)

$$Q_i = \frac{\lambda_{\mathrm{MRI}}}{h} = \frac{2\pi v_{A,i}}{\Omega h}, \tag{3.21}$$

where λ_{MRI} is the characteristic wavelength, $v_{A,i}$ is the i-component of the Alfven velocity, and h is the local spatial resolution. Similar to static grid codes, where h is typically set to the grid cell size (Hawley et al., 2011; Parkin & Bicknell, 2013a), we define it here as the effective diameter $d = 2\left(\frac{V}{4/3\pi}\right)^{1/3}$ of each Voronoi cell. Although $Q > 6$ is sufficient to properly resolve the linear growth of the MRI (see also the previous section), $Q_z > 10$ and $Q_y > 20$ are required to achieve convergence in the stresses for the case of a stratified net flux simulation (Hawley et al., 2011).

Although the definition of Q_i based on linear theory and the net flux case makes its application to the nonlinear regime questionable (especially for the zero net flux case), it is still a useful indicator to estimate whether the MRI can still be resolved. This applies especially in the stratified case, where the density and therefore spatial resolution strongly varies within the simulation box. In Table 3.1 we give an overview of all the primary simulations performed for this chapter, together with their principal numerical parameters.

Tensorial transport coefficients

To better understand the influence of the small-scale fluctuations on the large-scale field it is useful to use the concept of mean-field theory (Moffatt, 1978; Parker, 2019; Krause & Rädler, 2016; Ruzmaikin et al., 1988; Brandenburg & Subramanian, 2005). In the following, we will mostly follow the discussion in Wissing et al. (2022) to which we refer for a more in-depth coverage. By averaging the induction equation, the evolution of the mean magnetic field is given by:

$$\frac{\partial \overline{\boldsymbol{B}}}{\partial t} = \nabla \times [(\boldsymbol{v} - \boldsymbol{v}_0) \times \overline{\boldsymbol{B}}] + \nabla \times \mathcal{E}. \tag{3.22}$$

Here $\mathcal{E}$ is the electromotive force (EMF) generated by the fluctuations in the velocity and magnetic field:

$$\mathcal{E} = \overline{(\boldsymbol{v} - \boldsymbol{v}_0) \times \boldsymbol{b}}. \tag{3.23}$$

By splitting the velocity and magnetic field fluctuations into components independent of the mean-field and components linearly dependent on the applied mean-field, we can Taylor expand this expression to leading order under the assumptions of scale separation and the absence of correlations between the independent components of the mean magnetic field and the velocity perturbations:

$$\mathcal{E}_i = \alpha_{ij}\overline{B_j} - \eta_{ij}\overline{J_j} + ... \tag{3.24}$$

Here we introduced the mean-field current density

$$\overline{\boldsymbol{J}} = \overline{\nabla \times \boldsymbol{B}} \tag{3.25}$$

and the tensorial transport coefficients α and η. Since $\overline{B_z} = \overline{J_z} = 0$, this simplifies to:

$$\mathcal{E}_x = \alpha_{xx}\overline{B_x} + \alpha_{xy}\overline{B_y} - \eta_{xx}\overline{J_x} - \eta_{xy}\overline{J_y}, \tag{3.26}$$

$$\mathcal{E}_y = \alpha_{yx}\overline{B_x} + \alpha_{yy}\overline{B_y} - \eta_{yx}\overline{J_x} - \eta_{yy}\overline{J_y}. \tag{3.27}$$

By multiplying the two equations with $\left\{\overline{B_x},\, \overline{B_y},\, \overline{J_x},\, \overline{J_y}\right\}$ we obtain 8 equations for the 8 components of α and η which are in general functions of height z and time t.

A direct solution of the system of linear equations leads to quite noisy measurement results, which can be improved by using the approximations $\alpha_{xx} = \alpha_{yy}$, $\eta_{xx} = \eta_{yy}$ (which can be justified as in Hubbard et al., 2009; Gressel, 2010) and $\alpha_{yx} = 0 = \eta_{xy}$, which is justified due to $\overline{B_x} \ll \overline{B_y}$ (Squire & Bhattacharjee, 2015b). For the unstratified simulations, we then determine averaged transport coefficients in the z-direction by integrating the linear system of equations over the whole box in the z-direction, and assuming z-independent coefficients. This leads to a single linear system of equations for each time step, and thus gives access to the temporal evolution of the transport coefficients. With this in hand, we perform a standard temporal average of the transport coefficients, which is equivalent to averaging over many different realizations of the turbulent state (Squire & Bhattacharjee, 2015b).

For stratified simulations we allow nonzero α_{yx}, η_{xy} and $\alpha_{xx} \neq \alpha_{yy}$, as in Wissing et al. (2022) in order to simplify a direct comparison with other studies. In this case, we assume the transport coefficients to be independent of time, and try to calculate their structure as a function of z. For each z-value, we solve the overdetermined system of $8 \times N$ equations for the 7 independent transport coefficients by minimizing the residual, where N is the number of snapshots we use for our calculation. In general, we typically have five snapshots per orbit.

By inserting equation (3.24) into (3.22), the evolution of the averaged quantities is given by:

$$\frac{\partial \overline{B_x}}{\partial t} = -\partial_z(\alpha_{yx}\overline{B_x}) - \partial_z(\alpha_{yy}\overline{B_y}) + \partial_z(\eta_{yx}\overline{J_x}) + \partial_z(\eta_{yy}\overline{J_y}), \tag{3.28}$$

$$\frac{\partial \overline{B_y}}{\partial t} = -q\Omega\overline{B_x} + \partial_z(\alpha_{xx}\overline{B_x}) + \partial_z(\alpha_{xy}\overline{B_y}) - \partial_z(\eta_{xx}\overline{J_x}) - \partial_z(\eta_{xy}\overline{J_y}). \tag{3.29}$$

The components α_{xx} and α_{yy} are the main drivers of the α effect that can lead to the well-known $\alpha\omega$ dynamo in combination with differential rotation. It requires a statistical symmetry breaking, e.g. a stratification or a net helicity (Pouquet et al., 1976; Moffatt, 1978; Brandenburg & Subramanian, 2005). We, therefore, expect them to be zero in our unstratified simulations and antisymmetric relative to the mid-plane in the stratified simulations. The antisymmetric components α_{xy} and α_{yx} define the diamagnetic pumping term

$$\gamma_z = \frac{1}{2}\left(\alpha_{yx} - \alpha_{xy}\right) \tag{3.30}$$

that describes the transport of the mean fields by the turbulent components. It is expected to be non-zero for the stratified case. The diagonal terms η_{xx}, and η_{yy} describe the diffusion of the mean field, while the off-diagonal coefficients η_{xy} and η_{yx} are responsible for the dynamo produced by the $\Omega \times J$ effect (Rädler, 1969) and the shear current effect (Rogachevskii & Kleeorin, 2003; Squire & Bhattacharjee, 2015c,b,a). The latter requires $\eta_{yx} < 0$.

3.3 Unstratified simulations

In this section we discuss simulations without the gravitational term in the vertical direction (see equation 3.3). We start with a uniform Cartesian grid, set the initial velocity field to the ground state of the shearing box (3.6), and use an initially uniform density $\rho = 1$ with sound speed $c_s = 1$. To seed the MRI, we add random noise of maximum amplitude $0.05\,c_s$ to the background shear flow of every cell. We characterize the strength of the initial magnetic field with the volume-averaged plasma beta $\beta = 2p_{\mathrm{gas}}/B^2$.

3.3.1 Net flux

We use a box of size $L_x \times L_y \times L_z = 1 \times 6.28 \times 1$, which corresponds to the default case of Hawley et al. (1995), and is also discussed in Deng et al. (2019). We set up a constant vertical magnetic field,

$$\boldsymbol{B} = B_0 \hat{e}_z, \tag{3.31}$$

with field strength $\beta = 400$. As initial grid, we use a Cartesian mesh with $16 \times 100 \times 16$ cells. For higher resolution realizations, we multiply the number of cells per dimension with a constant factor.

In Fig. 3.2 we show the temporal evolution of several volume-weighted properties of the MRI for simulations with 48 cells per scale height and different c_{h0}. In all cases, we find a saturated, turbulent state. The magnetic and kinetic energy as well as the Maxwell and Reynolds stress, and the average $\nabla \cdot \boldsymbol{B}$ error decrease with c_{h0}. This can be explained by the increasing numerical resistivity in the case of stronger Dedner cleaning.

Due to the highly time-dependent behaviour of the saturated state, we show in Fig. 3.3 the volume averaged quantities additionally averaged over the last 150 orbits (starting after 50 orbits), as a function of c_{h0}. We also show results for four different resolutions, although due to the computational cost we evolved the highest resolution run only for $c_{h0} = 1$. Increasing the resolution reduces the $\nabla \cdot \boldsymbol{B}$ error and increases the average magnetic and kinetic energy as well as the Maxwell stress. The Reynolds stress itself is more independent of the resolution and also of c_{h0}, while α_{mag} only slightly increases with c_{h0} and resolution. This behaviour was also observed in small box simulations by Wissing et al. (2022), who found for 48 cells per scale height an average value of $\alpha_{\mathrm{mag}} \approx 0.65$, which is similar to our value for $c_{h0} = 1$. Our average magnetic energy (0.2 to 0.3) as well as the Maxwell stress (0.1 to 0.2) is smaller than in Hawley et al. (1995) (0.5 and 0.3) but the Maxwell stress compares well with results from Simon et al. (2009) (0.216 ± 0.116) that

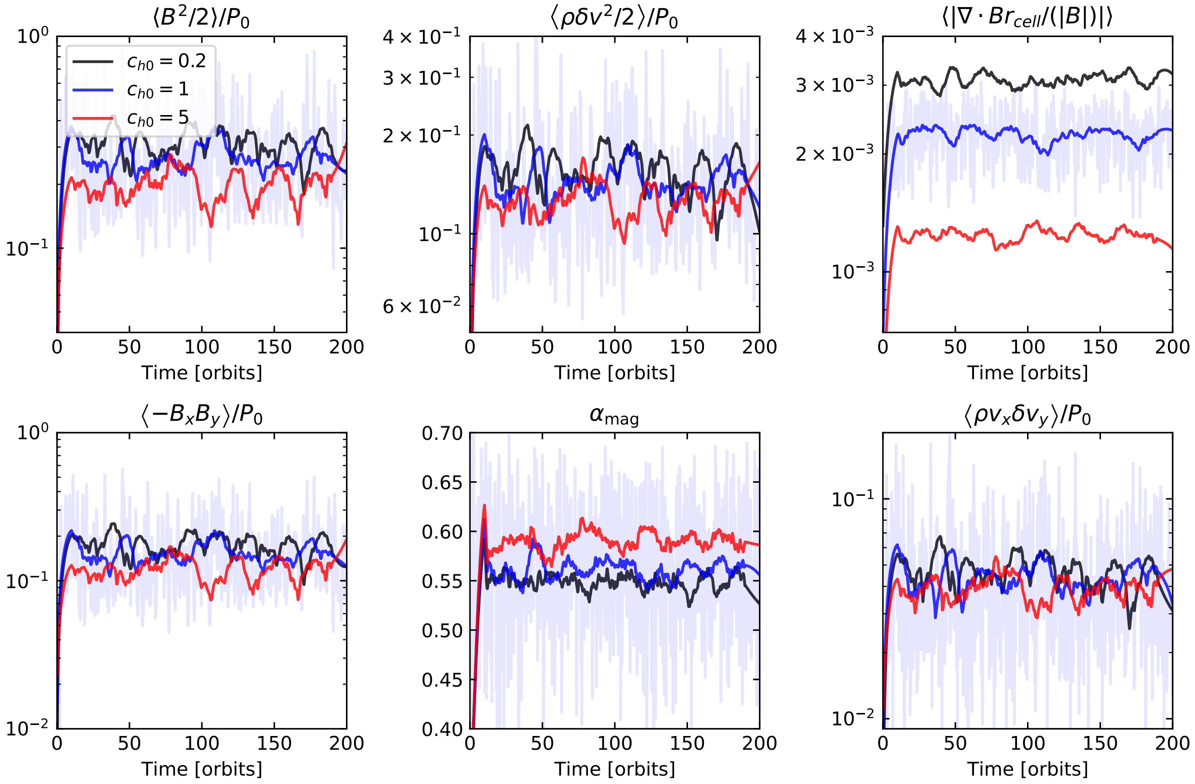

Figure 3.2: The temporal evolution of several volume weighted quantities for unstratified simulations with a net vertical magnetic field, box size $1 \times 6.28 \times 1$ and 48 cells per scale height. We vary the strength of the Dedner cleaning c_{h0}, as labelled. The shown quantities are (from left to right, and top to bottom): Magnetic field energy density, kinetic energy density, relative $\nabla \cdot \boldsymbol{B}$ error, Maxwell stress, normalized Maxwell stress (3.18) and Reynolds stress. We have smoothed the curves over 20 orbits using a Savitzky–Golay filter, and show the original unsmoothed curve for one example case as a transparent line in the background.

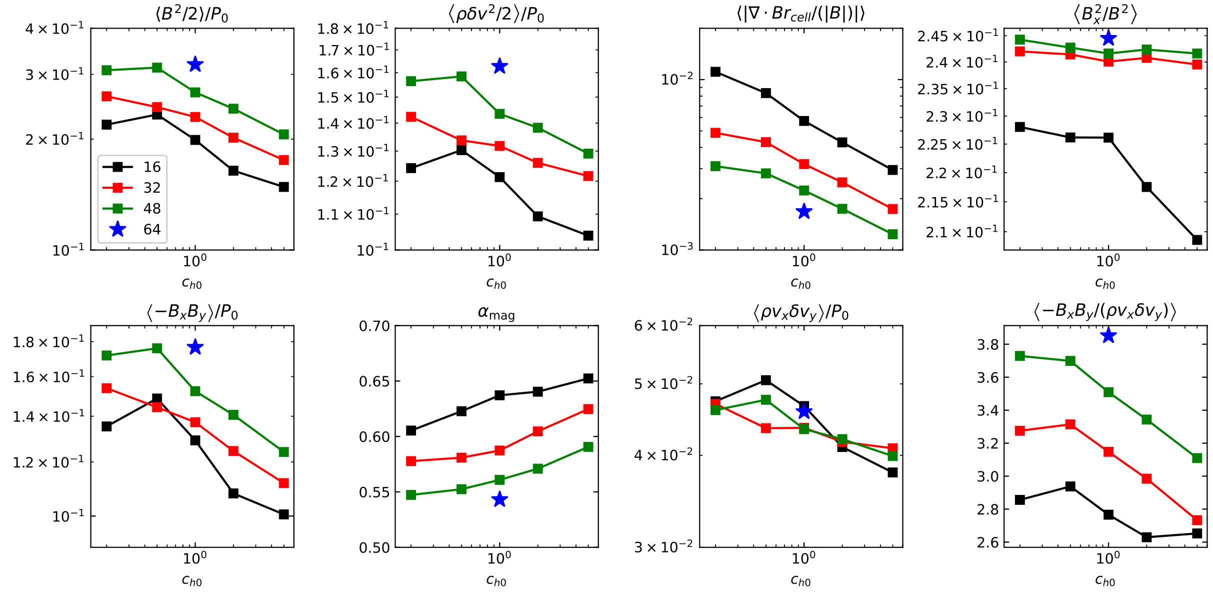

Figure 3.3: The temporal average of different quantities for unstratified simulations with a net vertical magnetic field and box size 1 × 6.28 × 1, as a function of the strength c_{h0} of the Dedner cleaning. All quantities are averaged over 150 orbits starting after 50 orbits. We also vary the resolution with 16, 32, 48 and 64 cells per scale height, as labelled. For the highest resolution we only performed one simulation with $c_{h0} = 1$ due to the high computational costs. Besides the quantities already shown in Fig. 3.2, we also include the ratio between radial and total magnetic field energy (top right) and the ratio of the Maxwell and Reynolds stress (bottom right).

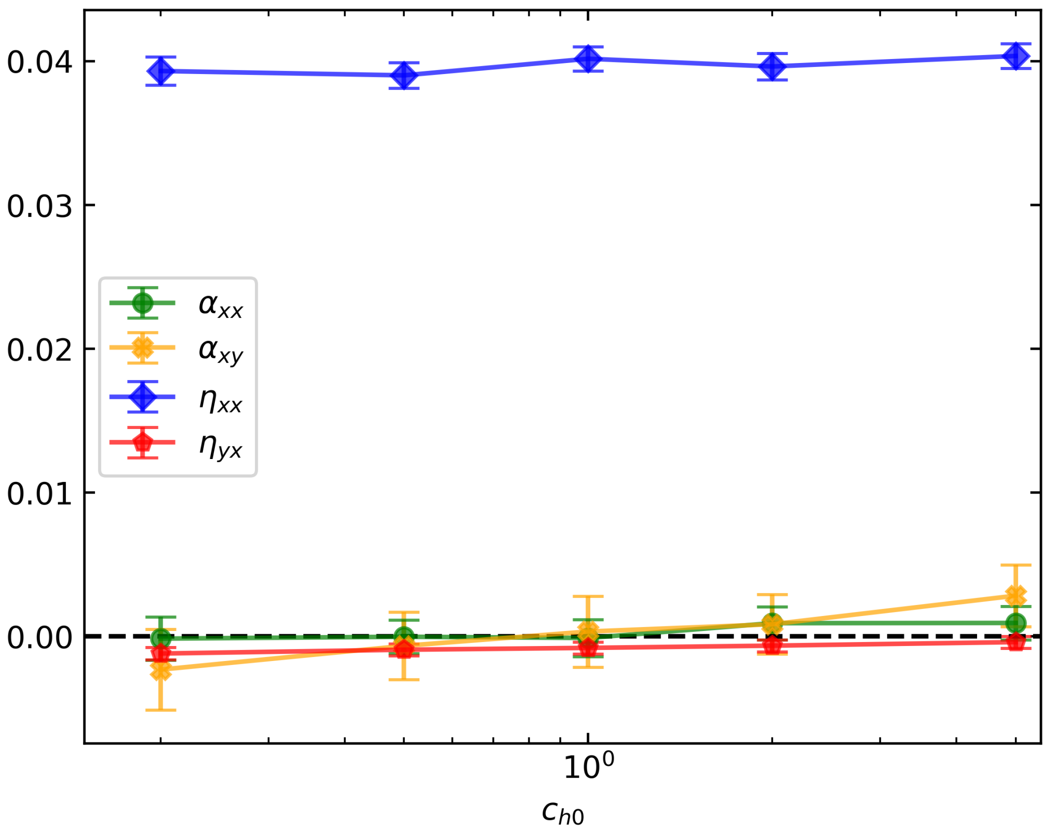

Figure 3.4: The time and spatially averaged transport coefficients as a function of c_{h0} for unstratified simulations with background field, 48 cells per scale height resolution and box size $L_x \times L_y \times L_z = 1 \times 6.28 \times 1$. The coefficients are averaged over a period of 150 orbits starting after 50 orbits. We additionally show the statistical error of the mean value for each coefficient. As expected, η_{xx} is the only coefficient differing significantly from zero.

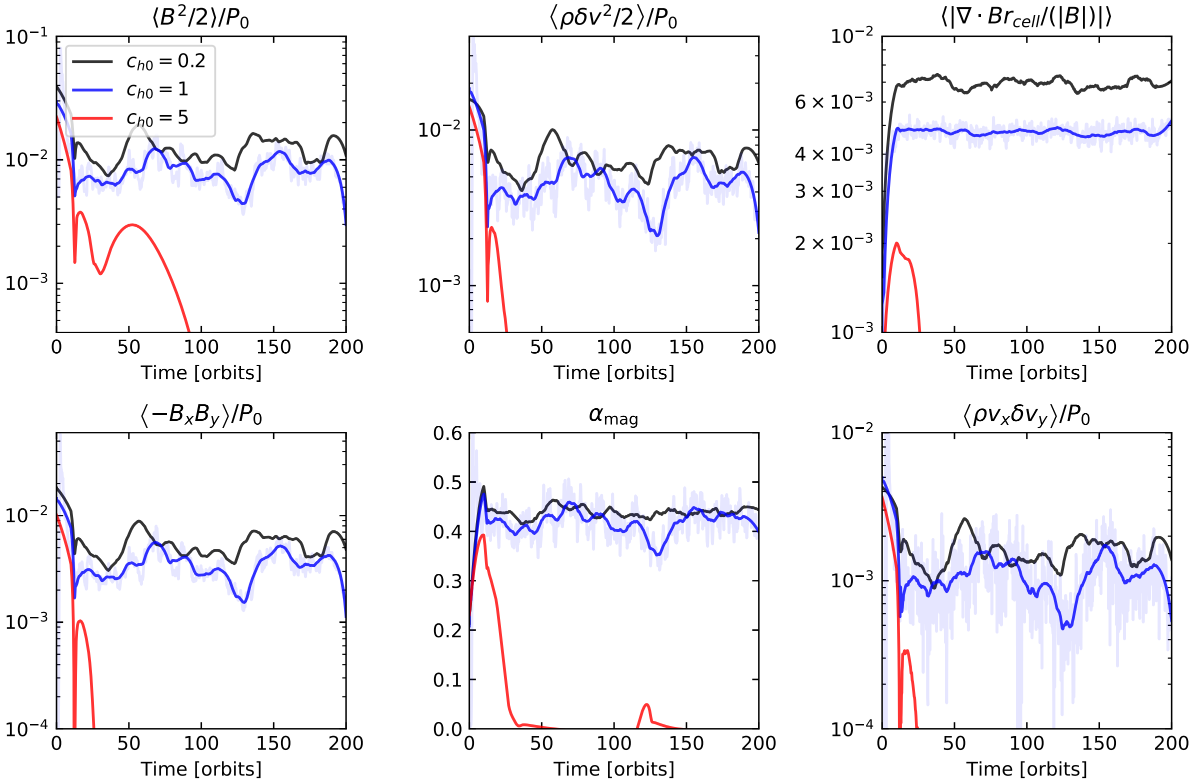

Figure 3.5: The temporal evolution of several volume weighted quantities for unstratified simulations without a net vertical magnetic field, box size $1 \times 4 \times 1$, and 48 cells per scale height. We vary the strength of Dedner cleaning c_{h0}. The shown quantities are (from left to right, and top to bottom): Magnetic field energy density, kinetic energy density, relative $\nabla \cdot \boldsymbol{B}$ error, Maxwell stress, normalized Maxwell stress (3.18) and Reynolds stress. We have smoothed the curves over 20 orbits using a Savitzky–Golay filter and show the original curve for one example case as a transparent line in the background.

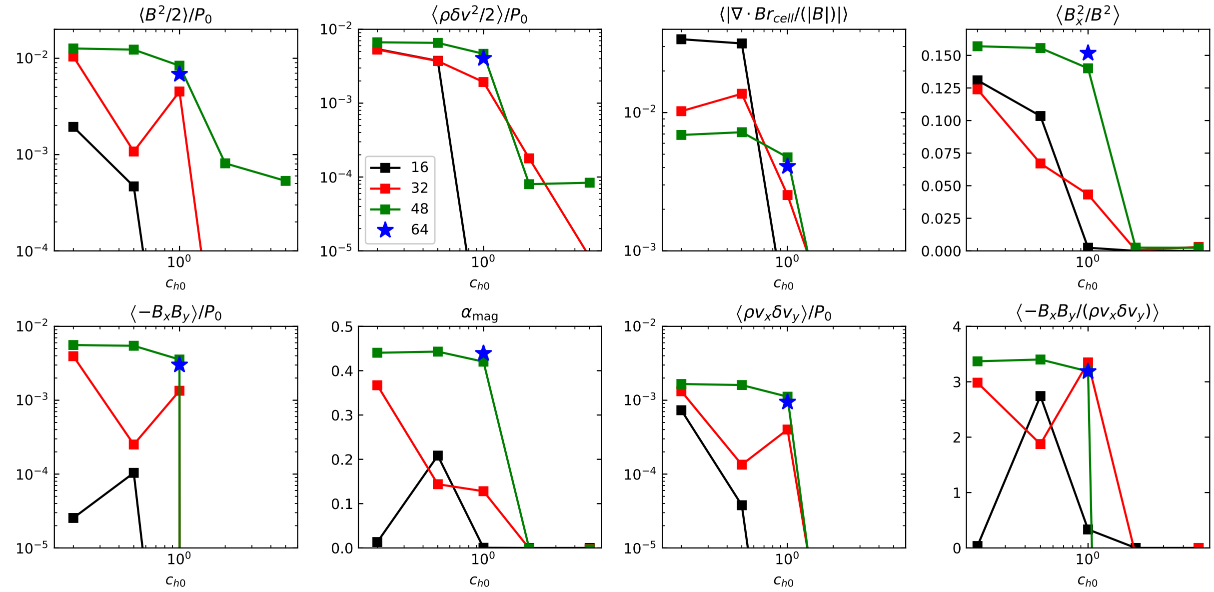

Figure 3.6: The temporal average of different quantities for unstratified simulations without a net vertical magnetic field and box size 1 × 4 × 1, as a function of the strength c_{h0} of the Dedner cleaning. All quantities are averaged over 150 orbits starting after 50 orbits. We also vary the resolution with 16, 32, 48 and 64 cells per scale height, as labelled. Besides the quantities already shown in Fig. 3.5, we also display the ratio between radial and total magnetic field energy (top right) and the ratio of the Maxwell and Reynolds stress (bottom right).

used a weaker magnetic background field ($\beta = 1500$). The ratio of the Maxwell stress to the Reynolds stress is between 3 and 4, and decreases with larger resistivity. This behaviour is similar to the one reported in Wissing et al. (2022) and also compares favourably to Hawley et al. (1995). In contrast, Simon et al. (2009) report a larger value of 7.60 ± 6.47. Clearly, the previous results reported in the literature vary significantly, reflecting in part the turbulent behaviour of the saturated state.

As we have discussed in Section 3.2.2, deviations from $\nabla \cdot \boldsymbol{B} = 0$ can generate a net azimuthal field. We also measured this field in our simulations and did not find that it decays with resolution or smaller $\nabla \cdot \boldsymbol{B}$ error. But the energy associated with this net field is typically smaller by a factor of at least 10^{-4} compared to the average magnetic field, which is why we are confident that it does not significantly affect the general field evolution.

Fig. 3.4 shows the average value of the transport coefficients α_{xx}, α_{xy}, η_{xx} and η_{yx}. As expected, we find values close to 0 for the components of α. Also, our measurements of η_{yx} are compatible with 0 considering the statistical errors. Only the turbulent diffusivity η_{xx} deviates significantly from 0 with a value of around 0.04. These results are qualitatively similar to Wissing et al. (2022) but our diffusivity is larger by a factor of around 5.

Smaller boxes typically lead to a stronger burst in the nonlinear regime of the MRI (Bodo et al., 2008; Lesaffre et al., 2009), since fewer active (non-axisymmetric) waves can fit in. As in Deng et al. (2019) we therefore also run some simulations in a smaller box with size $L_x \times L_y \times L_z = 1 \times 4 \times 1$, a standard resolution of $16 \times 64 \times 16$ cells and initial $\beta = 330$. The results are very similar to the ones obtained with the standard box, and thus we refer to Appendix 3.6 for the corresponding figures.

3.3.2 Zero net-flux

A more challenging class of setups for simulation codes are the so-called zero net flux simulations. They are defined by the condition $\langle \boldsymbol{B} \rangle = 0$, which means there is no background magnetic field that can drive the MRI. We follow the setup of Deng et al. (2019) and Wissing et al. (2022), and initialize a magnetic field as

$$\boldsymbol{B} = B_0 \sin(2\pi x)\, \hat{e}_z, \tag{3.32}$$

where the initial amplitude B_0 is chosen such that the volume-averaged plasma β is $\beta = 2p_{\mathrm{gas}}/B^2 = 400$. We first run simulations in a standard box $L_x \times L_y \times L_z = 1 \times \pi \times 1$, and use initially a Cartesian grid with base resolution $16 \times 50 \times 16$ cells. We also carried out simulations with higher resolution by multiplying the number of cells per dimension with a constant factor.

In Fig. 3.5 we show the temporal evolution of different volume-weighted quantities for a resolution of 48 cells per scale height and three different Dedner cleaning strengths. While for $c_{h0} = 5$ the MRI dies out after an initial burst we are able to sustain the MRI for at least 200 orbits for $c_{h0} \leq 1$. Additionally, we present in Fig. 3.6 time-averaged values of the volume-weighted quantities as a function of c_{h0} and resolution. Except for the lowest resolution calculation we find for all simulations with $c_{h0} \leq 1$ an active MRI whereas it dies out for $c_{h0} \geq 2$. The strong dependence on the numerical resistivity (set in our case by c_{h0}) of the MRI in simulations without net field and physical dissipation is also well known from the literature (Fromang & Papaloizou, 2007; Deng et al., 2019; Wissing et al., 2022). In particular, Fromang & Papaloizou (2007) showed in simulations with the finite difference code ZEUS that by increasing the resolution the MRI turbulence will be driven to smaller scales. Those scales are affected by the numerical viscosity and resistivity, and thus the final results strongly depend on numerical details.

Convergence can be regained by adding a physical viscosity and resistivity (Fromang et al., 2007). There seems to exist a critical magnetic Prandtl number Pr_m, which depends on the Reynolds number, below which turbulence will die out. In our case, the magnetic Prandtl number is given by the numerical viscosity and resistivity that cannot easily be measured. By increasing c_{h0} the resistivity also increases, and the numerical Prandtl number decreases, which explains the existence of a critical c_{h0} above which the turbulence dies out.

Experiments with SPH in Wissing et al. (2022) found a critical Prandtl number of around $\mathrm{Pr}_m = 2.5$ above which the MRI turbulence survives. In contrast to static grid codes, the total stress, as well as the magnetic energy, does not decrease if we increase the resolution (see e.g. Shi et al., 2016), which is similar to SPH for a constant magnetic Prandtl number (Wissing et al., 2022). This might be a hint that the magnetic Prandtl number scales differently with resolution for a moving mesh code with Dedner cleaning than for a static grid code.

For our highest resolution runs, we find a total stress $\alpha \approx 0.01$ and normalized magnetic stress $\alpha_{\mathrm{mag}} \approx 0.4$, which is consistent with previous results (Hawley et al., 1995; Simon et al., 2009; Wissing et al., 2022). Also, the ratio of Maxwell to Reynolds stress is in our case ≈ 3.5 and agrees well with previous results with Eulerian codes (Hawley et al., 1995; Stone et al., 1996; Hawley et al., 1999; Sano et al., 2004), while Wissing et al. (2022) found values of around 4.5 with SPH. In our highest resolution run, we obtain a ratio of the radial magnetic energy to the total energy of $\langle B_x^2/B^2 \rangle \approx 0.15$, which is close to the value of 0.14 reported in Shi et al. (2016) and higher than 0.1 as in Wissing et al. (2022).

3.3.3 Zero net-flux simulations in tall boxes

In boxes with larger vertical aspect radio ($L_z/L_x \geq 2.5$) a new and more vigorous MRI dynamo emerges. Shi et al. (2016) showed that in this case the stress becomes independent of the resolution, which simplifies the comparison of results of different codes. We therefore rerun the simulations from the previous subsection in a larger box, $L_x \times L_y \times L_z = 1 \times 4 \times 4$, with a base resolution of $16 \times 64 \times 64$ cells, and using the same initial field as in the smaller box.

In Fig. 3.7 we show the temporal evolution of volume-weighted quantities for a resolution of 48 cells per scale height and different Dedner cleaning speeds. In contrast to the smaller box, the MRI can sustain turbulence even for $c_{h0} = 5$. As one can see in Fig. 3.8, only for the lowest resolution and $c_{h0} \geq 1$ the MRI dies out, while in general

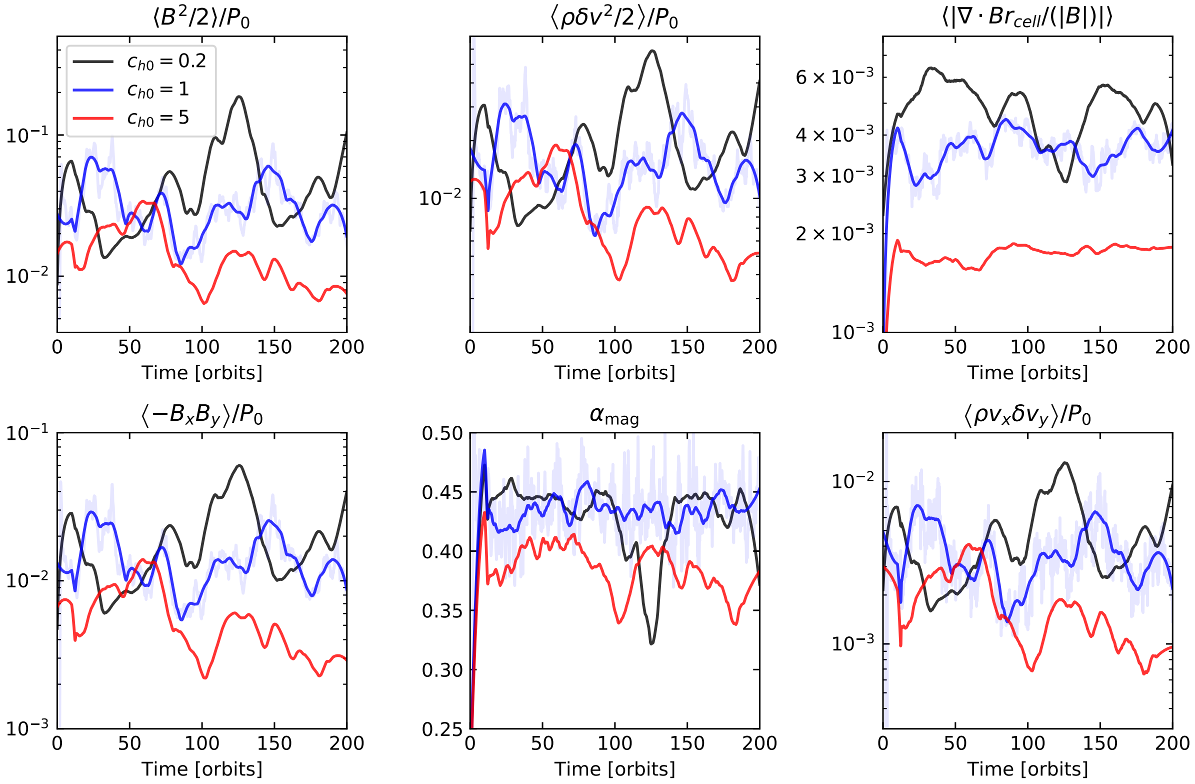

Figure 3.7: The temporal evolution of several volume weighted quantities for unstratified simulations without a net vertical magnetic field, with a box size $1\times4\times4$, and 48 cells per scale height. We vary the strength of Dedner cleaning c_{h0}, as labelled. The displayed quantities are (from left to right, and top to bottom): Magnetic field energy density, kinetic energy density, relative $\nabla\cdot\boldsymbol{B}$ error, Maxwell stress, normalized Maxwell stress (3.18) and Reynolds stress. We have smoothed the curves over 20 orbits using a Savitzky–Golay filter. The original measurement for one example case are included as a transparent line in the background.

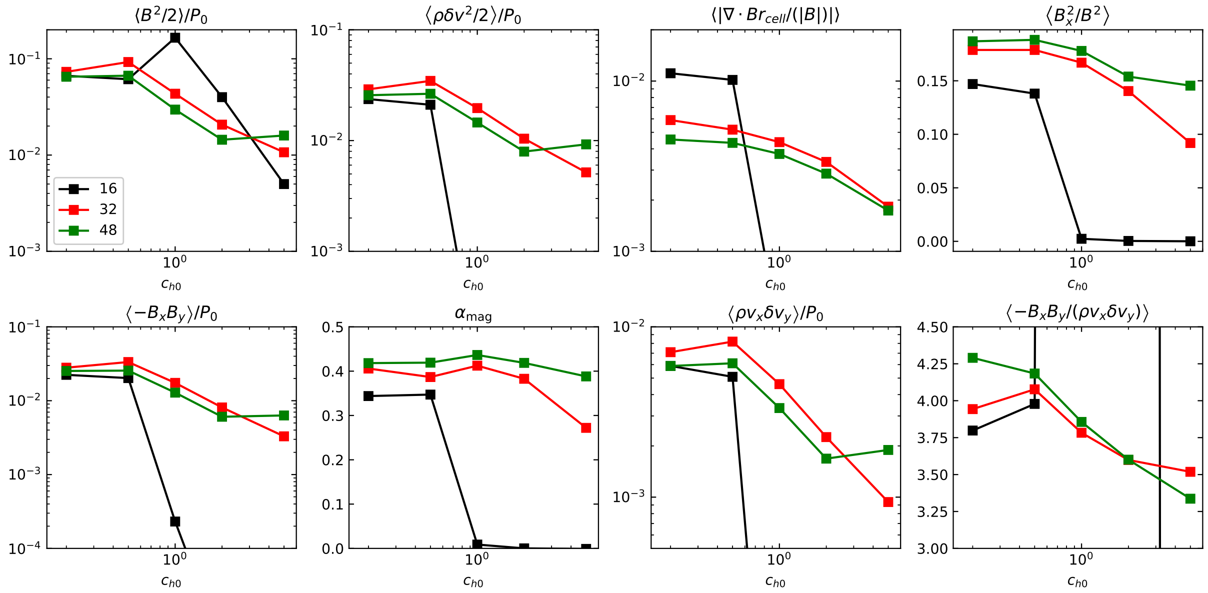

Figure 3.8: The temporal average of different quantities for unstratified simulations without a net vertical magnetic field, for a box size $1 \times 4 \times 4$, as a function of the strength c_{h0} of the Dedner cleaning. All quantities are averaged over 150 orbits starting after 50 orbits. We also vary the resolution by using 16, 32 or 48 cells per scale height, as labelled. Besides the quantities already shown in Fig. 3.7, we also show the ratio between radial and total magnetic field energy (top right) and the ratio of the Maxwell and Reynolds stress (bottom right).

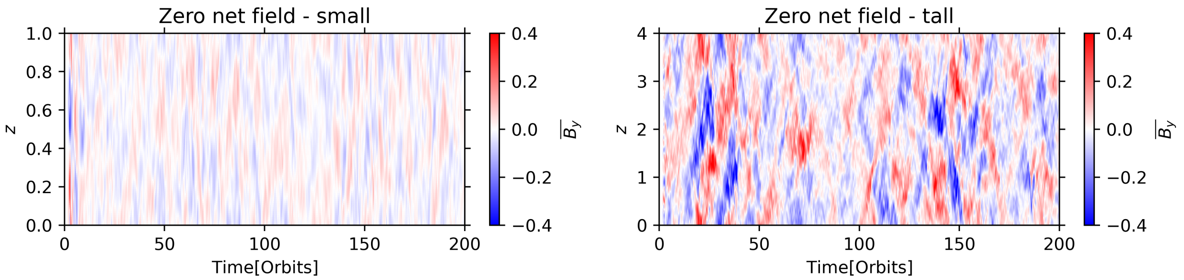

Figure 3.9: The evolution of the horizontally averaged azimuthal magnetic field in simulations with $c_{h0} = 1$ and 48 cells per scale height. Both simulations are evolved in an unstratified box without net field. In contrast to the small box, there is a strong large scale mean field in the tall box with comparable magnitude to the field reported in Shi et al. (2016).

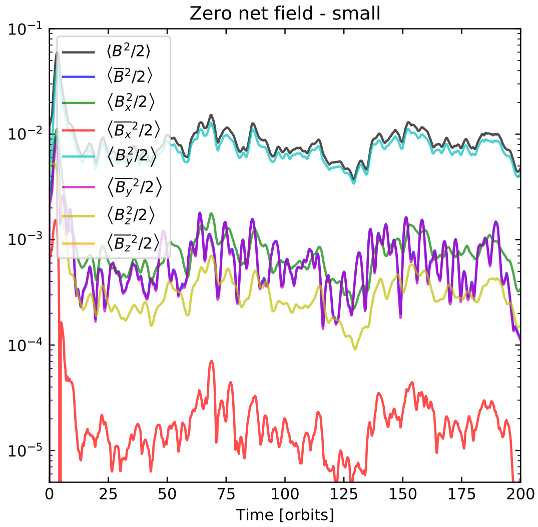

Figure 3.10: We show the evolution of the total magnetic energy and contributions of different magnetic field components to it. We use simulations with $c_{h0} = 1$ and 48 cells per scale height. Both simulations are computed in an unstratified box without net field. We note that the mean vertical field $(\bar{B}_z)$ vanishes and therefore is not shown. The mean field is fully dominated by the azimuthal component.

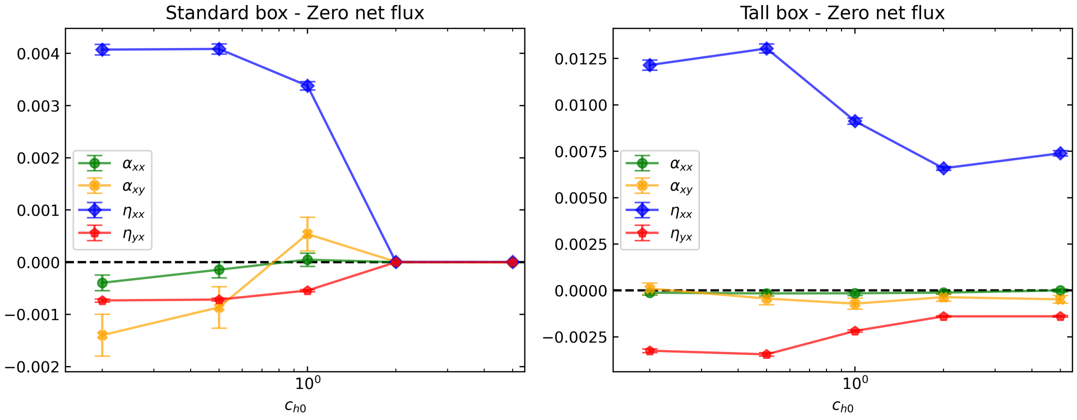

Figure 3.11: The transport coefficients as a function of c_{h0} for unstratified simulations without background field and a resolution of 48 cells per scale height. The coefficients are averaged in space, and in time over 150 orbits starting at 50 orbits. We also show the statistical error of the mean value. As expected, α_{xx} as well as α_{xy} vanish while we find a positive turbulent diffusivity η_{xx}. The component η_{yx} is significantly negative, especially in the case of a tall box, which allows the shear-current effect to be active and to generate a large scale mean field. We note that in the standard box the turbulence dies out for $c_{h0} \geq 2$.

the stress is larger by a factor of more than 4 compared to the small box. The magnetic energy and also the Maxwell and Reynolds stress have in our higher-resolution simulation a maximum at $c_{h0} = 0.5$ and decrease with stronger numerical resistivity. The dependence of the saturated quantities on c_{h0} is in this case stronger than for simulations with a net field.

The results for $c_{h0} = 0.5$ and the ones from Shi et al. (2016) compare in general very well for the same resolution of 32 cells per scale height. We find a total stress of $\alpha \approx 0.042$, whereas Shi et al. (2016) measure $\alpha \approx 0.052$. But it seems that our results are already converged with higher resolution while in their paper the stress further increases with higher resolution. In the case of the tall box, we find as expected a strong azimuthal mean field whose evolution is shown in Fig. 3.9. The amplitude is higher than in Wissing et al. (2022, see their Fig. 4) and compares qualitatively well with the results in Shi et al. (2016, see their Fig. 10).

In Fig. 3.10 we also show the distribution of the magnetic energy over the different spatial components and subdivide it by the mean and fluctuating parts. The total magnetic energy is dominated by the azimuthal component with a contribution of around 10% from the radial component. The energy of the mean magnetic field is fully dominated by the azimuthal component, which is as expected larger in the tall box simulation in comparison to the small box simulation. The mean azimuthal field is still smaller in comparison to the simulations in Shi et al. (2016), where it contributes around 50% of the magnetic energy. Times of lower magnetic energy in the mean-field component are also visible in the space diagrams in Fig. 3.9, where a large-scale magnetic field is missing (e.g. at around 80 orbits).

In Fig. 3.11 we show the spatially and temporally averaged transport coefficients. As expected, all components of α are close to 0 while we find both in the small and the tall box a significantly positive value for the turbulent diffusivity η_{xx}. Its value is around 0.003 for the standard box in the cases with sustained turbulence, and somewhat larger in the tall box. We also find that η_{yx} is slightly negative in the standard box, while it becomes more significantly negative in the tall box. These findings are consistent with the results of Shi et al. (2016) but opposite to those of Wissing et al. (2022) who found slightly positive values for the tall box case and vanishing values for the standard box case. This suggests that the shear-current effect can be followed in our simulations, explaining why we get a significant large-scale magnetic field as in Shi et al. (2016), in contrast to Wissing et al. (2022). Our result for the magnitude of η_{yx} compare well with the results from Shi et al. (2016), who equally found $\eta_{yx} \approx -10^{-3}$.

3.4 Stratified simulations

In this section, we present simulations that include the linearized vertical component of the gravitational force of the central object as presented in equation (3.3). For an isothermal gas the hydrostatic density profile is given by

$$\rho(z) = \rho_0 \exp\left(-\frac{z^2}{2H^2}\right), \tag{3.33}$$

with the scale height[1] $H = c_s/\Omega_0$ and the mid plane density $\rho_0 = 1$. To allow for outflows we require a relatively large L_z. But in this case $\rho(z)$ becomes very small which can lead to numerical problems, which is why we introduce a density floor $\rho_{\min} = 10^{-6}$ and replace the acceleration in the vertical direction by

$$a = \frac{\rho - \rho_{\min}}{\rho}\Omega_0^2\, z. \tag{3.34}$$

After each time step, we set the density to $\rho_{\min}$ for cells with $\rho < \rho_{\min}$ and keep the velocity and the magnetic field fixed.

AREPO allows the creation and destruction of new cells (refinement/derefinement in the following) during run time. These processes can be triggered by more or less arbitrary criteria, which are typically based on the mass and volume of the cells. In this section we define a target mass m_{target} and split cells with a mass higher than $2\, m_{\text{target}}$, and remove cells with a smaller mass than $0.5\, m_{\text{target}}$. To avoid too rapid local variations in the spatial resolution we impose a maximum allowed volume ratio of 10 between adjacent cells, and enforce a maximum volume of 0.05 per cell. The volume-based conditions become especially important in the low-density halo of the disk and avoid that a cell interacts with a periodic image of itself.

Without magnetic field the density profile (3.33) in combination with the background velocity shear profile from equation (3.6) should be stable. As in Deng et al. (2019) and Wissing et al. (2022) we use a box of size $L_x \times L_y \times L_z = \sqrt{2} \times 4\sqrt{2} \times 24$ and an initial magnetic field

$$\boldsymbol{B} = B_0 \hat{e}_y, \tag{3.35}$$

with plasma $\beta = 25$. We have run simulations with $c_{h0} = 0.5$ and $c_{h0} = 1$, combined with $m_{\text{target}} = 10^{-5}$ (approx. 1.6×10^6 cells) or $m_{\text{target}} = 5 \times 10^{-6}$ (approx. 3.2×10^6 cells).

In Fig. 3.12 we show the temporal evolution of several volume averaged quantities for our four runs averaged over the whole box, while in Fig. 3.13 we show the corresponding plot only for cells close to the mid plane ($\pm\sqrt{2}H$). In this volume the MRI is active, so that this filter avoids averaging over a magnetically dominated corona. In all simulations, the magnetic field gets amplified at the onset of the MRI and saturates later on into a turbulent state. Although the absolute energy, as well as the stresses, are dominated by the high-density region, they are larger in the low-density region after normalizing them with the average pressure.

In Fig. 3.14 we show additionally the temporal average of different quantities as a function of c_{h0}. As expected, the $\nabla \cdot \boldsymbol{B}$ error decreases with c_{h0} and also with higher resolution. The magnetic field and stress decrease for larger c_{h0} for the low-resolution simulation, while for the high-resolution simulation the results seem to be approximately independent of c_{h0}. The total stress is around $\alpha \approx 0.005 - 0.012$, and the normalized stress is $\alpha_{\text{mag}} \approx 0.3 - 0.4$ close to the mid plane region, which agrees well with the results in Wissing et al. (2022) for GDSPH with an artificial viscosity parameter $\alpha_B = 0.5$. Also, the

---

[1] We note that some studies add a factor $\sqrt{2}$ in the definition of the scale height (e.g. Simon et al., 2011).

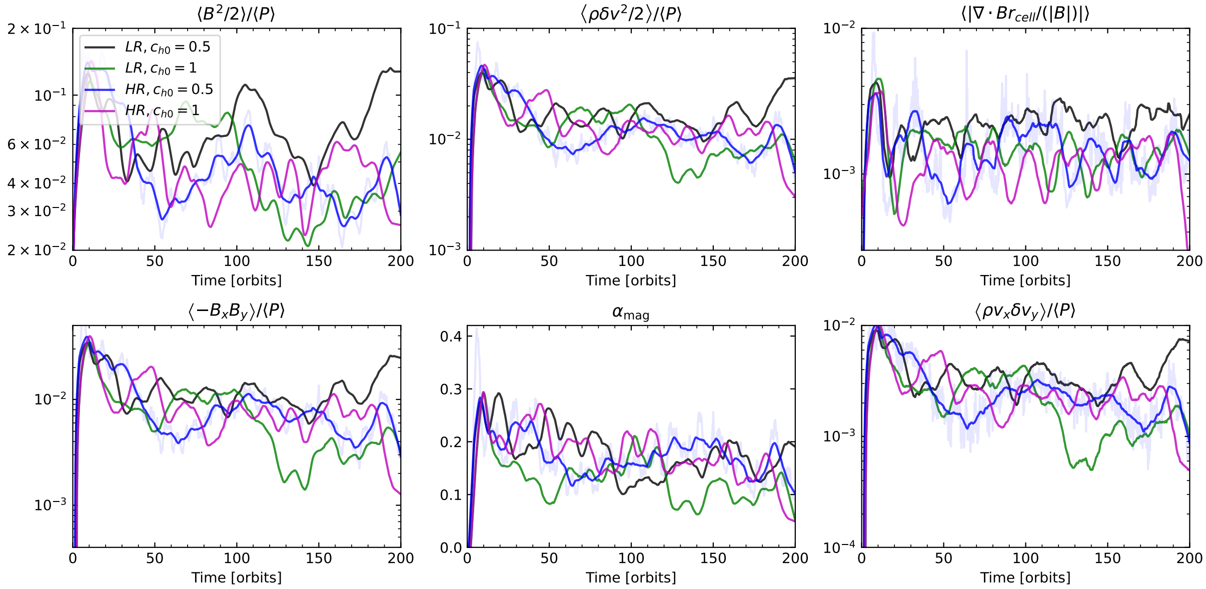

Figure 3.12: The temporal evolution of several volume weighted quantities for stratified simulations with box size $\sqrt{2}\times\sqrt{2}\times 24$, for two different resolutions (LR: $m_{\rm target} = 10^{-5}$, HR: $m_{\rm target} = 5\times10^{-6}$) and two different strengths of the Dedner cleaning c_{h0}. The shown quantities are (from left to right, and top to bottom): Magnetic field energy density, kinetic energy density, relative $\nabla\cdot\boldsymbol{B}$ error, Maxwell stress, normalized Maxwell stress (3.18) and Reynolds stress. The quantities are averaged over the whole simulation box. We have smoothed the curves over 10 orbits using a Savitzky–Golay filter, and show the original curve for one example case as a transparent line.

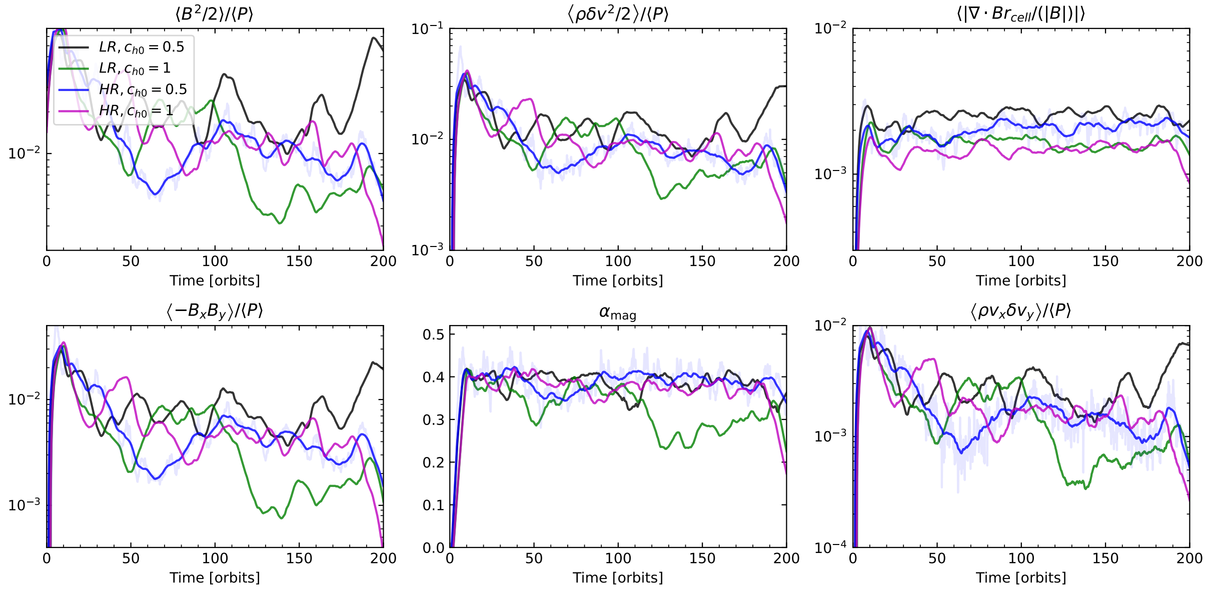

Figure 3.13: Same as Fig. 3.12, but we only consider gas close to the mid plane ($\pm\sqrt{2}H$).

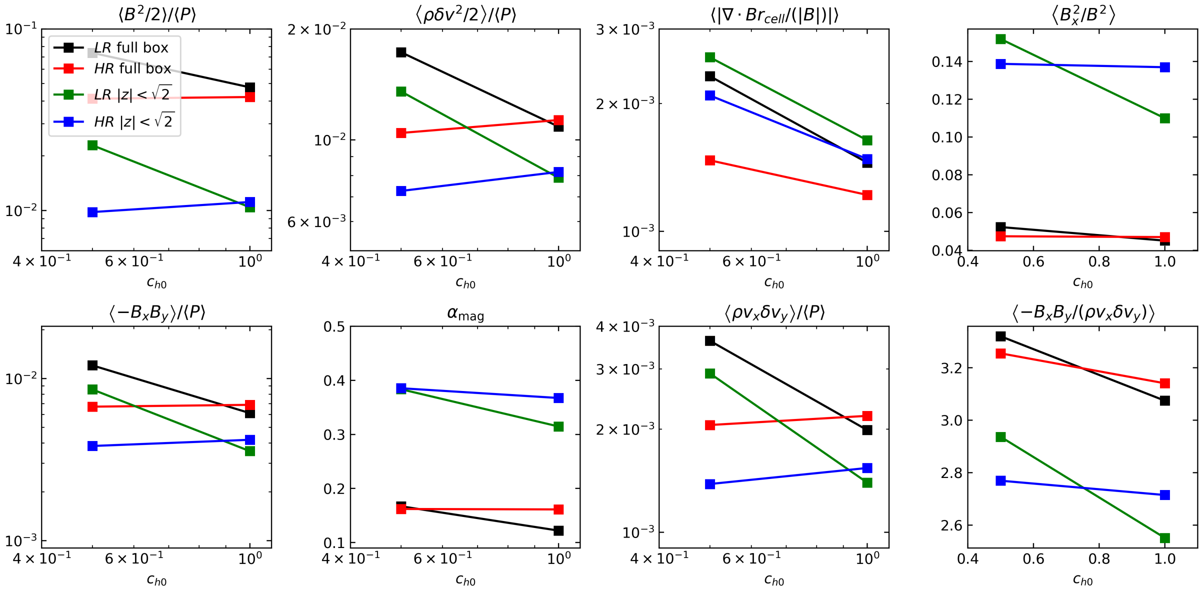

Figure 3.14: The temporal average of different quantities for stratified simulations with box size $\sqrt{2}\times\sqrt{2}\times 24$ as a function of the strength c_{h0} of the Dedner cleaning. All quantities are averaged over 150 orbits starting after 50 orbits. We also vary the resolution (LR: $m_{\mathrm{target}} = 10^{-5}$, HR: $m_{\mathrm{target}} = 5\times10^{-6}$). Besides the quantities already shown in Fig. 3.12 and Fig. 3.13 we also include the ratio between radial and total magnetic field energy (top right), and the ratio of the Maxwell and Reynolds stress (bottom right).

magnetic energy density is similar, but we find a ratio of Maxwell to Reynolds stress of $\approx 2.6-3$, in contrast to the value $\simeq 4$ found by Wissing et al. (2022). Hawley et al. (2011) compared several previous stratified MRI simulations run with static grid codes (Simon et al., 2011; Shi et al., 2010; Davis et al., 2010; Guan & Gammie, 2011) and found for the normalized stress $\alpha_{\mathrm{mag}} \approx 0.22-0.4$, for the total stress $\alpha \approx 0.01-0.03$ and the ratio of the square of the radial to total magnetic field $\langle B_x^2/B^2 \rangle \approx 0.07-0.18$ close to the mid plane ($\pm\sqrt{2}H$ for our definition of the scale height). Deng et al. (2019) found during the time period with active MRI similarly $\alpha_{\mathrm{mag}} \approx 0.4$ and $\alpha \approx 0.02-0.04$, which were calculated with a mass-weighted average. While our values for α_{mag} compare well with those previous studies our total stresses are at the lower end of the results previously reported in the literature.

As one can see in Fig. 3.15, all our simulations show the characteristic butterfly diagram in the horizontally averaged magnetic field. The azimuthal magnetic field gets buoyantly transported out of the mid-plane and flips sign in the central region. This behaviour can be observed over 100s of orbits in the inner region, whereas in the outer regions a positive azimuthal field forms in most simulations. In Fig. 3.16 we show the volume-averaged mean azimuthal field close to the mid-plane and its temporal Fourier transformation. We find in all simulations an average period of 14, which is consistent with the results from Simon et al. (2011).

There is a time lag between the radial and azimuthal fields which is characteristic of an active $\alpha\omega$ dynamo. A positive net radial field will decrease the net azimuthal field following the first term in equation (3.29). The net azimuthal field becomes negative and starts to damp the radial field following the second term in equation (3.28) if α_{yy} has a negative gradient in the z-direction. In Fig. 3.17 we, therefore, show the horizontally and temporally averaged transport coefficients as a function of z. Except for the low resolution run with $c_{h0} = 0.5$, we find for all four components of α clear gradients close to the mid-plane. All of them are antisymmetric with respect to the mid-plane position, as expected. α_{yy} has a negative gradient and can therefore create and amplify the radial magnetic field if there is a mean azimuthal field as given in our simulation. This means the $\alpha\omega$ dynamo is active in our simulations, a result that is consistent with previous findings in the literature (Brandenburg et al., 1995; Brandenburg & Sokoloff, 2002; Brandenburg, 2008; Shi et al., 2010; Wissing et al., 2022). α_{xx} has a positive gradient and therefore counteracts the rotational term for the evolution of $\overline{B_y}$, but the latter one still dominates. Finally, α_{xy} has a positive gradient while α_{yx} has a negative gradients, which means the diamagnetic pumping term $\gamma_z = 0.5\,(\alpha_{yx} - \alpha_{xy})$ is positive above the mid-plane and negative below. The mean magnetic field, therefore, gets transported away from the mid-plane in our simulations, which is consistent with the results in Shi et al. (2016) and Wissing et al. (2022). Also, the absolute amplitude of 0.01 to 0.02 compares well with Shi et al. (2016) in contrast to Wissing et al. (2022), who found $|\alpha_{yx}| \ll |\alpha_{xy}|$.

We find a positive turbulent diffusivity $\eta_{xx} \approx 0.01$ consistent with the results from Shi et al. (2016) and Wissing et al. (2022), with $\eta_{yx} < 0$ close to the mid plane. The latter result shows that the shear-current effect is active in our simulations, as in Shi et al. (2016), but unlike in the results of Wissing et al. (2022). This is similar to our findings for the unstratified, tall box simulation without a mean magnetic field. The quantitative value of $\approx -2 \times 10^{-3}$ also agrees well with Shi et al. (2016).

In Figure 3.18, we show additionally several vertical profiles for the HR simulation with $c_{h0} = 1$. In the region within a distance $\pm 2H$ from the mid-plane, we find an approximately constant Maxwell and Reynolds stress as well as uniform energy density. At the boundary of this region, β reaches unity and the system becomes magnetically dominated further away from the mid-plane. In the outer region, the turbulent, kinetic energy drops faster than the magnetic energy and the system is stable to the MRI.

This all agrees qualitatively well with the results in Simon et al. (2011) though we find a bump in the magnetic energy at the boundary between the MRI and magnetic field-dominated domains. This can also be observed in the butterfly diagrams in Fig. 3.15. Close to the mid-plane we always find $Q_z > 7$, $Q_x > 10$, and $Q_y > 30$, which is close to the condition $Q_z > 10$ and $Q_y > 20$ to reach convergence in the stresses (Hawley et al., 2011). The spatial resolution is, as expected, highest in the high-density region close to the mid-plane.

In summary, our simulations compare qualitatively well with previous simulations, though the saturated stresses and magnetic energy seem to lie at the lower end of reported results in the literature (Hawley et al., 2011; Deng et al., 2019; Wissing et al., 2022). This could be explained by the problem that in our simulations the Dedner cleaning speed is given by the maximum signal speed in the system, which we typically find in the corona of our disk. The maximum signal speed is on average 10 times larger than the sound speed (see Fig. 3.19), which is close to the signal speed in the mid-plane. This means that we typically clean the magnetic field much more strongly in the mid-plane as would be required locally, and therefore the numerical resistivity is also (needlessly) larger. Smaller values for c_{h0} would solve this problem but in this case the magnetic field evolution in the corona tends to become unstable.

3.5 Summary and Conclusions

In this chapter, we analyzed the ability of the moving-mesh code AREPO to simulate the linear and nonlinear stages of the magnetorotational instability using the shearing box approximation. The code can accurately resolve the linear growth rate of channel flows and shows close to third-order convergence in agreement with results obtained with the static grid code ATHENA (see Fig. 3.1). The Lagrangian method MFM on the other hand requires for similarly accurate results a much higher number of resolution elements and also the relatively large Wendland C4 kernel with 200 neighbours, which implies much higher computational costs.

After the exponential growth in the linear regime, the MRI saturates, and provided it does not die out a quasi-stationary turbulent state forms that can be described by time-averaged quantities. The exact behaviour depends on the numerical resistivity of the code, which can be increased/decreased in our simulations by imposing a stronger/weaker divergence cleaning. Stronger numerical resistivity leads typically to a weaker MRI, causing

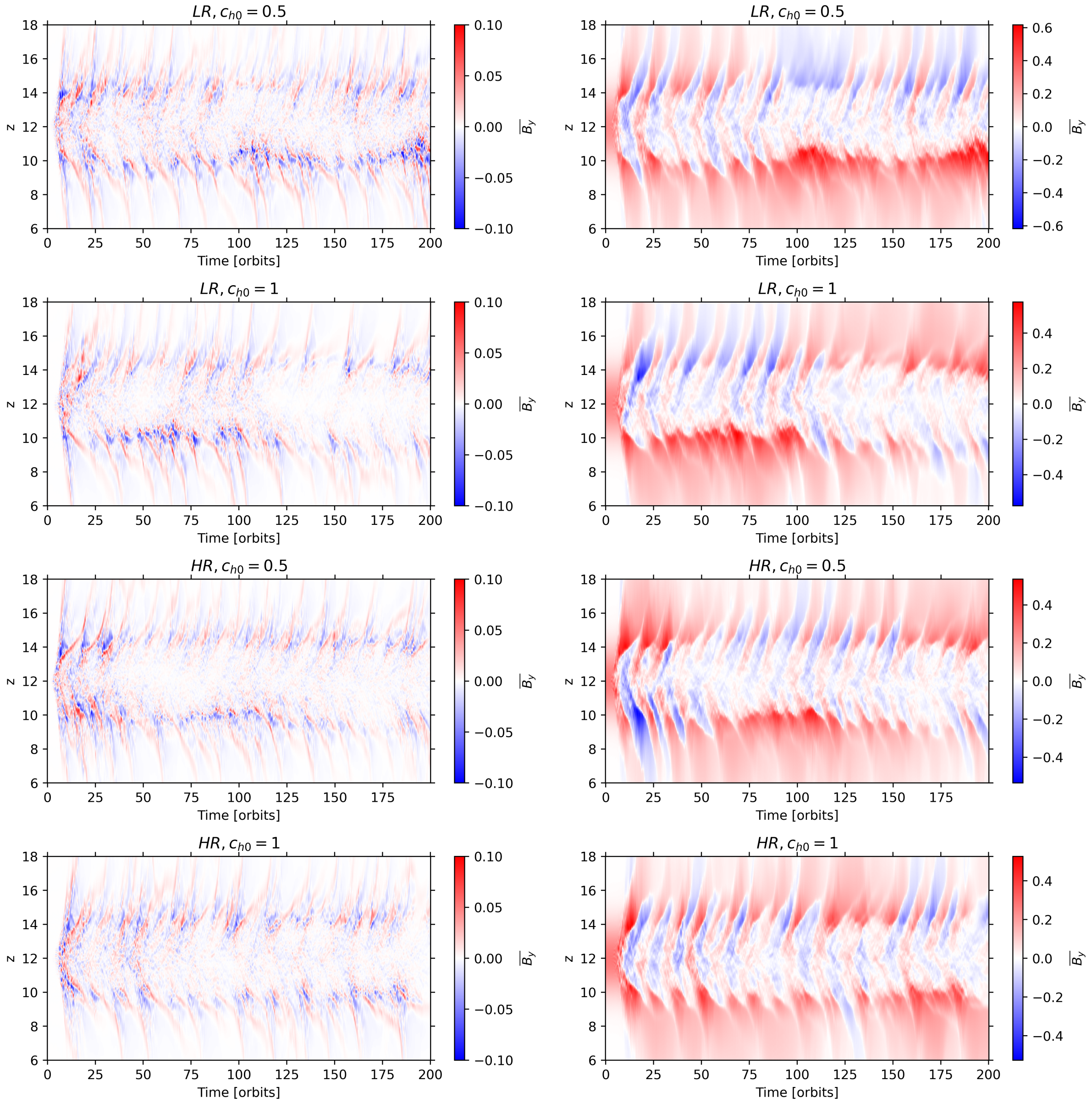

Figure 3.15: Space-time diagram of the horizontally averaged radial (left) and azimuthal (right) magnetic field for our four stratified simulations. In all simulations, we see remnants of the characteristic butterfly diagram, although the outer regions are dominated by a positive azimuthal net field.

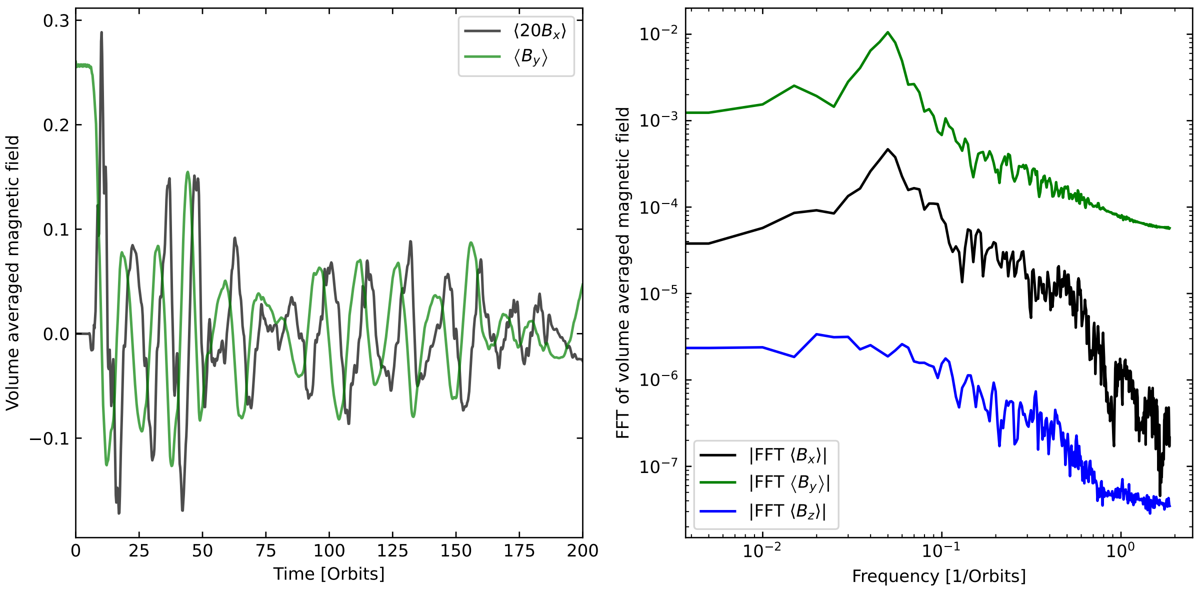

Figure 3.16: *Left panel:* The temporal evolution of the volume-averaged radial and azimuthal magnetic fields near the mid-plane ($\pm H$) for the HR simulation with $c_{h0} = 1$. For visual clarity, we multiplied B_x with a factor of 20. As also seen in Fig. 3.15, the mean field is oscillating with a period of around 14 orbits. There is a time lag between the radial and azimuthal fields which can be explained with an active $\alpha\omega$ dynamo and which is consistent with results from Simon et al. (2011). *Right panel:* Temporal power spectrum of the signal on the left panel, started after 50 orbits. One can see a peak for the radial and azimuthal fields for the oscillation frequency of the butterfly diagram.

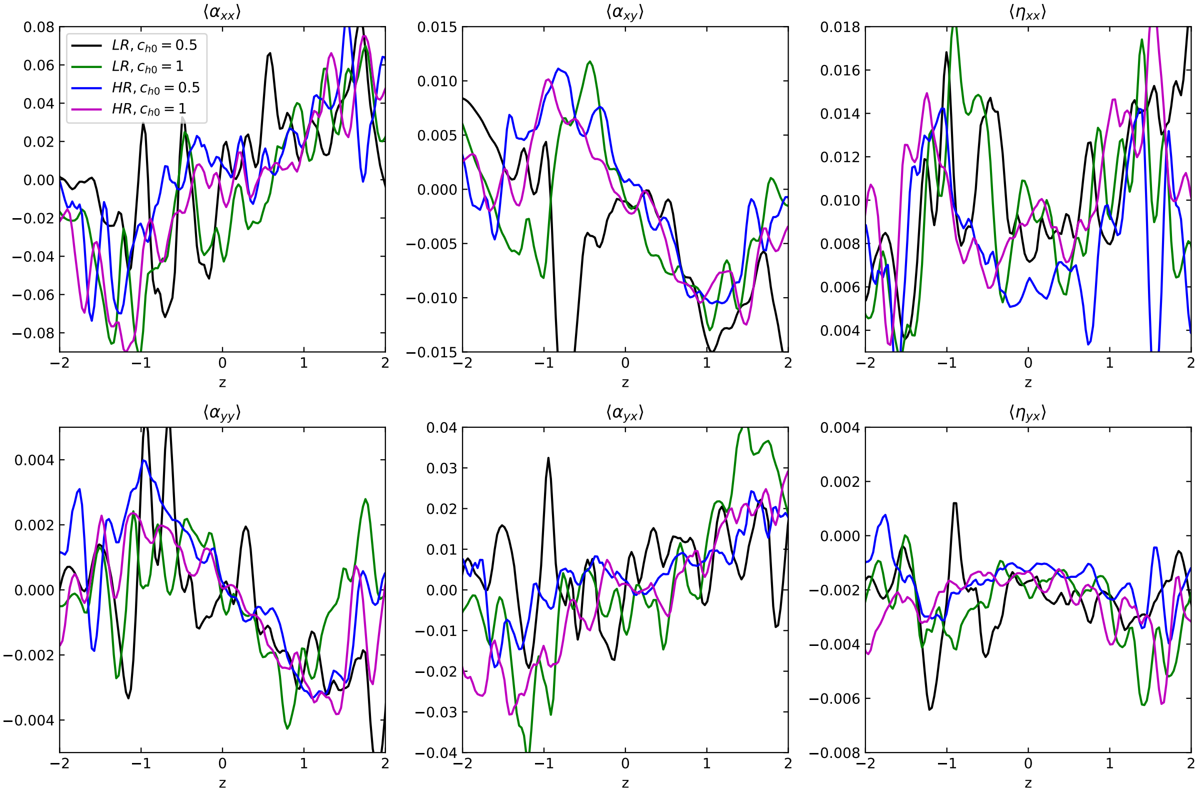

Figure 3.17: Temporally averaged transport coefficients as a function of z for stratified simulations with a net field. We averaged over 150 orbits starting after 50 orbits. Except for the low resolution simulation with $c_{h0} = 0.5$, all simulations show clear gradients in the four components of α close to the mid-plane at $z = 0$. We find an active $\alpha\omega$ dynamo (due to negative gradients of α_{yy}) and a transport of the mean field away from the mid-plane (due to a positive gradient in the diamagnetic pumping term γ_z, see equation 3.30). The turbulent diffusivity η_{xx} is positive, and the shear-current effect is active due to $\eta_{yx} < 0$.

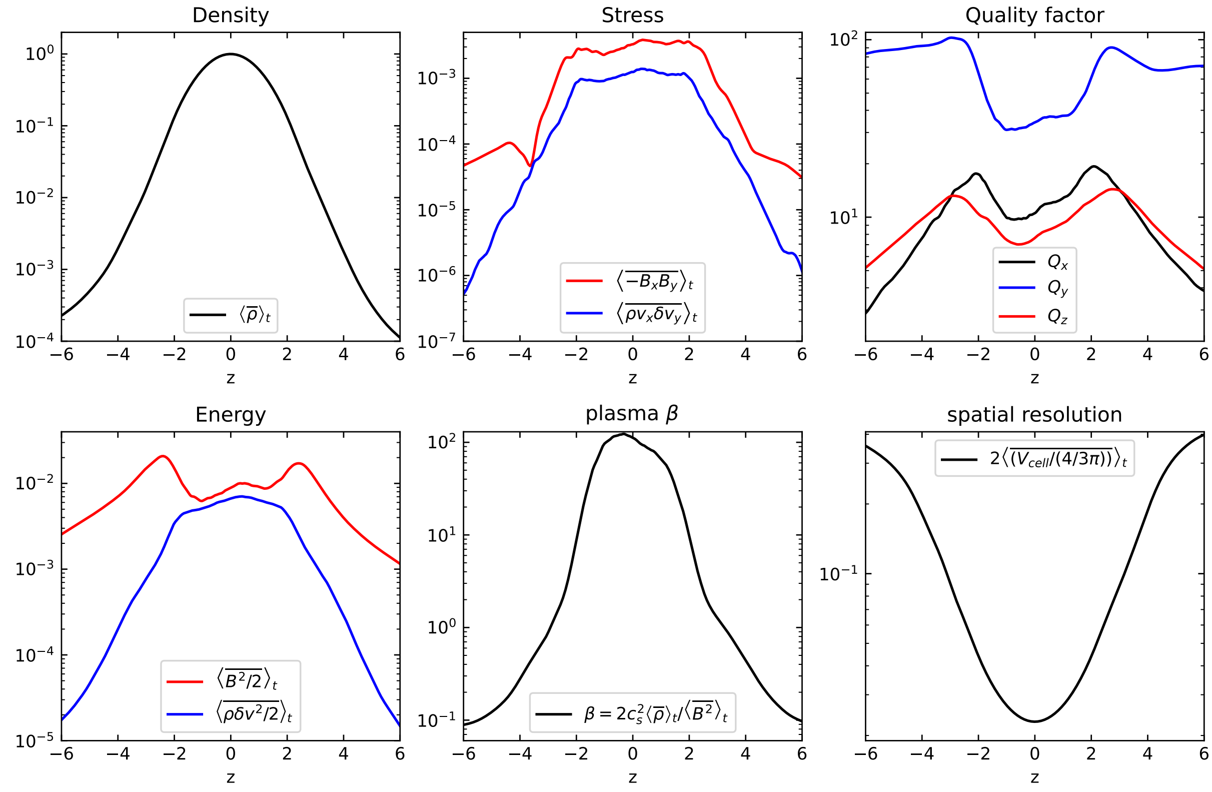

Figure 3.18: Horizontally and temporally averaged vertical profiles of different properties for the HR stratified simulation with $c_{h0} = 1$. From the left to right in the upper panel, we show the profiles of the density, stress, quality factor, energy, plasma β, and average cell diameter.

smaller average magnetic and turbulent kinetic energies as well as smaller stresses, and therefore weaker angular momentum transport. A stronger cleaning on the other hand also means that errors due to deviations from the condition $\nabla \cdot \boldsymbol{B} = 0$ are smaller.

In unstratified simulations with a net vertical field (NF), the MRI always survives even with strong cleaning and a rather small resolution of 16 resolution elements per scale height. This is in contrast to unstratified simulations without net field (ZNF), in which the MRI can die out for strong cleaning, especially for small boxes. However, a higher resolution can help in this case to sustain the MRI and increase its strength. This is in contrast to previous results for static grid codes, which found a non-convergence (Fromang & Papaloizou, 2007) of the saturated quantities of the MRI with increasing resolution. The authors explain this by a decreasing numerical Prandtl number with resolution, which also influences the strength of the MRI. Our results on the other hand show in this respect a more similar behavior to results obtained with SPH (Wissing et al., 2022), which hints that the numerical Prandtl number might scale differently between static and moving mesh codes.

We also performed unstratified ZNF simulations with larger boxes in vertical direction similar to Shi et al. (2016). We find in this case a large-scale mean-field dynamo similar to the results obtained with ATHENA, and in contrast to the SPH results in Wissing et al. (2022). We attribute this to an active shear current effect, since we find for the transport coefficient $\eta_{yx} < 0$, in contrast to Wissing et al. (2022) who found $\eta_{yx} > 0$. This dynamo increases the strength of the MRI, and only for our lowest resolution the MRI can die out for strong cleaning.

We furthermore carried out stratified shearing box simulations that include the vertical component of the gravitational force of the central object. Due to their higher computational cost we only performed 4 simulations with different resolutions and cleaning strengths. In all simulations, we find an active $\alpha\omega$ dynamo with a time-varying mean field in the mid-plane. The sign of this mean field changes with a period of around 15 orbits and leads to the characteristic butterfly diagram in the space-time diagram of the mean azimuthal field (see Fig. 3.14). In all our simulations the turbulence survived for at least 200 orbits (the time we stopped the simulations), and we find a magnetically dominated corona and an MRI-dominated mid-plane in agreement with previous results from the literature. Curiously, we find a bump in the magnetic energy in the boundary region. The MRI is in general a bit weaker in our runs in comparison to previous results for grid codes, and our results are in somewhat closer correspondence to simulations with strong cleaning in SPH (Wissing et al., 2022). We also analyzed the vertical profiles of the magnetic transport coefficients and found good agreement with previous results in the literature, and again we find an effective shear current effect, in contrast to Wissing et al. (2022).

To stabilize our code against divergence errors, we use the Dedner cleaning approach with a globally constant cleaning speed equal to the largest signal speed in the simulation. While in unstratified simulations the box is on average homogeneous and the differences in the signal speeds are smaller, this changes in stratified simulations. Here the corona is magnetically dominated and therefore the maximum signal speed is much larger than the typical sound speed (see Fig. 3.19). On the one hand, this leads to a stronger than required

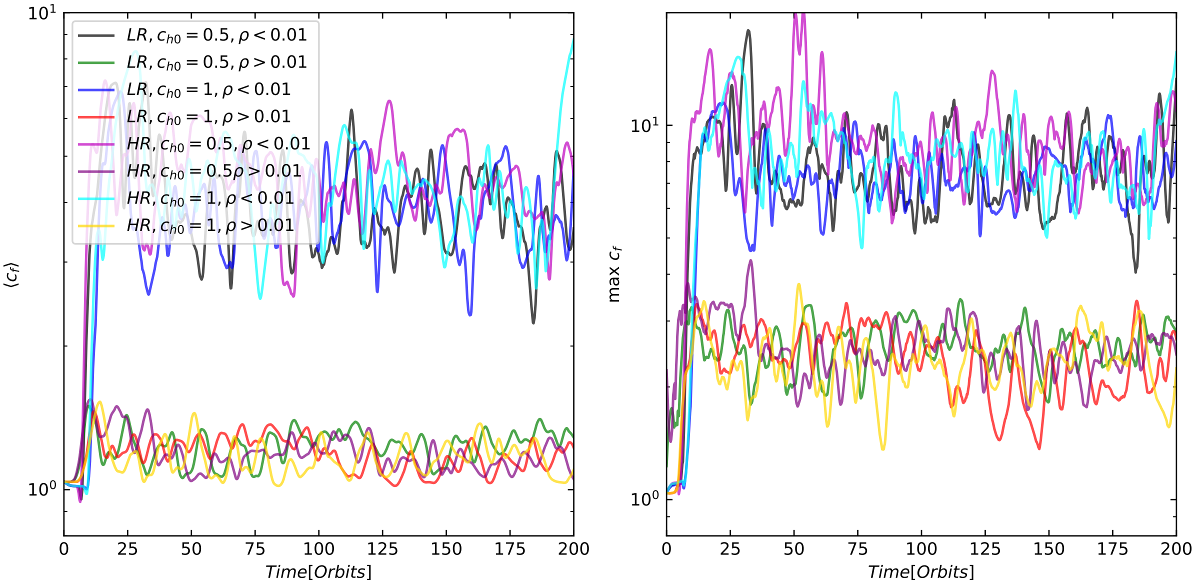

Figure 3.19: Temporal evolution of the volume-averaged (left) and maximum (right) signal speed (see equation 3.12) for our simulations in a stratified shearing box. We split the gas into a low-density component and a high-density component that resides close to the mid-plane. The maximum signal speed is a factor of around 3 larger in the low-density region compared to the high-density region, and around 8 times higher than the average signal speed in the high-density regions. Since the former sets the cleaning speed of the Dedner cleaning, our scheme applies a much stronger cleaning in the high-density region than is in principle required locally. For visual clarity, we have smoothed the curves over 4 orbits using a Savitzky–Golay filter.

cleaning in the mid-plane, and therefore larger numerical resistivity and a weaker MRI. On the other hand, this also leads to smaller time steps in the mid-plane, which makes such simulations more expensive. We therefore plan to implement alternative cleaning methods in future work (Tricco et al., 2016; Hopkins, 2016) that only require a local cleaning speed in the moving-mesh case. We also note that for global disk simulations we can revert to the standard Powell cleaning in AREPO, which does not suffer from those disadvantages.

Especially when we compare the resolution of our simulations with the one from static grid codes, we have to note that for our moving-mesh code the computational costs per resolution element are much larger for pure MHD simulations. Additional time has to be spent on the construction of the Voronoi mesh and on average cells have more faces than in a Cartesian grid which means there are more Riemann problems to solve. The unstructured mesh requires the more expensive higher order flux integration introduced in Zier & Springel (2022a) and also reduces the efficiency of memory accesses. Particle methods suffer from similar overhead and we, therefore, expect similar performance. As Deng et al. (2019) already noted the performance differences are highly problem dependent and if additional physical effects such as self-gravity dominate the total computational costs, the moving-mesh method will become more competitive in comparison to static grid codes.

Our main results can be summarized as follows:

- We find close to third order convergence for linear growth rates of channel modes with absolute errors almost identical to results obtained with ATHENA.
- The strength of the saturated state of the MRI decreases with stronger numerical resistivity (larger cleaning speed) but deviations from $\nabla \cdot \boldsymbol{B}$ also decrease.
- In unstratified NF simulations the MRI does not die out even for strong cleaning and low resolution.
- In small, unstratified ZNF simulations the MRI can die out for strong cleaning. The strength of the MRI however increases with higher resolution in contrast to results from static grid codes.
- In large, unstratified ZNF simulations we find a large-scale mean-field dynamo (in agreement with Shi et al., 2016) and an active shear current effect. The former is significantly weaker in SPH simulations presented by Wissing et al. (2022), which could be caused by a missing shear current effect in those simulations.
- We find the characteristic butterfly diagram in stratified simulations and can sustain turbulence for at least 200 orbits. The qualitative results compare well with previous results in the literature, though our MRI is a bit weaker. We attribute this to a too strong cleaning in the mid-plane due to a globally constant Dedner cleaning speed.

All in all, our results confirm the high accuracy of our moving-mesh approach for demanding simulations such as MRI-driven turbulence in accretion disks. Our results show

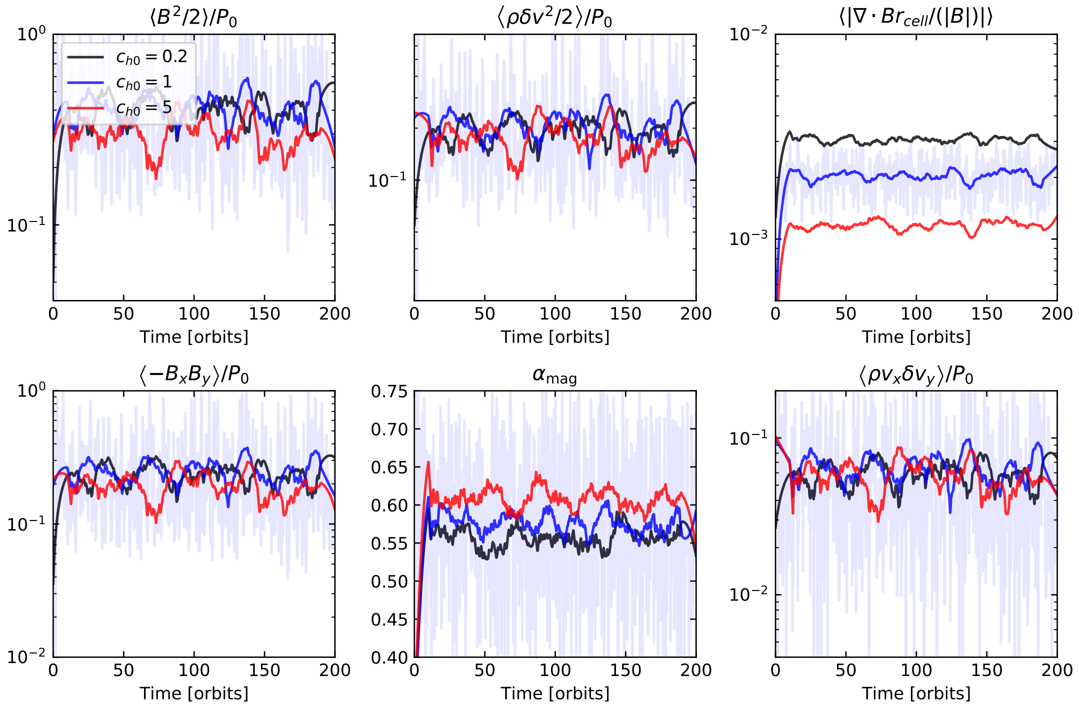

Figure 3.20: The temporal evolution of several volume weighted quantities for unstratified simulations with a net vertical magnetic field, for a box size $1\times4\times1$ and 48 cells per scale height. We vary the strength of the Dedner cleaning c_{h0}, as indicated in the legend. The shown quantities are (from left to right, and top to bottom): Magnetic field energy density, kinetic energy density, relative $\nabla\cdot\boldsymbol{B}$ error, Maxwell stress, normalized Maxwell stress (3.18) and Reynolds stress. We have smoothed the curves over 20 orbits using a Savitzky–Golay filter for visual clarity, and show the original curve for one example as a transparent line.

reassuring consistency with mesh-based findings, although the relatively high numerical resistivity of the Dedner cleaning approach compared to constrained transport approaches shows up in some of our results. However, our method is readily applicable and well adjusted to global disk simulations, where it represents a very competitive alternative to Eulerian mesh codes. Unlike in the shearing box case, in such simulations we can furthermore employ the Powell scheme for divergence control in our code, which is significantly less diffusive. It thus appears promising to consider full accretion disk calculations that account for the MRI with AREPO in future work.

3.6 Appendix: Net flux MRI in unstratified, smaller box

In this appendix, we show additional results for unstratified simulations with box size $L_x\times L_y\times L_z=1\times4\times1$, a standard resolution of $16\times64\times16$ cells, and initial plasma

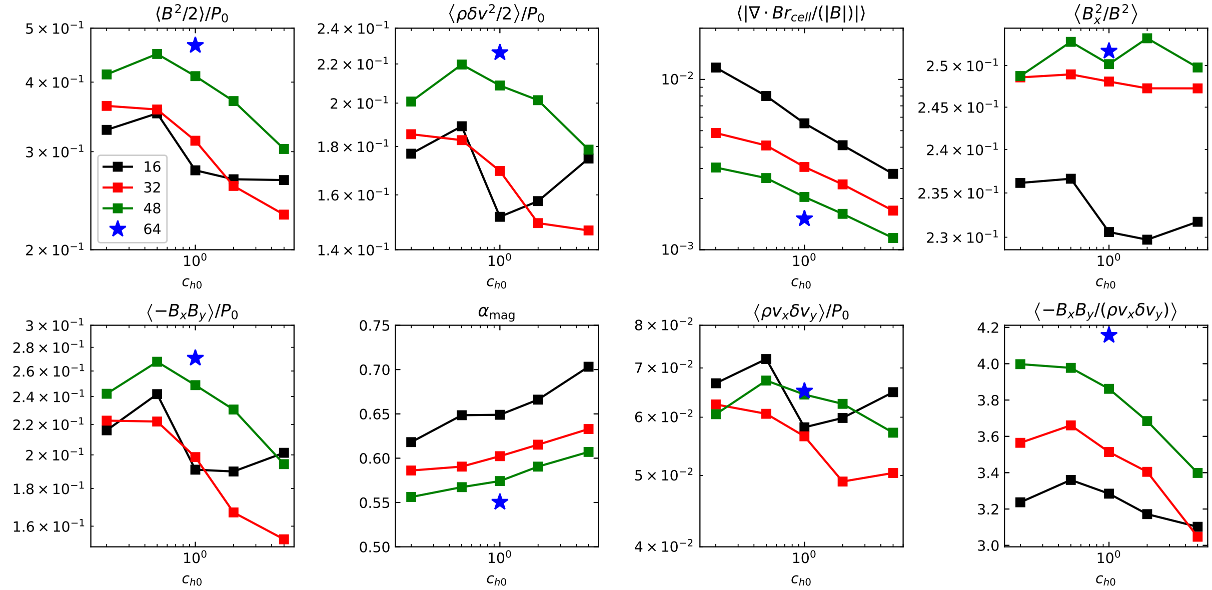

Figure 3.21: The temporal average of different quantities for unstratified simulations with a net vertical magnetic field and box size $1\times4\times1$, as a function of the strength c_{h0} of the Dedner cleaning. All quantities are averaged over 150 orbits starting after 50 orbits. We also vary the resolution by using 16, 32, 48 and 64 cells per scale height, as indicated in the legend. For the highest resolution we only performed one simulation with $c_{h0}=1$ due to the high computational cost of the corresponding run. Besides the quantities already displayed in Fig. 3.20, we also give the ratio between radial and total magnetic field energy (top right), and the ratio of the Maxwell and Reynolds stress (bottom right).

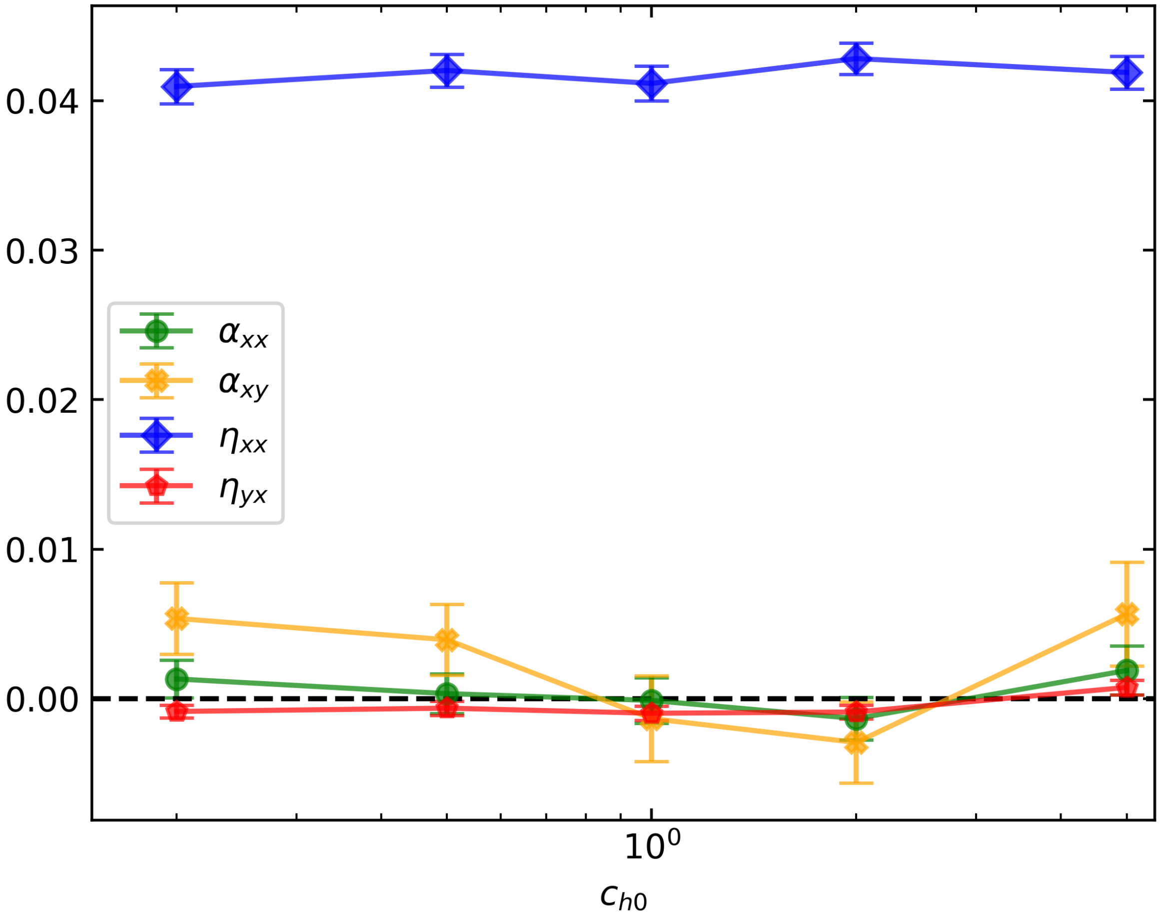

Figure 3.22: Temporally and spatially averaged transport coefficients as a function of the cleaning strength c_{h0} for unstratified simulations with background field, 48 cells per scale height resolution, and a box size $L_x \times L_y \times L_z = 1 \times 4 \times 1$. The coefficients are averaged over a period of 150 orbits starting after 50 orbits. We additionally included the statistical error of the mean value for each coefficient. As expected, η_{xx} is the only coefficient differing significantly from zero.

beta $\beta = 330$. In Fig. 3.20, we show the temporal evolution for three different cleaning strengths c_{h0} and a resolution of 48 cells per scale height. In Fig. 3.21, we show different spatially and temporally averaged properties describing the MRI as a function of c_{h0} for different resolutions. Fig. 3.22 shows the measured transport coefficients as a function of the cleaning strength. As in the larger box all coefficients except η_{xx} are compatible with zero.

Chapter 4

Gravito-turbulence in local disk simulations with an adaptive moving mesh

This work has been accepted for publication in the Monthly Notices of the Royal Astronomical Society.

Self-gravity plays an important role in the evolution of rotationally supported systems such as protoplanetary disks, accretion disks around black holes, or galactic disks, as it can both feed turbulence or lead to gravitational fragmentation. While such systems can be studied in the shearing box approximation with high local resolution, the large density contrasts that are possible in the case of fragmentation still limit the utility of Eulerian codes with constant spatial resolution. In this chapter, we present a novel self-gravity solver for the shearing box based on the TreePM method of the moving-mesh code AREPO. The spatial gravitational resolution is adaptive which is important to make full use of the quasi-Lagrangian hydrodynamical resolution of the code. We apply our new implementation to two- and three-dimensional, self-gravitating disks combined with a simple β-cooling prescription. For weak cooling we find a steady, gravito-turbulent state, while for strong cooling the formation of fragments is inevitable. To reach convergence for the critical cooling efficiency above which fragmentation occurs, we require a smoothing of the gravitational force in the two dimensional case that mimics the stratification of the three-dimensional simulations. The critical cooling efficiency we find, $\beta \approx 3$, as well as box-averaged quantities characterizing the gravito-turbulent state, agree well with various previous results in the literature. Interestingly, we observe stochastic fragmentation for $\beta > 3$, which slightly decreases the cooling efficiency required to observe fragmentation over the lifetime of a protoplanetary disk. The numerical method outlined here appears well suited to study the problem of galactic disks as well as magnetized, self-gravitating disks.

4.1 Introduction

Galactic disks, but also young protoplanetary disks as well as active galactic nuclei (AGN), are examples of self-gravitating disks. Their stability can be described by the Toomre parameter

$$Q = \frac{c_s \kappa}{\pi G \Sigma}, \tag{4.1}$$

with instability to axisymmetric perturbations expected for $Q < 1$ (Toomre, 1964) in razor thin disks. κ is here the epicyclic frequency (equal to the orbital frequency Ω for a circular Keplerian orbit), c_s is the sound speed, G is the gravitational constant, and Σ is the surface density. This gravitational instability (GI) becomes therefore important in cold and massive disks (Kratter & Lodato, 2016).

Already for Q slightly larger than unity disks typically become unstable to non-axisymmetric perturbations (Lau & Bertin, 1978; Papaloizou & Lin, 1989; Papaloizou & Savonije, 1991), which then heat the disk through the dissipation of spiral shocks (Cossins et al., 2009), thus increasing the Toomre Q. If radiative cooling is present in the system, the combination of heating and cooling can effectively yield an equilibrium with a so-called gravito-turbulent state where $Q = O(1)$ (Gammie, 2001; Shi & Chiang, 2014). This gravito-turbulent state can give rise to an effective viscosity, transporting angular momentum outwards, as required for accretion (Armitage, 2011; Turner et al., 2014). If the cooling is too strong the gravito-turbulent state is not able to generate enough heat, and the disk continues to cool. This leads to the formation of fragments, which could be, for example, an efficient way to form brown dwarfs, giants planets at large radii or binary stars (Boss, 1997; Kratter & Matzner, 2006; Stamatellos & Whitworth, 2009; Helled et al., 2014; Tobin et al., 2016).

To cleanly analyze the probability of the latter process, typically a simplified cooling description with a constant cooling time $t_{\mathrm{cool}} = \beta\,\Omega^{-1}$ and a free parameter β is used (Gammie, 2001). We note that some studies also employ a modified version of this law, taking into account stellar irradiation (Rice et al., 2011; Baehr & Klahr, 2015; Löhnert et al., 2020) or even radiative transfer (Hirose & Shi, 2019). Besides the analysis of the gravito-turbulent state as a function of β and the interaction of the GI with other instabilities such as the magnetorotational instability (MRI, Riols & Latter, 2018; Löhnert & Peeters, 2022), an important question is below which threshold value β_c the disk starts to fragment.

To answer this question, both global as well as local simulations of a small rectangular box with high resolution orbiting with the local rotational frequency (the so-called shearing box approximation, Hill, 1878; Goldreich & Lynden-Bell, 1965) have been performed in the literature. While the first approach allows capturing global behaviour like accretion, the second method allows for a higher resolution. Riols et al. (2017) found long term trends in small shearing boxes, while Booth & Clarke (2019) argued that a box size of $L > 64H$ in the horizontal direction is required to avoid spurious bursts. Although the bursts observed in smaller boxes might also occur for massive disks in global simulations (Rice et al., 2005), the apparent dependence of the shearing box results on the box size complicates their interpretation and direct application.

Gammie (2001) found in local, two-dimensional simulations $\beta_c \approx 3$ and showed that for an equilibrium state the total stress α (Shakura & Sunyaev, 1973) only depends on β and the adiabatic index γ:

$$\alpha = \frac{4}{9\gamma\,(\gamma-1)\,\beta}. \tag{4.2}$$

$\beta_c = 3$ therefore translates for $\gamma = 2$ to a maximum stress of $\alpha_{\max} \approx 0.07$ that a disk can sustain. The $\gamma = 2$ in 2D can be mapped in the low-frequency limit to $\gamma = 5/3$ for a non-self-gravitating disk and $\gamma = 2$ for a self-gravitating disk in 3D (Gammie, 2001). Meru & Bate (2011) found in global simulations with SPH that β_c increases with resolution and thus was not converged. Similar results were found in local two-dimensional simulations (Paardekooper, 2012; Baehr & Klahr, 2015; Klee et al., 2017). Furthermore, there seems to be a stochastic component involved (Paardekooper, 2012; Young & Clarke, 2015). For a gravito-turbulent state it was found that stochastic density fluctuations can produce over-densities that can collapse (Hopkins & Christiansen, 2013). This so-called stochastic fragmentation allows fragmentation at arbitrary high β, although this might become irrelevant if the probability for it to occur decreases fast enough for increasing β. Similar results were found by Brucy & Hennebelle (2021) in global simulations with the RAMSES code. As we will discuss further in Section 4.5.3, we expect $\beta \propto R_0^{-9/2}$ in the outer parts of protoplanetary disks (Paardekooper, 2012). This implies that only if stochastic fragmentation can significantly increase β_c it has an influence on the expected radius at which fragmentation can occur.

Deng et al. (2017) in contrast found convergence with the MFM method in 3D and obtained $\beta_c \approx 3 - 3.5$ in global simulations, which they attributed to the missing artificial viscosity in this method. Lately, also three-dimensional local simulation reported convergence (Baehr et al., 2017; Booth & Clarke, 2019) with $\beta_c \approx 3$. Booth & Clarke (2019) also found sometimes fragmentation for $\beta = 3 - 5$, and attributed this to stochastic fragmentation, although no fragmentation was observed for larger β. Klee et al. (2019) claims to be close to convergence in high-resolution two-dimensional simulations with $\beta_c \approx 10$.

All studies that found converged results had in common that they started with so-called relaxed initial conditions, which means that instead of a smooth initial state an already gravito-turbulent state obtained with simulations with higher β or lower resolution was adopted. Otherwise, the disk might cool too fast before gravito-turbulence as a heating source can set in and prevent prompt fragmentation (Paardekooper et al., 2011; Deng et al., 2017; Booth & Clarke, 2019). Convergence seems easier to achieve in three-dimensional simulations, which might be attributed to the implicit smoothing of gravitational forces over a scale height in 3D. Young & Clarke (2015) showed in two-dimensional shearing box simulations that an explicit smoothing of the gravitational potential over one scale height allows again convergence with $\beta_c \approx 3$. It was argued that with this smoothing only the direct fragmentation can be observed while a quasi-static collapse is not possible. But Young & Clarke (2016) showed that even with gravitational softening effects such as stochastic fragmentation can still be observed. Another important point affecting convergence seems to be the accuracy of the numerical method. For example, Deng et al. (2017) point out that the artificial viscosity in SPH could prevent convergence while Klee et al. (2017) argued that the limiter in finite volume methods can influence the results.

The goal of this chapter is to analyze the properties of gravito-turbulence and its convergence, and especially the convergence of β_c, with the moving-mesh code AREPO (Springel, 2010a; Pakmor et al., 2016b; Weinberger et al., 2020) that combines the advantage of a Lagrangian method with the high-accuracy of finite volume methods. In contrast to SPH, it does not require artificial viscosity, and in contrast to static grid codes, it automatically increases the spatial resolution in dense regions, which makes it especially suited to study the formation of fragments. To further increase the resolution and the numerical accuracy, we furthermore make use of the recent implementation of the shearing box approximation described in Zier & Springel (2022a), which was already applied successfully to the magnetorotational instability (Zier & Springel, 2022b). Applying this new numerical methodology to the problem can help to resolve the remaining discrepancies in the literature, and thus hopefully contribute to an emerging, increasingly firm understanding of the gravito-turbulent state and its fragmentation boundary.

This chapter is structured as follows: In Section 4.2, we introduce the moving mesh method and especially the shearing box approximation as implemented in the AREPO code. We also describe a new solver for the Poisson equation based on the TreePM method and introduce different quantities we will subsequently use to characterize the nonlinear, saturated state of the gravitational instability. In Section 4.3, we discuss two-dimensional shearing box simulations. We analyze the dependency of the saturated gravito-turbulent state on the box size, resolution, cooling efficiency β, and a smoothing scale to mimic the stratification in three dimensions. Subsequently, we analyze the formation of fragments as a function of the smoothing scale and numerical resolution, and show that β_c itself depends on the smoothing length. In Section 4.4, we repeat this analysis using full three-dimensional simulations. We find a good match between two- and three-dimensional simulations, with $\beta_c \approx 3$, if we smooth in the former the gravitational force over half a scale-height, but due to stochastic fragmentation we find fragments up to $\beta = 5$. In Section 4.5, we discuss the advantages of the moving-mesh method with self-gravity when applied to this problem. We compare the results of two- and three-dimensional simulations, and we comment on the implications of stochastic fragmentation for the direct formation of massive planets through disk instabilities. Finally, in Section 4.6 we summarize our results.

4.2 Methods

4.2.1 Shearing box approximation in three dimensions

The equations for the shearing box approximation (Hill, 1878; Goldreich & Lynden-Bell, 1965) can be obtained by transforming into a frame rotating with the local angular frequency Ω at a radius R_0. The resulting centrifugal and gravitational forces are then expanded to first order in the local Cartesian coordinates, x (radial direction), y (azimuthal direction), and z (standard z-coordinate of cylindrical coordinates). The resulting equations in three dimensions can be written as:

$$\frac{\partial \boldsymbol{U}}{\partial t} + \nabla \cdot \boldsymbol{F}(\boldsymbol{U}) = \boldsymbol{S}_{\mathrm{grav,e}} + \boldsymbol{S}_{\mathrm{cor}} + \boldsymbol{S}_{\mathrm{grav,self}} + \dot{Q}. \tag{4.3}$$

Here, we introduced a vector of conserved quantities $\boldsymbol{U}$, the flux function $\boldsymbol{F}$, the source term $\boldsymbol{S}_{\mathrm{grav,e}}$ due to the external gravitational and centrifugal force, the source term $\boldsymbol{S}_{\mathrm{cor}}$ due to the Coriolis force, and the source term $\boldsymbol{S}_{\mathrm{grav,self}}$ describing the self-gravity of the gas. Finally, $\dot{Q}$ describes an external cooling term. The full equations are given by:

$$\boldsymbol{U} = \begin{pmatrix} \rho \\ \rho \boldsymbol{v} \\ \rho e \end{pmatrix}, \quad F(\boldsymbol{U}) = \begin{pmatrix} \rho \boldsymbol{v} \\ \rho \boldsymbol{v}\boldsymbol{v}^T + P \\ \rho e \boldsymbol{v} + P\boldsymbol{v} \end{pmatrix}, \tag{4.4}$$

$$\boldsymbol{S}_{\mathrm{grav,e}} = \begin{pmatrix} 0 \\ \rho \Omega_0^2 \left(2qx\hat{e}_x - z\hat{e}_z\right) \\ \rho \Omega_0^2 \boldsymbol{v} \cdot \left(2qx\hat{e}_x - z\hat{e}_z\right) \end{pmatrix}, \tag{4.5}$$

$$\boldsymbol{S}_{\mathrm{cor}} = \begin{pmatrix} 0 \\ -2\rho\Omega_0 \hat{e}_z \times \boldsymbol{v} \\ 0 \end{pmatrix}, \quad \boldsymbol{S}_{\mathrm{grav,self}} = \begin{pmatrix} 0 \\ -\rho \nabla \phi \\ -\rho \left(\boldsymbol{v} \cdot \nabla \phi\right) \end{pmatrix}, \tag{4.6}$$

where ρ, $\boldsymbol{v}$, e, ϕ, and P are the density, velocity, total energy per unit mass, gravitational potential, and pressure, respectively.

The energy density $e = u + \frac{1}{2}\boldsymbol{v}^2$ consists of a thermal component u and a kinetic component $\frac{1}{2}\boldsymbol{v}^2$. The cooling term only modifies the total energy, and we choose

$$\dot{Q} = (0, 0, -u\rho/t_c), \tag{4.7}$$

with $t_c = \beta/\Omega$. Here, β is a global constant that can be used to modify the cooling efficiency. We note that some studies add a temperature floor to the cooling description by replacing u by $u - u_{\mathrm{floor}}$ (Rice et al., 2011; Lin & Kratter, 2016). The temperature floor increases the pressure support for strong cooling and therefore can stabilize small scale perturbations. The system of equations is closed by the equation of state (EOS), which describes the pressure as a function of other thermodynamical quantities. In this chapter, we use an adiabatic EOS

$$P = \rho u(\gamma - 1), \tag{4.8}$$

with adiabatic coefficient $\gamma = 5/3$ that also defines the sound speed:

$$c_s = \sqrt{\gamma P/\rho}. \tag{4.9}$$

$\boldsymbol{S}_{\mathrm{grav,e}}$ depends on the shearing parameter

$$q = -\frac{d\ln\Omega}{d\ln r}, \tag{4.10}$$

which simplifies to $q = 3/2$ for the Keplerian case that we exclusively discuss in this chapter. $\boldsymbol{S}_{\mathrm{grav,e}}$ contains a vertical component that leads to a stratification of the disk.

The gravitational potential ϕ can be calculated by solving the Poisson equation

$$\nabla^2\phi = 4\pi G\rho, \tag{4.11}$$

with the gravitational constant G. We will discuss our solver for this further in Section 4.2.3. For a velocity field

$$\boldsymbol{v} = (0, -q\Omega_0 x, 0), \tag{4.12}$$

the x- and y-components of $\boldsymbol{S}_{\mathrm{grav,e}} + \boldsymbol{S}_{\mathrm{cor}}$ vanish, and therefore this field corresponds to a ground state solution.

To solve equation (4.3) we employ the hydrodynamical code AREPO (Springel, 2010a; Pakmor et al., 2016b; Weinberger et al., 2020), which uses a moving, unstructured Voronoi mesh in combination with the finite volume method. We refer to Zier & Springel (2022a) for the details of the shearing box implementation without self-gravity in this code. For all simulations, we use a higher-order integration method for the flux as well as a second-order accurate Runge-Kutta time integration scheme. Although the moving mesh method is quasi-Lagrangian, the mass per cell can vary significantly over time. To ensure an approximate constant mass resolution, we therefore allow cells to be split (refined) and merged (derefinement) if they fulfil special conditions.

In all simulations considered here, we define a target mass m_{target} and in general refine (derefine) cells with mass $m > 2\,m_{\mathrm{target}}$ ($m < 0.5\,m_{\mathrm{target}}$). To avoid too rapid local variations in the spatial resolution in three-dimensional simulations, we impose a maximum allowed volume ratio of 10 between adjacent cells, and enforce a maximum volume of $0.1H^3$ per cell. The volume-based conditions become especially important in the low-density halo of the disk, and help to avoid that a cell can interact with a periodic image of itself in regions of extremely low density.

4.2.2 Boundary conditions

In the following, we will assume a box of size $L_x \times L_y \times L_z$. In the y- and the z-direction we use periodic boundary conditions (BCs):

$$f(x, y, z, t) = f(x, y \pm L_y, z \pm L_z, t) \tag{4.13}$$

for all hydrodynamic quantities $f \in \{\rho, v_x, v_y, v_z\}$. For the gravitational potential ϕ we assume periodic BCs in the y-direction and vacuum boundary conditions in the z-direction. We note that we could also use potentially more physical inflow-outflow BCs in the z-direction for the hydrodynamic quantities, but by using large enough boxes in the z-direction combined with the lack of significant outflows this should not affect our results while simplifying the numerics.

In the x-direction the standard periodic boundary conditions have to be modified to be compatible with the background flow of Eqn. (4.12):

$$f(x, y, z, t) = f(x \pm L_x, y \mp wt, z, t); \quad f \in \{\rho, \rho v_x, \rho v_z, \phi\}, \tag{4.14a}$$

$$\rho v_y(x,y,z,t) = \rho v_y(x \pm L_x, y \mp wt, z, t) \mp \rho w, \tag{4.14b}$$

$$e(x,y,z,t) = e(x \pm L_x, y \mp wt, z, t) \mp \rho v_y v_w + \frac{\rho w^2}{2}, \tag{4.14c}$$

with $w = q\Omega_0 L_x$. These boundary conditions are called shearing-periodic boundary conditions. In Zier & Springel (2022a) we discuss the implementation of the BCs in the AREPO code, modulo the gravitational potential ϕ, which requires special care and will be discussed in the following.

4.2.3 Self-gravity

To determine the gravitational force on a cell we do not only have to take into account the interactions with other cells in the primary simulation box but also those with the infinite number of periodic replicas of the primary box. It would be very expensive to exactly calculate the gravitational force between three-dimensional Voronoi cells (i.e. taking their detailed geometry into account). We therefore treat them instead as point sources with all their mass concentrated in their centre of mass. This leads to small inaccuracies in the gravitational force between close neighbours but should not influence the main results in this chapter, since the total gravitational force is typically much larger than the errors in the partial forces of close neighbours. For a discussion of these errors we refer to Appendix 4.8.

In the following we concentrate on the case of periodic boundary conditions in the x- and y-directions, and non-periodic BCs in the z-direction, which can easily be generalized to shearing box BCs as discussed below. The gravitational potential can be written as a sum over all Voronoi cells j, with primary position $\vec{x}_j$:

$$\phi(\vec{x}) = -\sum_{j=1}^{N} \sum_{\vec{n}=-\infty}^{\infty} G \left\{ \frac{m_j}{|\vec{x}_j - \vec{x} + \vec{q}_{\vec{n}}| + \epsilon(|\vec{x}_j - \vec{x} + \vec{q}_{\vec{n}}|)} \right\}. \tag{4.15}$$

Here $\vec{q}_{\vec{n}}$ denotes periodic displacement vectors given by $\vec{q}_{\vec{n}} = (n_x L_x, n_y L_y, 0)$, where $\vec{n} = (n_x, n_y)$ are integer pairs, and the sum over $\vec{n}$ extends over all these pairs. ϵ is the gravitational softening length that should only be non-zero for the closest image $\vec{q}_j^{\star} = \vec{q}_j^{\star}(\vec{x})$ that minimizes $|\vec{x}_j - \vec{x} + \vec{q}_j^{\star}|$. This enables us to rewrite the potential as

$$\begin{aligned} \phi(\vec{x}) \quad &= -\textstyle\sum_{j=1}^{N} \frac{m_j}{|\vec{x}_j - \vec{x} + \vec{q}_j^{\star}| + \epsilon(|\vec{x}_j - \vec{x} + \vec{q}_j^{\star}|)} \\ &\quad + \textstyle\sum_{j=1}^{N} m_j \psi(\vec{x}_j - \vec{x} + \vec{q}_j^{\star}), \end{aligned} \tag{4.16}$$

where we have introduced a correction potential given by

$$\psi(\vec{x}) = \frac{1}{|\vec{x}|} - \sum_{\vec{n}=-\infty}^{\infty} \left\{ \frac{1}{|\vec{x} + \vec{q}_{\vec{n}}|} \right\}. \tag{4.17}$$

For our boundary conditions, this slowly converging sum can be rewritten as (Grzybowski et al., 2000; Springel et al., 2021):

$$\begin{aligned}\psi(\vec{r}) \;=\; & \frac{1}{|\vec{r}|} + \frac{2\alpha}{\sqrt{\pi}} - \sum_{\vec{\tilde{p}}} \frac{\operatorname{erfc}(\alpha|\vec{r}-\vec{\tilde{p}}|)}{|\vec{r}-\vec{\tilde{p}}|} \\ & - \frac{\pi}{L_x L_y} \sum_{\vec{k}\neq 0} \frac{\exp\left(i\,\vec{k}\cdot\vec{r}\right)}{|\vec{k}|} \left[\exp(kz)\operatorname{erfc}\left(\frac{k}{2\alpha}+\alpha z\right)\right. \\ & \left. + \exp(-kz)\operatorname{erfc}\left(\frac{k}{2\alpha}-\alpha z\right)\right] \\ & + \frac{2\sqrt{\pi}}{L_x L_y}\left(\frac{\exp(-\alpha^2 z^2)}{\alpha} + \sqrt{\pi}\, z \operatorname{erf}(\alpha z)\right), \end{aligned} \tag{4.18}$$

with $\vec{r} = (x, y, z)$, and $\vec{k} = 2\pi(n_x/L_x, n_y/L_y, 0)$ with integer pairs (n_x, n_y), and α being an arbitrary positive number. The first sum over all periodic images converges fast in real space due to the fast decay of the *erfc*-function, and we can use the standard Barnes-Hut tree as implemented already in the code for the standard TreePM method (Springel, 2010a; Weinberger et al., 2020) to compute it. The remaining terms can be calculated in Fourier space by multiplying the Fourier-transformed density with the appropriate Green's function. We determine the Green's function in Fourier space by first setting it up in real space with zero padding in the z-direction, and then transforming it to k-space. Our implementation closely follows that in the public GADGET-4 code of Springel et al. (2021).

Shearing box boundary conditions

For the shearing periodic BCs, ϕ is invariant under coordinate transformations of the form:

$$\Delta \boldsymbol{x} = n_x \begin{pmatrix} L_x \\ q\Omega L_x t \end{pmatrix} + n_y \begin{pmatrix} 0 \\ L_y \end{pmatrix} = n_x \boldsymbol{a}_1 + n_y \boldsymbol{a}_2, \tag{4.19}$$

with integers n_x and n_y. The corresponding wavevectors can be written as

$$\boldsymbol{k} = n_x \frac{2\pi}{L_x} + n_y \frac{2\pi}{L_y} \begin{pmatrix} -q\Omega t \\ 1 \end{pmatrix} = 2\pi \begin{pmatrix} n_x/L_x \\ n_y/L_y \end{pmatrix} - \begin{pmatrix} q\Omega t k_y \\ 0 \end{pmatrix}, \tag{4.20}$$

where the last term is the correction for the background shear flow. In this case equation (4.18) is still valid[1], but the correction term has to be added in the calculation of $|k|$.

In order to still be able to use a standard FFT the density distribution $\rho(x, y, z)$ has to be replaced by $\rho(x, y + \Delta y, z)$ before the FFT, and ϕ has to be shifted by $-\Delta y$ in

---

[1] All steps in the deviation in Grzybowski et al. (2000) are independent of the periodicity except the Poisson summation formula. Kholopov (2007) proves that this equation also holds for non-orthogonal periodicity, the so-called Krazer–Prym formula.

the y-direction after the inverse FFT. $\Delta y = q\Omega x(t - t^{*})$ depends here on the time t^{*} when the system was periodic in the x-direction the last time. This idea was initially introduced in two-dimensional simulations by Gammie (2001) and is used since then as the default method for self-gravity in shearing boxes. As mentioned before, we use the TreePM method to calculate the gravitational potential, which means that we split the potential into a short-range component that can be calculated with a tree while the long-range force can be calculated with the PM method. For the latter case, we can absorb the shift in the y-direction for the density into the binning process of the Voronoi cells onto the uniform PM grid, while we can first calculate the gravitational force for each Voronoi cell in periodic coordinates and then add the correction term $\Delta a_x = \Omega q(t - t^{*})a_y$ to the radial component of the acceleration. We note that the Green's function in real space is a function of $\boldsymbol{k}$, which means that it is time-dependent for the shearing box. To avoid the computational costs of setting up the Green's function in each time step in real space, followed by a Fourier transform, we could also tabulate the Fourier transform of the Green's function in Fourier space for a set of different times and interpolate from it. However, since in our experiments the costs of the PM part are small we do not use this optimization in this study.

4.2.4 Thin disk approximation in two dimensions

By defining the surface density

$$\Sigma\left(x,y\right) = \int_{-\infty}^{\infty} \rho(x,y,z)\,\mathrm{d}z, \tag{4.21}$$

we can approximate the density as

$$\rho(x,y,z) = \Sigma\left(x,y\right)\delta\left(z\right) \tag{4.22}$$

for thin disks. To approximate a three-dimensional stratification we can furthermore smooth the Poisson equation with a smoothing length λ (Paardekooper, 2012; Young & Clarke, 2015):

$$\nabla^2\phi = 4\pi G\Sigma\delta(z-\lambda). \tag{4.23}$$

λ should be of the order of a scale height, such that forces and structures below λ are suppressed. This approximation simplifies the dynamics by turning it into a two-dimensional problem for $\Sigma(x,y)$, which significantly reduces the computational costs in comparison to three-dimensional simulations. To apply it, we have to replace ρ by Σ in equation (4.3) - (4.6), and remove the gravitational term in the z-direction. The calculation of the gravitational potential also simplifies, since we can set $z = \lambda$ in equation (4.18). Also, a pure PM method is sufficient to solve the Poisson equation with high enough resolution.

4.2.5 Analysis methods

To analyze the stochastic behaviour of gravito-turbulence we define the volume-weighted average of a quantity X as:

$$\langle X \rangle = \frac{\int X \, \mathrm{d}V}{\int \mathrm{d}V}, \tag{4.24}$$

and the density-weighted average as:

$$\langle X \rangle_w = \frac{\int \rho X \, \mathrm{d}V}{\int \rho \, \mathrm{d}V}, \tag{4.25}$$

the average per unit area:

$$\langle X \rangle_A = \frac{\int X \, \mathrm{d}V}{\int \mathrm{d}V} L_z, \tag{4.26}$$

as well as the temporal average of X:

$$\langle X \rangle_t = \frac{\int X \mathrm{d}t}{\int \mathrm{d}t}. \tag{4.27}$$

To characterize the stability of the disk we use the two-dimensional Toomre number:

$$Q = \frac{\langle c_s^2 \rangle_w^{1/2} \Omega}{\pi G \langle \Sigma \rangle}, \tag{4.28}$$

where $\langle \Sigma \rangle = L_z \langle \rho \rangle$ is its average surface density. The density-weighted r.m.s. sound speed $\langle c_s^2 \rangle_w^{1/2}$ we use here is typically a few per cent larger than the average sound speed $\langle c_s \rangle_w$ (Booth & Clarke, 2019). The total angular momentum transfer can be described by the total stress α, which is defined as a combination of the Reynold stress H_{xy} and the gravitational stress G_{xy}:

$$\alpha = \frac{2}{3\gamma \langle P \rangle} \langle H_{xy} + G_{xy} \rangle . \tag{4.29}$$

They are given by

$$H_{xy} = \rho v_x \delta v_y \tag{4.30}$$

and

$$G_{xy} = \frac{1}{4\pi G} \frac{\partial \Phi}{\partial x} \frac{\partial \Phi}{\partial y}, \tag{4.31}$$

respectively, where δv_y is the deviation of the azimuthal velocity from the ground state (4.12). While in two dimensions the volume average simplifies to a two-dimensional integral for H_{xy}, we still require for G_{xy} the calculation of a three-dimensional integral:

$$\langle G_{xy} \rangle_{2d} = \left\langle \int_{z=-\infty}^{z=\infty} G_{xy} \right\rangle_{xy} = \sum_{\boldsymbol{k}} \frac{\pi G k_x k_y \left| \Sigma_{\boldsymbol{k}} \right|^2}{\left| \boldsymbol{k} \right|^3}. \tag{4.32}$$

We calculate the Fourier sum (Gammie, 2001) with the same algorithm we use for the PM gravity calculation, and set the density of the PM mesh equal to the initial number of cells. The radial flux of angular momentum is the only heating source in the system, and thus it has to counterbalance the cooling. This leads to the condition:

$$\alpha = \frac{4}{9\gamma\left(\gamma - 1\right)\beta}, \tag{4.33}$$

which has to be fulfilled if the system is in equilibrium (Gammie, 2001). Additionally, we define the kinetic, $e_{\mathrm{kin}} = \frac{1}{2}\rho \boldsymbol{v}^2$, and thermal energy densities, $e_{\mathrm{th}} = P/\left(\gamma - 1\right)$.

4.2.6 Fragmentation criterion

To decide if a self-gravitating disk is stable it is essential to first define what a fragment is. The detailed criteria differ in the literature, and there are also differences between two and three-dimensional simulations, but the indicators typically have in common that a fragment should be self-gravitating and survive for a specific amount of time. Most studies in two dimensions demand an overdensity of 100 and a survival time of several orbits (Meru & Bate, 2011; Rice et al., 2011; Paardekooper, 2012), though Baehr & Klahr (2015) required the surface density to be above the Roche surface density $\Sigma_{\mathrm{Roche}} = 7c_s^2/\left(HG\right)$.

The Roche surface density is typically equivalent to an overdensity of $O(100)$ (Baehr & Klahr, 2015) and therefore leads to similar results. In three-dimensional simulations, Deng et al. (2017) required an overdensity of 100 and survival for one orbit while Brucy & Hennebelle (2021) showed that combining the two criteria of an overdensity of 30 in the surface density and explicit gravitational boundedness lead to similar results. In most of our simulations, the formation of a fragment leads to a runaway collapse, which means the (surface) density will drastically increase in a short amount of time. In this case, the threshold density for a fragment only has a minor influence and we, therefore, use an overdensity of 100 in two and three-dimensional simulations as a threshold for identifying fragmentation. If the density decreases later and the fragments get destroyed, we call those transient fragments and label the corresponding simulation with a 'T'. In contrast, if the overdensity of 100 survives for more than 5 orbits we call the simulation fragmented.

4.2.7 Initial conditions and overview of simulations

We measure times in units of Ω^{-1}, lengths in units of

$$H = \frac{\pi G \Sigma}{\Omega^2}, \tag{4.34}$$

and use in all simulations $\Sigma = 1$. Those choices imply $G = 1/\pi$ in code units and

$$H_p = QH \tag{4.35}$$

for the pressure scale height H_p. This means that H is equivalent to the pressure scale height for a Toomre parameter $Q = 1$, and the orbital time is $2\pi\Omega^{-1}$.

While in two dimensions setting up initial conditions in equilibrium is trivial, we have to choose the vertical structure of the temperature profile in stratified simulations. We follow the method from Riols et al. (2017) by assuming the vertical profile to be polytropic $P = K\rho^\gamma$. The constant $K = c_{s_0}^2/\left(\gamma\rho_0^{\gamma-1}\right)$ depends on the sound speed c_{s_0} and density ρ_0 in the mid plane. The equations describing hydrostatic equilibrium are given by:

$$K\left[\frac{1}{\rho}\frac{\mathrm{d}\rho^\gamma}{\mathrm{d}z}\right] + z\Omega^2 + \frac{\mathrm{d}\Phi}{\mathrm{d}z} = 0, \tag{4.36}$$

$$\frac{\mathrm{d}^2\Phi}{\mathrm{d}z^2} = 4\pi G\rho, \tag{4.37}$$

which we discuss further in Appendix 4.7.2. We use an initial Toomre $Q = 1$, and for three dimensional simulations first evolve the system for $10\,\Omega^{-1}$ without cooling so that through refinement and derefinement operations a stable mesh configuration can form. We check that the vertical profile does not change during this time. Afterwards, we add noise with a maximum amplitude $0.05\,c_{s_0}$ to each component of the ground state velocity (4.12) for each cell to seed the instability and start cooling.

The gravitational instability takes a finite amount of time to become active. In the meantime, the disk can cool down further and might trigger prompt fragmentation. Therefore, in many studies so-called relaxed initial conditions with already formed gravito-turbulence were used (Paardekooper et al., 2011; Deng et al., 2017; Booth & Clarke, 2019). Since the prompt fragmentation is resolution-dependent (see Section 4.4.3) and a higher resolution promotes easier fragmentation, we typically first simulate gravito-turbulence for a low resolution. We then use the final snapshot and reduce the target mass resolution setting, m_target, which causes the code to split cells until the requested resolution is achieved. Since in some cases we have also used the final snapshots from simulations with larger β, we will mention explicitly for each simulation which method has been used. In Table 4.1 and Table 4.3 we give an overview of all two-dimensional and three-dimensional simulations we have carried out.

4.3 Gravitational instability in two dimensions

In this section, we first perform two-dimensional simulations in a shearing box of size $L \times L$ using the thin disk approximation discussed in Section 4.2.4. As we have mentioned before we allow for a smoothing scale λ (see equation 4.23) to mimic vertical stratification. For $\lambda = 0$, arbitrary small structures are allowed to collapse if there is no implicit smoothing such as the binning on a PM grid in our method. We typically use $\lambda = 0.5H$ to analyze the gravito-turbulent state but we note that in the literature a variety of values were employed: Baruteau & Masset (2008) used $\lambda = 0.5H$, Müller et al. (2012) used $\lambda = 0.6H$ while Paardekooper (2012) and Young & Clarke (2015) used $\lambda = 1H$. To better understand the influence of λ on our results we perform a parameter study in Section 4.3.3.

For better comparison of the resolution with other studies, we define the number of cells per scale height $N = [M_\mathrm{tot}/(m_\mathrm{target}L^2)]^{1/2}$, where M_tot is the total mass. As an illustration

Box size	Resolution factors	β	λ	Section
8	1, 2, 4, 8, 16	10	0.5	4.3.1
16	1, 2, 4, 8	10	0.5	4.3.1
32	1, 2, 4, 8	10	0.5	4.3.1
64	1, 2, 4	10	0.5	4.3.1
128	1, 2	10	0.5	4.3.1
32	1, 2, 4, 8	8	0.5	4.3.2
32	1, 2, 4, 8	10	0.5	4.3.2
32	1, 2, 4, 8	15	0.5	4.3.2
32	1, 2, 4, 8	20	0.5	4.3.2
32	1, 2, 4, 8	35	0.5	4.3.2
32	1, 2, 4, 8	50	0.5	4.3.2
32	1, 2, 4, 8	100	0.5	4.3.2
32	1, 2, 4, 8	15	0.125	4.3.3
32	1, 2, 4, 8	15	0.25	4.3.3
32	1, 2, 4, 8	15	1	4.3.3
32	1, 2, 4, 8	15	2	4.3.3
32	1, 2, 4, 8	1	0.125, 0.25, 0.5, 1, 2	4.3.4
32	1, 2, 4, 8	2	0.125, 0.25, 0.5, 1, 2	4.3.4
32	1, 2, 4, 8	3	0.125, 0.25, 0.5, 1, 2	4.3.4
32	1, 2, 4, 8	4	0.125, 0.25, 0.5, 1, 2	4.3.4
32	1, 2, 4, 8	5	0.125, 0.25, 0.5, 1, 2	4.3.4
32	1, 2, 4, 8	6	0.125, 0.25, 0.5, 1, 2	4.3.4
32	1, 2, 4, 8	7	0.125, 0.25, 0.5, 1, 2	4.3.4
32	1, 2, 4, 8	8	0.125, 0.25, 0.5, 1, 2	4.3.4
32	1, 2, 4, 8	9	0.125, 0.25, 0.5, 1, 2	4.3.4
32	1, 2, 4, 8	10	0.125, 0.25, 0.5, 1, 2	4.3.4

Table 4.1: Overview of all two-dimensional simulations discussed in this chapter. We use a base resolution of 4 cells per scale height and obtain higher resolution simulations by multiplying the number of cells per scale height with an integer number, which we give in the second column. In the third column, we list the cooling efficiency β, and in the fourth column we state the smoothing length λ used to smooth the gravitational force. We also compute additional simulations for the fragmentation of the disk that can be found in Table 4.2.

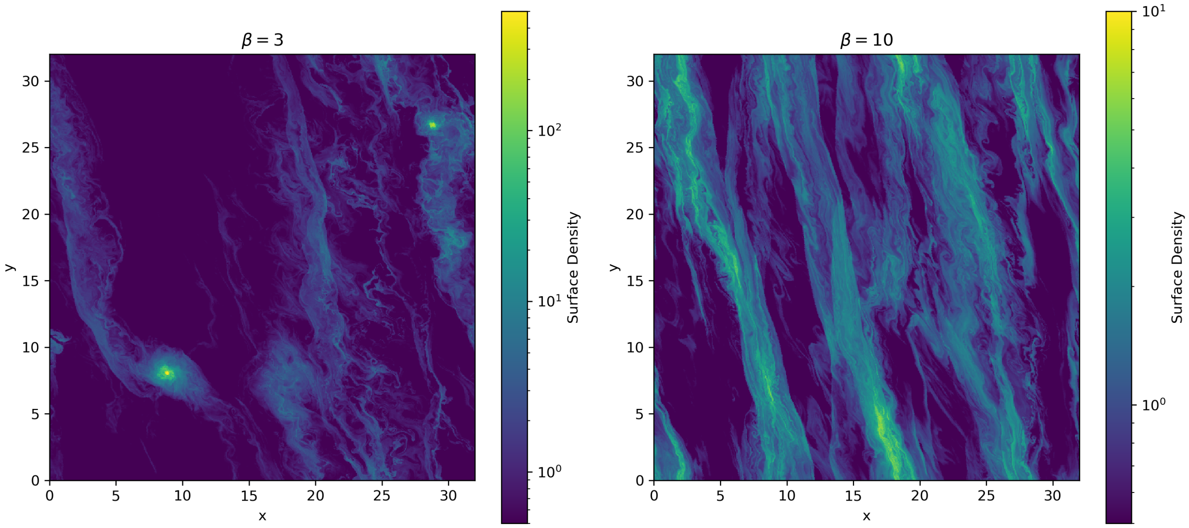

Figure 4.1: The surface density in two two-dimensional simulations with different cooling efficiency β, but with the same box size $L = 32\,H$, a resolution of 32 cells per scale height, and a smoothing with $\lambda = 0.5\,H$. The panel on the left hand side shows two fragments, while the panel on the right hand side displays the typical structure of a fully developed gravito-turbulent state.

of our simulation set, we show in Fig. 4.1 the surface density in a simulation with a fully developed gravito-turbulent state in the right panel, and a simulation where a fragment formed in the left panel.

4.3.1 Influence of box size and resolution on gravito-turbulence

In this section, we analyse the dependence of the gravito-turbulent state on the box size and resolution. We choose a constant $\beta = 10$, for which we find no fragmentation for $\lambda = 0.5H$. Here we first perform simulations with the lowest resolution, and then the final snapshots are used as the initial condition for higher-resolution simulations.

In Fig. 4.2 we show the temporal evolution of several averaged quantities for different box sizes. In all cases we find a turbulent state, and the normalized stress α is close to the expected one ($\alpha = 0.04$). In the smallest box, the stress α is burstier, but we do not observe any long-term trends. The larger boxes show in general a larger Toomre parameter and also a higher maximum density.

To better analyze the influence of the resolution we show in Fig. 4.3 several time-averaged quantities as a function of resolution and box size. Larger boxes are in general warmer and therefore allow larger stresses as required to reach the same α. The results for $L = 64\,H$ and $L = 128\,H$ are very similar and we conclude that a box size of $64\,H$ is sufficient to reach convergence with respect to the box size in global properties. But we note that already for $L = 32\,H$ the values are close to those obtained with $L = 64\,H$ but require less computational cost. Most quantities only weakly depend on the resolution, and it seems like 8 cells per scale height are enough to achieve convergence in most quantities.

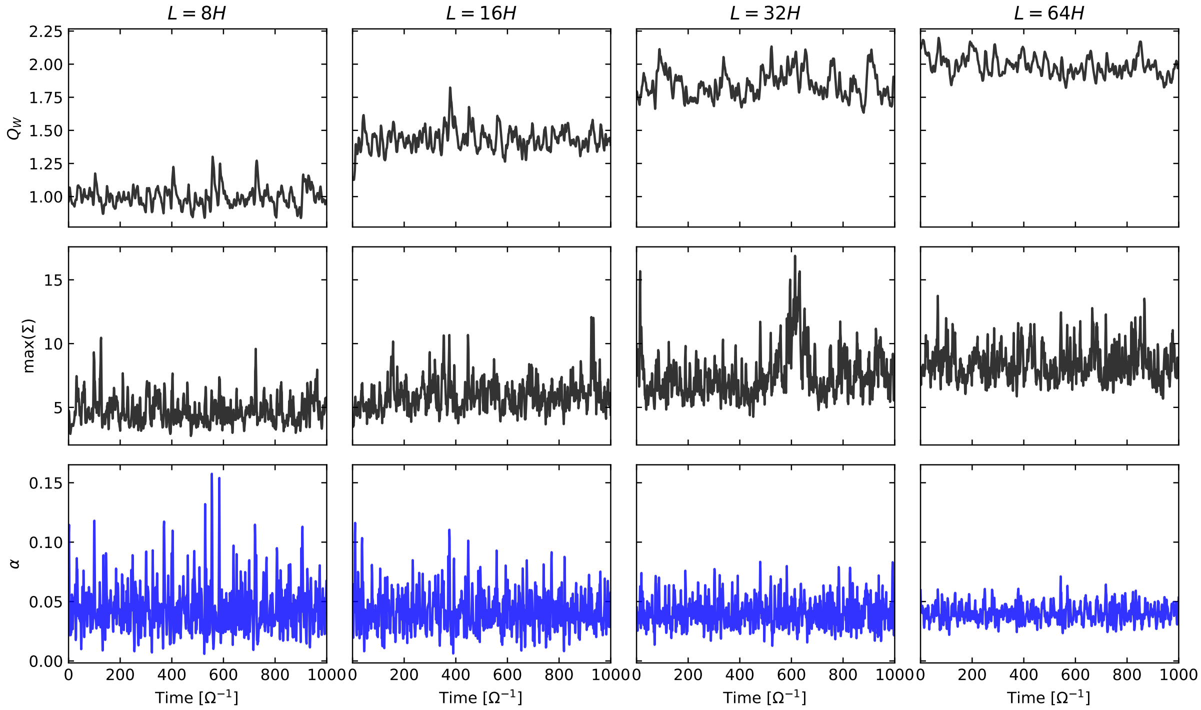

Figure 4.2: The temporal evolution of the Toomre parameter Q, the maximum surface density Σ and the normalized stress α in two-dimensional simulations with 16 cells per scale height and $\beta = 10$. We give results for four different box sizes, as labelled.

The box size dependency is well known in the literature (Booth & Clarke, 2019) and can be explained by the suppression of long-range modes in smaller boxes. Those modes cannot contribute to the heating of the disk, and therefore the value of the Toomre Q will decrease further, allowing short-range modes to become unstable (Mamatsashvili & Rice, 2010) before an equilibrium between heating and cooling is established. The value of 64 H we find above which gravito-turbulence becomes independent of the box size is consistent with the results of Booth & Clarke (2019). Also, the relatively low required resolution of 8 cells per scale height to reach convergence in global properties was reported in several studies (Gammie, 2001; Shi & Chiang, 2014; Riols et al., 2017; Booth & Clarke, 2019).

4.3.2 Influence of cooling time on the gravito-turbulent state

To better understand the dependency of the gravito-turbulent state on the cooling efficiency β, we performed a suite of simulations with a box size $L = 32\,H$ and different resolutions and different β. The box size is a compromise between the computational cost and the aim of being independent of the box size. In Fig. 4.4 we show different time and volume-averaged properties as a function of resolution and cooling efficiency. The thermal energy and the Toomre parameter Q increase with increasing β, while the gravitational and Reynolds stresses as well as the turbulent kinetic energy decrease. For a weaker cooling,

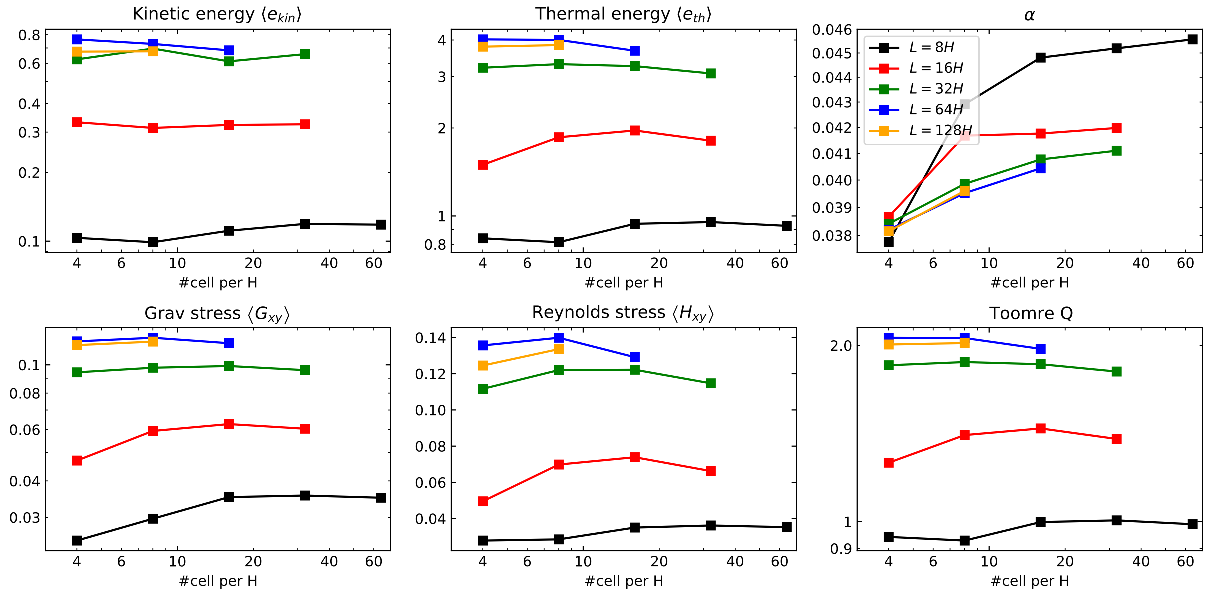

Figure 4.3: Different time-averaged quantities as a function of the number of cells per scale height for different box sizes in two-dimensional simulations with smoothing $\lambda = 0.5\,H$. We use a cooling efficiency $\beta = 10$ and average the quantities over the time interval $250\,\Omega^{-1} < t < 1000\,\Omega^{-1}$.

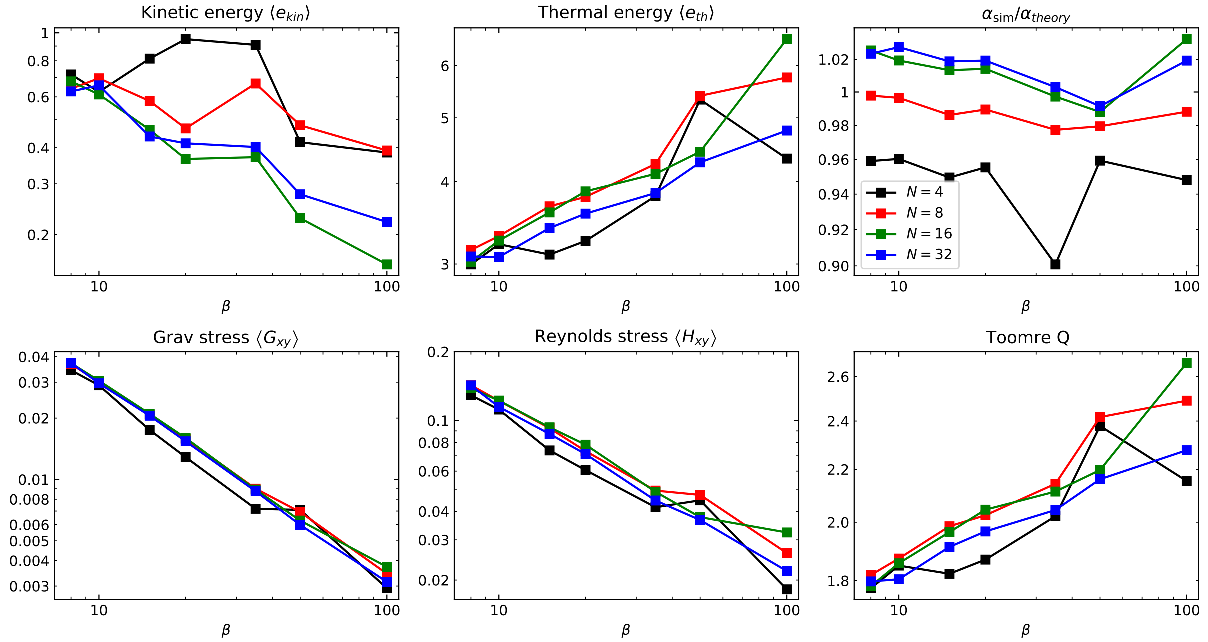

Figure 4.4: Different time-averaged quantities as a function of the cooling efficiency β for a different number of cells per scale height in two-dimensional simulations with smoothing $\lambda = 0.5\,H$. We use a box size $L_x = L_y = 32\,H$, and average the quantities over the interval $250\,\Omega^{-1} < t < 1000\,\Omega^{-1}$.

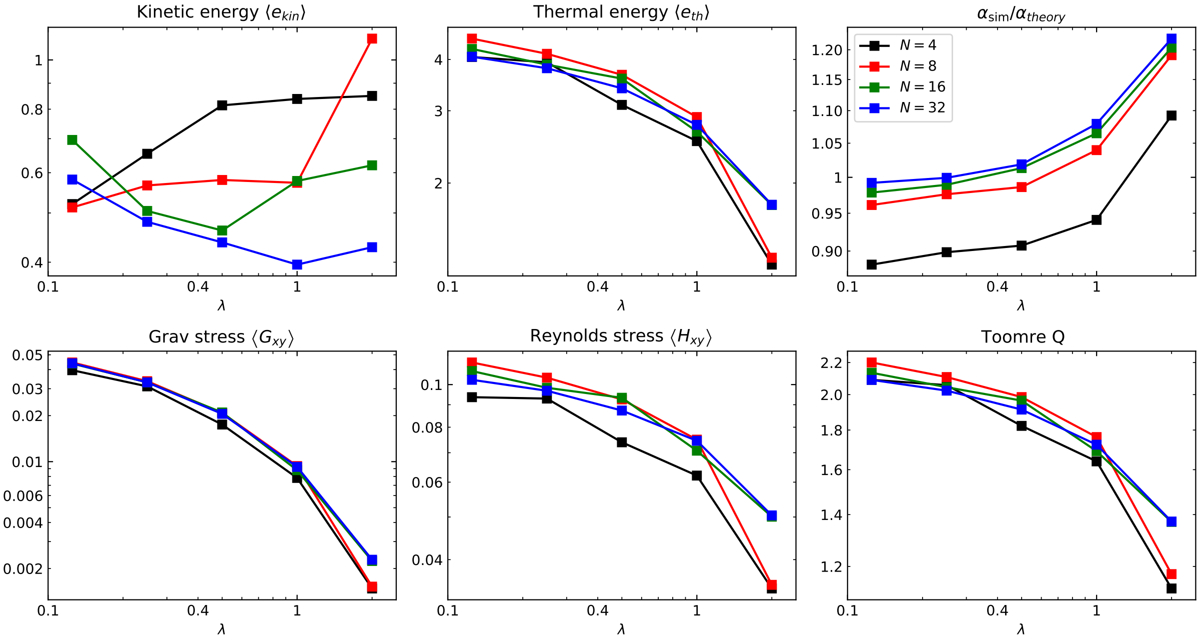

Figure 4.5: Different time-averaged quantities as a function of the smoothing length scale λ for a different number of cells per scale height in two-dimensional simulations with cooling efficiency $\beta = 15$. We use a box size $L_x = L_y = 32\,H$ and average the quantities over the time interval $250\,\Omega^{-1} < t < 1000\,\Omega^{-1}$.

Res. N	λ	$\beta=1$	$\beta=2$	$\beta=3$	$\beta=4$	$\beta=5$	$\beta=6$	$\beta=7$	$\beta=8$	$\beta=9$	$\beta=10$	$\beta=11$	$\beta=12$	$\beta=13$	$\beta=14$	$\beta=15$
4	2	no	no	no	no	no	no	no	no	no	no	-	-	-	-	no
8	2	no	no	no	no	no	no	no	no	no	no	-	-	-	-	no
16	2	T	no	no	no	no	no	no	no	no	no	-	-	-	-	no
32	2	T	no	no	no	no	-	-	-	-	no	-	-	-	-	no
4	1	18	no	no	no	no	no	no	no	no	no	-	-	-	-	no
8	1	14	no	no	no	no	no	no	no	no	no	-	-	-	-	no
16	1	7	T	no	no	no	no	no	no	no	no	-	-	-	-	no
32	1	5	T	no	no	no	no	no	no	no	no	-	-	-	-	no
4	1/2	7	16	40	92	351	no	no	no	no	no	-	-	-	-	no
8	1/2	4	13	56	125	160	no	no	no	no	no	-	-	-	-	no
16	1/2	3	7	12	59	56	no	no	no	no	no	-	-	-	-	no
32	1/2	4	8	64	689	no	no	no	no	no	no	-	-	-	-	no
4	1/4	3	6	16	25	128	53	no	no	383	no	-	-	-	-	no
8	1/4	3	6	9	23	17	16	29	463	48	T	1185	no	-	-	no
16	1/4	3	6	7	13	27	43	236	528	T	423	231	no	no	no	no
32	1/4	2	4	14	15	31	202	1053	1289	no	no	no	no	no	no	no
4	1/8	3	6	10	22	28	40	82	511	no	no	-	-	-	-	no
8	1/8	2	4	7	10	19	27	20	37	65	510	106	468	no	-	no
16	1/8	2	4	7	10	15	15	31	93	163	560	419	1240	T	T	no
32	1/8	2	3	6	10	21	35	46	240	868	616	1740	560	219	316	no

Table 4.2: Time until the first fragment forms in a given simulation with constant cooling efficiency β, starting from a gravito-turbulent state. The simulations are performed for different resolutions and box sizes in two dimensions. Sometimes only a transient fragment forms that is destroyed by shear again ('T'), and in some cases, no fragmentation occurs at all ('no').

the turbulence has to be weaker to reach an equilibrium, and the disk can therefore be warmer. We note that for all β the normalized stress α compares well with the expected one, especially for higher resolution. For $\beta = 100$ we find a stronger dependence of the Toomre parameter on the resolution, which we attribute to the quite long cooling time in comparison to the total simulation time. The lowest resolution shows some deviations from the other simulations, while for 8 cells per scale height the results seem to be converged again. The Toomre numbers are slightly lower than found by Riols & Latter (2016) in two-dimensional simulations ($Q = 3$ for $\beta = 50$, and $Q = 2$ for $\beta = 10$).

4.3.3 Influence of the smoothing length on the gravito-turbulent state

As we have mentioned before, the smoothing factor λ is used to approximate the disk stratification in three-dimensional simulations. Smaller values allow smaller structures to fragment and also to generate heat. We note that the use of a PM grid for the gravity solver leads to additional smoothing that depends on the grid size. To analyze the influence of λ on the gravito-turbulent state we ran several simulations in a box of size $L = 32\,H$ with different λ for a cooling efficiency $\beta = 15$. This larger β is required to avoid fragmentation for small λ.

In Fig. 4.5 we show several temporal and spatially averaged values as a function of λ and resolution. As expected, the Toomre Q, the thermal energy, and the gravitational and hydrodynamical stresses decrease with increasing λ. This is a natural consequence of the suppression of short-range modes by the smoothing that reduces the heating and requires a smaller Toomre Q to still reach an equilibrium. Since α should be constant, the cooler disks can sustain only smaller stresses. We note that for $\lambda \leq 0.5H$ the results only weakly depend on λ, and except for the lowest resolution we find $\alpha_{\mathrm{sim}} \approx \alpha_{\mathrm{theory}}$ in this case. For larger smoothing, the results depend more strongly on λ, and especially $\lambda = 2$ shows a much smaller Toomre parameter. In this case, the smoothing is probably too strong.

4.3.4 Fragmentation

After analysing the gravito-turbulent state we will focus in this section on the regime with stronger cooling, which might allow the formation of fragments. As already discussed in the introduction, the formation of fragments is a stochastic process, which means there cannot be a sharp β value below which the disk fragments and above which the disk is perfectly stable. Nevertheless, the probability for fragmentation decreases with increasing β, and the formation time of the first fragments can be used to qualitatively compare the probability for fragmentation.

As Young & Clarke (2015) showed, the introduction of a constant smoothing length in two-dimensional simulations strongly improves the convergence behaviour. We, therefore, run simulations with different resolutions, smoothing lengths λ and cooling efficiencies. As initial conditions, we use the results from the last section obtained with $\beta = 15$, but now evolved the simulations with $\beta = 10$. If we do not find fragmentation in these simulations, we take the last snapshot as the initial condition for simulations with yet smaller β. If we find fragmentation, we run simulations with larger β and use the snapshots obtained for $\beta = 15$ as initial conditions. In this case, we also compute simulations with $\beta < 10$ but take an earlier snapshot of the $\beta = 10$ run as initial conditions, at a time when there is no sign of fragmentation yet. All simulations were run for $t = 2000\,\Omega^{-1}$ or until the disk forms long-lasting fragments.

In Table 4.2 we show the formation times of the first fragment that then collapses further. In some cases, we only find transient fragments that get destroyed by shear. As expected, a larger λ requires stronger cooling, and for $\lambda = 2\,H$ we do not find fragmentation even for $\beta = 1$. We find good convergence of the critical β_c for a fixed λ if the cell size of the PM grid is smaller than λ. Otherwise, β_c increases with resolution, since the effective smoothing decreases. As we will show in the next section, the results for $\lambda = 0.5\,H$ compare well with those obtained also in three-dimensional simulations. Note that the stochastic nature of fragmentation is obvious, especially for smaller smoothing lengths.

Young & Clarke (2015) performed a similar study with the FARGO code as well as an SPH code with smoothing over $1H$, or no smoothing at all. They also found fragmentation with smoothing for $\beta = 2$ and no fragmentation for $\beta = 4$, which is consistent with our results. Without smoothing they reported with both methods fragmentation at $\beta = 10-12$ for a resolution of around 33 cells per scale height, which agrees very well with our results when the smallest smoothing length ($\lambda = 1/8H$) is used.

Box size	Resolution factors	β_0	δt	$t_{\mathrm{max}}\,[\Omega^{-1}]$	Relaxed IC?	Section
8	1, 2, 4	10	∞	1000, 1000, 500	yes	4.4.1
16	1, 2, 4	10	∞	1000, 1000, 250	yes	4.4.1
32	1, 2	10	∞	1000, 500	yes	4.4.1, 4.4.2
64	1	10	∞	1000	yes	4.4.1
32	1, 2	15	∞	1000, 250	yes	4.4.2
32	1, 2	20	∞	1000, 250	yes	4.4.2
32	1, 2	35	∞	1000, 250	yes	4.4.2
32	1, 2	50	∞	1000, 250	yes	4.4.2
32	1, 2	100	∞	1000, 250	yes	4.4.2
16	1, 2, 4	5	∞	100	no	4.4.3
16	1, 2, 4	10	∞	100	no	4.4.3
16	1, 2, 4	15	∞	100	no	4.4.3
16	1, 2, 4	20	∞	100	no	4.4.3
8	1, 2, 4	20	4π		yes	4.4.3
8	1, 2, 4	20	8π		yes	4.4.3
8	1, 2, 4	20	16π		yes	4.4.3
32	1, 2	20	4π		yes	4.4.3
32	1, 2	20	8π		yes	4.4.3
32	1, 2	20	16π		yes	4.4.3
8	1, 2, 4	1	∞	500, 500, 250	yes	4.4.3
8	1, 2, 4	2	∞	500, 500, 250	yes	4.4.3
8	1, 2, 4	3	∞	500, 500, 250	yes	4.4.3
8	1, 2, 4	4	∞	500, 500, 250	yes	4.4.3
8	1, 2, 4	5	∞	500, 500, 250	yes	4.4.3
8	1, 2, 4	6	∞	500, 500, 250	yes	4.4.3
8	1, 2, 4	7	∞	500, 500, 250	yes	4.4.3
32	1, 2	1	∞	500, 250	yes	4.4.3
32	1, 2	2	∞	500, 250	yes	4.4.3
32	1, 2	3	∞	500, 250	yes	4.4.3
32	1, 2	4	∞	500, 250	yes	4.4.3
32	1, 2	5	∞	500, 250	yes	4.4.3
32	1, 2	6	∞	500, 250	yes	4.4.3
32	1, 2	7	∞	500, 250	yes	4.4.3

Table 4.3: Overview of all three-dimensional simulations discussed in this chapter. We use a mass-based derefinement/refinement scheme with target mass m_{target} and only allow cell masses $0.5\,m_{\mathrm{target}} < m_{\mathrm{cell}} < 2\,m_{\mathrm{target}}$. To compare with previous results with a fixed spatial resolution we also introduce an effective resolution per scale height, which is defined as the uniform spatial resolution that is required so that the same amount of cells close to the mid-plane ($\pm 3\,H$) is expected (for details, see Section 4.4). We use a base resolution of 4 cells per scale height and multiply this number for a higher resolution by an integer which we state in the second column. In the third column, we give the initial cooling efficiency β_0, which can in some simulations be a function of time ($\beta = \beta_0 - t/\delta t$). We stop the simulations at time t_{max}, or when a collapsing fragment forms. We typically use initial conditions with already preformed gravito-turbulence, except in the simulations discussed in Section 4.4.3.

N	m_{target}
4	2.60×10^{-3}
8	3.25×10^{-4}
16	4.07×10^{-5}

Table 4.4: The resolution parameter N and the corresponding target mass m_{target} for three-dimensional simulations.

4.4 Gravitational instability in three dimensions

In this section, we now discuss three-dimensional simulations, which are substantially more expensive and therefore only allow us to analyse a smaller parameter space than in two dimensions. To avoid cells with too small densities that can destabilize the simulation we introduce a density floor $\rho_{\mathrm{min}} = 10^{-5}$ in the gravity calculation, which means all gravitational accelerations are multiplied with a factor $(\rho - \rho_{\mathrm{min}})/\rho$ and set to 0 for $\rho < \rho_{\mathrm{min}}$. If a cell reaches a density below ρ_{min}, we reinitialize it with $\rho = \rho_{\mathrm{min}}$, $\boldsymbol{v} = (0, -q\Omega_0 x, 0)$ and sounds speed $c_s = 1$. Our density floor is a bit smaller than the typical values of 10^{-4} used in other studies (Shi & Chiang, 2014; Riols et al., 2017; Baehr et al., 2017; Booth & Clarke, 2019), but our adaptive spatial resolution naturally decreases the resolution in low-density gas and therefore increases the allowed time steps. This adaptive nature allows us to use a relatively large box of $32\,H$ in the vertical direction, which is enough to ensure that the vertical boundary conditions do not influence the dynamics close to the mid-plane.

The density floor leads over time to an increase in the total mass in the box. Though this effect is typically small, we enforce a constant total mass in the box by multiplying at each global time step the mass, momentum and energy of each cell by a constant factor to renormalize the mass within the box. To set the target mass resolution, m_{target}, we measure the total mass M_{sys} in the simulation and compute the number of cells N_{tot} within $-3H < z < 3H$, that we would expect for a constant spatial resolution with N cells per scale height. We then define $m_{\mathrm{target}} = M_{\mathrm{sys}}/N_{\mathrm{tot}}$, but typically only cite N to characterize the resolution of our simulations. In Table 4.4 we give the corresponding m_{target} values for each used value of N.

4.4.1 Influence of box size and resolution on gravito-turbulence

As a first step, we analyze the gravito-turbulent state for $\beta = 10$ as a function of box size and resolution, similar to Booth & Clarke (2019). In Fig. 4.6 we show the temporal evolution of several box-averaged quantities for different box sizes. We find in all simulations a gravito-turbulent state which is burstier in smaller boxes. As already discussed in Section 4.3.1 for two-dimensional simulations, this can be explained by missing large-scale modes in smaller boxes, but we note that the influence is even more extreme than in two dimensions.

For a better quantitative comparison, we calculate temporal averages and show the results in Fig. 4.7. As in two dimensions, the Toomre Q, the turbulent kinetic energy, and

Resolution parameter N	$\beta = 5$	$\beta = 10$	$\beta = 15$	$\beta = 20$
4	16	no	no	no
8	14	21	28.75	no
16	15	22.7	29	no

Table 4.5: Time until the formation of the first fragment in three-dimensional simulations started with smooth initial conditions. Runs where no fragments over the simulated time span form are designated with 'no'. We use a box size of $L_x \times L_y \times L_z = 16\,H \times 16\,H \times 32\,H$.

the thermal energy increase with the box size. The gravitational stress also increases while the Reynolds stress decreases, in contrast to the two dimensional case. The normalized stress α agrees well for a resolution of 8 cells per scale height with the expected one of $\alpha = 0.04$, and the quantities seem to converge for this resolution. In general, our results compare well with those reported in Booth & Clarke (2019). Especially the turbulent kinetic energy, the ratio of the gravitational to the total stress and the normalized stress α, fit almost perfectly, except for the run with $L_x = L_y = 8H$. But even in this case, the difference is quite small. The Toomre parameters are similar except for the smallest box, where it is slightly higher in our simulations, which can be understood as being due to a hotter halo that forms in the low-density region around the midplane.

4.4.2 Influence of cooling time on gravito-turbulence

As a next step, we vary the cooling efficiency β and show in Fig. 4.8 different temporally and spatially average quantities. We choose a box size of $L_x = L_y = 32\,H$ as a compromise between a small influence of the box size and a large computational cost. As in two dimensions the stresses and turbulent kinetic energy decrease while the Toomre Q and thermal energy increase with increasing β. The normalized stress α agrees well with the expected one, though the deviations increase with β in the higher resolution runs. This might be attributed to the shorter simulation time relative to the cooling time. As in Shi & Chiang (2014) the gravitational stress dominates over the Reynolds stress for all β.

4.4.3 Fragmentation

Prompt Fragmentation

It is well known from global simulations (Paardekooper et al., 2011; Young & Clarke, 2015; Deng et al., 2017) that a disk might undergo spurious fragmentation before the gravito-turbulent state sets in. This typically happens at the boundary between the turbulent and non-turbulent regions due to the radially dependent cooling time. Since the size of the interface depends on the resolution it affects the convergence of β_c in global simulations (Deng et al., 2017). Booth & Clarke (2019) showed that a similar spurious fragmentation can also be observed in local simulations when the disk can cool for a finite time until gravito-turbulence sets in. During this time overdensities can form that can collapse. Since

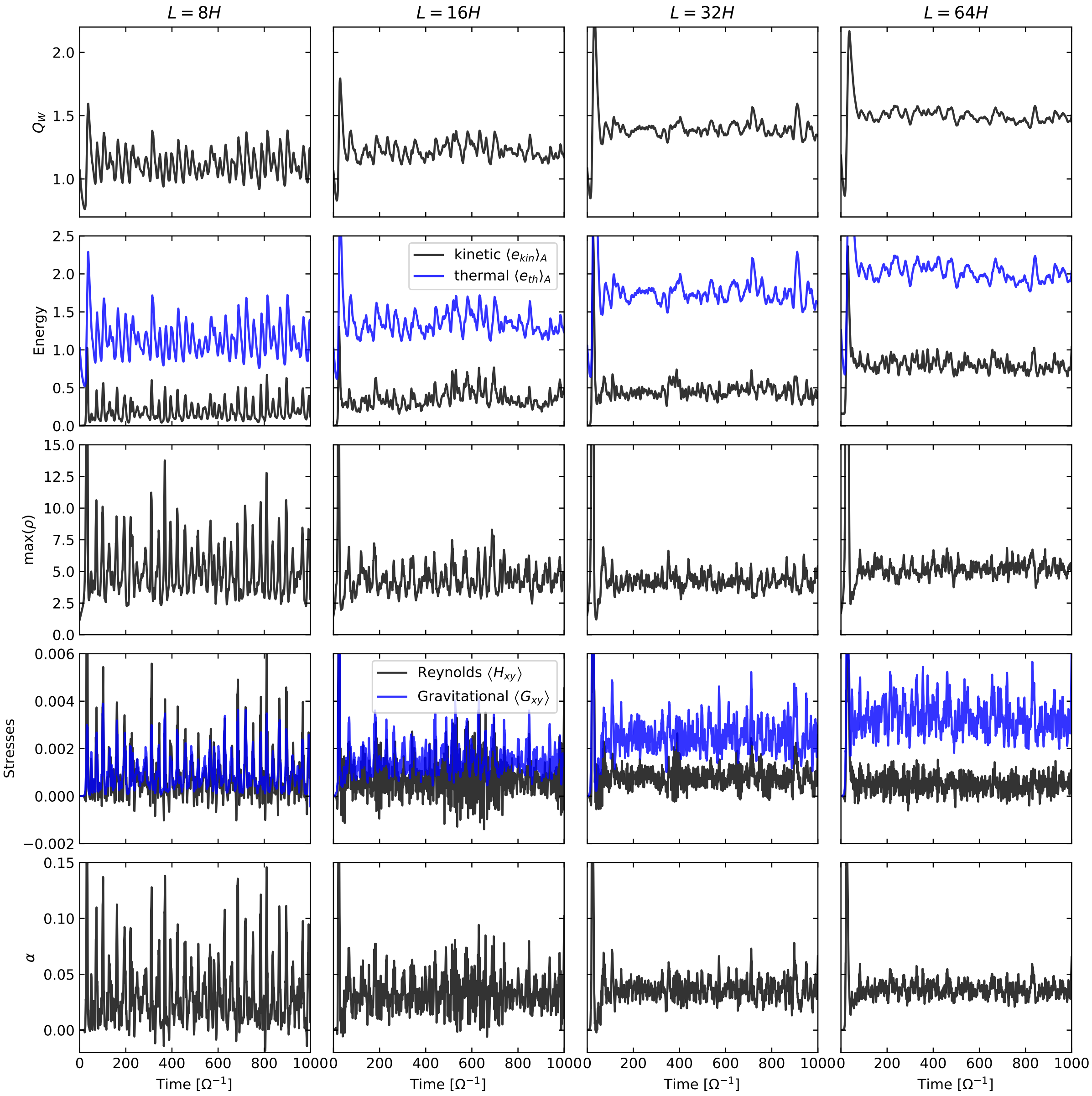

Figure 4.6: The temporal evolution of different quantities for three-dimensional simulations of gravito-turbulence with $\beta = 10$ in boxes of different sizes (shown in different columns) and the same resolution of initially 4 cells per scale height H. We use a Savitzky–Golay filter to smooth the data over $5\,\Omega^{-1}$. We show the Toomre Q (first row), energy density (2nd row), maximum density (3rd row), absolute stresses (4th row), and normalized stress α (5th row).

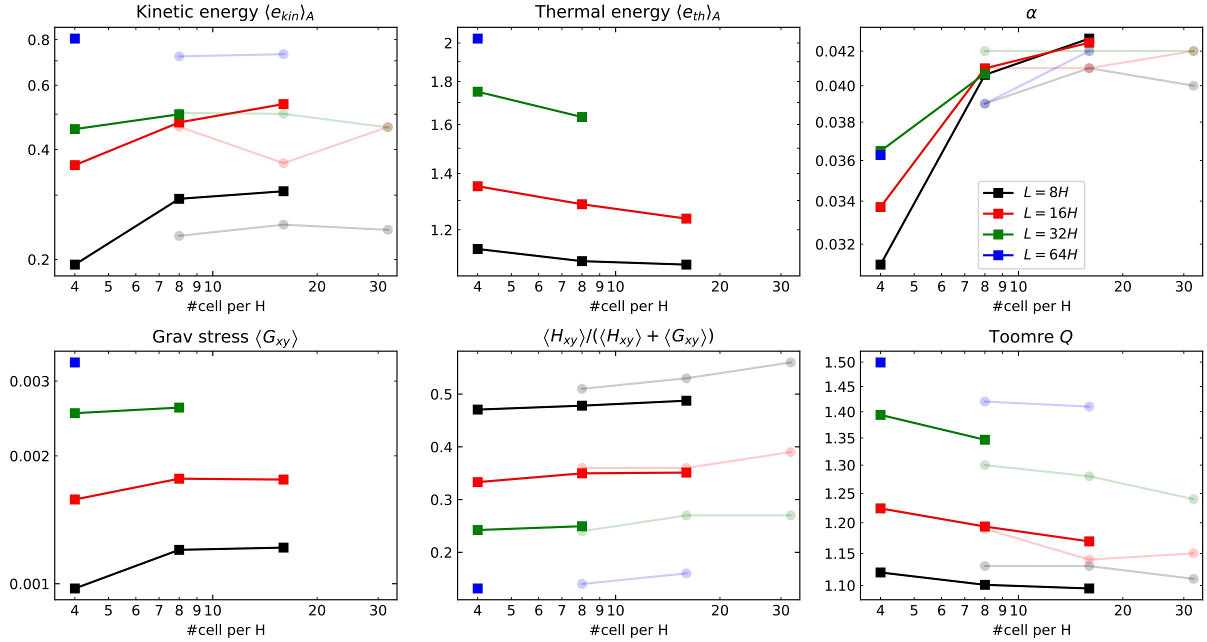

Figure 4.7: Different time-averaged quantities as a function of the number of cells per scale height for different box sizes in three-dimensional simulations. We use a cooling efficiency $\beta = 10$ and average the quantities from $t = 50\,\Omega^{-1}$ till the end of the simulation. The solid squares are the results from our simulations, while the opaque circles are from Booth & Clarke (2019).

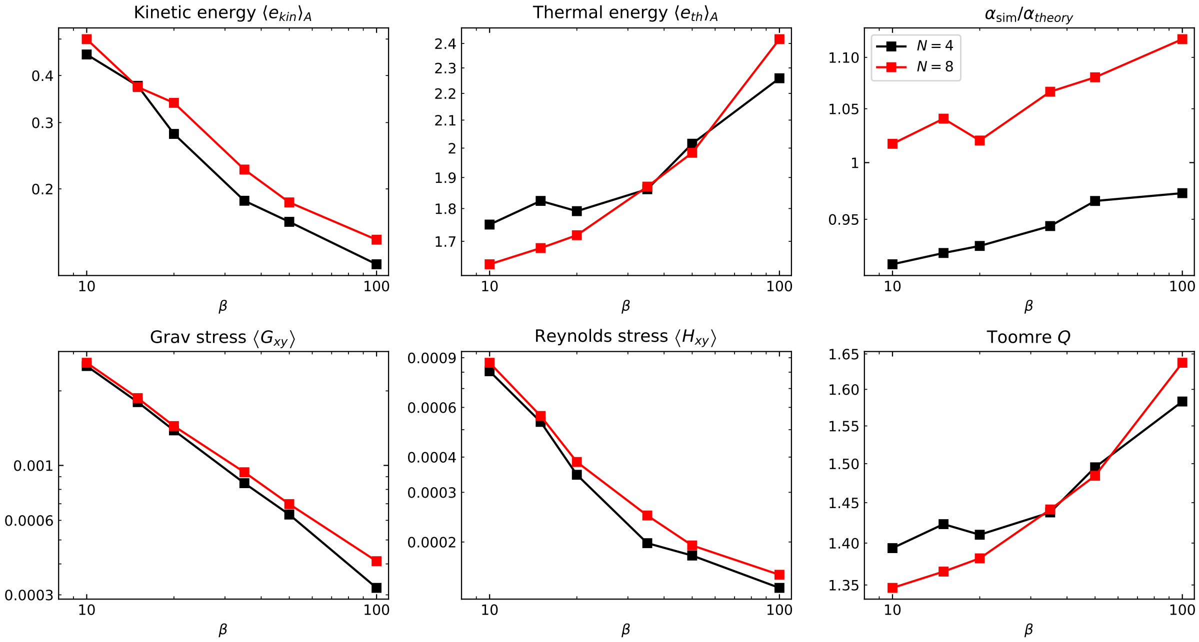

Figure 4.8: Different time-averaged quantities as a function of the cooling efficiency β, for different numbers of cells per scale height in three-dimensional simulations. We use a box size $L_x = L_y = 32\,H$ and average the quantities from $t = 50\,\Omega^{-1}$ till the end of the simulations.

the initial overdensity depends on the resolution also the convergence in local simulations is affected by the smoothness of the initial conditions.

Since this phenomenon crucially depends on details of the numerical schemes, we performed several simulations in a box of size $L_x \times L_y \times L_z = 16\,H \times 16\,H \times 32\,H$ for different resolutions and different β. In Table 4.5 we give the formation time of the first fragment. We observe even for quite large $\beta = 15$ fragmentation, and the boundary increases with higher resolution as also reported in Booth & Clarke (2019). In Fig. 4.9 we can see that indeed the density strongly increases at the beginning of the simulation before it decreases again, marking the formation of a gravito-turbulent state in some of the simulations. The initial peak grows faster for stronger cooling and becomes larger for higher resolution. And it is this peak that in some cases leads to a runaway collapse, while, e.g., for $\beta = 20$ and $N = 16$ the overdensity gets destroyed by shear again. To avoid being influenced this behaviour we will use in the next sections an already formed gravito-turbulent state as the initial conditions for our simulations.

Time-dependent cooling

In this section, we use a time-dependent $\beta(t) = \beta_0 - t/\delta t$, which decreases linearly in time. As was shown in Clarke et al. (2007) using global SPH simulations, the behaviour of the system can be divided into two regimes. For fast changes of β (small δt), the gravito-turbulent state takes longer to adjust to the new β than δt, which means fragmentation

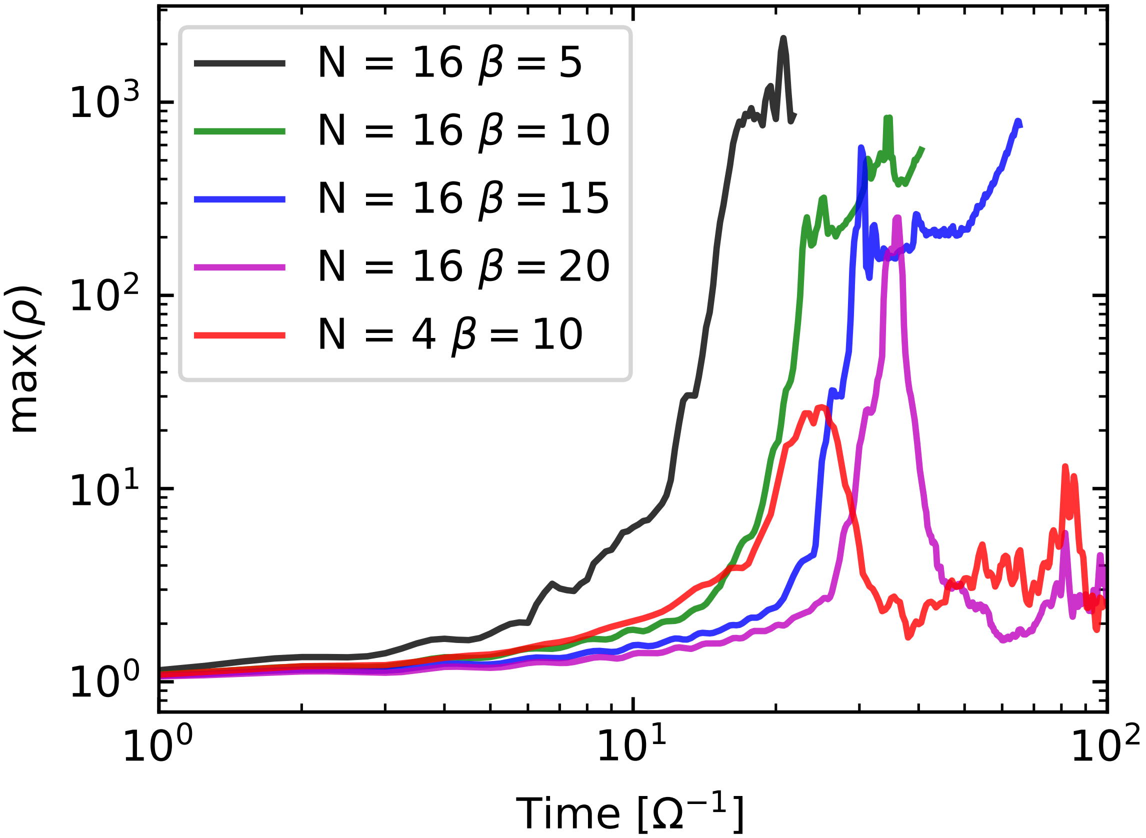

Figure 4.9: The temporal evolution of the maximum density in a three-dimensional box of size $L_x \times L_y \times L_z = 16\,H \times 16\,H \times 32\,H$ for different β and different effective resolutions N. Smooth initial conditions are used.

Box size	Res. parameter N	$\delta t = 4\pi$	$\delta t = 8\pi$	$\delta t = 16\pi$
8	4	3.29	3.57	3.68
8	8	2.63	3.52	4.46
8	16	2.63	5.22	3.26
32	4	3.03	3.50	3.09
32	8	2.48	2.39	3.22

Table 4.6: The critical cooling rate $\beta(t) = \beta_0 - t/\delta t$ at which we found fragmentation in simulations with a time-dependent cooling efficiency β. We varied the change rate of β (δt) as well as the effective number of cells per scale height (second column). The initial conditions are taken from the saturated simulations in the last sections with $\beta = 20$ or $\beta = 10$.

gets delayed to smaller β. If δt is larger the fragmentation boundary converged to $\beta_c = 3$ as in Gammie (2001). We note that if there is a stochastic component in the fragmentation, β_c would increase for large δt since the disk would spend more time at each β, and therefore the probability of fragmentation increases. Booth & Clarke (2019) extended this study to local simulations in a box of size $L_x = L_y = 16\,H$ and found fragmentation up to $\beta_c = 5$ for $\delta t = 16\pi$. Their value of $4 < \beta_c < 5$ is therefore a bit larger than the values of $\beta_c \approx 3$ found in Deng et al. (2017) and Baehr et al. (2017), which they attributed to stochastic fragmentation.

As we have seen in Fig. 4.6, a smaller box size leads to larger density fluctuations for the same β. This should increase the probability of stochastic fragmentation since those density peaks can become self-gravitating and collapse. We, therefore, run several simulations in a small box ($L_x = L_y = 8\,H$) and in a larger box that is more independent of the box size ($L_x = L_y = 32\,H$). In Table 4.6 we report the formation time of the first fragment that undergoes a collapse, taking as initial conditions the final snapshots from the simulations presented in the previous sections. We find in the larger box fragmentation in the range $2.5 < \beta < 3.5$, close to the standard $\beta_c = 3$ from Gammie (2001). In the smaller box, we can observe fragmentation even at $\beta_c = 5.22$, which supports the claim that in smaller boxes stochastic fragmentation becomes more important. In general, we find the lowest β_c for $\delta t = 4\pi$, which we attribute to the limited time spent in each β regime and therefore also limited fragmentation probability.

For both box sizes, we do not find a clear trend with resolution. In Fig. 4.10 and Fig. 4.11 we show the temporal evolution of the maximum density as a function of β in the small and large box. One can see the runaway nature of the gravitational collapse when the cooling is efficient enough. The density fluctuations are larger in the smaller box, and already for higher values of β a density peak is large enough to collapse.

Relaxed initial conditions

To further analyze the question of convergence of β_c with resolution, we focus in this section on simulations with a constant β. As initial conditions, we take the last snapshot from the simulations presented in Section 4.4.1. We again use a box of size $8\,H \times 8\,H \times 32\,H$,

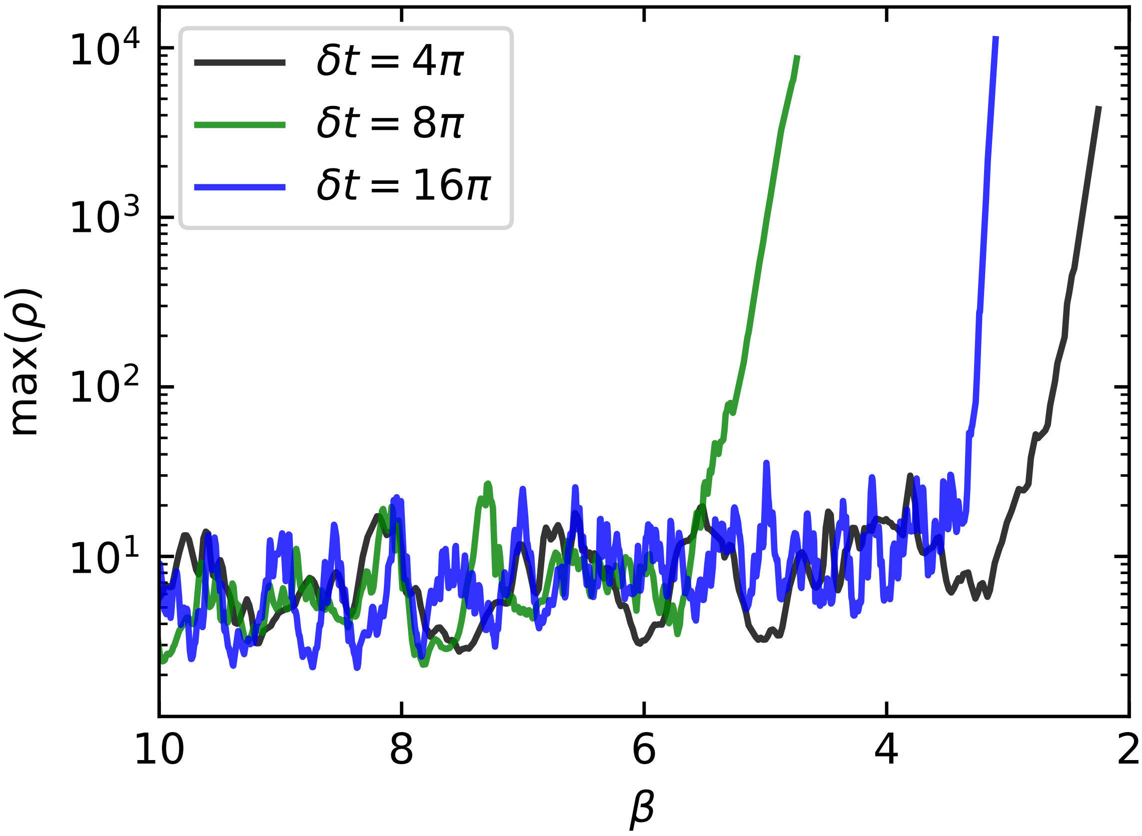

Figure 4.10: The maximum density in a three-dimensional box of size $L_x \times L_y \times L_z = 8\,H \times 8\,H \times 32\,H$ for a time-dependent cooling $\beta(t) = \beta_0 - \delta t/t$ and different δt. We use an effective resolution of $N = 16$.

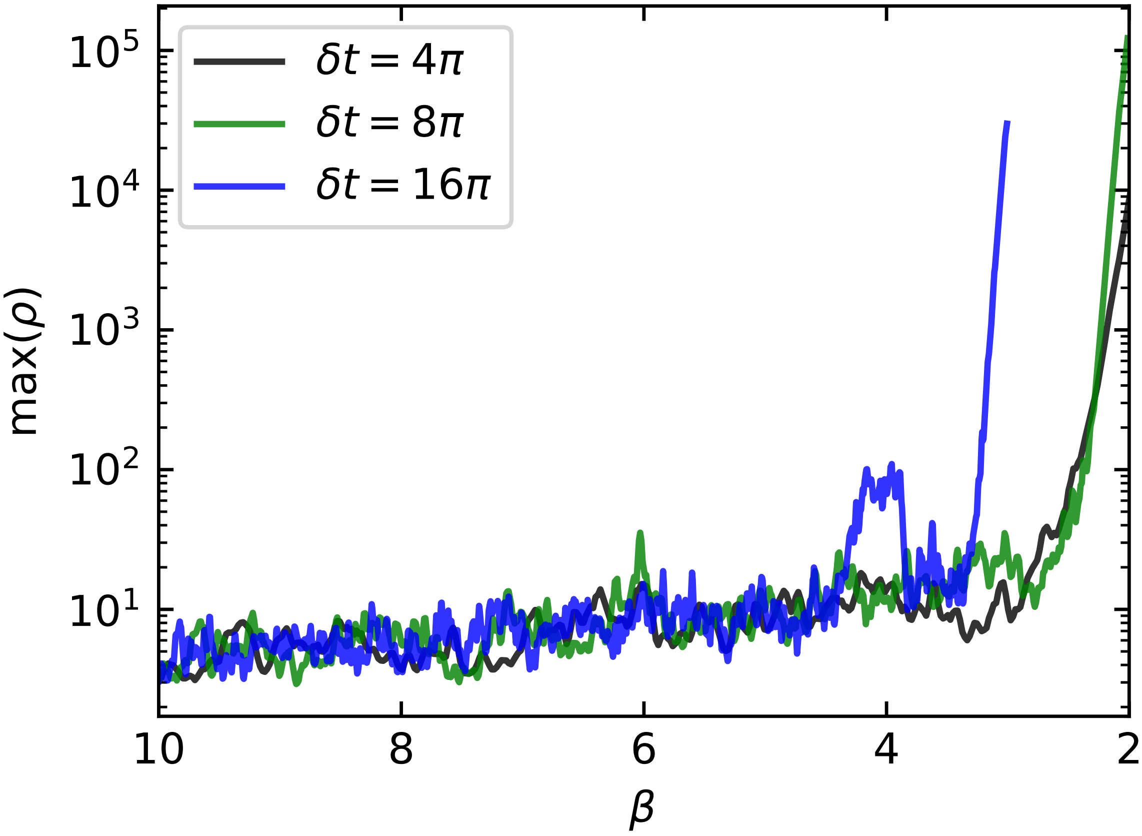

Figure 4.11: The maximum density in a three-dimensional box of size $L_x \times L_y \times L_z = 32\,H \times 32\,H \times 32\,H$, for a time-dependent $\beta(t) = \beta_0 - \delta t/t$ and different δt. We use an effective resolution of $N = 8$.

BS	N	$\beta = 1$	$\beta = 2$	$\beta = 3$	$\beta = 4$	$\beta = 5$	$\beta = 6$	$\beta = 7$
8	4	3.5	5.5	6.25	61.75	109	no	no
8	8	3.5	4.75	6.75	10.25	71	no	no
8	16	3.5	6.0	10	63.5	93	no	212
32	4	3.5	6.25	10	no	no	no	no
32	8	2.25	5.75	10	210.5	no	no	no

Table 4.7: Formation time of the first fragment (if any) if we abruptly change β from 10 to a lower value. The simulations were performed for different resolution parameters N and box sizes (BS) in three dimensions.

exemplary for a small box, and a box of size $32\,H \times 32\,H \times 32\,H$ as an example for a larger box. In Table 4.7 we show the formation time of the first fragment that leads to a runaway collapse. We note that we run our simulations longer than those presented in Booth & Clarke (2019) (only till $100\,\Omega^{-1}$), which allows a better analysis of stochastic fragmentation.

For $\beta \leq 3$, a fragment forms in all simulations within the cooling time scale. This is also expected since for $\beta < \sqrt{2\pi Q}/(5\gamma - 4) \approx 3$ the cooling is efficient enough to prevent the formation of pressure support stabilizing the disk on small scales (Kratter & Murray-Clay, 2011). For $\beta = 4$ we find fragmentation in the large box only after $210\,\Omega^{-1}$ due to stochastic fragmentation. The difference between a direct fragmentation and stochastic fragmentation can also be appreciated in Fig. 4.12, where one can see that for $\beta = 4$ a gravito-turbulent state forms with a random overdensity collapsing at a later time.

In the smaller box, we find stochastic fragmentation in all simulations for $\beta = 4$ and $\beta = 5$, and even for $\beta = 7$ in the highest resolution simulation. As we show in Fig. 4.13, this fragmentation is again triggered by random overdensities and differs from the free fall collapse for $\beta \leq 3$. Similar results with a higher probability of fragmentation in smaller boxes were also found in Booth & Clarke (2019), but due to their short run time they did not observe stochastic fragmentation for $\beta \geq 5$.

4.5 Discussion

4.5.1 Adaptive resolution with the moving mesh method

The TreePM method we implemented in this chapter in two and three dimensions for the shearing box allows for an adaptive spatial resolution in the calculation of gravitational forces. This is important for Lagrangian methods, since for a pure PM method the spatial resolution is limited by the size of the used Cartesian grid. As we have shown in Section 4.4, the maximum overdensities found in the gravito-turbulent state without fragmentation are around 10 times larger than the average densities close to the midplane (see also Fig. 4.6). In this case, the adaptive spatial resolution of the Lagrangian method is only by factor two larger than the average resolution. If the disk starts to fragment, relative overdensities of

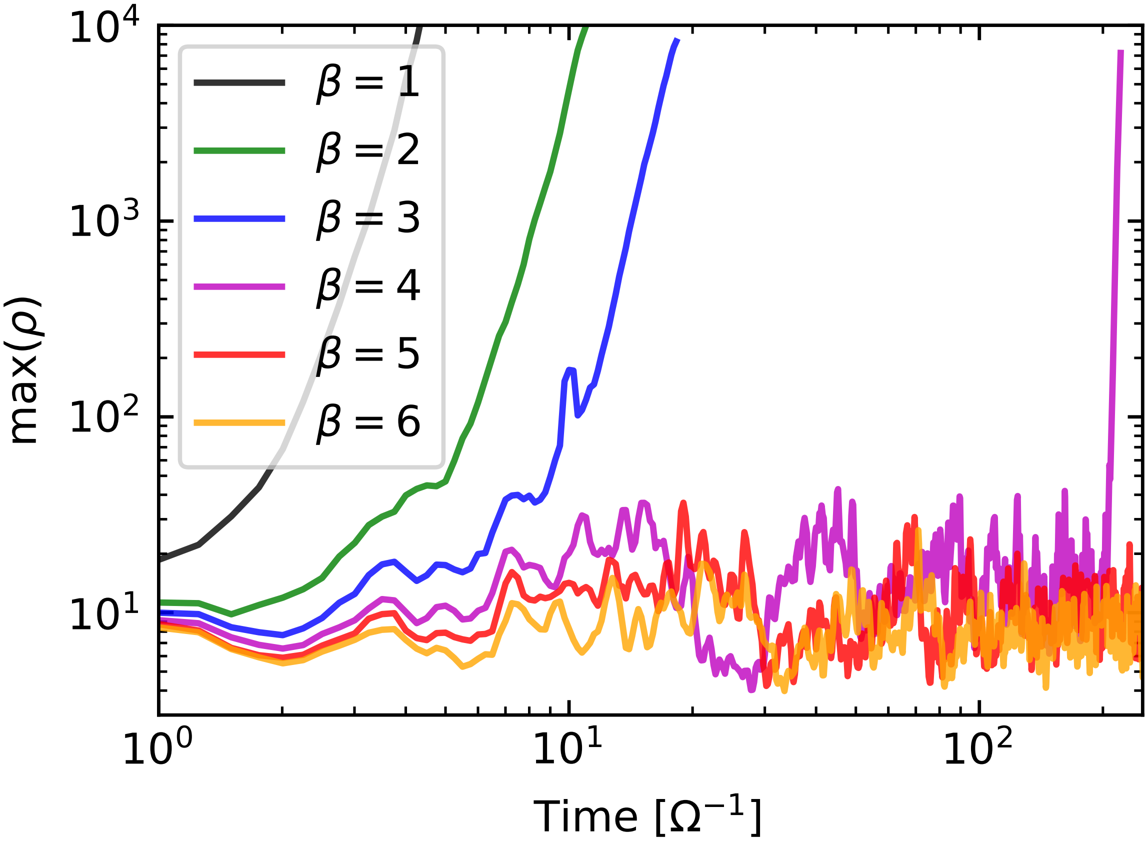

Figure 4.12: The temporal evolution of the maximum density in a three-dimensional box of size $L_x \times L_y \times L_z = 32\,H \times 32\,H \times 32\,H$ for different β with an effective resolution of 8 cells per scale height.

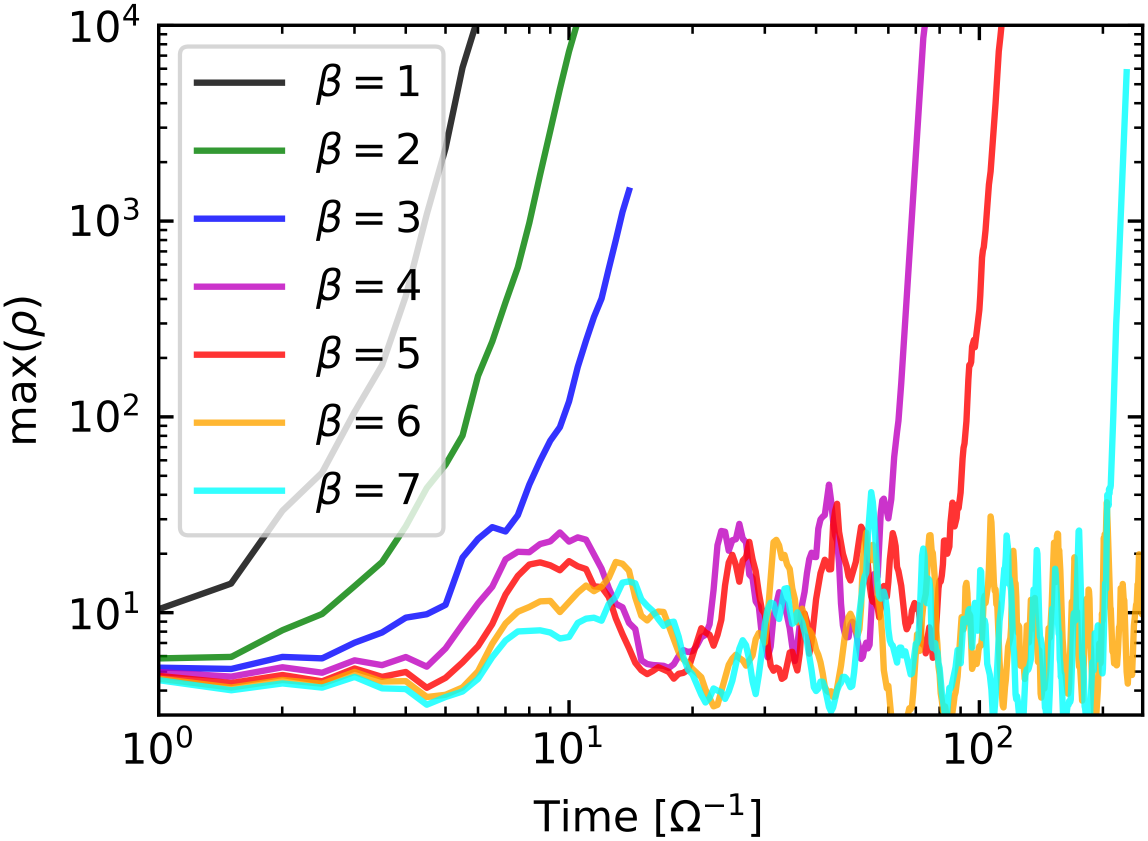

Figure 4.13: The temporal evolution of the maximum density in a three-dimensional box of size $L_x \times L_y \times L_z = 8\,H \times 8\,H \times 32\,H$ for different β, with an effective resolution of 16 cells per scale height.

several hundred can be found, which means that the spatial resolution is increased by a factor of 5 or even more compared to the environment. This means that our implementation is especially useful if one is interested in following the detailed collapse and evolution of such fragments.

Deng et al. (2021) showed that in global simulations with ideal MHD and self-gravity the magnetic pressure can stabilize smaller clumps and prevent them from getting destroyed by shear. Our setup would be ideal to study such problems with higher resolution, and by adding additional effects such as non-ideal MHD. Another possible application is the simulation of patches of the ISM as already realized in the TIGRESS (Kim & Ostriker, 2017) and SILCC (Walch et al., 2015) projects. In the dense phase of molecular clouds, the density can become higher by a factor of several hundred, and therefore our Lagrangian approach would automatically yield a much higher spatial resolution in these structures. Since molecular clouds are the birthplace of new stars, this increased resolution would allow us to follow the feedback of individual stars.

4.5.2 Relationship between two and three-dimensional simulations

Two-dimensional simulations are significantly cheaper than three-dimensional calculations for the same resolution, which means they allow the investigation of a much larger parameter space. As already mentioned in Young & Clarke (2015), the gravitational force in two dimensions has to be smoothed to find convergence in the critical cooling efficiency β below which we expect fragmentation. By comparing Table 4.2 and Table 4.7 we find for $\lambda = 0.5H$ a good agreement for two and three-dimensional simulations. The value is close to the standard scale height and is therefore naturally incorporated in three dimensions by the stratification in the z-direction. We note that the scale height can change especially in the case of fragmentation, which would mean that the smoothing factor would have to be time-dependent and also non-uniform in space.

Another option to improve the convergence in two dimensions would be the introduction of a temperature floor in the cooling description. The temperature floor would increase the pressure support in very cold regions and therefore stabilize the disk especially on small scales. Lin & Kratter (2016) shows using analytical methods that small-scale modes are more unstable in 2D compared to 3D, which means a temperature floor or smoothing would have more influence in 2D.

As we have shown in Fig. 4.3 and Fig. 4.7, the Toomre Q increases if we increase the box size up to $L_x = L_y = 64\,H$. But only in the three-dimensional case the gravito-turbulent state is significantly burstier in smaller boxes, while for larger boxes the box becomes warmer in two dimensions than in three dimensions. In three dimensions and for large boxes, the gravitational stress dominates while in the two-dimensional case the Reynolds stress is typically as large as the gravitational stress, independent of the box size. In both cases the average normalized stress α agrees well with the analytic estimate (4.2), and box-averaged quantities seem to converge for $L_x = L_y > 64\,H$ and a resolution of 8 cells per scale height.

Booth & Clarke (2019) showed that on large scales the three-dimensional gravito-turbulence becomes effectively two-dimensional because no large-scale motion in the z-direction is possible. But on small scales below one scale height, the turbulence is genuinely three-dimensional and cannot be studied properly with two-dimensional simulations. In summary, we conclude that for parameter studies and the analysis of large-scale effects, two-dimensional simulations with smoothing can be sufficient, but the results always require confirmation with full three-dimensional simulations.

4.5.3 Importance of stochastic fragmentation for planet formation

In two-dimensional simulations with a smoothing $\lambda = 0.5H$, as well as in three-dimensional simulations, we found direct fragmentation for $\beta \leq 3$. For larger β, a gravito-turbulent state can form that leads to random overdensities. From time to time these overdensities become strong enough to collapse, which means the time to onset of fragmentation is a stochastic quantity. This stochastic component becomes obvious in the results presented in Table 4.2, where for lower cooling efficiencies fragments might form earlier than with the higher cooling efficiency.

For our simulations with up to $t_{\max} = 2000\,\Omega^{-1}$ and $\lambda = 0.5\,H$ we never find fragmentation above $\beta = 5$. Direct gravitational fragmentation is typically thought to occur in the outer parts of protoplanetary disks, where $\beta \propto R_0^{-9/2}$ (Paardekooper, 2012) is expected. This means that the case of smaller, burstier boxes with a higher probability of stochastic fragmentation might only be applicable close to the star where β is too large to form fragments. The increase for the larger boxes of β_c to $\beta_c = 5$ due to stochastic fragmentation therefore only slightly increases the expected radius at which fragmentation might become important. Protoplanetary disks are expected to only stay self-gravitating for around 10^5 years (see e.g. Laughlin & Bodenheimer, 1994), which is equivalent to $t_{\max} = 628\,\Omega^{-1}$ for a position of the box at $R_0 = 100\,\mathrm{AU}$ for a disk around a solar mass star. Stochastic fragmentation, therefore, does not significantly change the results obtained for β_c.

4.6 Summary and Conclusions

In this chapter, we have introduced an adaptive self-gravity solver using the TreePM method for the shearing box in a Lagrangian code in two and three dimensions. We have applied the new method to the problem of a self-gravitating disk with the commonly employed, simple β cooling prescription and analyzed the resulting gravito-turbulent state as well as gravitational fragmentation in two and three dimensions. Our main findings for the gravito-turbulent state are:

1. A larger box size leads typically to a warmer box (larger Toomre parameter), in the regime $L_x = L_y < 64\,H$.

2. Box-averaged quantities converge for a resolution of 8 cells per scale height.
3. In three-dimensional simulations the gravitational stress dominates over the hydrodynamic stress for larger boxes, while in two dimensions they are typically of similar size.
4. The normalized stresses agree well with those obtained analytically from an energy conservation argument (even for weak cooling with $\beta = 100$).

Our main findings about the critical cooling rate β_c below which we expect fragmentation are:

5. To reach convergence we require a start with a developed gravito-turbulent state, and not from smooth initial conditions.
6. Two-dimensional simulations require a fixed smoothing length λ of the gravitational force to reach convergence.
7. For $\lambda = 0.5\,H$, we find good agreement between two and three dimensional simulations.
8. For $\beta \leq 3$, the disk starts to fragment on a cooling time scale.
9. For $3 \leq \beta \leq 6$, we find stochastic fragmentation.
10. Stochastic fragmentation has a higher probability to occur in smaller boxes, which exhibit a burstier gravito-turbulent state.
11. Our results are in general in good agreement with literature results obtained with static grid codes.

The reassuring agreement between our adaptive quasi-Lagrangian moving-mesh results with those obtained with Eulerian mesh codes for the shearing box is an important validation of our new implementation. The Lagrangian resolution adaptivity offered by our technique is an important advantage, however, especially for tracking the fate of collapsing fragments. We plan to focus on this question in future work. Also, we plan as a next step to apply the implementation to disks with self-gravity and magnetic fields as well as patches of galactic disks.

4.7 Appendix: Tests of gravity solver

In this section, we test our implementations of self-gravity for the shearing box described in Section 4.2.3. While for the two-dimensional case there exist analytic solutions we have to compare our results to numerical results in three dimensions.

4.7.1 Two dimensions

For two dimensions, we follow mostly the tests already presented in Riols & Latter (2016) and analyze the evolution of small perturbations added to the ground state of the shearing box. We use more accurate binning onto the PM mesh presented in Appendix 4.8. In the following, quantities with subscript 0 correspond to the value of the background state while quantities with subscript 1 denote small perturbations to it. The linearized equations without smoothing can be written as:

$$\frac{\partial \Sigma_1}{\partial t} = q\Omega_0 x \frac{\partial \Sigma_1}{\partial y} - \Sigma_0 \nabla \cdot (\boldsymbol{v}_1), \tag{4.38}$$

$$\frac{\partial v_{x1}}{\partial t} = q\Omega_0 x \frac{\partial v_{x1}}{\partial y} + 2\Omega_0 v_{y1} - \frac{1}{\Sigma_0}\frac{\partial P_1}{\partial x} - \frac{\partial \Phi_1}{\partial x}, \tag{4.39}$$

$$\frac{\partial v_{y1}}{\partial t} = q\Omega_0 x \frac{\partial v_{y1}}{\partial y} + q\Omega_0 v_{x1} - 2\Omega_0 v_{x1} - \frac{1}{\Sigma_0}\frac{\partial P_1}{\partial y} - \frac{\partial \Phi_1}{\partial y}, \tag{4.40}$$

$$\frac{\partial P_1}{\partial t} = q\Omega_0 x \frac{\partial P_1}{\partial y} + \gamma \frac{P_0}{\Sigma_0} \nabla \cdot (\boldsymbol{v}_1), \tag{4.41}$$

$$\nabla^2 \Phi_1 = 2\pi G \Sigma_1, \tag{4.42}$$

and simplify for an isothermal EOS ($P = \Sigma c_s^2$) to:

$$\frac{\partial \Sigma_1}{\partial t} = q\Omega_0 x \frac{\partial \Sigma_1}{\partial y} - \Sigma_0 \nabla \cdot (\boldsymbol{v}_1), \tag{4.43}$$

$$\frac{\partial v_{x1}}{\partial t} = q\Omega_0 x \frac{\partial v_{x1}}{\partial y} + 2\Omega_0 v_{y1} - \frac{c_s^2}{\Sigma_0}\frac{\partial \Sigma_1}{\partial x} - \frac{\partial \Phi_1}{\partial x}, \tag{4.44}$$

$$\frac{\partial v_{y1}}{\partial t} = q\Omega_0 x \frac{\partial v_{y1}}{\partial y} + q\Omega_0 v_{x1} - 2\Omega_0 v_{x1} - \frac{c_s^2}{\Sigma_0}\frac{\partial \Sigma_1}{\partial y} - \frac{\partial \Phi_1}{\partial y}, \tag{4.45}$$

$$\nabla^2 \Phi_1 = 2\pi G \Sigma_1. \tag{4.46}$$

Axisymmetric case (isothermal)

We first analyze the evolution of axisymmetric perturbations of the form:

$$\begin{pmatrix} \Sigma_1 \\ v_{x1} \\ v_{y1} \end{pmatrix} = e^{i(k_x x - \omega t)} \begin{pmatrix} \Sigma_{1,c} \\ v_{x1,c} \\ v_{y1,c} \end{pmatrix}, \tag{4.47}$$

where the subscript c denotes the initial amplitude of the perturbation, which is uniform in space and independent of time. Plugging this ansatz into (4.43)-(4.46) leads to the dispersion relationship:

$$\omega^2 = k_x^2 c_s^2 + \Omega_0^2 - 2k_x \Omega_0 c_s / Q, \tag{4.48}$$

with the Toomre parameter $Q = \Omega_0 c_s / (\pi G \Sigma_0)$. The eigenvector is given by:

$$\begin{pmatrix} \Sigma_{1,c} \\ v_{x1,c} \\ v_{y1,c} \end{pmatrix} = C_0 \begin{pmatrix} \Sigma_0 k_x \\ \pm\omega \\ i(2-q)\Omega_0 \end{pmatrix} \tag{4.49}$$

with a constant C_0 defining the initial amplitude. For $Q < 1$ the frequency ω becomes imaginary for wave numbers:

$$\frac{\Omega_0}{c_s}\left(\frac{1}{Q} - \sqrt{\frac{1}{Q^2} - 1}\right) \leq k_x \leq \frac{\Omega_0}{c_s}\left(\frac{1}{Q} + \sqrt{\frac{1}{Q^2} - 1}\right), \tag{4.50}$$

which means perturbations grow exponentially with growth rate $\gamma^2 = -\omega^2$. For other wavelengths, or $Q > 1$, the perturbations lead to an oscillation.

To test our code, we setup a box of size $L_x = L_y = 2\pi$, background density $\Sigma_0 = 1$, orbital frequency $\Omega_0 = 1$, isothermal sound speed $c_s = 1$ and add a perturbation with $k_x = 1$ of the form of the eigenvector (4.49) and $C_0 = 10^{-5}/(\Sigma_0 k_x)$. By varying G we can also change the initial Toomre number. For $Q < 1$ we determine the growth rate γ of the instability by integrating the square of the density deviations from the ground state, and for $Q > 1$ we define the oscillation frequency by measuring the position of the maximum and minimum of Σ_1. For $Q < 1$ we stop the simulation when Σ_1 grew by two orders of magnitudes and reaches an amplitude of 10^{-3}, while for $Q > 1$ we simulate until $t = 5$. We use two different initial resolutions of 128^2 and 512^2 cells with an initial Cartesian grid.

As one can see from the results in Fig. 4.14, both resolutions accurately describe the growth/oscillation of the perturbations away from $Q = 1$. Close to $Q = 1$ we find for the lower resolution run a smaller growth rate/larger frequency in comparison to the analytical result, but this deviation decreases for the higher resolution simulations.

Non-axisymmetric case (isothermal and adiabatic)

In the following, we will discuss non-axisymmetric perturbations ($k_y \neq 0$). In this case, the wavevector becomes time-dependent:

$$(k_x, k_y) = (k_{x0} + q\Omega_0 k_{y0} t, k_{y0}). \tag{4.51}$$

We set up a perturbation with $k_{x0} = -2$, $k_y = 1$ in a box of size $L_x = L_y = 2\pi$, with initial amplitudes

$$\begin{pmatrix}\Sigma_{1,c}\\ v_{x1,c}\\ v_{y1,c}\end{pmatrix} = 10^{-3}\begin{pmatrix}1\\ 1\\ i\end{pmatrix}, \tag{4.52}$$

isothermal sound speed $c_s = 1$ and Toomre parameter $Q_0 = 1.1358$, which corresponds to a gravitational constant $G = 0.280252$. There exists no analytical solution, which means we have to integrate equations (4.43)-(4.46) numerically. We use different initial resolutions and always a Cartesian grid, and compare in Fig. 4.15 the evolution of the rms velocity fluctuations with the expected one. If we increase the resolution, our results converge to the semi-analytical result.

We rerun these simulations with an adiabatic equation of state, which means we additionally have perturbations in the sound speed. We choose the adiabatic coefficient $\gamma = 5/3$, the same initial amplitude (4.52), constant background pressure $P_0 = 1$ and amplitude of the initial pressure perturbation $P_{1,c} = 10^{-3}$. As we show in Fig. 4.15, the results of our code converge to ones obtained by integrating equations (4.38)-(4.42).

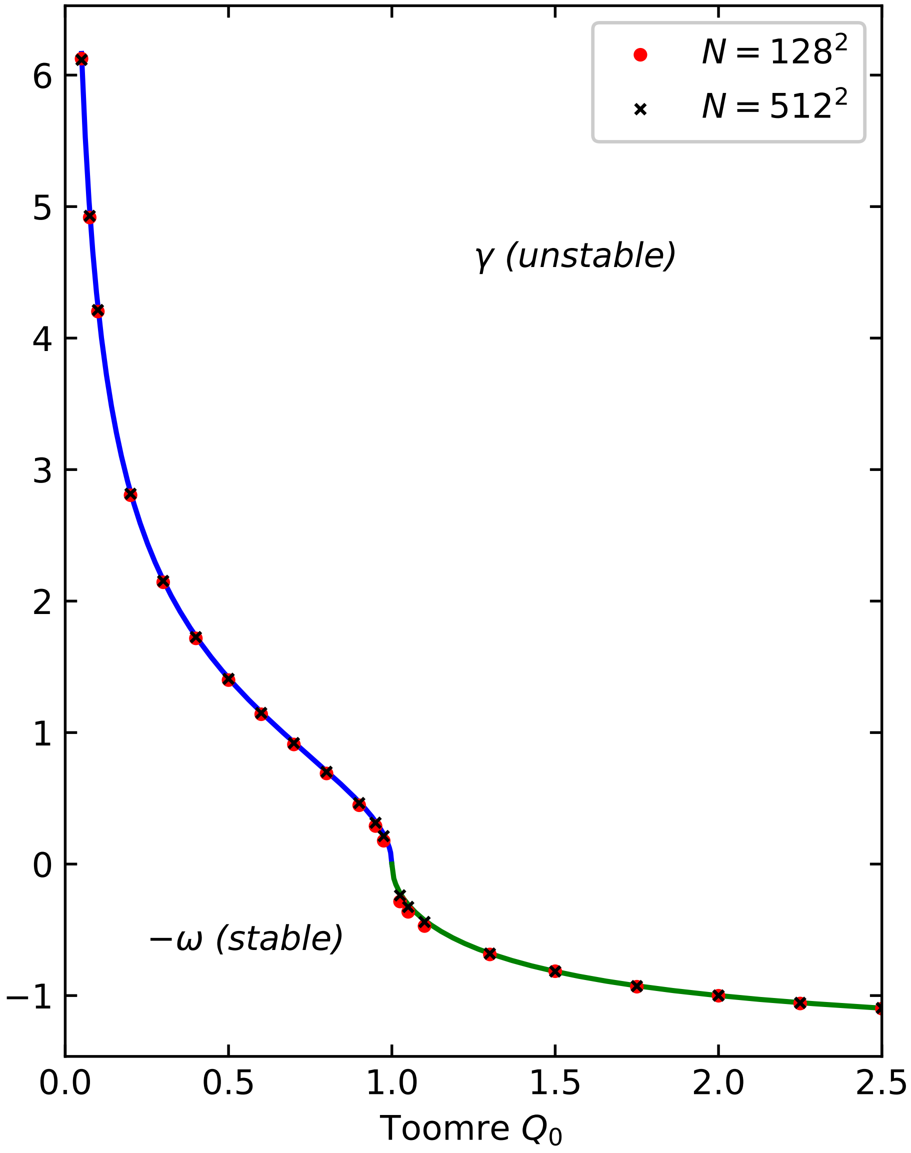

Figure 4.14: For the positive ordinate we show the linear growth rate γ of an axisymmetric perturbation as a function of the Toomre parameter Q_0, while for the negative ordinate we give the oscillation frequency $-\omega$. The solid lines present the solution of equation (4.48) and the symbols show results for simulations carried out with two different resolutions.

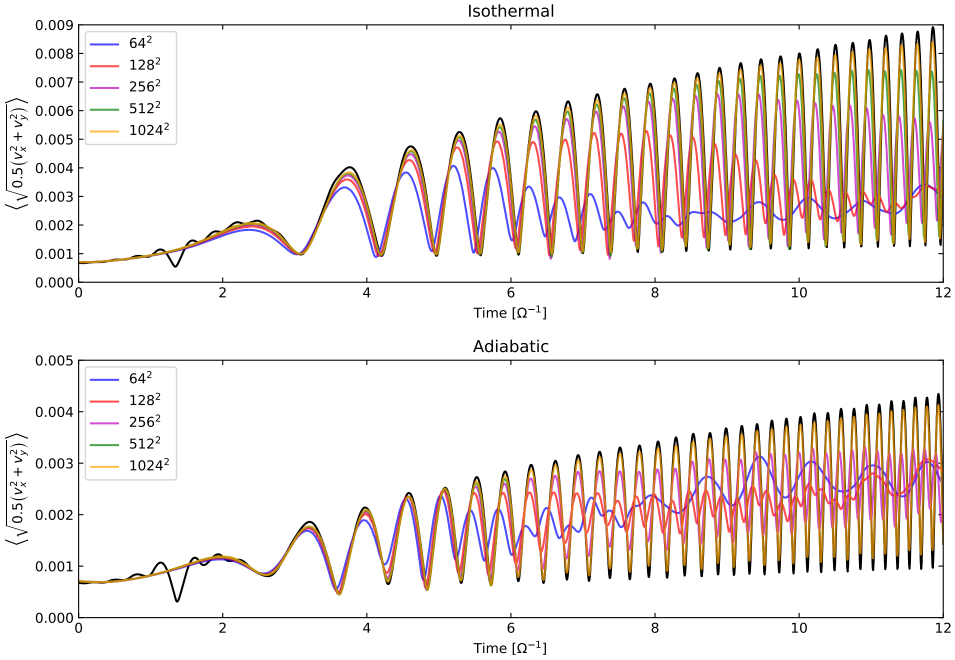

Figure 4.15: Root mean square velocity fluctuations of a non-axisymmetric hydrodynamic shearing wave. The upper panel shows the result for an isothermal equation of state, the lower panel gives them for an adiabatic equation of state. The black line is the semi-analytic solution obtained by integrating the linearized Euler equations. The coloured lines give the simulation results for different resolutions. Our numerical results converge to the expected solution.

4.7.2 Hydrostatic equilibrium in three dimensions

In this section, we test how well our code can sustain a vertical, hydrostatic equilibrium following the tests of Riols et al. (2017). We first introduce the sounds speed c_{s0} and density ρ_0 in the midplane, which leads to the definition of the isothermal Toomre parameter,

$$Q_{2\mathrm{D}_0} = \frac{c_{s0}\Omega}{\pi G \Sigma}, \tag{4.53}$$

as well as scale height $H_0 = c_{s0}/\Omega$.

The total vertical gravitational force is the sum of the contributions of self-gravity and the tidal potential, and only for the special cases that one of them can be neglected, an analytic solution exists. Otherwise, we have to solve the Poisson equation and the equation of hydrostatic equilibrium numerically. Following Riols et al. (2017), they can be combined into the single dimensionless equation:

$$\frac{1}{\gamma}\frac{\mathrm{d}}{\mathrm{d}\overline{z}}\left[\frac{1}{\overline{\rho}}\frac{\mathrm{d}\overline{\rho}^{\gamma}}{\mathrm{d}\overline{z}}\right] + 1 + \frac{\Delta}{Q_{2\mathrm{D}_0}}\overline{\rho} = 0, \tag{4.54}$$

where we introduced the dimensionless quantities $\overline{z} = z/H_0$, $\overline{\rho} = \rho/\rho_0$ and the ratio $\Delta = 4H_0\rho_0/\Sigma$. By fixing $\Sigma = 1$ and a value for $Q_{2\mathrm{D}_0}$ we can first start with a guess for ρ_0 which gives us the initial Δ. We then solve equation (4.54) with a finite-difference method and calculate the corresponding surface density. We compare it with our expected value, adapt our initial guess for ρ_0 and repeat the process iteratively until we find convergence in the surface density of our profile.

As a test, we calculate the profile for $Q_{2\mathrm{D}_0} = 1$ and an isothermal equation of state ($\gamma = 1$) as well as an adiabatic EOS ($\gamma = 5/3$). As one can see in Fig. 4.16 the additional self-gravity compresses the disk and leads to a smaller effective scale height.

To test our self-gravity implementation we set up a box of size $L_x \times L_y \times L_z = 1 \times 1 \times 12$, surface density $\Sigma = 1$, Toomre $Q_{2\mathrm{D}_0} = 1$, $c_{s0} = 1$ and an initial resolution of 20 cells per scale height. We use a target mass of $m_{\mathrm{target}} = 5 \times 10^{-5}$ and allow a maximum relative volume difference of 10 between neighbouring cells. We let the profile evolve for a time $1000\,\Omega^{-1}$ and show in Fig. 4.16 its final shape. In the isothermal case, the code can stabilize the profile. In the polytropic setup, the disk heats up in the low-density region which leads to an expansion of the disk. Close to the midplane the density profile stays stable.

4.8 Appendix: Inaccuracies in the PM force

The particle-mesh method can be divided into several sub-steps:

1. Binning of mass of the Voronoi cells onto a Cartesian grid.
2. Fourier transformation of the density.
3. Multiplication with the Green's function.

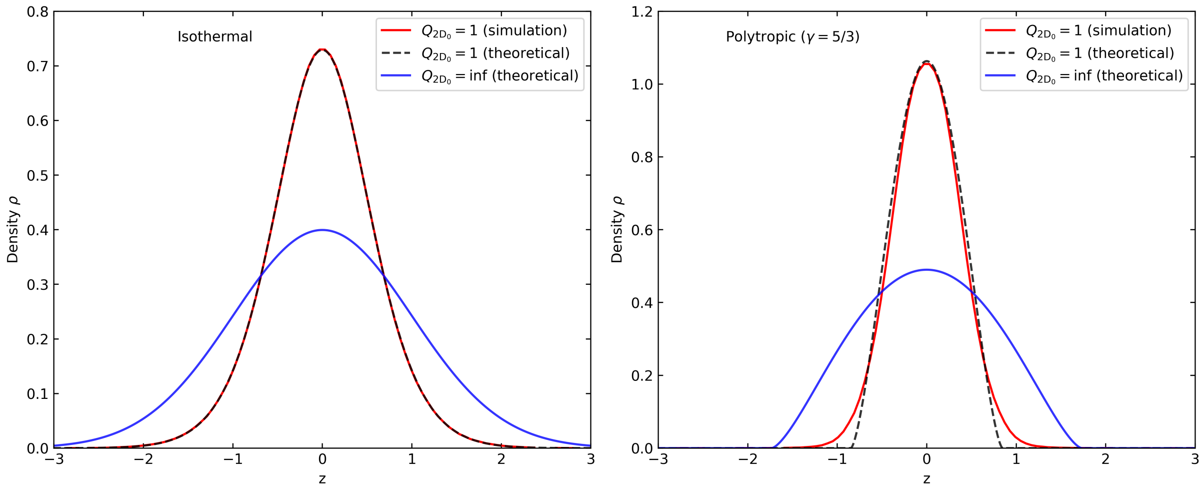

Figure 4.16: The vertical density profile for an isothermal (left) and polytropic gas with $\gamma = 5/3$ (right) in hydrostatic equilibrium. By comparing the blue and black-dashed lines we can see the compression of the disk by self-gravity. The red line shows measured profiles in our test simulations at $t = 1000\,\Omega^{-1}$. In the isothermal case, our code can sustain the profile to high quality while for the polytropic case the profile starts to broaden at the outer edge of the disk.

4. Inverse Fourier transformation.

5. Calculation of a force field by linear differencing.

6. Interpolating of forces from the Cartesian grid to the positions of the Voronoi mesh cells.

To ensure momentum conservation we have to use for the binning onto the Cartesian grid and for the interpolation of the force onto the Voronoi mesh the same kernel. Following Weinberger et al. (2020) we use the cloud-in-cell (CIC) assignment, which does not take into account the explicit geometric shape of the Voronoi cells. This can lead to the situation that even in a medium with constant hydrodynamic density, the density is not constant on the Cartesian grid and spurious forces can emerge. A similar effect can be observed for the tree algorithm, in which we also do not take into account the spatial extension of the Voronoi cells.

The physical density in a PM cell with volume V_j is given by:

$$\rho_{\mathrm{PM,j}} = \frac{\int_{V_j} \rho \,\mathrm{d}V}{\int_{V_j} \mathrm{d}V} = \frac{\sum_i \rho_i V_{i\cup j}}{\sum_i V_{i\cup j}} = \frac{\sum_i c_{i,j} \rho_i V_i}{\sum_i c_{i,j} V_i}, \tag{4.55}$$

where i denotes the Voronoi cells, and $V_{i\cup j}$ is the overlap of the two cells. We introduced here $c_{i,j} = V_{i\cup j}/V_i$, which is however very expensive to calculate due to its dependence on $V_{i\cup j}$. Since this expression represents a weighted average of densities, no new extrema can form. By introducing the weighting function

$$W_j(i) = c_{i,j} \frac{V_j}{\sum_i c_{i,j} V_i}, \tag{4.56}$$

equation (4.55) can be rewritten as:

$$\rho_{\mathrm{PM,j}} = \sum_i W_j(i) \rho_i V_i / V_j. \tag{4.57}$$

In the standard PM method, the weighting function gets approximated by replacing $c_{i,j}$ by the CIC assignment approximation in the numerator, and evaluating the denominator exactly, which means $\sum_i c_{i,j} V_i = V_j$. With this approximation, new extrema can form since the density on the PM grid is not a simple weighted sum of the densities on the Voronoi mesh.

As a natural extension, we could also use the CIC approximation in the denominator of the weighting function, which means the mass, as well as the volume of a Voronoi cell, get binned onto the mesh. This scheme is also momentum conserving if the same weighting function is used to interpolate the forces back onto the Voronoi mesh, but it does not conserve the mass, especially if there are empty PM cells from the CIC assignment. We, therefore, use in all production runs the standard PM binning except for the two-dimensional tests presented in Appendix 4.7.1.

Chapter 5

Rossby wave instability on a moving mesh

In this chapter, I present two-dimensional, global simulations of the Rossby wave instability. The results are not yet published in a scientific journal but I plan to submit them in the near future.

5.1 Introduction

Recent observations of protoplanetary disks (PPDs) have revealed a variety of non-axisymmetric distributions of dust (van der Marel et al., 2013; Long et al., 2019; Francis & van der Marel, 2020; van der Marel et al., 2021). They suggest therefore the presence of non-axisymmetric structures such as vortices in these disks (van der Marel et al., 2013; Baruteau et al., 2019). These vortices are of interest both from an observational and from a theoretical perspective. They can act as effective dust traps, locally increasing the dust density and facilitating the formation of planetesimals through gravitational collapse (Raettig et al., 2015, 2021). Additionally, vortices can interact with existing planets and influence their orbital migration (Li et al., 2009; Yu et al., 2010; Lin & Papaloizou, 2010; McNally et al., 2019). Vortices in simulations are often long living as the vortensity is approximately conserved. Therefore, from a theoretical perspective, one would expect to observe vortices if they are able to form (Lin & Pierens, 2018).

Several different instabilities have been proposed as potential mechanisms for the formation of vortices in protoplanetary disks, including the baroclinic instability (Klahr & Bodenheimer, 2003), the vertical shear instability (Arlt & Urpin, 2004; Nelson et al., 2013), the zombie vortex instability (Marcus et al., 2015), and the Rossby wave instability (Lovelace et al., 1999). Of these, the Rossby wave instability (RWI) is of particular interest. This instability can be triggered when disk properties change rapidly as a function of radius, such as in regions where gaps have been created by orbiting planets (Cimerman & Rafikov, 2023) or at the boundary between a magnetically dead region and an MRI active region (Varnière & Tagger, 2006; Lyra & Mac Low, 2012). As these regions are likely to exist in PPDs, the RWI is considered a likely mechanism for the formation of vortices in these disks.

The RWI can be described in two dimensions. Lovelace et al. (1999) derived as a necessary condition for the RWI that the background flow contains at least one extremum in the vortensity profile:

$$\mathcal{L} = \frac{\Omega\Sigma}{\kappa^2} S^{2/\gamma}, \tag{5.1}$$

where we introduced the entropy $S = P/\Sigma^\gamma$, the surface density Σ, the rotational frequency Ω, the epicycle frequency κ, and the adiabatic coefficient γ. Ono et al. (2016) performed a linear stability analysis in a simplified model assuming a barotropic equation of state and an axisymmetric density variation. They derived a necessary and sufficient condition for the RWI semi-analytically. In Ono et al. (2018) they extended this study by performing direct simulations using the ATHENA++ code and verified the linear stability analysis. They also investigated the saturation of the RWI and found the formation of a single, long-living vortex that slowly migrates inwards. However, this study neglected important physics that can have an influence on the RWI, such as self-gravity (Lovelace & Hohlfeld, 2013; Yellin-Bergovoy et al., 2016; Lin & Pierens, 2018; Rendon Restrepo & Barge, 2022), magnetic fields (Yu & Li, 2009), viscosity (Lin, 2014), the interaction with dust (Lyra et al., 2008, 2009), or a non-barotropic equation of state (Tarczay-Nehéz et al., 2020; Fung & Ono, 2021; Huang & Yu, 2022). Despite these limitations, this setup is attractive for a parameter study due to its simplicity and includes the most important physics to trigger the RWI.

To accurately model the nonlinear evolution of a vortex, a numerical method with low numerical viscosity is necessary. One option is to use a grid geometry that is specifically tailored to the problem, such as the polar grid used in Ono et al. (2018) or specialized codes like DISCO (Duffell, 2016). Another option is to use a moving mesh code like AREPO (Springel, 2010a; Weinberger et al., 2020), which allows the computational mesh to move with the gas flow. Unlike static grid codes, AREPO is Galilei invariant and has low advection errors, as the rotation can be incorporated into the mesh movement and its quasi-Lagrangian nature allows for higher resolution in dense regions. However, the irregularity of the mesh can introduce numerical errors. Indeed, the moving-mesh method has been known to suffer from so-called grid noise, which can however be reduced by using a higher-order flux integration as discussed in Zier & Springel (2022a).

In this Chapter, we demonstrate that AREPO can accurately simulate the linear and nonlinear evolution of the RWI by comparing our results with those obtained by Ono et al. (2018). This research corroborates our previous studies, which have shown that AREPO can resolve the magnetorotational instability (MRI) and the gravitational instability (GI) with similar accuracy to static grid codes (Zier & Springel, 2022b, 2023). Therefore, we conclude that AREPO can be used to achieve high-accuracy simulations of disk systems, particularly in cases where an optimized grid geometry cannot be constructed from the initial conditions or when a spatially varying resolution is needed. This is especially relevant for studying with high resolution the inner evolution of vortices formed by the RWI.

This Chapter is organized as follows: In Section 5.2, we present the initial conditions and numerical techniques utilized in this study. We also introduce a new Fourier filter for the AREPO code, which allows for the analysis and manipulation of different Fourier modes during runtime. In Section 5.3, we investigate the impact of resolution and accuracy on the linear and nonlinear evolution of the RWI. We also use the Fourier filter to compare the exponential growth rate of modes in isolation with theoretical predictions. Finally, in Section 5.4, we summarize and discuss our results.

5.2 Disk model and numerical methods

5.2.1 Model

In the present study we use the model h10w3g1 described in Ono et al. (2016) and Ono et al. (2018), which can be concisely summarized as follows. We consider a global, purely hydrodynamic two-dimensional disk with surface density profile $\Sigma(r, \phi)$ and velocity $\boldsymbol{v}$, which rotates around a central object with mass M at $(x, y) = (0, 0)$. The temporal evolution of the gas can be described by the Euler equations in Cartesian coordinates,

$$\frac{\partial U}{\partial t} + \nabla \cdot \boldsymbol{F} = \boldsymbol{S}_{\rm grav}. \tag{5.2}$$

$\boldsymbol{U}$ describes the conserved variables, $F(\boldsymbol{U})$ gives the flux function, and $\boldsymbol{S}_{\rm grav}$ is a source term due to the central object. They are given explicitly by:

$$\boldsymbol{U} = \begin{pmatrix} \Sigma \\ \Sigma \boldsymbol{v} \end{pmatrix}; F(\boldsymbol{U}) = \begin{pmatrix} \Sigma \boldsymbol{v} \\ \Sigma \boldsymbol{v}\boldsymbol{v}^T + P \end{pmatrix}; \boldsymbol{S}_{grav} = \begin{pmatrix} 0 \\ -\Sigma \frac{GM}{r^2} \frac{\boldsymbol{r}}{r} \end{pmatrix} \tag{5.3}$$

in the local rest frame with $\boldsymbol{r} = (x, y)$. The system of equations is closed by a barotropic equation of state:

$$P = S_0 \Sigma^{\Gamma}, \tag{5.4}$$

where P is the pressure, S_0 is the constant entropy and $\Gamma = 5/3$ is the adiabatic index. In the following, we will use cylindrical coordinates r, ϕ, although we note that we will solve the Euler equations using Cartesian coordinates. We use static $(\partial/\partial t = 0)$, axisymmetric $(\partial/\partial \phi = 0)$ initial conditions with a purely circular flow $(v_r = 0)$. The initial density profile is given by:

$$\Sigma_0(r) = \Sigma_{\rm back} \left(1 + A_0 \exp\left[-\frac{1}{2} \left(\frac{r - r_n}{\Delta w_0} \right)^2 \right] \right), \tag{5.5}$$

where $\Sigma_{\rm back} = 1$ describes the background density and the second term is a superimposed Gaussian peak that can be unstable to the RWI. $A_0 = 0.439$ gives the height of the peak, $r_n = 1$ the position of maximum density, and $\Delta w_0 = 0.0632$ is the width of the peak. As in Ono et al. (2018) we define the non-dimensional parameter:

$$h = \frac{\sqrt{\Gamma S_0 \Sigma_{\rm back}^{\Gamma - 1}}}{r_n \Omega_n}, \tag{5.6}$$

where $\Omega_n = \sqrt{GM/r_n^3}$ is the Keplerian frequency at radius r_n. The initial entropy S_0 is then given by:

$$S_0 = \frac{h^2}{\Gamma} \frac{(r_n \Omega_n)^2}{\Sigma_{\text{back}}^{\Gamma-1}}, \tag{5.7}$$

which means h can be understood as a measure of the initial disk temperature. We use $h = 0.1$ exclusively in this chapter. The condition $\partial v_r / \partial t = 0$ leads to the rotation profile:

$$v_{\phi,0} = \sqrt{\frac{GM}{r} + r \frac{\mathrm{d}\Pi_0}{\mathrm{d}r}}, \tag{5.8}$$

with the pressure function $\Pi_0(r) = \Gamma S_0 \Sigma_0^{\Gamma-1}/(\Gamma - 1)$. The initial conditions can therefore be uniquely characterized by the parameters A_0, Δw_0 and h. They also determine the growth rate $\gamma_*(A_0, \Delta w_0, h)$ of the fastest growing mode, which is, in general, a monotonous function of A_0 for fixed Δw_0 and h (Ono et al., 2016).

5.2.2 Numerical methods

To solve equation (5.2) we use the AREPO code (Springel, 2010a; Pakmor et al., 2016b; Weinberger et al., 2020) that employs a moving, unstructured Voronoi mesh in combination with the finite volume method. In Zier & Springel (2022a) we showed that the original version of the code suffered from noise on the grid scale for shear flows as present in a Keplerian disk. We, therefore, use in this paper typically the higher order flux integration rules presented in Zier & Springel (2022a) that drastically reduce the grid noise, but in some examples, we also use the old integration rules for comparison. We use the HLLC Riemann solver and implement the gravity source term by using a standard Strang splitting scheme in the time integration.

We use a natural system of units where $r_n = 1$, $M = 1$, and $G = 4\pi^2$, such that one time unit is equal to the rotational period at $r = r_n$ for a purely Keplerian orbit. Our simulations cover the disk radius of $r_{\text{in}} < r < r_{\text{out}}$ with $r_{\text{in}} = 0.25$ and $r_{\text{out}} = 2.6$. Since we are interested in the Rossby wave instability, which appears close to $r = r_n$, we want to avoid that the boundaries can influence the results. We especially want to prevent any waves being reflected or launched at the boundaries. Ono et al. (2018) used non-reflective boundary conditions (Godon, 1996), which are complicated to implement on a Voronoi mesh and we, therefore, use instead a wave damping region, whose implementation we will discuss in the next section in detail.

To ensure a constant mass resolution during the simulation time we allow the splitting or merging (refinement and derefinement operations) of cells if their mass m_i exceeds a predefined target mass m_{target} by a factor two, or falls below half of the target mass. As in Ono et al. (2018) we want to resolve h (see equation (5.6)) by at least 25 cells. Since we cannot guarantee a fixed spatial resolution with our refinement/derefinement strategy, we use the background density Σ_{back} and set the target mass to $m_{\text{target}} = \Sigma_{\text{back}} \left(0.04h\right)^2$.

For the initial conditions, we use a cylindrical mesh that is iteratively constructed starting from $r = r_{\text{in}}$. The radial size of each subsequent circle of cells is determined by calculating the density $\Sigma(r)$ at the current radius r and setting $\Delta r = \sqrt{m_{\rm target}/\Sigma(r)}$. The number of cells in the ϕ direction is then set to $N_\phi = 2\pi r/\Delta r$, which guarantees cells with a nearly unity aspect ratio. The mesh generation ends when $r = r_{\rm out}$ is reached. This minimizes the number of initial refinement and derefinement operations, which can add unwanted noise to the initial conditions.

Implementation of boundary conditions

To reduce the impact of the boundary on the RWI we use a multi-level approach. First, we create two circular layers of cells that touch each other at $r = r_{\rm in}$ and rotate with the angular frequency $\Omega = \sqrt{GM/r_{\rm in}^3}$. Besides the cell movement, we treat the outer layers as normal hydrodynamic cells, while we do not save the hydrodynamic state of the inner layer. Instead, we use inflow-outflow boundary conditions for the Riemann problems between cells from the inner and outer layers. Cells which come close to the outer layer and can potentially penetrate the surface at $r = r_{\rm in}$ are automatically derefined. For $r_{\rm in} < r < r_1$ we set the state of all cells at every time step to their initial values. This ensures that at $r = r_1$ the non-Lagrangian motion of the cells at $r = r_{\rm in}$ does not influence the boundaries anymore. In tests we found that this boundary treatment between freely evolving cells and cells with fixed hydrodynamic states allows for the reflection of generated hydrodynamic waves. We therefore add another area, $r_1 < r < r_2$, in which we relax the hydrodynamic quantities to their initial values. In practice we use the following expression for the relaxation:

$$\frac{\mathrm{d}\boldsymbol{X}}{\mathrm{d}t} = -\frac{\boldsymbol{X} - \boldsymbol{X}_0}{T\left(r_0\right)} C \left(\frac{r_2 - r}{r_2 - r_1}\right)^2 , \tag{5.9}$$

with $\boldsymbol{X} = (\Sigma, v_r, v_\phi)$, $\boldsymbol{X}_0$ being the background state, the constant $C = 8$ is used to describe the strength of the relaxation, and the orbital time at $r = r_0$ is $T\left(r_0\right)$. For the outer boundary at $r_{\rm out}$ we use a similar approach with relaxation:

$$\frac{\mathrm{d}\boldsymbol{X}}{\mathrm{d}t} = -\frac{\boldsymbol{X} - \boldsymbol{X}_0}{T\left(r_3\right)} C \left(\frac{r - r_4}{r_3 - r_4}\right)^2 . \tag{5.10}$$

We choose the radii $r_{\rm in} = 0.2$, $r_1 = 0.25$, $r_2 = 0.5$, $r_{\rm out} = 2.6$, $r_4 = 2.5$ and $r_3 = 2.125$. In Fig. 5.1 we show an example of the different areas in our simulation, and in Appendix 5.5 we demonstrate that our implementation of the boundary conditions significantly damps hydrodynamic waves and reduces the artefacts due to the boundaries.

Fourier filtering

To analyze the growth of instabilities it is often useful to decompose the density and velocity fields into Fourier modes, e.g.:

$$\Sigma(r, \phi) = \sum_m \Re\left(\Sigma_m(r) e^{\mathrm{i}m\phi}\right) . \tag{5.11}$$

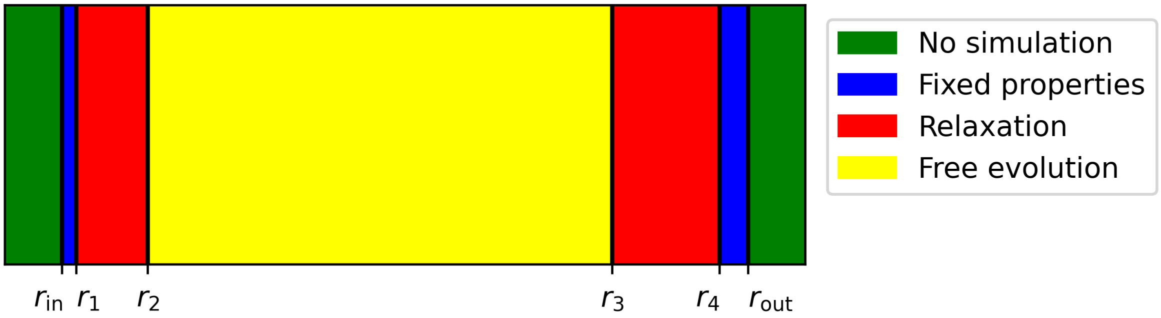

Figure 5.1: Sketch of the employed strategy to reduce the effect of boundary conditions. Between r_{in} and r_1 as well as between r_4 and r_{out} we overwrite at each time step the properties of cells with the initial conditions. Between r_1 and r_2 as well as between r_3 and r_4 we relax the hydrodynamic quantities over a finite time to the initial ones and between r_2 and r_3 we let them freely evolve.

Here $\Sigma_m(r)$ are the Fourier coefficients, which are functions of radius r and can evolve in time. The idea to filter specific modes in Fourier space to analyze the evolution of individual modes of the RWI was already implemented in Ono et al. (2018) for a cylindrical mesh in Athena++. For this mesh configuration, the Fourier coefficients can be obtained by one fast Fourier transformation (FFT) per cell ring. On a Voronoi mesh, the Fourier transformation is not directly possible. Instead, we additionally have to implement a mapping from the Voronoi mesh to a regular cylindrical grid, and for our Fourier cleaning approach, an additional mapping back to the Voronoi mesh. For the cylindrical mesh, we use a uniform size of the cells in the radial and azimuthal directions. We choose the number of cells in both directions, such that the cells at $r = r_n$ have an aspect ratio of 1, which means $r_n \mathrm{d}\phi = \mathrm{d}r$ should hold. To ensure an accurate representation of the density and velocity fields on the cylindrical grid we demand that a Voronoi cell at $r = r_n$ with density $\rho_{\max} = 1 + A_0$ should be resolved by approximately 16 cells. This leads to the condition $m_{\text{target}} \approx 16\rho_{\max} r_n \mathrm{d}\phi\, \mathrm{d}r = 16\rho_{\max}\mathrm{d}r^2$ or

$$\mathrm{d}r = \sqrt{\frac{m_{\text{target}}}{16\rho_{\max}}}. \tag{5.12}$$

For the mapping of the Voronoi mesh to the cylindrical mesh, we first find for every cell of the cylindrical mesh the Voronoi cell in which its centre lies. We then extrapolate the density or velocity from the centre of the Voronoi cell to the centre of the cylindrical cell using the gradient information of the code. For mapping the cylindrical mesh back to the Voronoi mesh we perform a bilinear interpolation in cylindrical coordinates using the 4 nearest cells of the cylindrical grid.

We perform these operations for the density Σ as well as the radial velocity v_r and the azimuthal velocity v_ϕ. Even without modifications of the Fourier coefficients the mapping to the cylindrical mesh and back to the Voronoi mesh is not conservative but it adds additional noise. To reduce this noise we actually use the velocity $v_\phi - v_{\text{keplerian}}(r)$ instead of

v_ϕ in the steps above. Also, we specifically calculate the gradients of v_r and $v_\phi - v_{\mathrm{keplerian}}(r)$ for the binning to the cylindrical mesh instead of the standard gradients of v_x and v_y. In Appendix 5.6 we show that the impact of the noise from this method on a simulation without Fourier filtering is negligible.

5.2.3 Overview of simulations

In Table 5.1 we give an overview of all simulations we discuss in this chapter. We perform simulations in which we use the Fourier filter only to measure the evolution of Fourier modes but otherwise do not change the properties of the Voronoi cell. To better understand the evolution of individual modes we also perform simulations with a mode-filtering for the density Σ and the velocity components v_r and v_ϕ, which means we decompose the fields into their Fourier modes and set some of the Fourier coefficients to zero. We call it an axisymmetric filter if we set all components $m \neq 0$ to 0 and a single-mode filter if we remove all modes except the axisymmetric mode and a specific mode $m = k$. This mode-filtering is performed every 0.04 time units and is described in more detail in Section 5.2.2.

We also use the Fourier technique to create well-defined initial conditions. First, we set up the grid as described above, and in simulations with a single-mode filter, we set for the radial velocity $v_{r,k} = 10^{-6}\, v_{\phi,0} \exp\left(\left[\left(r/r_n - 1\right)/0.2\right]^2\right)$ to trigger the instability. For simulations without mode filtering, we add this noise to the Fourier coefficients of all modes with $1 \leq m \leq 128$.

5.3 Evolution of the Rossby wave instability

In Fig. 5.2 we show the temporal evolution of the surface density in our default run without Fourier filtering. At approximately $t = 7.5$ the ring starts to become unstable leading to the formation of five vortices, which are still connected by over-dense regions. Subsequently, density waves are generated which can transport angular momentum. By $t = 9$ the formation of five distinct vortices has been completed. Over time, the vortices continue to merge until only one large vortex remains at $t = 22$. This final vortex rotates around the central object and gradually moves closer to it. This evolution is qualitatively consistent with the findings in Ono et al. (2018), although they reported the initial formation of four vortices instead of five.

5.3.1 Linear growth

To quantitatively analyse the RWI we use in this section the Fourier filter to better understand the exponential growth rate of different modes in the linear and weakly nonlinear regime. In Fig. 5.3 we show the evolution of different modes in simulations in which we let all modes evolve freely. Initially, the amplitudes of all modes are quite noisy, but later one can observe a nearly perfect exponential growth with the expected growth rate, especially for the fastest growing modes ($m = 4, 5$). The initial noise can be explained on the one

Name	m_{target}	N_r	N_ϕ	Flux integration	Modes	Section
AllNRO	1.6×10^{-5}	3200	7800	2nd order	all	5.3.1 & 5.3.2
AllNR	1.6×10^{-5}	3200	7800	4th order	all	5.3.1 & 5.3.2
AllLR	6.4×10^{-5}	1600	3900	4th order	all	5.3.1 & 5.3.2
AllHR	4×10^{-6}	6400	15600	4th order	all	5.3.1 & 5.3.2
M1NR	1.6×10^{-5}	3200	7800	4th order	0, 1	5.3.1
M2NR	1.6×10^{-5}	3200	7800	4th order	0, 2	5.3.1
M3NR	1.6×10^{-5}	3200	7800	4th order	0, 3	5.3.1
M4NR	1.6×10^{-5}	3200	7800	4th order	0, 4	5.3.1
M5NR	1.6×10^{-5}	3200	7800	4th order	0, 5	5.3.1
M6NR	1.6×10^{-5}	3200	7800	4th order	0, 6	5.3.1
M7NR	1.6×10^{-5}	3200	7800	4th order	0, 7	5.3.1
M8NR	1.6×10^{-5}	3200	7800	4th order	0, 8	5.3.1
M9NR	1.6×10^{-5}	3200	7800	4th order	0, 9	5.3.1
M1NRO	1.6×10^{-5}	3200	7800	2nd order	0, 1	5.3.1
M2NRO	1.6×10^{-5}	3200	7800	2nd order	0, 2	5.3.1
M3NRO	1.6×10^{-5}	3200	7800	2nd order	0, 3	5.3.1
M4NRO	1.6×10^{-5}	3200	7800	2nd order	0, 4	5.3.1
M5NRO	1.6×10^{-5}	3200	7800	2nd order	0, 5	5.3.1
M6NRO	1.6×10^{-5}	3200	7800	2nd order	0, 6	5.3.1
M7NRO	1.6×10^{-5}	3200	7800	2nd order	0, 7	5.3.1
M8NRO	1.6×10^{-5}	3200	7800	2nd order	0, 8	5.3.1
M9NRO	1.6×10^{-5}	3200	7800	2nd order	0, 9	5.3.1
M0LR	6.4×10^{-5}	1600	3900	4th order	0	5.5
M0NR	1.6×10^{-5}	3200	7800	4th order	0	5.5
M0HR	4×10^{-6}	6400	15600	4th order	0	5.5
AllNRBin	4×10^{-6}	3200	7800	4th order	all (with binning)	5.6

Table 5.1: Overview of all simulations performed in this chapter. A target mass resolution, m_{target}, is defined, and for the polar mesh, there are N_r cells in the radial direction and N_ϕ cells in the polar direction. We typically use the higher-order flux integration method presented in Zier & Springel (2022a), but sometimes revert to the older second-order accurate method for comparison. In certain simulations, a Fourier filter is utilized to allow only certain modes to grow.

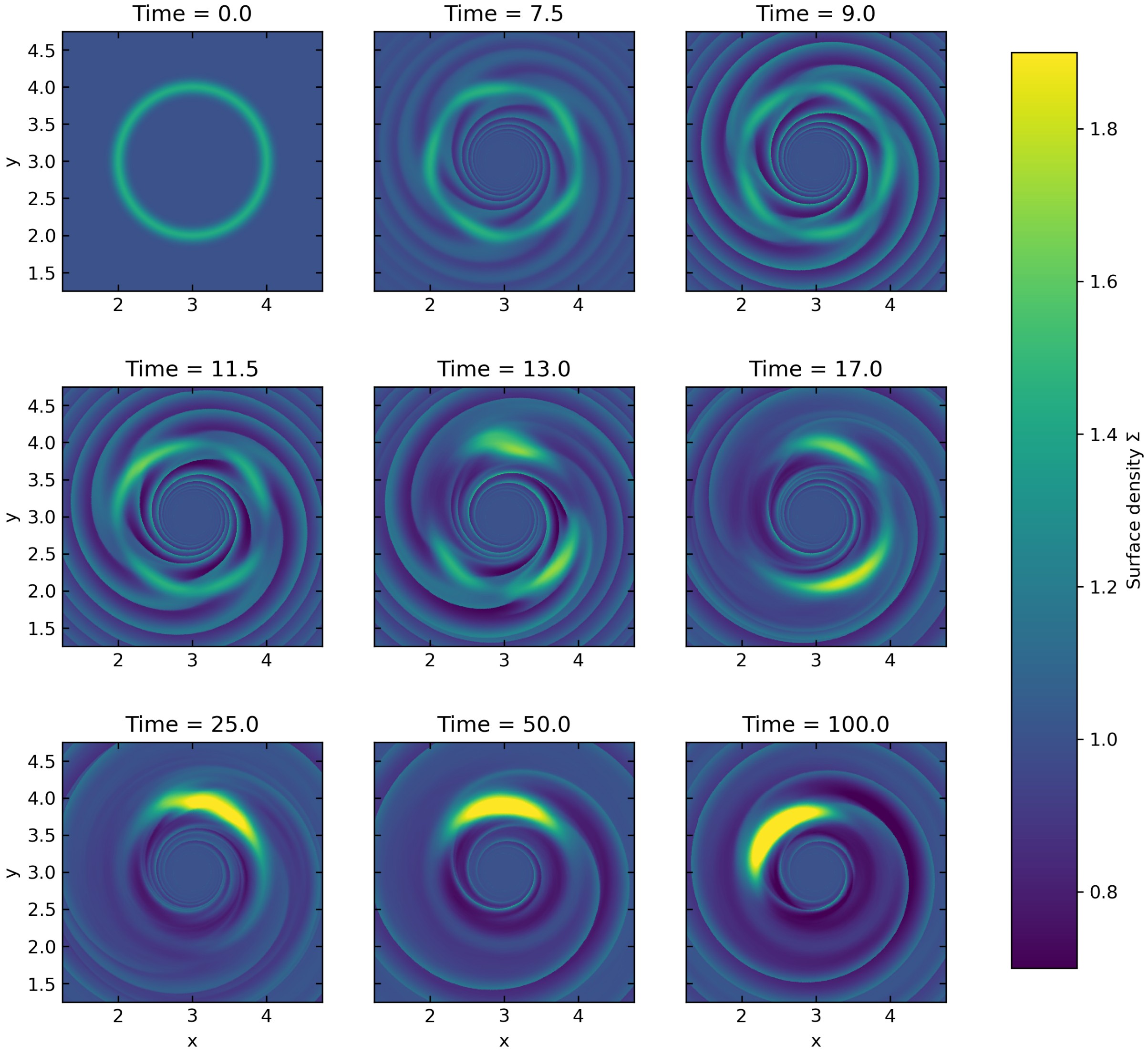

Figure 5.2: The surface density at different times in the simulation AllNR.

Mode m	$\lambda\,[\Omega^{-1}]$ (isolation)	$\lambda\,[\Omega^{-1}]$ (mode coupling)
1	0.103	0.478 (4 - 3)
2	0.184	-
3	0.232	-
4	0.246	-
5	0.230	-
6	0.188	-
7	0.122	0.478 (4 + 3)
8	0.04	0.492 (4 + 4)
9	0	0.476 (4 + 5)

Table 5.2: The linear growth rates λ of the Rossby wave instability for different modes. Mode coupling can cause some modes to grow faster in the nonlinear regime, but we only present the relevant modes that impacted our simulations.

hand by numerical noise and on the other hand by a finite amount of time until the system finds the eigenvector with the largest growth rate. The noise becomes smaller if we increase the resolution, and if we use the higher order flux integration from Zier & Springel (2022a). At a later time, we can also observe a larger growth rate in the $m = 1, 7, 8, 9$ modes which can be explained by the coupling of faster-growing modes in the weakly nonlinear regime. But also for the nonlinear regime, the new higher-order flux integration leads to cleaner results, since the old integration scheme continuously adds new noise on the grid scale. This is especially severe for modes with smaller wavelengths. The linear regime for the fastest-growing modes ends when the modes approximately reach an amplitude of 0.1.

To suppress the nonlinear coupling between modes we have also performed simulations with filtering in Fourier space, which means we only allow a certain mode m and the corresponding axisymmetric mode to evolve. In Fig. 5.4 we show the temporal evolution of the amplitude of those modes. In all simulations except for the modes $m = 8$, and 9 we find a regime of exponential growth with perfect agreement with the expected growth rate. The simulations with the less accurate flux integration show initially larger noise, but at later times the results are very similar to those obtained with the higher order flux integration. The growth saturates after reaching an amplitude of around 0.1. For the $m = 8$ mode, we also observe a growth of the instability with both flux integration methods. But the growth cannot be described by an exponential growth but seems to grow faster than expected. This can be explained by the fact that the $m = 8$ mode is dominated by the density waves and actually not by vortices in our simulations. The density waves can be influenced by the inner boundary which could lead to numerical artefacts. The $m = 9$ mode should be stable, but we nevertheless see some slow growth which seems to be fuelled initially by numerical noise.

Our results with the higher order flux integration compare well with those from Ono et al. (2018), with the exception of the $m = 8$ and $m = 9$ modes. They however also observed initially some noise in the modes before the exponential growth starts, and the modes also saturated when they reached an amplitude of around 0.1.

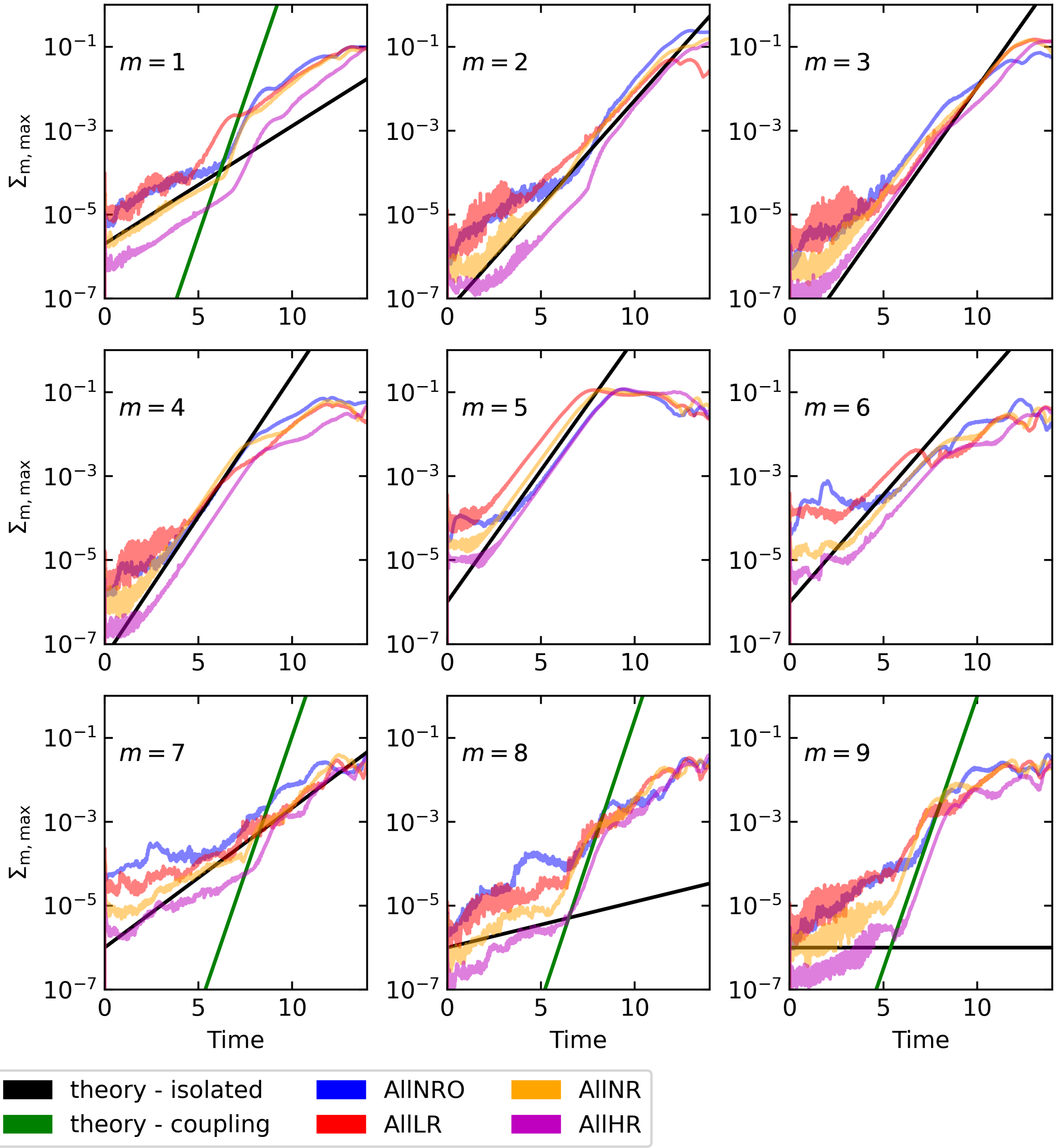

Figure 5.3: The temporal evolution of the maximum absolute value $\Sigma_{\rm m,max}$ of the Fourier mode $\Sigma_m(r)$ in the radial range $0.8 < r < 1.2$. We use the white noise simulations for this plot, and allow all Fourier modes to evolve freely. The black line corresponds to the isolated linear growth rate from semi-analytic calculations, and the green line to the linear growth rate by mode coupling (see Table 5.2).

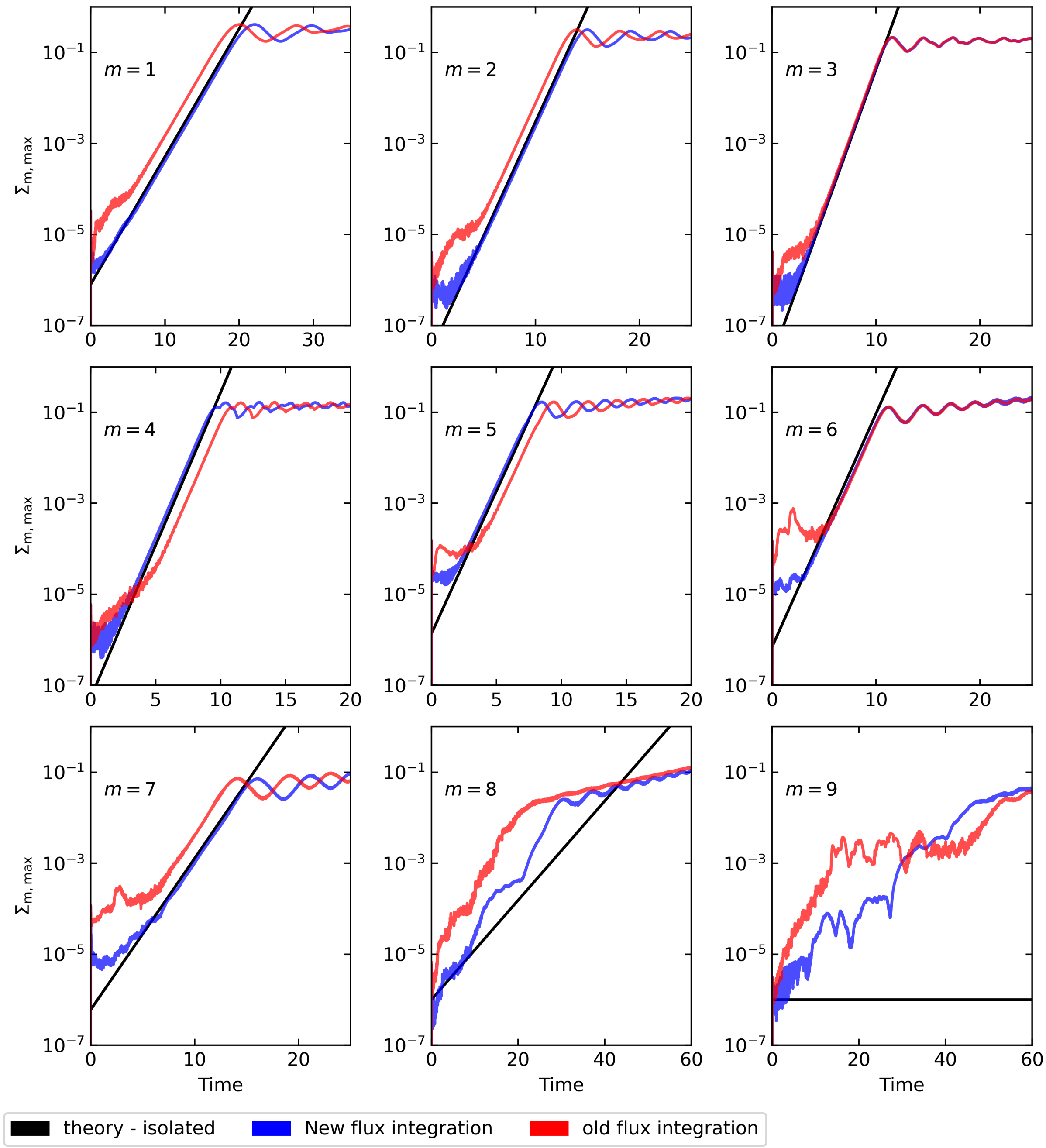

Figure 5.4: The temporal evolution of the maximum absolute value $\Sigma_{\mathrm{m,max}}$ of the Fourier mode $\Sigma_m(r)$ in the radial range $0.8 < r < 1.2$. In this plot, we show the results of simulations in which we use the Fourier filter to only allow the evolution of the mode m and the corresponding axisymmetric mode. The black line corresponds to the linear growth rate from semi-analytic calculations (see Table 5.2).

Simulation	$m = 5$	$m = 4$	$m = 3$	$m = 2$	$m = 1$
AllNRO	8.0 - 11.4	11.4 - 12.8	12.8 - 13.4	13.4 - 20.4	20.4 -
AllLR	7 - 11.4	11.4 - 12.6	12.6 - 16.4	16.4 - 36.8	36.8 -
AllNR	7.4 - 11.6	11.6 - 12.2	12.2 - 14.8	14.8 - 22	22 -
AllHR	8.0 - 12.8	12.8 - 13.4	13.4 - 15.3	15.3 -21.6	21.6-

Table 5.3: The intervals in which we find m vortices.

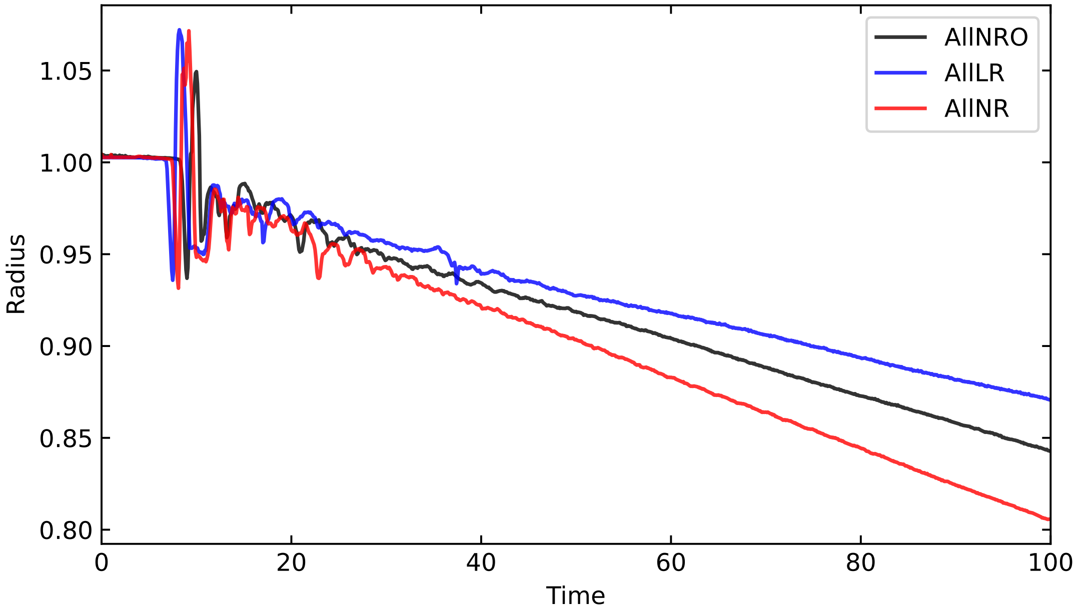

Figure 5.5: The temporal evolution of the distance between the central object and the vortices (see equation (5.13)). One can observe in all simulations a radial migration inwards.

5.3.2 Nonlinear evolution

As we can see in Fig. 5.2, the vortices merge over time into a single vortex. As in Ono et al. (2018) we observed the remaining vortex to migrate inwards and be finally destroyed. To estimate the probability to observe a specific amount of vortices it is therefore important to measure the lifetime of each individual phase. For all our simulations without a Fourier filter we, therefore, measure the time of how long a certain number of vortices survived. We identify the number of vortices by visual inspection and use the quantify $v_\phi - v_{\mathrm{keplerian}}$. Since the merger of two vortices takes a finite amount of time this leads to small inaccuracies of a few tenths of an orbit. In Table 5.3 we summarize our results for the different simulations. The regimes with more than two orbits only last for a maximum of 4 orbits whereas two vortices can survive for up to 20 orbits. The remaining vortex is stable and can survive for several 100 orbits. As mentioned by Ono et al. (2018), the survival time of several vortices can depend on the initial phases of different Fourier modes, and we do not expect any convergence for the survival time if we increase the resolution.

To analyse the radial migration of the remaining vortex we define its average distance to the central object as:

$$r_{\mathrm{vortex}} = \frac{\sum_i r_i M_i}{\sum_i M_i}, \tag{5.13}$$

where the sums go over all Voronoi cells with 0.8 times the maximum density in the simulation. This ensures that we only take into account the densest gas. In Fig. 5.5 we show the temporal evolution of the radial coordinate and we observe in all simulations a migration with approximately constant radial velocity. The radial migration can be explained by the density waves we also observe in Fig. 5.2. These waves can transport angular momentum outwards and inwards, but due to geometrical effects the outer waves transport more angular momentum (Paardekooper et al., 2010), which causes the vortex to lose angular momentum. The resulting migration rate depends on the size as well as the shape of the vortex, as well as on the properties of the background disk. If we increase the resolution the vortex migrates faster, with a distance of around $0.8\, r_n$ after 100 orbits, which compares well with the results from Fig. 9 in Ono et al. (2018). The simulation with the less accurate flux integration lies between the standard and low-resolution simulation, hinting that the lower-order flux integration decreases the effective resolution of the simulation.

5.4 Discussion and summary

In this chapter, we analyzed the linear and nonlinear evolution of the Rossby wave instability in two-dimensional, global simulations of a barotropic disk with an axisymmetric overdensity on a moving mesh. This relatively simple system is very attractive since it allows for a linear stability analysis (Ono et al., 2016). To compare our results with the theoretical expectations we implemented a novel Fourier filter for the moving mesh code AREPO that maps hydrodynamic properties from a Voronoi mesh to a polar mesh on which we can perform Fourier transformations. After modifying the Fourier coefficients we can map the quantities back onto the Voronoi mesh. By using this filter we found almost perfect agreement between the linear growth rates in our simulations and the semi-analytical ones from Ono et al. (2016). We also observed in the weakly nonlinear regime the growth of additional modes through mode coupling. Using the more accurate flux integration from Zier & Springel (2022a) reduced in general the initial noise and allowed us to observe the exponential growth over a larger time interval. For the $m = 8$ mode, we observed larger noise and not a perfectly exponential growth in our simulations, which we attribute to the potential effects of the inner boundary. For all other modes, our results compare well with those from Ono et al. (2018), which were obtained on a static, polar grid which is specifically optimized for this problem.

In the nonlinear regime, we found that the vortices merge within approximately 20 orbits. The remaining vortex migrates inwards within several hundred orbits, due to the interaction with density waves launched from the vortex.

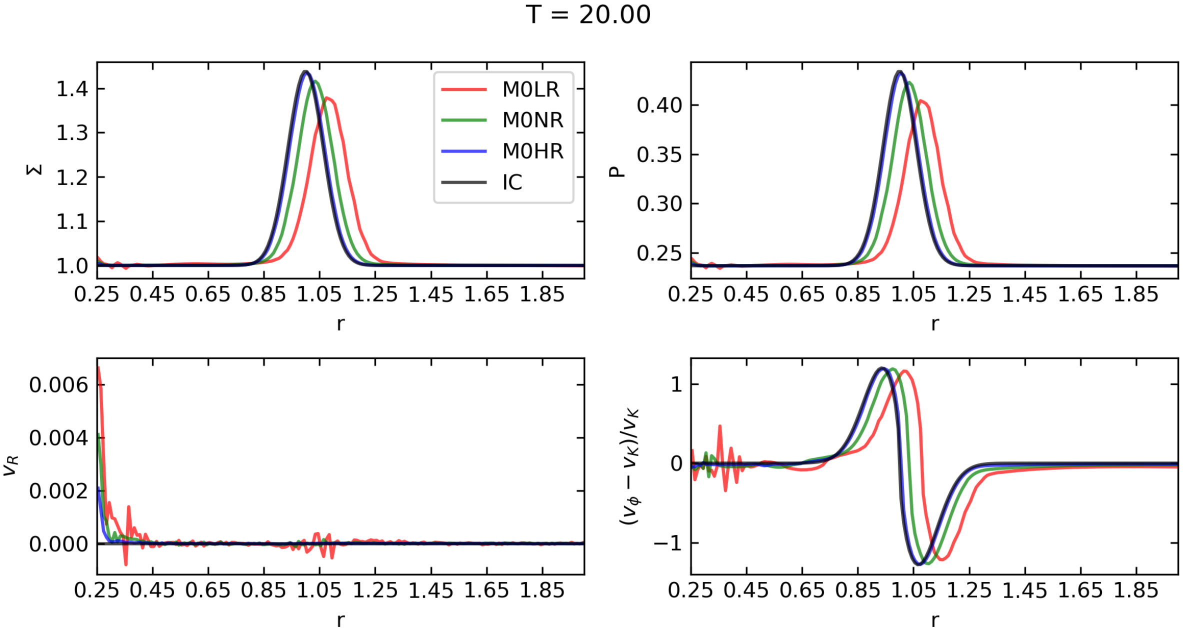

Figure 5.6: The average radial structure at time $T = 20$ for simulations with the axisymmetric Fourier filter and different resolutions. The initial conditions (IC, black line) should be stable. We show the surface density, pressure, radial velocity and the relative difference between the orbital velocity v_ϕ and the Keplerian velocity v_K.

We can conclude that the moving mesh method is able to resolve the RWI and gives results of comparable quality to static grid codes on a polar mesh. The higher order flux integration rules from Zier & Springel (2022a) reduce the noise in the disk which can influence the initial growth of small perturbations. Although the long-term behaviour seems to be less affected by the noise we note that this can change if one does not use a barotropic equation of state but evolves the thermal energy of the gas. In this case, the numerical noise can lead to artificial heating of the disk.

5.5 Appendix: Tests of boundary conditions

Both the inner and outer boundaries can reflect or generate waves, which can then interact with the initial overdensity and impact the instability's evolution. To minimize the effects of boundary conditions on our results, we used a multi-level approach with a damping region, as previously discussed in Section 5.2.2. To evaluate the precision of our methods, we conducted several simulations in which only the axisymmetric mode was allowed to evolve. We varied the resolution and evaluated the evolution of the initial ring-like density enhancement. Thanks to constant noise removal, we expect the radial profiles to be stable. The profiles for different resolutions at $T = 20$ are shown in Fig. 5.6.

The density enhancement shifts towards larger radii, resulting in a decrease in its am-

Simulation	$m = 5$	$m = 4$	$m = 3$	$m = 2$	$m = 1$
AllNR	7.4 - 11.6	11.6 - 12.2	12.2 - 14.8	14.8 - 22	22 -
AllNRBin	7.8 - 12.9	12.9 - 14.2	14.2 - 17	17 - 25.2	25.2 -

Table 5.4: The influence of the binning on a polar mesh on the formation and merging of vortices. We give the time interval in which we observe m vortices.

plitude. As expected, the shift becomes smaller as the resolution is increased and the shape of the peak is stable.

5.6 Appendix: Influence of Fourier filtering on results

The application of a Fourier filter affects the simulation in two ways: by eliminating certain modes and by mapping data onto a polar grid and back. To study the impact of the latter, which only occurs in unstructured mesh simulations, we reran our standard simulation without filtering modes but still mapped in each global time step the hydrodynamic quantities from the Voronoi mesh to the polar mesh and back. This results in approximately 1000 mappings per time unit. As shown in Fig. 5.7, there are small differences between the two simulations in the linear regime, but both simulations accurately describe the exponential growth of the fastest-growing modes and their weakly nonlinear mode coupling. The initial noise level is also similar in both simulations. As one can see in Table 5.4, the vortices have a similar survival time in both simulations, and we can conclude that our mapping between different grids is accurate.

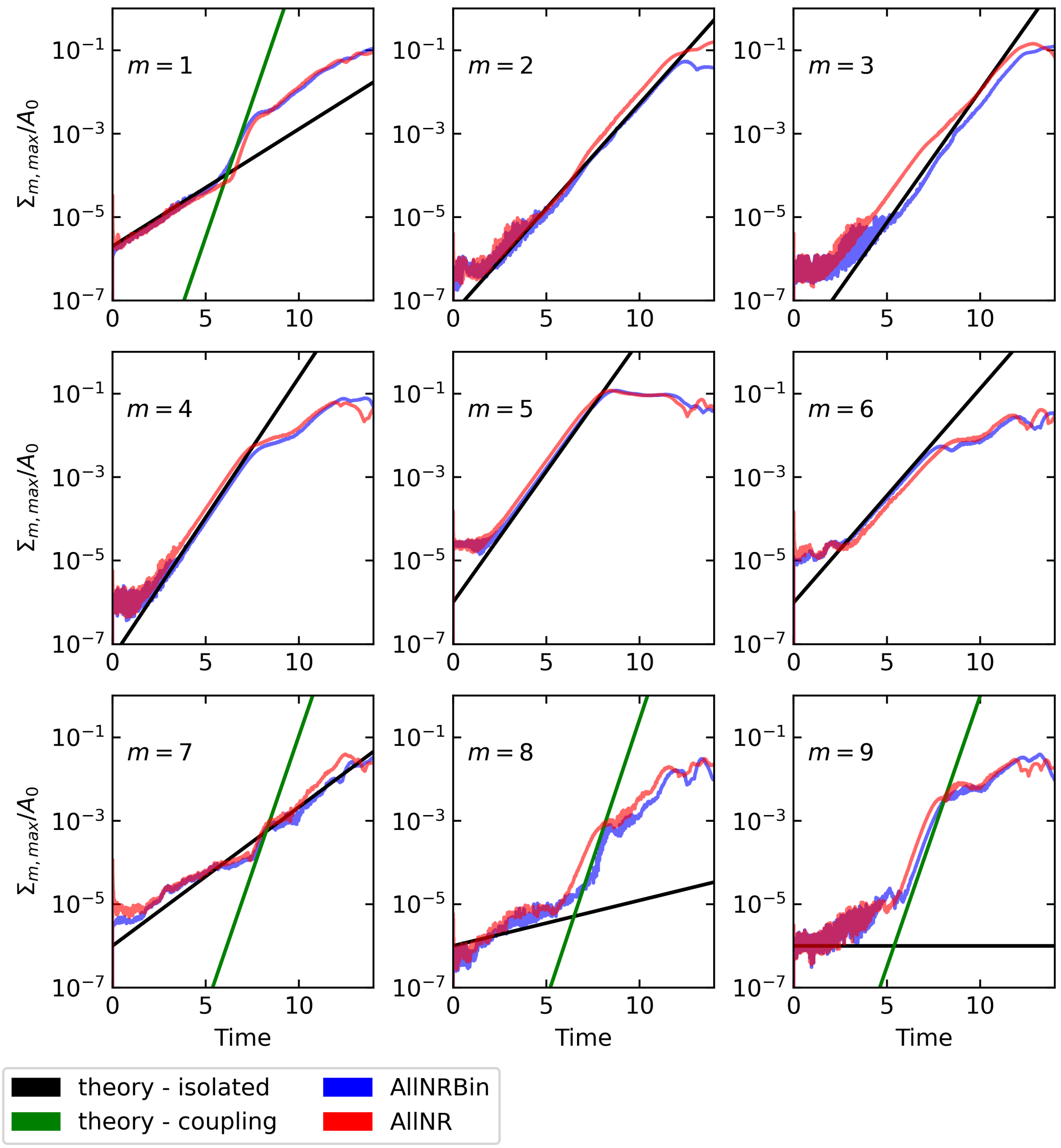

Figure 5.7: The temporal evolution of the maximum absolute value $\Sigma_{\mathrm{m,max}}$ of the Fourier mode $\Sigma_m(r)$ in the radial range $0.8 < r < 1.2$. We use the white noise simulations for this plot, with standard resolution. The only difference between the simulations is that in AllNRBin we bin the data from the Voronoi mesh to the polar mesh and back. The black line corresponds to the isolated linear growth rate from semi-analytic calculations, and the green line to the linear growth rate by mode coupling (see Table 5.2).

Chapter 6

Discussion and outlook

In this chapter, we summarize the results of the thesis and give an outlook for possible studies in the future. For a general overview and the background of this thesis, we refer to Section 1.5.

6.1 Summary of this thesis

The goal of this thesis was to assess how well the moving-mesh method as implemented in the AREPO code performs in simulations of cold gas disks, and to implement new numerical methods to extend its applicability in this field. We concentrated on studying the growth and nonlinear evolution of important fluid instabilities in idealized simulations that allow for a comparison with results obtained by other codes or by analytic theory. Given that the accuracy of different physics modules in a code can vary, we selected the magnetorotational instability, the gravitational instability, and the Rossby wave instability as examples, which rely on the accuracy of the MHD solver, the self-gravity solver, and the hydrodynamic solver, respectively.

As a first step, I implemented the shearing box approximation in AREPO in Chapter 2 and showed that I can achieve second-order convergence in standardised test problems. In contrast to the previous implementations in static grid codes, the code allows a flexible spatial resolution by merging and splitting cells and automatically allows larger time steps due to its quasi-Lagrangian nature. In my first test simulations with the original code version, I observed numerical noise on the grid scale for a moving mesh as well as a static, but unstructured mesh. The main origin of this noise was the use of a second-order accurate integration rule to integrate the flux function over the interface between cells. I implemented higher order integration rules which can fully remove the noise on an unstructured and static grid for a linear shear flow, which highly improves the accuracy for a moving mesh. In particular, the removal of this grid noise is crucial to simulate cold disks, and it was therefore also used in the subsequent projects.

In Chapter 3 I performed an extensive shearing box study of the magnetorotational instability (MRI) in AREPO and compared its evolution with previous results from the literature. I showed that even in the challenging case of an unstratified, tall box without a net field AREPO can, in contrast to other Lagrangian methods such as SPH or MFM, sustain turbulence with a large-scale magnetic field and an active shear current effect. Additionally, a turbulent state with the characteristic butterfly diagram forms in stratified simulations.

In Chapter 4, I presented an adaptive self-gravity solver for the shearing box that is based on the standard TreePM method. I analysed the gravitational instability (GI) with a simplified cooling function that uses a fixed cooling time $t_{\mathrm{cool}} = \beta\Omega^{-1}$ given by a constant β and the orbital frequency Ω. I showed that for weak cooling a gravito-turbulent state with an equilibrium between the explicit cooling and heating through shocks forms. For $0 < \beta < 3 - 4$ the disk always fragments on the cooling time scale while for $\beta > 6$ it is always stable. In the intermediate regime, I observed so-called stochastic fragmentation and the results seem to be converged with resolution.

In Chapter 5, I performed global, two-dimensional simulations of a barotropic disk with an initially circular overdensity with a Gaussian profile. The system is unstable to the Rossby wave instability (RWI) and allows a semi-analytical calculation of linear growth rates. I implemented a module in AREPO that allows the analysis and modification of Fourier modes on the fly and compared the measured growth rates with the expected ones. In the nonlinear regime, the vortices formed by the RWI merge into one vortex that continues orbiting around the central object while slowly migrating inwards. I found perfect agreement with results obtained by Ono et al. (2018) using the ATHENA++ code.

The main conclusion from this thesis is that the use of the moving mesh method with higher order flux integration rules yields results that are at least as accurate as those produced by static grid codes, even when they use an optimized polar grid. All fluid instabilities we discussed in this thesis can be well resolved, confirming that AREPO is a valuable and promising tool to study cold, gaseous disks in the future. Especially if it is not possible to create an optimized grid for a simulation ab initio, AREPO suggests itself as the method of choice.

6.2 Future extension of this thesis

The implementation of the shearing box approximation as well as the removal of the grid noise allows us to conduct several new research projects that were not possible before with AREPO. To this end I also implemented a full nonideal MHD module (not reported here) based on the diffusion solver described in Pakmor et al. (2016a), which will be useful for follow-up projects.

A natural extension of this thesis would be local simulations of accretion disks with self-gravity and ideal MHD to analyze the interaction of MRI and GI and the influence of different cooling descriptions. Riols & Latter (2018) found for this case with the simple β cooling a new, spiral wave dynamo that is different from the normal pure MRI dynamo. In contrast, Löhnert & Peeters (2022) found a coexistence of MRI and GI for a modified cooling function that contains a heating term. Those studies were performed with quite large cooling times for which no fragmentation is expected. As a next step, I could use my nonideal MHD implementation to analyse the importance of different nonideal MHD effects and their interaction with the GI and MRI. Deng et al. (2021) recently found in global simulations that magnetic fields can stop the further growth of fragments which would lead to a more realistic population of protoplanets, but it is unclear if this effect would also be present with nonideal MHD and especially higher resolution.

Although local simulations with the shearing box approximation allow higher resolution than global simulations, they do not allow capturing global phenomena such as accretion and the formation of winds and jets. Especially the GI depends on the box size as long as the size is smaller than ≈ 50 scale heights, therefore this regime might be relevant at small radii. As an extension of my shearing box simulations, I could therefore perform similar, global simulations and compare the results with those obtained in local simulations.

As already discussed in Section 1.1.1, modern computing resources are not powerful enough to simulate full Milky Way-sized galaxies with high enough resolution to resolve the Sedov-Taylor phase of individual supernovae. One possibility to circumvent this is to perform simulations of a cubical patch of the ISM as realized in the TIGRESS and SILCC projects. Both projects use static grid codes (ATHENA, FLASH), but only the first one includes the galactic shear by using a shearing box, which is necessary to model the magnetic field realistically. Since ATHENA does not support dynamical AMR in the shearing box, the spatial resolution is constant in the disk. SILCC also uses a constant spatial resolution in the standard simulations but allows zoom-in simulations for clouds with small bulk velocities. I could implement a similar model in the AREPO code, which would make use of my shearing box implementation including the self-gravity solver. Simpson et al. (2016) performed already similar simulations in AREPO with a mass resolution of $10\,\mathrm{M}_\odot$ without the shearing box. Due to improvements of the algorithms in AREPO as well as due to the growing computational power of modern clusters, a resolution of $1\,\mathrm{M}_\odot$ per cell is realistic in the near term. Especially in the dense regions, this would lead to a higher spatial resolution ($0.7\,\mathrm{pc}$ in gas with $n_\mathrm{H} = 100\,\mathrm{cm}^{-3}$) than the previous projects. By using super refinement strategies I could perform zoom-in simulations that allow me to resolve the details of the internal evolution of molecular clouds and especially their chemical evolution, the influence of early feedback and nonideal MHD effects. I could also further analyse the importance of cosmic rays (CR) on the ISM and outflows, which requires the galactic shear to realistically model the magnetic field.

Bibliography

Akin, J. E. (2005), *Finite element analysis with error estimators: An introduction to the FEM and adaptive error analysis for engineering students*, Elsevier

Arlt, R., Urpin, V. (2004), *Simulations of vertical shear instability in accretion discs*, A&A, 426, 755

Armitage, P. J. (2011), *Dynamics of Protoplanetary Disks*, ARA&A, 49(1), 195

Armitage, P. J. (2022), *Lecture notes on accretion disk physics*, arXiv e-prints, arXiv:2201.07262

Baehr, H., Klahr, H. (2015), *The Role of the Cooling Prescription for Disk Fragmentation: Numerical Convergence and Critical Cooling Parameter in Self-gravitating Disks*, ApJ, 814(2), 155

Baehr, H., Klahr, H., Kratter, K. M. (2017), *The Fragmentation Criteria in Local Vertically Stratified Self-gravitating Disk Simulations*, ApJ, 848(1), 40

Balbus, S. A., Hawley, J. F. (1991), *A Powerful Local Shear Instability in Weakly Magnetized Disks. I. Linear Analysis*, ApJ, 376, 214

Balbus, S. A., Hawley, J. F. (1992), *A Powerful Local Shear Instability in Weakly Magnetized Disks. IV. Nonaxisymmetric Perturbations*, ApJ, 400, 610

Balbus, S. A., Hawley, J. F. (2006), *An Exact, Three-dimensional, Time-dependent Wave Solution in Local Keplerian Flow*, ApJ, 652(2), 1020

Baruteau, C., Barraza, M., Pérez, S., Casassus, S., Dong, R., Lyra, W., Marino, S., Christiaens, V., Zhu, Z., Carmona, A., Debras, F., Alarcon, F. (2019), *Dust traps in the protoplanetary disc MWC 758: two vortices produced by two giant planets?*, MNRAS, 486(1), 304

Baruteau, C., Masset, F. (2008), *Type I Planetary Migration in a Self-Gravitating Disk*, ApJ, 678(1), 483

Berger, M. J., Colella, P. (1989), *Local Adaptive Mesh Refinement for Shock Hydrodynamics*, J. Comput. Phys., 82(1), 64

Binney, J., Tremaine, S. (2008), *Galactic Dynamics: Second Edition*, Princeton university press

Bodo, G., Cattaneo, F., Ferrari, A., Mignone, A., Rossi, P. (2011), *Symmetries, Scaling Laws, and Convergence in Shearing-box Simulations of Magneto-rotational Instability Driven Turbulence*, ApJ, 739(2), 82

Bodo, G., Mignone, A., Cattaneo, F., Rossi, P., Ferrari, A. (2008), *Aspect ratio dependence in magnetorotational instability shearing box simulations*, A&A, 487(1), 1

Bolton, S. J., Adriani, A., Adumitroaie, V., Allison, M., Anderson, J., Atreya, S., Bloxham, J., Brown, S., Connerney, J. E. P., DeJong, E., Folkner, W., Gautier, D., Grassi, D., Gulkis, S., Guillot, T., Hansen, C., Hubbard, W. B., Iess, L., Ingersoll, A., Janssen, M., Jorgensen, J., Kaspi, Y., Levin, S. M., Li, C., Lunine, J., Miguel, Y., Mura, A., Orton, G., Owen, T., Ravine, M., Smith, E., Steffes, P., Stone, E., Stevenson, D., Thorne, R., Waite, J., Durante, D., Ebert, R. W., Greathouse, T. K., Hue, V., Parisi, M., Szalay, J. R., Wilson, R. (2017), *Jupiter's interior and deep atmosphere: The initial pole-to-pole passes with the Juno spacecraft*, Science, 356(6340), 821

Booth, R. A., Clarke, C. J. (2019), *Characterizing gravito-turbulence in 3D: turbulent properties and stability against fragmentation*, MNRAS, 483(3), 3718

Boss, A. P. (1997), *Giant planet formation by gravitational instability.*, Science, 276, 1836

Brandenburg, A. (2008), *The dual role of shear in large-scale dynamos*, Astron. Nachr., 329(7), 725

Brandenburg, A., Johansen, A., Bourdin, P. A., Dobler, W., Lyra, W., Rheinhardt, M., Bingert, S., Haugen, N. E. L., Mee, A., Gent, F., et al. (2020), *The Pencil Code, a modular MPI code for partial differential equations and particles: multipurpose and multiuser-maintained*, arXiv preprint arXiv:2009.08231

Brandenburg, A., Nordlund, Å., Stein, R., Torkelsson, U. (1995), *Dynamo generated turbulence in discs*, in *Small-Scale Structures in Three-Dimensional Hydrodynamic and Magnetohydrodynamic Turbulence*, 385–390, Springer

Brandenburg, A., Nordlund, A., Stein, R. F., Torkelsson, U. (1996), *The Disk Accretion Rate for Dynamo-generated Turbulence*, ApJ, 458, L45

Brandenburg, A., Sokoloff, D. (2002), *Local and Nonlocal Magnetic Diffusion and Alpha-Effect Tensors in Shear Flow Turbulence*, Geophys. Astrophys. Fluid Dyn., 96(4), 319

Brandenburg, A., Subramanian, K. (2005), *Astrophysical magnetic fields and nonlinear dynamo theory*, Phys. Rep., 417(1-4), 1

Brucy, N., Hennebelle, P. (2021), *A two-step gravitational cascade for the fragmentation of self-gravitating discs*, MNRAS, 503(3), 4192

Chandrasekhar, S. (1960), *The Stability of Non-Dissipative Couette Flow in Hydromagnetics*, Proceedings of the National Academy of Science, 46(2), 253

Cimerman, N. P., Rafikov, R. R. (2023), *Emergence of vortices at the edges of planet-driven gaps in protoplanetary discs*, MNRAS, 519(1), 208

Clarke, C. J., Harper-Clark, E., Lodato, G. (2007), *The response of self-gravitating protostellar discs to slow reduction in cooling time-scale: the fragmentation boundary revisited*, MNRAS, 381(4), 1543

Cockburn, B., Karniadakis, G. E., Shu, C.-W. (2012), *Discontinuous Galerkin methods: theory, computation and applications*, Springer Science & Business Media

Cossins, P., Lodato, G., Clarke, C. J. (2009), *Characterizing the gravitational instability in cooling accretion discs*, MNRAS, 393(4), 1157

Cullen, L., Dehnen, W. (2010), *Inviscid smoothed particle hydrodynamics*, MNRAS, 408(2), 669

Curry, C., Pudritz, R. E., Sutherland, P. G. (1994), *On the Global Stability of Magnetized Accretion Disks. I. Axisymmetric Modes*, ApJ, 434, 206

Davis, S. W., Stone, J. M., Pessah, M. E. (2010), *Sustained Magnetorotational Turbulence in Local Simulations of Stratified Disks with Zero Net Magnetic Flux*, ApJ, 713(1), 52

Dedner, A., Kemm, F., Kröner, D., Munz, C. D., Schnitzer, T., Wesenberg, M. (2002), *Hyperbolic Divergence Cleaning for the MHD Equations*, J. Comput. Phys., 175(2), 645

Deng, H., Mayer, L., Helled, R. (2021), *Formation of intermediate-mass planets via magnetically controlled disk fragmentation*, Nature Astronomy, 5, 440

Deng, H., Mayer, L., Latter, H. (2020), *Global Simulations of Self-gravitating Magnetized Protoplanetary Disks*, ApJ, 891(2), 154

Deng, H., Mayer, L., Latter, H., Hopkins, P. F., Bai, X.-N. (2019), *Local Simulations of MRI turbulence with Meshless Methods*, ApJS, 241(2), 26

Deng, H., Mayer, L., Meru, F. (2017), *Convergence of the Critical Cooling Rate for Protoplanetary Disk Fragmentation Achieved: The Key Role of Numerical Dissipation of Angular Momentum*, ApJ, 847(1), 43

Duffell, P. C. (2016), *DISCO: A 3D Moving-mesh Magnetohydrodynamics Code Designed for the Study of Astrophysical Disks*, ApJS, 226(1), 2

Dullemond, C. P. (2013), *Formation of (exo-)planets*, Astron. Nachr., 334(6), 589

Ebrahimi, F., Pharr, M. (2022), *A Nonlocal Magneto-curvature Instability in a Differentially Rotating Disk*, ApJ, 936(2), 145

Evans, C. R., Hawley, J. F. (1988), *Simulation of Magnetohydrodynamic Flows: A Constrained Transport Model*, ApJ, 332, 659

Event Horizon Telescope Collaboration, Akiyama, K., Alberdi, A., Alef, W., Asada, K., Azulay, R., Baczko, A.-K., Ball, D., Baloković, M., Barrett, J., Bintley, D., Blackburn, L., Boland, W., Bouman, K. L., Bower, G. C., Bremer, M., Brinkerink, C. D., Brissenden, R., Britzen, S., Broderick, A. E., Broguiere, D., Bronzwaer, T., Byun, D.-Y., Carlstrom, J. E., Chael, A., Chan, C.-k., Chatterjee, S., Chatterjee, K., Chen, M.-T., Chen, Y., Cho, I., Christian, P., Conway, J. E., Cordes, J. M., Crew, G. B., Cui, Y., Davelaar, J., De Laurentis, M., Deane, R., Dempsey, J., Desvignes, G., Dexter, J., Doeleman, S. S., Eatough, R. P., Falcke, H., Fish, V. L., Fomalont, E., Fraga-Encinas, R., Friberg, P., Fromm, C. M., Gómez, J. L., Galison, P., Gammie, C. F., García, R., Gentaz, O., Georgiev, B., Goddi, C., Gold, R., Gu, M., Gurwell, M., Hada, K., Hecht, M. H., Hesper, R., Ho, L. C., Ho, P., Honma, M., Huang, C.-W. L., Huang, L., Hughes, D. H., Ikeda, S., Inoue, M., Issaoun, S., James, D. J., Jannuzi, B. T., Janssen, M., Jeter, B., Jiang, W., Johnson, M. D., Jorstad, S., Jung, T., Karami, M., Karuppusamy, R., Kawashima, T., Keating, G. K., Kettenis, M., Kim, J.-Y., Kim, J., Kim, J., Kino, M., Koay, J. Y., Koch, P. M., Koyama, S., Kramer, M., Kramer, C., Krichbaum, T. P., Kuo, C.-Y., Lauer, T. R., Lee, S.-S., Li, Y.-R., Li, Z., Lindqvist, M., Liu, K., Liuzzo, E., Lo, W.-P., Lobanov, A. P., Loinard, L., Lonsdale, C., Lu, R.-S., MacDonald, N. R., Mao, J., Markoff, S., Marrone, D. P., Marscher, A. P., Martí-Vidal, I., Matsushita, S., Matthews, L. D., Medeiros, L., Menten, K. M., Mizuno, Y., Mizuno, I., Moran, J. M., Moriyama, K., Moscibrodzka, M., Muller, C., Nagai, H., Nagar, N. M., Nakamura, M., Narayan, R., Narayanan, G., Natarajan, I., Neri, R., Ni, C., Noutsos, A., Okino, H., Olivares, H., Oyama, T., Özel, F., Palumbo, D. C. M., Patel, N., Pen, U.-L., Pesce, D. W., Piétu, V., Plambeck, R., PopStefanija, A., Porth, O., Prather, B., Preciado-López, J. A., Psaltis, D., Pu, H.-Y., Ramakrishnan, V., Rao, R., Rawlings, M. G., Raymond, A. W., Rezzolla, L., Ripperda, B., Roelofs, F., Rogers, A., Ros, E., Rose, M., Roshanineshat, A., Rottmann, H., Roy, A. L., Ruszczyk, C., Ryan, B. R., Rygl, K. L. J., Sánchez, S., Sánchez-Arguelles, D., Sasada, M., Savolainen, T., Schloerb, F. P., Schuster, K.-F., Shao, L., Shen, Z., Small, D., Sohn, B. W., SooHoo, J., Tazaki, F., Tiede, P., Tilanus, R. P. J., Titus, M., Toma, K., Torne, P., Trent, T., Trippe, S., Tsuda, S., van Bemmel, I., van Langevelde, H. J., van Rossum, D. R., Wagner, J., Wardle, J., Weintroub, J., Wex, N., Wharton, R., Wielgus, M., Wong, G. N., Wu, Q., Young, A., Young, K., Younsi, Z., Yuan, F., Yuan, Y.-F., Zensus, J. A., Zhao, G., Zhao, S.-S., Zhu, Z., Anczarski, J., Baganoff, F. K., Eckart, A., Farah, J. R., Haggard, D., Meyer-Zhao, Z., Michalik, D., Nadolski, A., Neilsen, J., Nishioka, H., Nowak, M. A., Pradel, N., Primiani, R. A., Souccar, K., Vertatschitsch, L., Yamaguchi, P., Zhang, S. (2019a), *First M87 Event Horizon Telescope Results. V. Physical Origin of the Asymmetric Ring*, ApJ, 875(1), L5

Event Horizon Telescope Collaboration, Akiyama, K., Alberdi, A., Alef, W., Asada, K., Azulay, R., Baczko, A.-K., Ball, D., Baloković, M., Barrett, J., Bintley, D., Blackburn, L., Boland, W., Bouman, K. L., Bower, G. C., Bremer, M., Brinkerink, C. D., Brissenden, R., Britzen, S., Broderick, A. E., Broguiere, D., Bronzwaer, T., Byun, D.-Y., Carlstrom, J. E., Chael, A., Chan, C.-k., Chatterjee, S., Chatterjee, K., Chen, M.-T., Chen, Y., Cho, I., Christian, P., Conway, J. E., Cordes, J. M., Crew, G. B., Cui, Y., Davelaar, J., De Laurentis, M., Deane, R., Dempsey, J., Desvignes, G., Dexter, J., Doeleman, S. S., Eatough, R. P., Falcke, H., Fish, V. L., Fomalont, E., Fraga-Encinas, R., Freeman, W. T., Friberg, P., Fromm, C. M., Gómez, J. L., Galison, P., Gammie, C. F., García, R., Gentaz, O., Georgiev, B., Goddi, C., Gold, R., Gu, M., Gurwell, M., Hada, K., Hecht, M. H., Hesper, R., Ho, L. C., Ho, P., Honma, M., Huang, C.-W. L., Huang, L., Hughes, D. H., Ikeda, S., Inoue, M., Issaoun, S., James, D. J., Jannuzi, B. T., Janssen, M., Jeter, B., Jiang, W., Johnson, M. D., Jorstad, S., Jung, T., Karami, M., Karuppusamy, R., Kawashima, T., Keating, G. K., Kettenis, M., Kim, J.-Y., Kim, J., Kim, J., Kino, M., Koay, J. Y., Koch, P. M., Koyama, S., Kramer, M., Kramer, C., Krichbaum, T. P., Kuo, C.-Y., Lauer, T. R., Lee, S.-S., Li, Y.-R., Li, Z., Lindqvist, M., Liu, K., Liuzzo, E., Lo, W.-P., Lobanov, A. P., Loinard, L., Lonsdale, C., Lu, R.-S., MacDonald, N. R., Mao, J., Markoff, S., Marrone, D. P., Marscher, A. P., Martí-Vidal, I., Matsushita, S., Matthews, L. D., Medeiros, L., Menten, K. M., Mizuno, Y., Mizuno, I., Moran, J. M., Moriyama, K., Moscibrodzka, M., Müller, C., Nagai, H., Nagar, N. M., Nakamura, M., Narayan, R., Narayanan, G., Natarajan, I., Neri, R., Ni, C., Noutsos, A., Okino, H., Olivares, H., Ortiz-León, G. N., Oyama, T., Özel, F., Palumbo, D. C. M., Patel, N., Pen, U.-L., Pesce, D. W., Piétu, V., Plambeck, R., PopStefanija, A., Porth, O., Prather, B., Preciado-López, J. A., Psaltis, D., Pu, H.-Y., Ramakrishnan, V., Rao, R., Rawlings, M. G., Raymond, A. W., Rezzolla, L., Ripperda, B., Roelofs, F., Rogers, A., Ros, E., Rose, M., Roshanineshat, A., Rottmann, H., Roy, A. L., Ruszczyk, C., Ryan, B. R., Rygl, K. L. J., Sánchez, S., Sánchez-Arguelles, D., Sasada, M., Savolainen, T., Schloerb, F. P., Schuster, K.-F., Shao, L., Shen, Z., Small, D., Sohn, B. W., SooHoo, J., Tazaki, F., Tiede, P., Tilanus, R. P. J., Titus, M., Toma, K., Torne, P., Trent, T., Trippe, S., Tsuda, S., van Bemmel, I., van Langevelde, H. J., van Rossum, D. R., Wagner, J., Wardle, J., Weintroub, J., Wex, N., Wharton, R., Wielgus, M., Wong, G. N., Wu, Q., Young, K., Young, A., Younsi, Z., Yuan, F., Yuan, Y.-F., Zensus, J. A., Zhao, G., Zhao, S.-S., Zhu, Z., Algaba, J.-C., Allardi, A., Amestica, R., Anczarski, J., Bach, U., Baganoff, F. K., Beaudoin, C., Benson, B. A., Berthold, R., Blanchard, J. M., Blundell, R., Bustamente, S., Cappallo, R., Castillo-Domínguez, E., Chang, C.-C., Chang, S.-H., Chang, S.-C., Chen, C.-C., Chilson, R., Chuter, T. C., Córdova Rosado, R., Coulson, I. M., Crawford, T. M., Crowley, J., David, J., Derome, M., Dexter, M., Dornbusch, S., Dudevoir, K. A., Dzib, S. A., Eckart, A., Eckert, C., Erickson, N. R., Everett, W. B., Faber, A., Farah, J. R., Fath, V., Folkers, T. W., Forbes, D. C., Freund, R., Gómez-Ruiz, A. I., Gale, D. M., Gao, F., Geertsema, G., Graham, D. A., Greer, C. H., Grosslein, R., Gueth, F., Haggard, D., Halverson, N. W., Han, C.-C., Han, K.-C., Hao, J., Hasegawa, Y., Henning, J. W., Hernández-Gómez, A., Herrero-Illana, R., Heyminck, S., Hirota, A., Hoge, J., Huang, Y.-D., Impellizzeri, C. M. V., Jiang, H., Kamble, A., Keisler, R., Kimura, K., Kono, Y., Kubo, D., Kuroda, J., Lacasse, R., Laing, R. A., Leitch, E. M., Li, C.-T., Lin, L. C. C., Liu, C.-T., Liu, K.-Y., Lu, L.-M., Marson, R. G., Martin-Cocher, P. L., Massingill, K. D., Matulonis, C., McColl, M. P., McWhirter, S. R., Messias, H., Meyer-Zhao, Z., Michalik, D., Montaña, A., Montgomerie, W., Mora-Klein, M., Muders, D., Nadolski, A., Navarro, S., Neilsen, J., Nguyen, C. H., Nishioka, H., Norton, T., Nowak, M. A., Nystrom, G., Ogawa, H., Oshiro, P., Oyama, T., Parsons, H., Paine, S. N., Peñalver, J., Phillips, N. M., Poirier, M., Pradel, N., Primiani, R. A., Raffin, P. A., Rahlin, A. S., Reiland, G., Risacher, C., Ruiz, I., Sáez-Madaín, A. F., Sassella, R., Schellart, P., Shaw, P., Silva, K. M., Shiokawa, H., Smith, D. R., Snow, W., Souccar, K., Sousa, D., Sridharan, T. K., Srinivasan, R., Stahm, W., Stark, A. A., Story, K., Timmer, S. T., Vertatschitsch, L., Walther, C., Wei, T.-S., Whitehorn, N., Whitney, A. R., Woody, D. P., Wouterloot, J. G. A., Wright, M., Yamaguchi, P., Yu, C.-Y., Zeballos, M., Zhang, S., Ziurys, L. (2019b), *First M87 Event Horizon Telescope Results. I. The Shadow of the Supermassive Black Hole*, ApJ, 875(1), L1

Francis, L., van der Marel, N. (2020), *Dust-depleted Inner Disks in a Large Sample of Transition Disks through Long-baseline ALMA Observations*, ApJ, 892(2), 111

Fricke, K. (1969), *Stability of Rotating Stars II. The Influence of Toroidal and Poloidal Magnetic Fields*, A&A, 1, 388

Fromang, S., Hennebelle, P., Teyssier, R. (2006), *A high order Godunov scheme with constrained transport and adaptive mesh refinement for astrophysical magnetohydrodynamics*, A&A, 457(2), 371

Fromang, S., Lesur, G. (2019), *Angular momentum transport in accretion disks: a hydrodynamical perspective*, in *EAS Publications Series*, volume 82 of *EAS Publications Series*, 391–413

Fromang, S., Papaloizou, J. (2007), *MHD simulations of the magnetorotational instability in a shearing box with zero net flux. I. The issue of convergence*, A&A, 476(3), 1113

Fromang, S., Papaloizou, J., Lesur, G., Heinemann, T. (2007), *MHD simulations of the magnetorotational instability in a shearing box with zero net flux-II. the effect of transport coefficients*, A&A, 476(3), 1123

Fromang, S., Papaloizou, J., Lesur, G., Heinemann, T. (2007), *MHD simulations of the magnetorotational instability in a shearing box with zero net flux. II. The effect of transport coefficients*, A&A, 476(3), 1123

Fung, J., Ono, T. (2021), *Cooling-induced Vortex Decay in Keplerian Disks*, ApJ, 922(1), 13

Gammie, C. F. (2001), *Nonlinear Outcome of Gravitational Instability in Cooling, Gaseous Disks*, ApJ, 553(1), 174

Gingold, R. A., Monaghan, J. J. (1977), *Smoothed particle hydrodynamics: theory and application to non-spherical stars.*, MNRAS, 181, 375

Godon, P. (1996), *Non-reflective boundary conditions and the viscous instability in accretion discs*, MNRAS, 282(4), 1107

Gogichaishvili, D., Mamatsashvili, G., Horton, W., Chagelishvili, G. (2018), *Active Modes and Dynamical Balances in MRI Turbulence of Keplerian Disks with a Net Vertical Magnetic Field*, ApJ, 866(2), 134

Gogichaishvili, D., Mamatsashvili, G., Horton, W., Chagelishvili, G., Bodo, G. (2017), *Nonlinear Transverse Cascade and Sustenance of MRI Turbulence in Keplerian Disks with an Azimuthal Magnetic Field*, ApJ, 845(1), 70

Goldreich, P., Lynden-Bell, D. (1965), *II. Spiral arms as sheared gravitational instabilities*, MNRAS, 130, 125

Gong, M., Ivlev, A. V., Zhao, B., Caselli, P. (2020), *Impact of Magnetorotational Instability on Grain Growth in Protoplanetary Disks. I. Relevant Turbulence Properties*, ApJ, 891(2), 172

Goodman, J., Xu, G. (1994), *Parasitic Instabilities in Magnetized, Differentially Rotating Disks*, ApJ, 432, 213

Gourgouliatos, K. N., Komissarov, S. S. (2018), *Relativistic centrifugal instability*, MNRAS, 475(1), L125

Gressel, O. (2010), *A mean-field approach to the propagation of field patterns in stratified magnetorotational turbulence*, MNRAS, 405(1), 41

Gressel, O., Ziegler, U. (2007), *Shearingbox-implementation for the central-upwind, constraint-transport MHD-code NIRVANA*, Comput. Phys. Commun., 176(11-12), 652

Grzybowski, A., GwóźdŹ, E., Bródka, A. (2000), *Ewald summation of electrostatic interactions in molecular dynamics of a three-dimensional system with periodicity in two directions*, Phys. Rev. B, 61(10), 6706

Guan, X., Gammie, C. F. (2011), *Radially Extended, Stratified, Local Models of Isothermal Disks*, ApJ, 728(2), 130

Guan, X., Gammie, C. F., Simon, J. B., Johnson, B. M. (2009), *Locality of MHD Turbulence in Isothermal Disks*, ApJ, 694(2), 1010

Harten, A., Lax, P. D., Leer, B. v. (1983), *On upstream differencing and Godunov-type schemes for hyperbolic conservation laws*, SIAM review, 25(1), 35

Hawley, J. F., Balbus, S. A., Winters, W. F. (1999), *Local Hydrodynamic Stability of Accretion Disks*, ApJ, 518(1), 394

Hawley, J. F., Gammie, C. F., Balbus, S. A. (1995), *Local Three-dimensional Magnetohydrodynamic Simulations of Accretion Disks*, ApJ, 440, 742

Hawley, J. F., Gammie, C. F., Balbus, S. A. (1996), *Local Three-dimensional Simulations of an Accretion Disk Hydromagnetic Dynamo*, ApJ, 464, 690

Hawley, J. F., Guan, X., Krolik, J. H. (2011), *Assessing Quantitative Results in Accretion Simulations: From Local to Global*, ApJ, 738(1), 84

Hawley, J. F., Richers, S. A., Guan, X., Krolik, J. H. (2013), *Testing Convergence for Global Accretion Disks*, ApJ, 772(2), 102

Haynes, W. M. (2014), *CRC Handbook of Chemistry and Physics*, CRC press

Heinemann, T., McWilliams, J. C., Schekochihin, A. A. (2011), *Large-Scale Magnetic Field Generation by Randomly Forced Shearing Waves*, Phys. Rev. Lett., 107(25), 255004

Held, L. E., Mamatsashvili, G. (2022), *MRI turbulence in accretion discs at large magnetic Prandtl numbers*, MNRAS

Helled, R., Bodenheimer, P., Podolak, M., Boley, A., Meru, F., Nayakshin, S., Fortney, J. J., Mayer, L., Alibert, Y., Boss, A. P. (2014), *Giant Planet Formation, Evolution, and Internal Structure*, in *Protostars and Planets VI*, edited by H. Beuther, R. S. Klessen, C. P. Dullemond, T. Henning, 643

Hill, G. (1878), *Collected Works, Memoir No. 32." also Amer*, J. Math, 1, 5

Hirose, S., Krolik, J. H., Stone, J. M. (2006), *Vertical Structure of Gas Pressure-dominated Accretion Disks with Local Dissipation of Turbulence and Radiative Transport*, ApJ, 640(2), 901

Hirose, S., Shi, J.-M. (2019), *Non-linear outcome of gravitational instability in an irradiated protoplanetary disc*, MNRAS, 485(1), 266

Hopkins, P. F. (2015), *A new class of accurate, mesh-free hydrodynamic simulation methods*, MNRAS, 450(1), 53

Hopkins, P. F. (2016), *A constrained-gradient method to control divergence errors in numerical MHD*, MNRAS, 462(1), 576

Hopkins, P. F., Christiansen, J. L. (2013), *Turbulent Disks are Never Stable: Fragmentation and Turbulence-promoted Planet Formation*, ApJ, 776(1), 48

Huang, S., Yu, C. (2022), *Rossby wave instabilities of protoplanetary discs with cooling*, MNRAS, 514(2), 1733

Hubbard, A., Del Sordo, F., Käpylä, P. J., Brandenburg, A. (2009), *The α effect with imposed and dynamo-generated magnetic fields*, MNRAS, 398(4), 1891

Johansen, A., Youdin, A. (2007), *Protoplanetary Disk Turbulence Driven by the Streaming Instability: Nonlinear Saturation and Particle Concentration*, ApJ, 662(1), 627

Johnson, B. M. (2007), *Magnetohydrodynamic Shearing Waves*, ApJ, 660(2), 1375

Johnson, B. M., Gammie, C. F. (2005), *Linear Theory of Thin, Radially Stratified Disks*, ApJ, 626(2), 978

Kafle, P. R., Sharma, S., Lewis, G. F., Bland-Hawthorn, J. (2014), *On the Shoulders of Giants: Properties of the Stellar Halo and the Milky Way Mass Distribution*, ApJ, 794(1), 59

Kersalé, E., Hughes, D. W., Ogilvie, G. I., Tobias, S. M., Weiss, N. O. (2004), *Global Magnetorotational Instability with Inflow. I. Linear Theory and the Role of Boundary Conditions*, ApJ, 602(2), 892

Kholopov, E. V. (2007), *A simple general proof of the Krazer Prym theorem and related famous formulae resolving convergence properties of Coulomb series in crystals*, Journal of Physics A Mathematical General, 40(23), 6101

Kim, C.-G., Ostriker, E. C. (2017), *Three-phase Interstellar Medium in Galaxies Resolving Evolution with Star Formation and Supernova Feedback (TIGRESS): Algorithms, Fiducial Model, and Convergence*, ApJ, 846(2), 133

Klahr, H., Hubbard, A. (2014), *Convective Overstability in Radially Stratified Accretion Disks under Thermal Relaxation*, ApJ, 788(1), 21

Klahr, H., Pfeil, T., Schreiber, A. (2018), *Instabilities and Flow Structures in Protoplanetary Disks: Setting the Stage for Planetesimal Formation*, in *Handbook of Exoplanets*, edited by H. J. Deeg, J. A. Belmonte, 138, Springer Cham

Klahr, H. H., Bodenheimer, P. (2003), *Turbulence in Accretion Disks: Vorticity Generation and Angular Momentum Transport via the Global Baroclinic Instability*, ApJ, 582(2), 869

Klee, J., Illenseer, T. F., Jung, M., Duschl, W. J. (2017), *The impact of numerical oversteepening on the fragmentation boundary in self-gravitating disks*, A&A, 606, A70

Klee, J., Illenseer, T. F., Jung, M., Duschl, W. J. (2019), *Closing the gap to convergence of gravitoturbulence in local simulations*, A&A, 632, A35

Kratter, K., Lodato, G. (2016), *Gravitational Instabilities in Circumstellar Disks*, ARA&A, 54, 271

Kratter, K. M., Matzner, C. D. (2006), *Fragmentation of massive protostellar discs*, MNRAS, 373(4), 1563

Kratter, K. M., Murray-Clay, R. A. (2011), *Fragment Production and Survival in Irradiated Disks: A Comprehensive Cooling Criterion*, ApJ, 740(1), 1

Krause, F., Rädler, K.-H. (2016), *Mean-field magnetohydrodynamics and dynamo theory*, Elsevier

Kreidberg, L., Bean, J. L., Désert, J.-M., Line, M. R., Fortney, J. J., Madhusudhan, N., Stevenson, K. B., Showman, A. P., Charbonneau, D., McCullough, P. R., Seager, S., Burrows, A., Henry, G. W., Williamson, M., Kataria, T., Homeier, D. (2014), *A Precise Water Abundance Measurement for the Hot Jupiter WASP-43b*, ApJ, 793(2), L27

Latter, H. N., Lesaffre, P., Balbus, S. A. (2009), *MRI channel flows and their parasites*, MNRAS, 394(2), 715

Lau, Y. Y., Bertin, G. (1978), *Discrete spiral modes, spiral waves, and the local dispersion relationship.*, ApJ, 226, 508

Laughlin, G., Bodenheimer, P. (1994), *Nonaxisymmetric Evolution in Protostellar Disks*, ApJ, 436, 335

Lesaffre, P., Balbus, S. A., Latter, H. (2009), *A comparison of local simulations and reduced models of MRI-induced turbulence*, MNRAS, 396(2), 779

Lesur, G. (2020), *Magnetohydrodynamics of protoplanetary discs*, arXiv e-prints, arXiv:2007.15967

Li, H., Lubow, S. H., Li, S., Lin, D. N. C. (2009), *Type I Planet Migration in Nearly Laminar Disks*, ApJ, 690(1), L52

Lin, M.-K. (2014), *Testing large-scale vortex formation against viscous layers in three-dimensional discs*, MNRAS, 437(1), 575

Lin, M.-K., Kratter, K. M. (2016), *On the Gravitational Stability of Gravito-turbulent Accretion Disks*, ApJ, 824(2), 91

Lin, M.-K., Papaloizou, J. C. B. (2010), *Type III migration in a low-viscosity disc*, MNRAS, 405(3), 1473

Lin, M.-K., Pierens, A. (2018), *Vortex survival in 3D self-gravitating accretion discs*, MNRAS, 478(1), 575

Liska, M., Tchekhovskoy, A., Quataert, E. (2020), *Large-scale poloidal magnetic field dynamo leads to powerful jets in GRMHD simulations of black hole accretion with toroidal field*, MNRAS, 494(3), 3656

Löhnert, L., Krätschmer, S., Peeters, A. G. (2020), *Saturation mechanism and generated viscosity in gravito-turbulent accretion disks*, A&A, 640, A53

Löhnert, L., Peeters, A. G. (2022), *Combined dynamo of gravitational and magneto-rotational instability in irradiated accretion discs*, A&A, 663, A176

Long, F., Herczeg, G. J., Harsono, D., Pinilla, P., Tazzari, M., Manara, C. F., Pascucci, I., Cabrit, S., Nisini, B., Johnstone, D., Edwards, S., Salyk, C., Menard, F., Lodato, G., Boehler, Y., Mace, G. N., Liu, Y., Mulders, G. D., Hendler, N., Ragusa, E., Fischer, W. J., Banzatti, A., Rigliaco, E., van de Plas, G., Dipierro, G., Gully-Santiago, M., Lopez-Valdivia, R. (2019), *Compact Disks in a High-resolution ALMA Survey of Dust Structures in the Taurus Molecular Cloud*, ApJ, 882(1), 49

Lovelace, R. V. E., Hohlfeld, R. G. (2013), *Rossby wave instability with self-gravity*, MNRAS, 429(1), 529

Lovelace, R. V. E., Li, H., Colgate, S. A., Nelson, A. F. (1999), *Rossby Wave Instability of Keplerian Accretion Disks*, ApJ, 513(2), 805

Lucy, L. B. (1977), *A numerical approach to the testing of the fission hypothesis.*, AJ, 82, 1013

Lynden-Bell, D., Pringle, J. E. (1974), *The evolution of viscous discs and the origin of the nebular variables*, MNRAS, 168(3), 603

Lyra, W. (2014), *Convective Overstability in Accretion Disks: Three-dimensional Linear Analysis and Nonlinear Saturation*, ApJ, 789(1), 77

Lyra, W., Johansen, A., Klahr, H., Piskunov, N. (2008), *Embryos grown in the dead zone. Assembling the first protoplanetary cores in low mass self-gravitating circumstellar disks of gas and solids*, A&A, 491(3), L41

Lyra, W., Johansen, A., Zsom, A., Klahr, H., Piskunov, N. (2009), *Planet formation bursts at the borders of the dead zone in 2D numerical simulations of circumstellar disks*, A&A, 497(3), 869

Lyra, W., Mac Low, M.-M. (2012), *Rossby Wave Instability at Dead Zone Boundaries in Three-dimensional Resistive Magnetohydrodynamical Global Models of Protoplanetary Disks*, ApJ, 756(1), 62

Mamatsashvili, G., Chagelishvili, G., Pessah, M. E., Stefani, F., Bodo, G. (2020), *Zero Net Flux MRI Turbulence in Disks: Sustenance Scheme and Magnetic Prandtl Number Dependence*, ApJ, 904(1), 47

Mamatsashvili, G. R., Rice, W. K. M. (2010), *Axisymmetric modes in vertically stratified self-gravitating discs*, MNRAS, 406(3), 2050

Marcus, P. S., Pei, S., Jiang, C.-H., Barranco, J. A., Hassanzadeh, P., Lecoanet, D. (2015), *Zombie Vortex Instability. I. A Purely Hydrodynamic Instability to Resurrect the Dead Zones of Protoplanetary Disks*, ApJ, 808(1), 87

Marois, C., Macintosh, B., Barman, T., Zuckerman, B., Song, I., Patience, J., Lafrenière, D., Doyon, R. (2008), *Direct Imaging of Multiple Planets Orbiting the Star HR 8799*, Science, 322(5906), 1348

Masset, F. (2000), *FARGO: A fast eulerian transport algorithm for differentially rotating disks*, A&AS, 141, 165

McNally, C. P., Nelson, R. P., Paardekooper, S.-J., Benítez-Llambay, P. (2019), *Migrating super-Earths in low-viscosity discs: unveiling the roles of feedback, vortices, and laminar accretion flows*, MNRAS, 484(1), 728

Meru, F., Bate, M. R. (2011), *Non-convergence of the critical cooling time-scale for fragmentation of self-gravitating discs*, MNRAS, 411(1), L1

Mignone, A., Bodo, G., Massaglia, S., Matsakos, T., Tesileanu, O., Zanni, C., Ferrari, A. (2007), *PLUTO: A Numerical Code for Computational Astrophysics*, ApJS, 170(1), 228

Miranda, R., Muñoz, D. J., Lai, D. (2017), *Viscous hydrodynamics simulations of circumbinary accretion discs: variability, quasi-steady state and angular momentum transfer*, MNRAS, 466(1), 1170

Miyoshi, T., Kusano, K. (2005), *A multi-state HLL approximate Riemann solver for ideal magnetohydrodynamics*, J. Comput. Phys., 208(1), 315

Mo, H., Van den Bosch, F., White, S. (2010), *Galaxy formation and evolution*, Cambridge University Press

Mocz, P., Vogelsberger, M., Hernquist, L. (2014), *A constrained transport scheme for MHD on unstructured static and moving meshes*, MNRAS, 442(1), 43

Moffatt, H. K. (1978), *Magnetic field generation in electrically conducting fluids*, Cambridge University Press, Cambridge, London, New York, Melbourne, 2, 5

Mousavi, S., Xiao, H., Sukumar, N. (2010), *Generalized Gaussian quadrature rules on arbitrary polygons*, International Journal for Numerical Methods in Engineering, 82(1), 99

Muñoz, D. J., Lai, D., Kratter, K., Miranda, R. (2020), *Circumbinary Accretion from Finite and Infinite Disks*, ApJ, 889(2), 114

Muñoz, D. J., Miranda, R., Lai, D. (2019), *Hydrodynamics of Circumbinary Accretion: Angular Momentum Transfer and Binary Orbital Evolution*, ApJ, 871(1), 84

Müller, T. W. A., Kley, W., Meru, F. (2012), *Treating gravity in thin-disk simulations*, A&A, 541, A123

Nelson, R. P., Gressel, O., Umurhan, O. M. (2013), *Linear and non-linear evolution of the vertical shear instability in accretion discs*, MNRAS, 435(3), 2610

Nipoti, C. (2023), *Local gravitational instability of stratified rotating fluids: three-dimensional criteria for gaseous discs*, MNRAS, 518(4), 5154

Noble, S. C., Krolik, J. H., Hawley, J. F. (2010), *Dependence of Inner Accretion Disk Stress on Parameters: The Schwarzschild Case*, ApJ, 711(2), 959

O'Connell, R. W. (2018), *Cosmic history*, `http://www.faculty.virginia.edu/rwoclass/astr1210/im/anatomy-of-the-MW.jpg`, [Online; accessed 16-January-2019]

Ono, T., Muto, T., Takeuchi, T., Nomura, H. (2016), *Parametric Study of the Rossby Wave Instability in a Two-dimensional Barotropic Disk*, ApJ, 823(2), 84

Ono, T., Muto, T., Tomida, K., Zhu, Z. (2018), *Parametric Study of the Rossby Wave Instability in a Two-dimensional Barotropic Disk. II. Nonlinear Calculations*, ApJ, 864(1), 70

Paardekooper, S.-J. (2012), *Numerical convergence in self-gravitating shearing sheet simulations and the stochastic nature of disc fragmentation*, MNRAS, 421(4), 3286

Paardekooper, S.-J., Baruteau, C., Meru, F. (2011), *Numerical convergence in self-gravitating disc simulations: initial conditions and edge effects*, MNRAS, 416(1), L65

Paardekooper, S.-J., Lesur, G., Papaloizou, J. C. B. (2010), *Vortex Migration in Protoplanetary Disks*, ApJ, 725(1), 146

Pakmor, R., Bauer, A., Springel, V. (2011), *Magnetohydrodynamics on an unstructured moving grid*, MNRAS, 418(2), 1392

Pakmor, R., Pfrommer, C., Simpson, C. M., Kannan, R., Springel, V. (2016a), *Semi-implicit anisotropic cosmic ray transport on an unstructured moving mesh*, MNRAS, 462(3), 2603

Pakmor, R., Springel, V. (2013), *Simulations of magnetic fields in isolated disc galaxies*, MNRAS, 432(1), 176

Pakmor, R., Springel, V., Bauer, A., Mocz, P., Munoz, D. J., Ohlmann, S. T., Schaal, K., Zhu, C. (2016b), *Improving the convergence properties of the moving-mesh code AREPO*, MNRAS, 455(1), 1134

Papaloizou, J. C., Savonije, G. J. (1991), *Instabilities in self-gravitating gaseous discs*, MNRAS, 248, 353

Papaloizou, J. C. B., Lin, D. N. C. (1989), *Nonaxisymmetric Instabilities in Thin Self-gravitating Rings and Disks*, ApJ, 344, 645

Parker, E. N. (2019), *Cosmical magnetic fields: Their origin and their activity*, Oxford university press

Parkin, E. R., Bicknell, G. V. (2013a), *Equilibrium Disks, Magnetorotational Instability Mode Excitation, and Steady-state Turbulence in Global Accretion Disk Simulations*, ApJ, 763(2), 99

Parkin, E. R., Bicknell, G. V. (2013b), *Global simulations of magnetorotational turbulence - I. Convergence and the quasi-steady state*, MNRAS, 435(3), 2281

Penna, R. F., McKinney, J. C., Narayan, R., Tchekhovskoy, A., Shafee, R., McClintock, J. E. (2010), *Simulations of magnetized discs around black holes: effects of black hole spin, disc thickness and magnetic field geometry*, MNRAS, 408(2), 752

Petersen, M. R., Julien, K., Stewart, G. R. (2007a), *Baroclinic Vorticity Production in Protoplanetary Disks. I. Vortex Formation*, ApJ, 658(2), 1236

Petersen, M. R., Stewart, G. R., Julien, K. (2007b), *Baroclinic Vorticity Production in Protoplanetary Disks. II. Vortex Growth and Longevity*, ApJ, 658(2), 1252

Pouquet, A., Frisch, U., Léorat, J. (1976), *Strong MHD helical turbulence and the nonlinear dynamo effect*, J. Fluid Mech., 77(2), 321

Powell, K. G., Roe, P. L., Linde, T. J., Gombosi, T. I., De Zeeuw, D. L. (1999), *A Solution-Adaptive Upwind Scheme for Ideal Magnetohydrodynamics*, J. Comput. Phys., 154(2), 284

Price, D. J. (2012), *Smoothed particle hydrodynamics and magnetohydrodynamics*, J. Comput. Phys., 231(3), 759

Pringle, J. E. (1981), *Accretion discs in astrophysics*, ARA&A, 19, 137

Rädler, K.-H. (1969), *Zur Elektrodynamik in turbulenten, Coriolis-Kräften unterworfenen leitenden Medien.*, Monatsber. Deutsch. Akad Wissenschaftliche Berlin, 11, 194

Raettig, N., Klahr, H., Lyra, W. (2015), *Particle Trapping and Streaming Instability in Vortices in Protoplanetary Disks*, ApJ, 804(1), 35

Raettig, N., Lyra, W., Klahr, H. (2021), *Pebble Trapping in Vortices: Three-dimensional Simulations*, ApJ, 913(2), 92

Rayleigh, L. (1917), *On the Dynamics of Revolving Fluids*, Proceedings of the Royal Society of London Series A, 93(648), 148

Regev, O., Umurhan, O. M. (2008), *On the viability of the shearing box approximation for numerical studies of MHD turbulence in accretion disks*, A&A, 481(1), 21

Rendon Restrepo, S., Barge, P. (2022), *Morphology and dynamical stability of self-gravitating vortices. Numerical simulations*, A&A, 666, A92

Ribas, Á., Bouy, H., Merín, B. (2015), *Protoplanetary disk lifetimes vs. stellar mass and possible implications for giant planet populations*, A&A, 576, A52

Rice, W. K. M., Armitage, P. J., Mamatsashvili, G. R., Lodato, G., Clarke, C. J. (2011), *Stability of self-gravitating discs under irradiation*, MNRAS, 418(2), 1356

Rice, W. K. M., Lodato, G., Armitage, P. J. (2005), *Investigating fragmentation conditions in self-gravitating accretion discs*, MNRAS, 364(1), L56

Riols, A., Latter, H. (2016), *Gravitoturbulence in magnetized protostellar discs*, MNRAS, 460(2), 2223

Riols, A., Latter, H. (2018), *Magnetorotational instability and dynamo action in gravito-turbulent astrophysical discs*, MNRAS, 474(2), 2212

Riols, A., Latter, H. (2019), *Gravitoturbulent dynamos in astrophysical discs*, MNRAS, 482(3), 3989

Riols, A., Latter, H., Paardekooper, S. J. (2017), *Gravitoturbulence and the excitation of small-scale parametric instability in astrophysical discs*, MNRAS, 471(1), 317

Rogachevskii, I., Kleeorin, N. (2003), *Electromotive force and large-scale magnetic dynamo in a turbulent flow with a mean shear*, Phys. Rev. E, 68(3), 036301

Rogachevskii, I., Kleeorin, N. (2004), *Nonlinear theory of a "shear-current" effect and mean-field magnetic dynamos*, Phys. Rev. E, 70(4), 046310

Rusanov, V. (1961), *Calculation of intersection of non-steady shock waves with obstacles*, J. Comput. Math. Phys. USSR, 1, 267

Ruzmaikin, A., Sokolov, D., Shukurov, A. (1988), *Magnetism of spiral galaxies*, Nature, 336(6197), 341

Rybicki, G. B., Lightman, A. P. (1986), *Radiative Processes in Astrophysics*, John Wiley & Sons

Sano, T., Inutsuka, S.-i., Turner, N. J., Stone, J. M. (2004), *Angular Momentum Transport by Magnetohydrodynamic Turbulence in Accretion Disks: Gas Pressure Dependence of the Saturation Level of the Magnetorotational Instability*, ApJ, 605(1), 321

Shakura, N. I., Sunyaev, R. A. (1973), *Black holes in binary systems. Observational appearance.*, A&A, 24, 337

Shen, Y., Stone, J. M., Gardiner, T. A. (2006), *Three-dimensional Compressible Hydrodynamic Simulations of Vortices in Disks*, ApJ, 653(1), 513

Shi, J., Krolik, J. H., Hirose, S. (2010), *What is the Numerically Converged Amplitude of Magnetohydrodynamics Turbulence in Stratified Shearing Boxes?*, ApJ, 708(2), 1716

Shi, J.-M., Chiang, E. (2014), *Gravito-turbulent Disks in Three Dimensions: Turbulent Velocities versus Depth*, ApJ, 789(1), 34

Shi, J.-M., Stone, J. M., Huang, C. X. (2016), *Saturation of the magnetorotational instability in the unstratified shearing box with zero net flux: convergence in taller boxes*, MNRAS, 456(3), 2273

Silant'ev, N. A. (2000), *Magnetic dynamo due to turbulent helicity fluctuations*, A&A, 364, 339

Simon, J. B., Hawley, J. F. (2009), *Viscous and Resistive Effects on the Magnetorotational Instability with a Net Toroidal Field*, ApJ, 707(1), 833

Simon, J. B., Hawley, J. F., Beckwith, K. (2009), *Simulations of Magnetorotational Turbulence with a Higher-Order Godunov Scheme*, ApJ, 690(1), 974

Simon, J. B., Hawley, J. F., Beckwith, K. (2011), *Resistivity-driven State Changes in Vertically Stratified Accretion Disks*, ApJ, 730(2), 94

Simpson, C. M., Pakmor, R., Marinacci, F., Pfrommer, C., Springel, V., Glover, S. C. O., Clark, P. C., Smith, R. J. (2016), *The Role of Cosmic-Ray Pressure in Accelerating Galactic Outflows*, ApJ, 827(2), L29

Springel, V. (2010a), *E pur si muove: Galilean-invariant cosmological hydrodynamical simulations on a moving mesh*, MNRAS, 401(2), 791

Springel, V. (2010b), *Smoothed Particle Hydrodynamics in Astrophysics*, ARA&A, 48, 391

Springel, V., Hernquist, L. (2002), *Cosmological smoothed particle hydrodynamics simulations: the entropy equation*, MNRAS, 333(3), 649

Springel, V., Pakmor, R., Zier, O., Reinecke, M. (2021), *Simulating cosmic structure formation with the GADGET-4 code*, MNRAS, 506(2), 2871

Squire, J., Bhattacharjee, A. (2014), *Nonmodal Growth of the Magnetorotational Instability*, Phys. Rev. Lett., 113(2), 025006

Squire, J., Bhattacharjee, A. (2015a), *Electromotive force due to magnetohydrodynamic fluctuations in sheared rotating turbulence*, Phys. Rev. E, 92(5), 053101

Squire, J., Bhattacharjee, A. (2015b), *Generation of Large-Scale Magnetic Fields by Small-Scale Dynamo in Shear Flows*, Phys. Rev. Lett., 115(17), 175003

Squire, J., Bhattacharjee, A. (2015c), *Statistical Simulation of the Magnetorotational Dynamo*, Phys. Rev. Lett., 114(8), 085002

Stamatellos, D., Whitworth, A. P. (2009), *The properties of brown dwarfs and low-mass hydrogen-burning stars formed by disc fragmentation*, MNRAS, 392(1), 413

Stone, J. M., Gardiner, T. A. (2010), *Implementation of the Shearing Box Approximation in Athena*, ApJS, 189(1), 142

Stone, J. M., Gardiner, T. A., Teuben, P., Hawley, J. F., Simon, J. B. (2008), *Athena: A New Code for Astrophysical MHD*, ApJS, 178(1), 137

Stone, J. M., Hawley, J. F., Gammie, C. F., Balbus, S. A. (1996), *Three-dimensional Magnetohydrodynamical Simulations of Vertically Stratified Accretion Disks*, ApJ, 463, 656

Stone, J. M., Norman, M. L. (1992a), *ZEUS-2D: A Radiation Magnetohydrodynamics Code for Astrophysical Flows in Two Space Dimensions. I. The Hydrodynamic Algorithms and Tests*, ApJS, 80, 753

Stone, J. M., Norman, M. L. (1992b), *ZEUS-2D: A Radiation Magnetohydrodynamics Code for Astrophysical Flows in Two Space Dimensions. II. The Magnetohydrodynamic Algorithms and Tests*, ApJS, 80, 791

Subramanian, K., Brandenburg, A. (2004), *Nonlinear Current Helicity Fluxes in Turbulent Dynamos and Alpha Quenching*, Phys. Rev. Lett., 93(20), 205001

Tarczay-Nehéz, D., Regály, Z., Vorobyov, E. (2020), *On the vortex evolution in non-isothermal protoplanetary discs*, MNRAS, 493(2), 3014

Tobin, J. J., Kratter, K. M., Persson, M. V., Looney, L. W., Dunham, M. M., Segura-Cox, D., Li, Z.-Y., Chandler, C. J., Sadavoy, S. I., Harris, R. J., Melis, C., Pérez, L. M. (2016), *A triple protostar system formed via fragmentation of a gravitationally unstable disk*, Nature, 538(7626), 483

Toomre, A. (1964), *On the gravitational stability of a disk of stars.*, ApJ, 139, 1217

Toro, E. F. (2013), *Riemann solvers and numerical methods for fluid dynamics: a practical introduction*, Springer Science & Business Media

Tricco, T. S., Price, D. J., Bate, M. R. (2016), *Constrained hyperbolic divergence cleaning in smoothed particle magnetohydrodynamics with variable cleaning speeds*, J. Comput. Phys., 322, 326

Turner, N. J., Fromang, S., Gammie, C., Klahr, H., Lesur, G., Wardle, M., Bai, X. N. (2014), *Transport and Accretion in Planet-Forming Disks*, in *Protostars and Planets VI*, edited by H. Beuther, R. S. Klessen, C. P. Dullemond, T. Henning, 411

van der Marel, N., Birnstiel, T., Garufi, A., Ragusa, E., Christiaens, V., Price, D. J., Sallum, S., Muley, D., Francis, L., Dong, R. (2021), *On the Diversity of Asymmetries in Gapped Protoplanetary Disks*, AJ, 161(1), 33 van der Marel, N., van Dishoeck, E. F., Bruderer, S., Birnstiel, T., Pinilla, P., Dullemond, C. P., van Kempen, T. A., Schmalzl, M., Brown, J. M., Herczeg, G. J., Mathews, G. S., Geers, V. (2013), *A Major Asymmetric Dust Trap in a Transition Disk*, Science, 340(6137), 1199

Varnière, P., Tagger, M. (2006), *Reviving Dead Zones in accretion disks by Rossby vortices at their boundaries*, A&A, 446(2), L13

Velikhov, E. (1959), *Stability of an ideally conducting liquid flowing between cylinders rotating in a magnetic field*, Sov. Phys. JETP, 36(9), 995

Vishniac, E. T., Brandenburg, A. (1997), *An incoherent α-ω dynamo in accretion disks*, ApJ, 475(1), 263

Vishniac, E. T., Cho, J. (2001), *Magnetic Helicity Conservation and Astrophysical Dynamos*, ApJ, 550(2), 752

Vogelsberger, M., Sijacki, D., Kereš, D., Springel, V., Hernquist, L. (2012), *Moving mesh cosmology: numerical techniques and global statistics*, MNRAS, 425(4), 3024

Wadsley, J. W., Keller, B. W., Quinn, T. R. (2017), *Gasoline2: a modern smoothed particle hydrodynamics code*, MNRAS, 471(2), 2357

Walch, S., Girichidis, P., Naab, T., Gatto, A., Glover, S. C. O., Wünsch, R., Klessen, R. S., Clark, P. C., Peters, T., Derigs, D., Baczynski, C. (2015), *The SILCC (SImulating the LifeCycle of molecular Clouds) project - I. Chemical evolution of the supernova-driven ISM*, MNRAS, 454(1), 238

Weinberger, R., Springel, V., Pakmor, R. (2020), *The AREPO Public Code Release*, ApJS, 248(2), 32

Williams, J. P., Cieza, L. A. (2011), *Protoplanetary disks and their evolution*, Annual Review of Astronomy and Astrophysics, 49, 67

Wissing, R., Shen, S. (2020), *Smoothed particle magnetohydrodynamics with the geometric density average force expression*, A&A, 638, A140

Wissing, R., Shen, S., Wadsley, J., Quinn, T. (2022), *Magnetorotational instability with smoothed particle hydrodynamics*, A&A, 659, A91

Wurster, J., Price, D. J., Bate, M. R. (2016), *Can non-ideal magnetohydrodynamics solve the magnetic braking catastrophe?*, MNRAS, 457(1), 1037

Yee, H. C., Vinokur, M., Djomehri, M. J. (2000), *Entropy Splitting and Numerical Dissipation*, J. Comput. Phys., 162(1), 33

Yellin-Bergovoy, R., Heifetz, E., Umurhan, O. M. (2016), *On the mechanism of self gravitating Rossby interfacial waves in proto-stellar accretion discs*, Geophys. Astrophys. Fluid Dyn., 110(3), 274

Youdin, A., Johansen, A. (2007), *Protoplanetary Disk Turbulence Driven by the Streaming Instability: Linear Evolution and Numerical Methods*, ApJ, 662(1), 613

Young, M. D., Clarke, C. J. (2015), *Dependence of fragmentation in self-gravitating accretion discs on small-scale structure*, MNRAS, 451(4), 3987

Young, M. D., Clarke, C. J. (2016), *Quantification of stochastic fragmentation of self-gravitating discs*, MNRAS, 455(2), 1438

Yu, C., Li, H. (2009), *Nonaxisymmetric Rossby Vortex Instability with Toroidal Magnetic Fields in Radially Structured Disks*, ApJ, 702(1), 75

Yu, C., Li, H., Li, S., Lubow, S. H., Lin, D. N. C. (2010), *Type I Planet Migration in Nearly Laminar Disks: Long-Term Behavior*, ApJ, 712(1), 198

Zier, O., Springel, V. (2022a), *Simulating cold shear flows on a moving mesh*, MNRAS, 515(1), 525

Zier, O., Springel, V. (2022b), *Simulating the magnetorotational instability on a moving mesh with the shearing box approximation*, MNRAS, 517(2), 2639

Zier, O., Springel, V. (2023), *Gravito-turbulence in local disk simulations with an adaptive moving mesh*, MNRAS

Acknowledgements

I am deeply thankful to my supervisor, Volker Springel, for his constant support and invaluable guidance during my thesis journey. His prompt response to my email and immediate assistance was of tremendous help, particularly during the lockdowns when maintaining a normal level of productivity was challenging. I am also grateful to Rüdiger Pakmor for his assistance in mastering the AREPO code and to Klaus Dolag for his role as the second assessor for my thesis.

My thanks go to all members of the computational astrophysics group and the secretaries and IT group at MPA, who played a crucial role in ensuring smooth operations during the pandemic. Their hard work and dedication are greatly appreciated.

I want to thank the amazing group of friends I made right at the start of my PhD journey, particularly Nahir, Daniel, Miha, and Simon. Their friendship and support has left a lasting impression on me, and I will always remember the bar evenings, hikes, ”Among Us” games during the lockdown, and table football games we shared. I am grateful to Nahir for being there to listen during my PhD's more challenging times. I am already looking forward to our trip to Chile ;)

To my Chinese friends - Zhiyuan, Xueying, Yi, Bocheng, and Han - thank you for the countless happy memories we made over the past two years, from the lunches and cocktail evenings to the adventurous hikes we undertook. I will always remember our Christmas and New Year parties, both Western and Lunar, as well as our trip to Spain. I already anticipate our next journey together to Jerusalem and our yearly Zugspitze hike.

Lastly, my sincere gratitude goes out to Verena, Emanuel, and Lan for their unwavering emotional support during the dark times of the pandemic and my loving parents, who have always been there to offer a supportive hand.